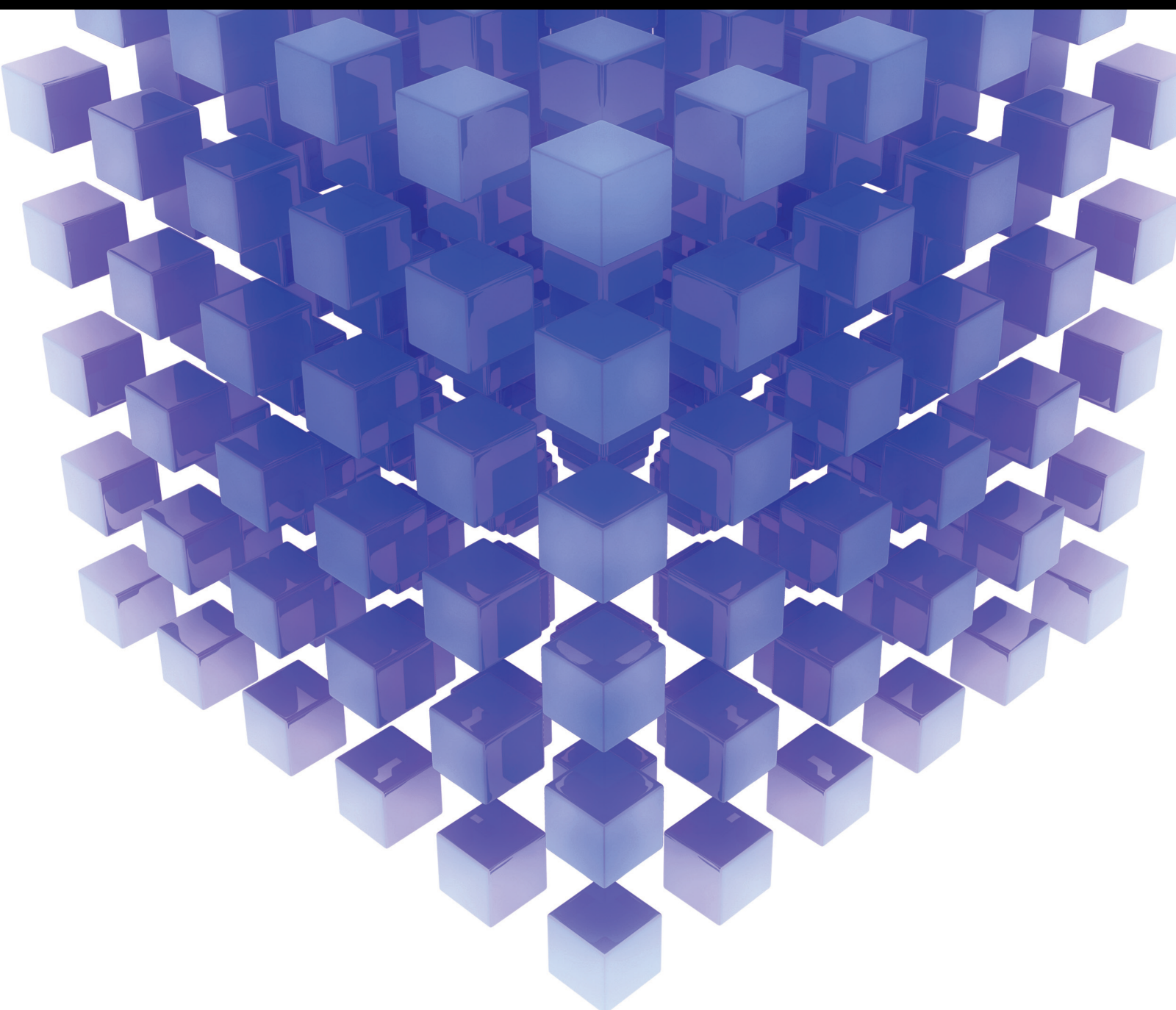


Array Signal Processing with Imperfect Scenarios

Lead Guest Editor: Fangqing Wen

Guest Editors: Xianpeng Wang, Jianfeng Li, and Liangtian Wan



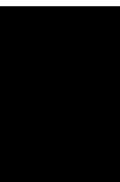
Array Signal Processing with Imperfect Scenarios

Mathematical Problems in Engineering

Array Signal Processing with Imperfect Scenarios

Lead Guest Editor: Fangqing Wen


Guest Editors: Xianpeng Wang, Jianfeng Li, and
Liangtian Wan



Copyright © 2020 Hindawi Limited. All rights reserved.

This is a special issue published in “Mathematical Problems in Engineering.” All articles are open access articles distributed under the Creative Commons Attribution License, which permits unrestricted use, distribution, and reproduction in any medium, provided the original work is properly cited.

Chief Editor

Guangming Xie , China

Academic Editors

Kumaravel A , India
Waqas Abbasi, Pakistan
Mohamed Abd El Aziz , Egypt
Mahmoud Abdel-Aty , Egypt
Mohammed S. Abdo, Yemen
Mohammad Yaghoub Abdollahzadeh
Jamalabadi , Republic of Korea
Rahib Abiyev , Turkey
Leonardo Acho , Spain
Daniela Addressi , Italy
Arooj Adeel , Pakistan
Waleed Adel , Egypt
Ramesh Agarwal , USA
Francesco Aggogeri , Italy
Ricardo Aguilar-Lopez , Mexico
Afaq Ahmad , Pakistan
Naveed Ahmed , Pakistan
Elias Aifantis , USA
Akif Akgul , Turkey
Tareq Al-shami , Yemen
Guido Ala, Italy
Andrea Alaimo , Italy
Reza Alam, USA
Osamah Albahri , Malaysia
Nicholas Alexander , United Kingdom
Salvatore Alfonzetti, Italy
Ghous Ali , Pakistan
Nouman Ali , Pakistan
Mohammad D. Aliyu , Canada
Juan A. Almendral , Spain
A.K. Alomari, Jordan
José Domingo Álvarez , Spain
Cláudio Alves , Portugal
Juan P. Amezcua-Sanchez, Mexico
Mukherjee Amitava, India
Lionel Amodeo, France
Sebastian Anita, Romania
Costanza Arico , Italy
Sabri Arik, Turkey
Fausto Arpino , Italy
Rashad Asharabi , Saudi Arabia
Farhad Aslani , Australia
Mohsen Asle Zaem , USA

Andrea Avanzini , Italy
Richard I. Avery , USA
Viktor Avrutin , Germany
Mohammed A. Awadallah , Malaysia
Francesco Aymerich , Italy
Sajad Azizi , Belgium
Michele Baccocchi , Italy
Seungik Baek , USA
Khaled Bahlali, France
M.V.A Raju Bahubalendruni, India
Pedro Balaguer , Spain
P. Balasubramaniam, India
Stefan Balint , Romania
Ines Tejado Balsera , Spain
Alfonso Banos , Spain
Jerzy Baranowski , Poland
Tudor Barbu , Romania
Andrzej Bartoszewicz , Poland
Sergio Baselga , Spain
S. Caglar Baslamisli , Turkey
David Bassir , France
Chiara Bedon , Italy
Azeddine Beghdadi, France
Andriette Bekker , South Africa
Francisco Beltran-Carbajal , Mexico
Abdellatif Ben Makhlof , Saudi Arabia
Denis Benasciutti , Italy
Ivano Benedetti , Italy
Rosa M. Benito , Spain
Elena Benvenuti , Italy
Giovanni Berselli, Italy
Michele Betti , Italy
Pietro Bia , Italy
Carlo Bianca , France
Simone Bianco , Italy
Vincenzo Bianco, Italy
Vittorio Bianco, Italy
David Bigaud , France
Sardar Muhammad Bilal , Pakistan
Antonio Bilotta , Italy
Sylvio R. Bistafa, Brazil
Chiara Boccaletti , Italy
Rodolfo Bontempo , Italy
Alberto Borboni , Italy
Marco Bortolini, Italy

Paolo Boscariol, Italy
Daniela Boso , Italy
Guillermo Botella-Juan, Spain
Abdesselem Boulkroune , Algeria
Boulaïd Boulkroune, Belgium
Fabio Bovenga , Italy
Francesco Braghin , Italy
Ricardo Branco, Portugal
Julien Bruchon , France
Matteo Bruggi , Italy
Michele Brun , Italy
Maria Elena Bruni, Italy
Maria Angela Butturi , Italy
Bartłomiej Błachowski , Poland
Dhanamjayulu C , India
Raquel Caballero-Águila , Spain
Filippo Cacace , Italy
Salvatore Caddemi , Italy
Zuowei Cai , China
Roberto Caldelli , Italy
Francesco Cannizzaro , Italy
Maosen Cao , China
Ana Carpio, Spain
Rodrigo Carvajal , Chile
Caterina Casavola, Italy
Sara Casciati, Italy
Federica Caselli , Italy
Carmen Castillo , Spain
Inmaculada T. Castro , Spain
Miguel Castro , Portugal
Giuseppe Catalanotti , United Kingdom
Alberto Cavallo , Italy
Gabriele Cazzulani , Italy
Fatih Vehbi Celebi, Turkey
Miguel Cerrolaza , Venezuela
Gregory Chagnon , France
Ching-Ter Chang , Taiwan
Kuei-Lun Chang , Taiwan
Qing Chang , USA
Xiaoheng Chang , China
Prasenjit Chatterjee , Lithuania
Kacem Chehdi, France
Peter N. Cheimets, USA
Chih-Chiang Chen , Taiwan
He Chen , China



































Kebing Chen , China
Mengxin Chen , China
Shyi-Ming Chen , Taiwan
Xizhong Chen , Ireland
Xue-Bo Chen , China
Zhiwen Chen , China
Qiang Cheng, USA
Zeyang Cheng, China
Luca Chiapponi , Italy
Francisco Chicano , Spain
Tirivanhu Chinyoka , South Africa
Adrian Chmielewski , Poland
Seongim Choi , USA
Gautam Choubey , India
Hung-Yuan Chung , Taiwan
Yusheng Ci, China
Simone Cinquemani , Italy
Roberto G. Citarella , Italy
Joaquim Ciurana , Spain
John D. Clayton , USA
Piero Colajanni , Italy
Giuseppina Colicchio, Italy
Vassilios Constantoudis , Greece
Enrico Conte, Italy
Alessandro Contento , USA
Mario Cools , Belgium
Gino Cortellessa, Italy
Carlo Cosentino , Italy
Paolo Crippa , Italy
Erik Cuevas , Mexico
Guozeng Cui , China
Mehmet Cunkas , Turkey
Giuseppe D'Aniello , Italy
Peter Dabnichki, Australia
Weizhong Dai , USA
Zhifeng Dai , China
Purushothaman Damodaran , USA
Sergey Dashkovskiy, Germany
Adiel T. De Almeida-Filho , Brazil
Fabio De Angelis , Italy
Samuele De Bartolo , Italy
Stefano De Miranda , Italy
Filippo De Monte , Italy

José António Fonseca De Oliveira
Correia , Portugal
Jose Renato De Sousa , Brazil
Michael Defoort, France
Alessandro Della Corte, Italy
Laurent Dewasme , Belgium
Sanku Dey , India
Gianpaolo Di Bona , Italy
Roberta Di Pace , Italy
Francesca Di Puccio , Italy
Ramón I. Diego , Spain
Yannis Dimakopoulos , Greece
Hasan Dinçer , Turkey
José M. Domínguez , Spain
Georgios Dounias, Greece
Bo Du , China
Emil Dumic, Croatia
Madalina Dumitriu , United Kingdom
Premraj Durairaj , India
Saeed Eftekhari Azam, USA
Said El Kafhali , Morocco
Antonio Elipse , Spain
R. Emre Erkmen, Canada
John Escobar , Colombia
Leandro F. F. Miguel , Brazil
FRANCESCO FOTI , Italy
Andrea L. Facci , Italy
Shahla Faisal , Pakistan
Giovanni Falsone , Italy
Hua Fan, China
Jianguang Fang, Australia
Nicholas Fantuzzi , Italy
Muhammad Shahid Farid , Pakistan
Hamed Faruqi, Iran
Yann Favennec, France
Fiorenzo A. Fazzolari , United Kingdom
Giuseppe Fedele , Italy
Roberto Fedele , Italy
Baowei Feng , China
Mohammad Ferdows , Bangladesh
Arturo J. Fernández , Spain
Jesus M. Fernandez Oro, Spain
Francesco Ferrise, Italy
Eric Feulvarch , France
Thierry Floquet, France















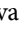
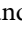
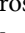
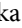






Eric Florentin , France
Gerardo Flores, Mexico
Antonio Forcina , Italy
Alessandro Formisano, Italy
Francesco Franco , Italy
Elisa Francomano , Italy
Juan Frausto-Solis, Mexico
Shujun Fu , China
Juan C. G. Prada , Spain
HECTOR GOMEZ , Chile
Matteo Gaeta , Italy
Mauro Gaggero , Italy
Zoran Gajic , USA
Jaime Gallardo-Alvarado , Mexico
Mosè Gallo , Italy
Akemi Gálvez , Spain
Maria L. Gandarias , Spain
Hao Gao , Hong Kong
Xingbao Gao , China
Yan Gao , China
Zhiwei Gao , United Kingdom
Giovanni Garcea , Italy
José García , Chile
Harish Garg , India
Alessandro Gasparetto , Italy
Stylianos Georgantzinou, Greece
Fotios Georgiades , India
Parviz Ghadimi , Iran
Ştefan Cristian Gherghina , Romania
Georgios I. Giannopoulos , Greece
Agathoklis Giaralis , United Kingdom
Anna M. Gil-Lafuente , Spain
Ivan Giorgio , Italy
Gaetano Giunta , Luxembourg
Jefferson L.M.A. Gomes , United Kingdom
Emilio Gómez-Déniz , Spain
Antonio M. Gonçalves de Lima , Brazil
Qunxi Gong , China
Chris Goodrich, USA
Rama S. R. Gorla, USA
Veena Goswami , India
Xunjie Gou , Spain
Jakub Grabski , Poland

Antoine Grall , France
George A. Gravvanis , Greece
Fabrizio Greco , Italy
David Greiner , Spain
Jason Gu , Canada
Federico Guarracino , Italy
Michele Guida , Italy
Muhammet Gul , Turkey
Dong-Sheng Guo , China
Hu Guo , China
Zhaoxia Guo, China
Yusuf Gurefe, Turkey
Salim HEDDAM , Algeria
ABID HUSSANAN, China
Quang Phuc Ha, Australia
Li Haitao , China
Petr Hájek , Czech Republic
Mohamed Hamdy , Egypt
Muhammad Hamid , United Kingdom
Renke Han , United Kingdom
Weimin Han , USA
Xingsi Han, China
Zhen-Lai Han , China
Thomas Hanne , Switzerland
Xinan Hao , China
Mohammad A. Hariri-Ardebili , USA
Khalid Hattaf , Morocco
Defeng He , China
Xiao-Qiao He, China
Yanchao He, China
Yu-Ling He , China
Ramdane Hedjar , Saudi Arabia
Jude Hemanth , India
Reza Hemmati, Iran
Nicolae Herisanu , Romania
Alfredo G. Hernández-Díaz , Spain
M.I. Herreros , Spain
Eckhard Hitzer , Japan
Paul Honeine , France
Jaromir Horacek , Czech Republic
Lei Hou , China
Yingkun Hou , China
Yu-Chen Hu , Taiwan
Yunfeng Hu, China
Can Huang , China
Gordon Huang , Canada
Linsheng Huo , China
Sajid Hussain, Canada
Asier Ibeas , Spain
Orest V. Iftime , The Netherlands
Przemyslaw Ignaciuk , Poland
Giacomo Innocenti , Italy
Emilio Insfran Pelozo , Spain
Azeem Irshad, Pakistan
Alessio Ishizaka, France
Benjamin Ivorra , Spain
Breno Jacob , Brazil
Reema Jain , India
Tushar Jain , India
Amin Jajarmi , Iran
Chiranjibe Jana , India
Łukasz Jankowski , Poland
Samuel N. Jator , USA
Juan Carlos Jáuregui-Correa , Mexico
Kandasamy Jayakrishna, India
Reza Jazar, Australia
Khalide Jbilou, France
Isabel S. Jesus , Portugal
Chao Ji , China
Qing-Chao Jiang , China
Peng-fei Jiao , China
Ricardo Fabricio Escobar Jiménez , Mexico
Emilio Jiménez Macías , Spain
Maolin Jin, Republic of Korea
Zhuo Jin, Australia
Ramash Kumar K , India
BHABEN KALITA , USA
MOHAMMAD REZA KHEDMATI , Iran
Viacheslav Kalashnikov , Mexico
Mathiyalagan Kalidass , India
Tamas Kalmar-Nagy , Hungary
Rajesh Kaluri , India
Jyottheswara Reddy Kalvakurthi, India
Zhao Kang , China
Ramani Kannan , Malaysia
Tomasz Kapitaniak , Poland
Julius Kaplunov, United Kingdom
Konstantinos Karamanos, Belgium
Michal Kawulok, Poland

Irfan Kaymaz , Turkey
Vahid Kayvanfar , Qatar
Krzysztof Kecik , Poland
Mohamed Khader , Egypt
Chaudry M. Khalique , South Africa
Mukhtaj Khan , Pakistan
Shahid Khan , Pakistan
Nam-Il Kim, Republic of Korea
Philipp V. Kiryukhantsev-Korneev ,
Russia
P.V.V Kishore , India
Jan Koci , Czech Republic
Ioannis Kostavelis , Greece
Sotiris B. Kotsiantis , Greece
Frederic Kratz , France
Vamsi Krishna , India
Edyta Kucharska, Poland
Krzysztof S. Kulpa , Poland
Kamal Kumar, India
Prof. Ashwani Kumar , India
Michal Kunicki , Poland
Cedrick A. K. Kwuimy , USA
Kyandoghere Kyamakya, Austria
Ivan Kyrchei , Ukraine
Márcio J. Lacerda , Brazil
Eduardo Lalla , The Netherlands
Giovanni Lancioni , Italy
Jaroslaw Latalski , Poland
Hervé Laurent , France
Agostino Lauria , Italy
Aimé Lay-Ekuakille , Italy
Nicolas J. Leconte , France
Kun-Chou Lee , Taiwan
Dimitri Lefebvre , France
Eric Lefevre , France
Marek Lefik, Poland
Yaguo Lei , China
Kauko Leiviskä , Finland
Ervin Lenzi , Brazil
ChenFeng Li , China
Jian Li , USA
Jun Li , China
Yueyang Li , China
Zhao Li , China






























Zhen Li , China
En-Qiang Lin, USA
Jian Lin , China
Qibin Lin, China
Yao-Jin Lin, China
Zhiyun Lin , China
Bin Liu , China
Bo Liu , China
Heng Liu , China
Jianxu Liu , Thailand
Lei Liu , China
Sixin Liu , China
Wanquan Liu , China
Yu Liu , China
Yuanchang Liu , United Kingdom
Bonifacio Llamazares , Spain
Alessandro Lo Schiavo , Italy
Jean Jacques Loiseau , France
Francesco Lolli , Italy
Paolo Lonetti , Italy
António M. Lopes , Portugal
Sebastian López, Spain
Luis M. López-Ochoa , Spain
Vassilios C. Loukopoulos, Greece
Gabriele Maria Lozito , Italy
Zhiguo Luo , China
Gabriel Luque , Spain
Valentin Lychagin, Norway
YUE MEI, China
Junwei Ma , China
Xuanlong Ma , China
Antonio Madeo , Italy
Alessandro Magnani , Belgium
Toqeer Mahmood , Pakistan
Fazal M. Mahomed , South Africa
Arunava Majumder , India
Sarfranz Nawaz Malik, Pakistan
Paolo Manfredi , Italy
Adnan Maqsood , Pakistan
Muazzam Maqsood, Pakistan
Giuseppe Carlo Marano , Italy
Damijan Markovic, France
Filipe J. Marques , Portugal
Luca Martinelli , Italy
Denizar Cruz Martins, Brazil

Francisco J. Martos , Spain
Elio Masciari , Italy
Paolo Massioni , France
Alessandro Mauro , Italy
Jonathan Mayo-Maldonado , Mexico
Pier Luigi Mazzeo , Italy
Laura Mazzola, Italy
Driss Mehdi , France
Zahid Mehmood , Pakistan
Roderick Melnik , Canada
Xiangyu Meng , USA
Jose Merodio , Spain
Alessio Merola , Italy
Mahmoud Mesbah , Iran
Luciano Mescia , Italy
Laurent Mevel , France
Constantine Michailides , Cyprus
Mariusz Michta , Poland
Prankul Middha, Norway
Aki Mikkola , Finland
Giovanni Minafò , Italy
Edmondo Minisci , United Kingdom
Hiroyuki Mino , Japan
Dimitrios Mitsotakis , New Zealand
Ardashir Mohammadzadeh , Iran
Francisco J. Montáns , Spain
Francesco Montefusco , Italy
Gisele Mophou , France
Rafael Morales , Spain
Marco Morandini , Italy
Javier Moreno-Valenzuela , Mexico
Simone Morganti , Italy
Caroline Mota , Brazil
Aziz Moukrim , France
Shen Mouquan , China
Dimitris Mourtzis , Greece
Emiliano Mucchi , Italy
Taseer Muhammad, Saudi Arabia
Ghulam Muhiuddin, Saudi Arabia
Amitava Mukherjee , India
Josefa Mula , Spain
Jose J. Muñoz , Spain
Giuseppe Muscolino, Italy
Marco Mussetta , Italy

Hariharan Muthusamy, India
Alessandro Naddeo , Italy
Raj Nandkeolyar, India
Keivan Navaie , United Kingdom
Soumya Nayak, India
Adrian Neagu , USA
Erivelton Geraldo Nepomuceno , Brazil
AMA Neves, Portugal
Ha Quang Thinh Ngo , Vietnam
Nhon Nguyen-Thanh, Singapore
Papakostas Nikolaos , Ireland
Jelena Nikolic , Serbia
Tatsushi Nishi, Japan
Shanzhou Niu , China
Ben T. Nohara , Japan
Mohammed Nouari , France
Mustapha Nourelfath, Canada
Kazem Nouri , Iran
Ciro Núñez-Gutiérrez , Mexico
Włodzimierz Ogryczak, Poland
Roger Ohayon, France
Krzysztof Okarma , Poland
Mitsuhiro Okayasu, Japan
Murat Olgun , Turkey
Diego Oliva, Mexico
Alberto Olivares , Spain
Enrique Onieva , Spain
Calogero Orlando , Italy
Susana Ortega-Cisneros , Mexico
Sergio Ortobelli, Italy
Naohisa Otsuka , Japan
Sid Ahmed Ould Ahmed Mahmoud , Saudi Arabia
Taoreed Owolabi , Nigeria
EUGENIA PETROPOULOU , Greece
Arturo Pagano, Italy
Madhumangal Pal, India
Pasquale Palumbo , Italy
Dragan Pamučar, Serbia
Weifeng Pan , China
Chandan Pandey, India
Rui Pang, United Kingdom
Jürgen Pannek , Germany
Elena Panteley, France
Achille Paolone, Italy

George A. Papakostas , Greece
Xosé M. Pardo , Spain
You-Jin Park, Taiwan
Manuel Pastor, Spain
Pubudu N. Pathirana , Australia
Surajit Kumar Paul , India
Luis Payá , Spain
Igor Pažanin , Croatia
Libor Pekař , Czech Republic
Francesco Pellicano , Italy
Marcello Pellicciari , Italy
Jian Peng , China
Mingshu Peng, China
Xiang Peng , China
Xindong Peng, China
Yuexing Peng, China
Marzio Pennisi , Italy
Maria Patrizia Pera , Italy
Matjaz Perc , Slovenia
A. M. Bastos Pereira , Portugal
Wesley Peres, Brazil
F. Javier Pérez-Pinal , Mexico
Michele Perrella, Italy
Francesco Pesavento , Italy
Francesco Petrini , Italy
Hoang Vu Phan, Republic of Korea
Lukasz Pieczonka , Poland
Dario Piga , Switzerland
Marco Pizzarelli , Italy
Javier Plaza , Spain
Goutam Pohit , India
Dragan Poljak , Croatia
Jorge Pomares , Spain
Hiram Ponce , Mexico
Sébastien Poncet , Canada
Volodymyr Ponomaryov , Mexico
Jean-Christophe Ponsart , France
Mauro Pontani , Italy
Sivakumar Poruran, India
Francesc Pozo , Spain
Aditya Rio Prabowo , Indonesia
Anchasa Pramuanjaroenkij , Thailand
Leonardo Primavera , Italy
B Rajanarayan Prusty, India

Krzysztof Puszynski , Poland
Chuan Qin , China
Dongdong Qin, China
Jianlong Qiu , China
Giuseppe Quaranta , Italy
DR. RITU RAJ , India
Vitomir Racic , Italy
Carlo Rainieri , Italy
Kumbakonam Ramamani Rajagopal, USA
Ali Ramazani , USA
Angel Manuel Ramos , Spain
Higinio Ramos , Spain
Muhammad Afzal Rana , Pakistan
Muhammad Rashid, Saudi Arabia
Manoj Rastogi, India
Alessandro Rasulo , Italy
S.S. Ravindran , USA
Abdolrahman Razani , Iran
Alessandro Reali , Italy
Jose A. Reinoso , Spain
Oscar Reinoso , Spain
Haijun Ren , China
Carlo Renno , Italy
Fabrizio Renno , Italy
Shahram Rezapour , Iran
Ricardo Rianza , Spain
Francesco Riganti-Fulginei , Italy
Gerasimos Rigatos , Greece
Francesco Ripamonti , Italy
Jorge Rivera , Mexico
Eugenio Roanes-Lozano , Spain
Ana Maria A. C. Rocha , Portugal
Luigi Rodino , Italy
Francisco Rodríguez , Spain
Rosana Rodríguez López, Spain
Francisco Rossomando , Argentina
Jose de Jesus Rubio , Mexico
Weiguo Rui , China
Rubén Ruiz , Spain
Ivan D. Rukhlenko , Australia
Dr. Eswaramoorthi S. , India
Weichao SHI , United Kingdom
Chaman Lal Sabharwal , USA
Andrés Sáez , Spain

Bekir Sahin, Turkey
Laxminarayan Sahoo , India
John S. Sakellariou , Greece
Michael Sakellariou , Greece
Salvatore Salamone, USA
Jose Vicente Salcedo , Spain
Alejandro Salcido , Mexico
Alejandro Salcido, Mexico
Nunzio Salerno , Italy
Rohit Salgotra , India
Miguel A. Salido , Spain
Sinan Salih , Iraq
Alessandro Salvini , Italy
Abdus Samad , India
Sovan Samanta, India
Nikolaos Samaras , Greece
Ramon Sancibrian , Spain
Giuseppe Sanfilippo , Italy
Omar-Jacobo Santos, Mexico
J Santos-Reyes , Mexico
José A. Sanz-Herrera , Spain
Musavarah Sarwar, Pakistan
Shahzad Sarwar, Saudi Arabia
Marcelo A. Savi , Brazil
Andrey V. Savkin, Australia
Tadeusz Sawik , Poland
Roberta Sburlati, Italy
Gustavo Scaglia , Argentina
Thomas Schuster , Germany
Hamid M. Sedighi , Iran
Mijanur Rahaman Seikh, India
Tapan Senapati , China
Lotfi Senhadji , France
Junwon Seo, USA
Michele Serpilli, Italy
Silvestar Šesnić , Croatia
Gerardo Severino, Italy
Ruben Sevilla , United Kingdom
Stefano Sfarra , Italy
Dr. Ismail Shah , Pakistan
Leonid Shaikhet , Israel
Vimal Shanmuganathan , India
Prayas Sharma, India
Bo Shen , Germany
Hang Shen, China

Xin Pu Shen, China
Dimitri O. Shepelsky, Ukraine
Jian Shi , China
Amin Shokrollahi, Australia
Suzanne M. Shontz , USA
Babak Shotorban , USA
Zhan Shu , Canada
Angelo Sifaleras , Greece
Nuno Simões , Portugal
Mehakpreet Singh , Ireland
Piyush Pratap Singh , India
Rajiv Singh, India
Seralathan Sivamani , India
S. Sivasankaran , Malaysia
Christos H. Skiadas, Greece
Konstantina Skouri , Greece
Neale R. Smith , Mexico
Bogdan Smolka, Poland
Delfim Soares Jr. , Brazil
Alba Sofi , Italy
Francesco Soldovieri , Italy
Raffaele Solimene , Italy
Yang Song , Norway
Jussi Sopanen , Finland
Marco Spadini , Italy
Paolo Spagnolo , Italy
Ruben Specogna , Italy
Vasilios Spitas , Greece
Ivanka Stamova , USA
Rafał Stanisławski , Poland
Miladin Stefanović , Serbia
Salvatore Strano , Italy
Yakov Strelniker, Israel
Kangkang Sun , China
Qiuqin Sun , China
Shuaishuai Sun, Australia
Yanchao Sun , China
Zong-Yao Sun , China
Kumarasamy Suresh , India
Sergey A. Suslov , Australia
D.L. Suthar, Ethiopia
D.L. Suthar , Ethiopia
Andrzej Swierniak, Poland
Andras Szekrenyes , Hungary
Kumar K. Tamma, USA

Yong (Aaron) Tan, United Kingdom
Marco Antonio Taneco-Hernández , Mexico
Lu Tang , China
Tianyou Tao, China
Hafez Tari , USA
Alessandro Tasora , Italy
Sergio Teggi , Italy
Adriana del Carmen Téllez-Anguiano , Mexico
Ana C. Teodoro , Portugal
Efstathios E. Theotokoglou , Greece
Jing-Feng Tian, China
Alexander Timokha , Norway
Stefania Tomasiello , Italy
Gisella Tomasini , Italy
Isabella Torcicollo , Italy
Francesco Tornabene , Italy
Mariano Torrisi , Italy
Thang nguyen Trung, Vietnam
George Tsiatas , Greece
Le Anh Tuan , Vietnam
Nerio Tullini , Italy
Emilio Turco , Italy
Ilhan Tuzcu , USA
Efstratios Tzirtzilakis , Greece
FRANCISCO UREÑA , Spain
Filippo Ubertini , Italy
Mohammad Uddin , Australia
Mohammad Safi Ullah , Bangladesh
Serdar Ulubeyli , Turkey
Mati Ur Rahman , Pakistan
Panayiotis Vafeas , Greece
Giuseppe Vairo , Italy
Jesus Valdez-Resendiz , Mexico
Eusebio Valero, Spain
Stefano Valvano , Italy
Carlos-Renato Vázquez , Mexico
Martin Velasco Villa , Mexico
Franck J. Vernerey, USA
Georgios Veronis , USA
Vincenzo Vespri , Italy
Renato Vidoni , Italy
Venkatesh Vijayaraghavan, Australia

Anna Vila, Spain
Francisco R. Villatoro , Spain
Francesca Vipiana , Italy
Stanislav Vitek , Czech Republic
Jan Vorel , Czech Republic
Michael Vynnycky , Sweden
Mohammad W. Alomari, Jordan
Roman Wan-Wendner , Austria
Bingchang Wang, China
C. H. Wang , Taiwan
Dagang Wang, China
Guoqiang Wang , China
Huaiyu Wang, China
Hui Wang , China
J.G. Wang, China
Ji Wang , China
Kang-Jia Wang , China
Lei Wang , China
Qiang Wang, China
Qingling Wang , China
Weiwei Wang , China
Xinyu Wang , China
Yong Wang , China
Yung-Chung Wang , Taiwan
Zhenbo Wang , USA
Zhibo Wang, China
Waldemar T. Wójcik, Poland
Chi Wu , Australia
Qihong Wu, China
Yuqiang Wu, China
Zhibin Wu , China
Zhizheng Wu , China
Michalis Xenos , Greece
Hao Xiao , China
Xiao Ping Xie , China
Qingzheng Xu , China
Binghan Xue , China
Yi Xue , China
Joseph J. Yame , France
Chuanliang Yan , China
Xinggang Yan , United Kingdom
Hongtai Yang , China
Jixiang Yang , China
Mijia Yang, USA
Ray-Yeng Yang, Taiwan


Zaoli Yang , China
Jun Ye , China
Min Ye , China
Luis J. Yebra , Spain
Peng-Yeng Yin , Taiwan
Muhammad Haroon Yousaf , Pakistan
Yuan Yuan, United Kingdom
Qin Yuming, China
Elena Zaitseva , Slovakia
Arkadiusz Zak , Poland
Mohammad Zakwan , India
Ernesto Zambrano-Serrano , Mexico
Francesco Zammori , Italy
Jessica Zangari , Italy
Rafal Zdunek , Poland
Ibrahim Zeid, USA
Nianyin Zeng , China
Junyong Zhai , China
Hao Zhang , China
Haopeng Zhang , USA
Jian Zhang , China
Kai Zhang, China
Lingfan Zhang , China
Mingjie Zhang , Norway
Qian Zhang , China
Tianwei Zhang , China
Tongqian Zhang , China
Wenyu Zhang , China
Xianming Zhang , Australia
Xuping Zhang , Denmark
Yinyan Zhang, China
Yifan Zhao , United Kingdom
Debao Zhou, USA
Heng Zhou , China
Jian G. Zhou , United Kingdom
Junyong Zhou , China
Xueqian Zhou , United Kingdom
Zhe Zhou , China
Wu-Le Zhu, China
Gaetano Zizzo , Italy
Mingcheng Zuo, China

Contents



Corrigendum to “Object Detection from the Video Taken by Drone via Convolutional Neural Networks”

Chenfan Sun, Wei Zhan , Jinhui She, and Yangyang Zhang
Corrigendum (1 page), Article ID 4806359, Volume 2020 (2020)


Gridless DOA Estimation for Minimum-Redundancy Linear Array in Nonuniform Noise

Changyun Qi, Gong Zhang , and Jiawen Yuan
Research Article (8 pages), Article ID 1580391, Volume 2020 (2020)

Wireless Localization Based on Deep Learning: State of Art and Challenges

Yun-Xia Ye, An-Nan Lu, Ming-Yi You , Kai Huang , and Bin Jiang
Review Article (8 pages), Article ID 5214920, Volume 2020 (2020)

Object Detection from the Video Taken by Drone via Convolutional Neural Networks

Chenfan Sun, Wei Zhan , Jinhui She, and Yangyang Zhang
Research Article (10 pages), Article ID 4013647, Volume 2020 (2020)

Flexible MIMO Radar Antenna Selection for Vehicle Positioning in IIOT Based on CNN

Yang Xiong , and Ke Wang 
Research Article (10 pages), Article ID 2048606, Volume 2020 (2020)



Direction of Arrival Based on the Multioutput Least Squares Support Vector Regression Model

Kai Huang , Ming-Yi You , Yun-Xia Ye, Bin Jiang, and An-Nan Lu
Research Article (8 pages), Article ID 8601376, Volume 2020 (2020)

Partition Selection for Large-Scale Data Management Using KNN Join Processing

Yue Hu , Ge Peng , Zehua Wang , Yanrong Cui , and Hang Qin 
Research Article (14 pages), Article ID 7898230, Volume 2020 (2020)




On-Chip Embedded Debugging System Based on Leach Algorithm Parameter on Detection of Wireless Sensor Networks

Wenguang Song , Haiyu Chen , Qiujuan Zhang, Bingxin Zhang, Hao Wang, and Hao Xu
Research Article (7 pages), Article ID 7249674, Volume 2020 (2020)

Study on Extraction Methods for Different Components in a Carbonate Digital Core

Xiaoling Xiao, Jiarui Zhang, Xinyu Li, Jing Zhang, and Xiang Zhang 
Research Article (6 pages), Article ID 8972494, Volume 2020 (2020)


A Review on Machine Learning-Based Radio Direction Finding

Ming-Yi You , An-Nan Lu, Yun-Xia Ye , Kai Huang , and Bin Jiang
Review Article (9 pages), Article ID 8345413, Volume 2020 (2020)

Single Snapshot DOA Estimation by Minimizing the Fraction Function in Sparse Recovery




Changlong Wang, Jibin Che , Feng Zhou, Jinyong Hou, and Chen Li
Research Article (8 pages), Article ID 6163529, Volume 2020 (2020)

Sparsity-Based DOA Estimation with Gain and Phase Error Calibration of Generalized Nested Array

Ziang Feng , Guoping Hu, and Hao Zhou

Research Article (9 pages), Article ID 1720310, Volume 2020 (2020)

Key-Frame Detection and Super-Resolution of Hyperspectral Video via Sparse-Based Cumulative Tensor Factorization

Ruofei Zhou , Gang Wang , Bo Li , Jinlong Wang, Tianzhu Liu, and Chungang Liu






Research Article (20 pages), Article ID 9548749, Volume 2020 (2020)

ISAR Imaging Based on Multiple Measurement Vector Model Sparse Signal Recovery Algorithm

Junjie Feng 


Research Article (8 pages), Article ID 1743593, Volume 2020 (2020)

JPEG Lifting Algorithm Based on Adaptive Block Compressed Sensing

Yongjun Zhu , Wenbo Liu , Qian Shen , Yin Wu , and Han Bao 

Research Article (17 pages), Article ID 2873830, Volume 2020 (2020)

Improved Shrinkage Estimator of Large-Dimensional Covariance Matrix under the Complex Gaussian Distribution

Bin Zhang 

Research Article (8 pages), Article ID 6527462, Volume 2020 (2020)

Corrigendum

Corrigendum to “Object Detection from the Video Taken by Drone via Convolutional Neural Networks”

Chenfan Sun, Wei Zhan , Jinhui She, and Yangyang Zhang

School of Computer Science, Yangtze University, Jingzhou, Hubei, China

Correspondence should be addressed to Wei Zhan; zhanwei814@yangtzeu.edu.cn

Received 5 December 2020; Accepted 5 December 2020; Published 14 December 2020

Copyright © 2020 Chenfan Sun et al. This is an open access article distributed under the Creative Commons Attribution License, which permits unrestricted use, distribution, and reproduction in any medium, provided the original work is properly cited.

In the article titled “Object Detection from the Video Taken by Drone via Convolutional Neural Networks” [1], there was a spell error in author Jinhui She’s name in the author list, where “Jinhiu She” should have read as “Jinhui She.” This is corrected as shown above.

References

- [1] C. Sun, W. Zhan, J. She, and Y. Zhang, “Object detection from the video taken by drone via convolutional neural networks,” *Mathematical Problems in Engineering*, vol. 2020, Article ID 4013647, 10 pages, 2020.

Research Article

Gridless DOA Estimation for Minimum-Redundancy Linear Array in Nonuniform Noise

Changyun Qi, Gong Zhang , and Jiawen Yuan

School of Electronic Information and Engineering, Nanjing University of Aeronautics and Astronautics, Nanjing 211106, China

Correspondence should be addressed to Gong Zhang; g Zhang@nuaa.edu.cn

Received 24 July 2020; Revised 10 September 2020; Accepted 4 October 2020; Published 24 October 2020

Academic Editor: Fangqing Wen

Copyright © 2020 Changyun Qi et al. This is an open access article distributed under the Creative Commons Attribution License, which permits unrestricted use, distribution, and reproduction in any medium, provided the original work is properly cited.

A gridless direction-of-arrival (DOA) estimation method to improve the estimation accuracy and resolution in nonuniform noise is proposed in this paper. This algorithm adopts the structure of minimum-redundancy linear array (MRA) and can be composed of two stages. In the first stage, by minimizing the rank of the covariance matrix of the true signal, the covariance matrix that filters out nonuniform noise is obtained, and then a gridless residual energy constraint scheme is designed to reconstruct the signal covariance matrix of the Hermitian Toeplitz structure. Finally, the unknown DOAs can be determined from the recovered covariance matrix, and the number of sources can be acquired as a byproduct. The proposed algorithm can be regarded as a gridless version method based on sparsity. Simulation results indicate that the proposed method has higher estimation accuracy and resolution compared with existing algorithms.

1. Introduction

Direction-of-arrival (DOA) estimation is one of the most important topics in the field of array signal processing [1]; its main purpose is to estimate the angle information of unknown signals spatially based on the array sensor model. Many existing DOA estimation algorithms have good estimation accuracy and resolution [2–5] in additive white Gaussian noise. However, in practical applications, the noise is usually considered to be nonuniform due to the misalignment of the antenna array or the nonidealities of the receiving channels. This nonuniformity leads to a decrease in the estimation accuracy of many DOA estimation algorithms based on the Gaussian white noise.

In recent decades, many measures have been taken to improve the performance of DOA estimation in nonuniform noise. He et al. [6] proposed a DOA estimation algorithm based on the sparse representation of the covariance vector. A linear transformation matrix is designed to remove the nonuniform noise power component, and then it is converted to solve the sparse reconstruction problem based on L1 norm. This algorithm is an improvement of the L1 norm-based array covariance vector sparse representation (L1-SRACV)

algorithm [7], so it is also called improved L1-SRACV (IL1-SRACV) algorithm. Yet the diagonal term information of the signal covariance is lost in the process of removing nonuniform noise power. Yang et al. [8] proposed a sparse parameter estimation technique (SPA) without discretization, using the same covariance matching criteria as sparse iterative covariance-based estimation (SPICE) [9] to transform the covariance fitting problem into a positive semidefinite programming (SDP) [10] problem to solve, and then the post-processing technology is used to estimate the target position, noise variance, and other information from the covariance matrix. This algorithm has many significant advantages, but its performance is poor under low signal-to-noise ratio (SNR). Liao et al. [11] proposed a rank and trace minimization (RTM) algorithm, which transforms the rank minimization problem of the covariance matrix into the noise power maximization problem and then uses the received signal and the nonuniform noise covariance matrix to perform difference to achieve DOA estimation. The algorithm is simple to implement and has low computational complexity, but the structural characteristics of the signal covariance matrix are not taken into account, and the estimation accuracy is low.

Besides, most of the algorithms are based on uniform linear arrays, which results in the resolution being affected by the array aperture. Using well-designed sparse arrays, such as minimum-redundant arrays (MRAs) [12], nested arrays [13], and coprime arrays [14], fewer array elements can be used to obtain larger antenna apertures, and therefore, it becomes an effective way to improve resolution. Among them, MRA is defined as the minimum redundancy of the array element position difference under the condition that the number of array element position difference is continuous. Given the number of array elements, the relative position can be easily determined by looking up the minimum-redundant array structure given in reference [15].

In order to overcome the defects of the existing DOA estimation algorithms in nonuniform noise and combine the advantages of sparse arrays, this paper proposes a gridless DOA estimation algorithm for MRA in nonuniform noise. First, the matrix minimization problem is solved to obtain the noise-removed signal covariance matrix. Since the actual covariance matrix is obtained from the finite snapshot, even if the noise is suppressed in the early stage, the covariance matrix estimation error caused by the finite snapshot still exists. In order to reduce the estimation error and improve the estimation accuracy, a gridless residual constraint scheme that does not rely on noise parameters is designed, and the noiseless Toeplitz matrix is reconstructed. By operating on this matrix, we can not only obtain target angle information but also get the number of sources as a byproduct. The proposed algorithm can be viewed as a gridless version of method based on sparsity, which overcomes the problem of basis mismatch in compressed sensing algorithms.

2. Signal Model and Assumptions

Suppose that a sensor array composed of M elements receives K sources in unknown directions, taking the first array element as the reference array element and the position information of the array element $D = [d_1, d_2, \dots, d_M] = d \times [0, c_1, c_2, \dots, c_{M-1}]$, where d is usually taken as the half wavelength of the signal. The schematic diagram of the array reception of the sparse linear array is shown in Figure 1.

Assuming $K < M$, the received data can be formulated as follows:

$$\mathbf{y}(t) = \mathbf{A}(\theta)\mathbf{s}(t) + \mathbf{n}(t), \quad t = 1, 2, \dots, L, \quad (1)$$

where t is the snapshot index, L stands for the number of snapshots, $\mathbf{y}(t) = [y_1(t), y_2(t), \dots, y_M(t)]^T \in \mathbb{C}^M$ denotes the observation vector, $\mathbf{s}(t) = [s_1(t), s_2(t), \dots, s_K(t)]^T \in \mathbb{C}^K$ represents the source signal vector, and $\mathbf{n}(t) = [n_1(t), n_2(t), \dots, n_M(t)]^T \in \mathbb{C}^M$ is the noise vector, in which the superscript T means transpose operation. \mathbb{C} represents the set of complex numbers, $\theta = [\theta_1, \theta_2, \dots, \theta_K]^T \in \mathbb{C}^K$, where $\theta_k \in [-90^\circ, 90^\circ]$ denotes unknown source directions, and $\mathbf{A}(\theta) = [\mathbf{a}(\theta_1), \mathbf{a}(\theta_2), \dots, \mathbf{a}(\theta_K)]^T \in \mathbb{C}^{M \times K}$ denotes the array manifold matrix, where the steering vector of the k th signal $a(\theta_k)$ satisfies the following equation:

$$\mathbf{a}(\theta_k) = \left[1, e^{j\pi c_1 \sin(\theta_k)}, \dots, e^{j\pi c_{M-1} \sin(\theta_k)} \right]^T \in \mathbb{C}^M. \quad (2)$$

It is easy to see the sparse array can be regarded as a uniform linear array with missing elements. In other words, the received signal can be further expressed as follows:

$$\mathbf{y}(t) = \Phi \mathbf{A}_1(\theta)\mathbf{s}(t) + \Phi \mathbf{n}_1(t), \quad t = 1, 2, \dots, L, \quad (3)$$

where $\mathbf{A}_1(\theta) \in \mathbb{C}^{C \times K}$ refers to the array manifold matrix of a uniform linear array with C sensors, where $C = c_{M-1} + 1$, $\Phi \in \{0, 1\}^{M \times C}$ represents a selection matrix, and in the i th row of which, only the position of the column corresponding to $(c_{i-1} + 1)$ is 1, and the others are 0. Since the aperture of the array has been expanded from $(M-1)d$ to $(C-1)d$, a sparse array composed of the same number of elements has a higher resolution.

Some standard assumptions are formulated here for the solution of the problem. We assume that the signal and the nonuniform noise are considered to be uncorrelated spatially and temporarily and independent of each other:

$$\begin{aligned} E\{\mathbf{s}(t_1)\mathbf{s}^H(t_2)\} &= \mathbf{P}\delta_{t_1, t_2}, \\ E\{\mathbf{n}(t_1)\mathbf{n}^H(t_2)\} &= \mathbf{Q}\delta_{t_1, t_2}, \\ E\{\mathbf{s}(t_1)\mathbf{n}^H(t_2)\} &= E\{\mathbf{n}(t_1)\mathbf{s}^H(t_2)\} = 0, \end{aligned} \quad (4)$$

$$\mathbf{Q} = \text{diag}\{\boldsymbol{\sigma}\},$$

$$\boldsymbol{\sigma} = [\sigma_1^2, \sigma_2^2, \dots, \sigma_M^2]^T,$$

where $E\{\bullet\}$ denotes the mathematical expectation and $(\bullet)^H$ represents conjugate transpose operation. δ_{t_1, t_2} represents the Kronecker delta function, the value of which is one when $t_1 = t_2$, and otherwise, it is zero. $\mathbf{P} \in \mathbb{C}^{K \times K}$ and $\mathbf{Q} \in \mathbb{C}^{M \times M}$ represent the signal correlation matrix and noise correlation matrix, respectively, $\text{diag}(\bullet)$ denotes the diagonal matrix formed by the vectors in brackets, and σ_m^2 represents the noise variance superimposed on the m th sensor.

Based on the above assumptions, the covariance matrix of the signal received by an array can be modelled as follows:

$$\begin{aligned} \mathbf{R} &= E[\mathbf{y}(t)\mathbf{y}^H(t)] = \mathbf{A}(\theta)\mathbf{P}\mathbf{A}^H(\theta) + \mathbf{Q} \\ &= \Phi \mathbf{A}_1(\theta)\mathbf{P}\mathbf{A}_1^H(\theta)\Phi^H + \Phi \mathbf{Q}_1\Phi^H. \end{aligned} \quad (5)$$

It should be noted that in practical applications, the covariance matrix is usually replaced by the sampling covariance matrix \mathbf{R}_e :

$$\mathbf{R}_e = \frac{1}{L} \sum_{t=1}^L \mathbf{y}(t)\mathbf{y}^H(t). \quad (6)$$

3. Rank Minimization-Based Gridless DOA Estimation

The gridless DOA estimation algorithm refers to the angle estimation in the continuous domain to avoid discretization of the angle [16], which effectively overcomes the base mismatch problem in the compressed sensing algorithm [17] and provides a fresh way to improve the estimation accuracy and resolution.

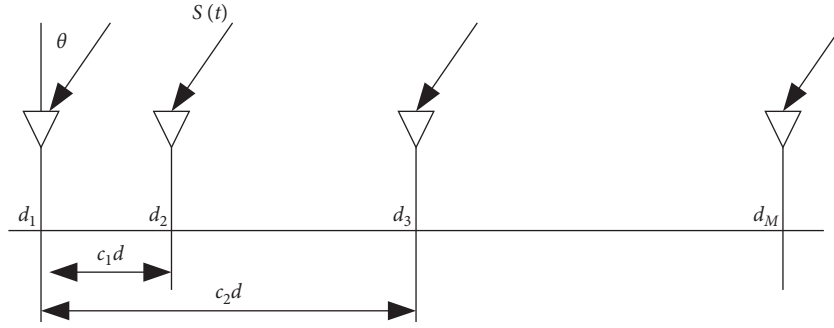


FIGURE 1: Schematic diagram of sparse linear array reception.

3.1. *Denoising Method Based on Rank Minimization.* For noncoherent sources, $\text{rank}(\mathbf{R}_e - \mathbf{Q}) = \text{rank}(\Phi \mathbf{A}_1 \mathbf{P} \mathbf{A}_1^H \Phi^H) = K$, where $\text{rank}(\bullet)$ denotes the rank operation of the matrix in brackets. For any diagonal matrix Λ composed of real numbers, $\text{rank}(\mathbf{R}_e - \Lambda) = \text{rank}(\Phi \mathbf{A}_1(\theta) \mathbf{P} \mathbf{A}_1^H(\theta) \Phi^H + \Phi \mathbf{Q}_1 \Phi^H - \Lambda) \geq K$, and the equality holds if and only if $\Lambda = \Phi \mathbf{Q}_1 \Phi^H$. On account of $K < M$, the problem of estimating the noise covariance matrix \mathbf{Q} can be formulated as follows:

$$\begin{aligned} & \underset{\mathbf{Q}}{\text{minimize}} \text{rank}(\mathbf{R}_e - \Phi \mathbf{Q}_1 \Phi^H), \\ & \text{s.t. } \mathbf{R}_e - \Phi \mathbf{Q}_1 \Phi^H \geq 0, \quad \mathbf{Q}_1 \in \mathbf{Z}^+, \end{aligned} \quad (7)$$

where ≥ 0 means matrix $\mathbf{R}_e - \Phi \mathbf{Q}_1 \Phi^H$ is positive semidefinite and \mathbf{Z}^+ represents a collection of positive definite matrices. Since rank minimization problem is nonconvex and not easy to solve [18], a common method is to use nuclear norm minimization to approximate rank minimization through convex relaxation; since the matrix $\mathbf{R}_e - \Phi \mathbf{Q}_1 \Phi^H$ is a Hermitian matrix and has the characteristic of positive semidefinite, $\text{trace}(\mathbf{R}_e - \Phi \mathbf{Q}_1 \Phi^H)$ is able to be used to take the place of $\|\mathbf{R}_e - \Phi \mathbf{Q}_1 \Phi^H\|_*$. Consequently, the following expression can be obtained:

$$\begin{aligned} & \underset{\mathbf{Q}}{\text{minimize}} \text{trace}(\mathbf{R}_e - \Phi \mathbf{Q}_1 \Phi^H), \\ & \text{s.t. } \mathbf{R}_e - \Phi \mathbf{Q}_1 \Phi^H \geq 0, \quad \mathbf{Q}_1 \in \mathbf{Z}^+, \end{aligned} \quad (8)$$

where $\text{trace}(\bullet)$ represents the trace operation of the matrix which returns the sum of the elements on the main diagonal of the matrix. According to the properties of the matrix trace and the real diagonal characteristics of nonuniform noise, we can easily obtain

$$\begin{aligned} \text{trace}(\mathbf{R}_e - \Phi \mathbf{Q}_1 \Phi^H) &= \text{trace}(\mathbf{R}_e) - \text{trace}(\Phi \mathbf{Q}_1 \Phi^H) \\ &= \text{trace}(\mathbf{R}_e) - E_M \sigma, \end{aligned} \quad (9)$$

where $E_M \in \{0, 1\}^{C \times 1}$ denotes a vector, in which only the elements at the $(c_i + 1)$ position are 1 and the others are 0. Based on equations (8) and (9), the minimization problem in equation (7) can be further transformed as follows:

$$\begin{aligned} & \underset{\sigma}{\text{maximize}} E_M \sigma, \\ & \text{s.t. } \mathbf{R}_e - \Phi \text{diag}(\sigma) \Phi^H \geq 0, \\ & \sigma_m^2 \geq 0, \quad m = 1, 2, \dots, C, \end{aligned} \quad (10)$$

where $\text{diag}(\sigma)$ signifies the diagonal matrix where the diagonal terms are in turn the elements in the vector σ . The optimal estimate of the noise power \mathbf{Q}_e can be acquired by using the CVX optimization toolbox [19] to solve the above positive semidefinite problem. Then, through the difference of the covariance matrices:

$$\mathbf{R}_w = \mathbf{R}_e - \Phi \mathbf{Q}_e \Phi^H, \quad (11)$$

the signal covariance matrix with the noise component removed can be obtained.

3.2. *Residual Constraint Scheme Based on Covariance Matching Criteria.* Since the actual covariance matrix is obtained from the finite snapshot, even if the noise is suppressed in the early stage, the estimation error of the covariance matrix caused by the finite snapshot still exists. To make this problem solved, this paper puts forward a gridless residual constraint scheme that does not depend on the statistical parameters of noise and combines the structural priors of the covariance to achieve the reconstruction of the covariance matrix.

Inspired by the prior information of the low-rank and semidefinite Toeplitz structure of the noise-free signal covariance matrix $T(u)$ and based on the covariance fitting criterion CMC2 [20], the following low-rank matrix reconstruction model can be established:

$$\begin{aligned} & \underset{\mathbf{u}}{\text{minimize}} \text{rank}(\mathbf{T}(\mathbf{u})), \\ & \|\mathbf{R}_e^{-1/2}(\mathbf{R}_e - \Phi \mathbf{R} \Phi^H) \mathbf{R}_e^{-1/2}\|_F^2 \leq \beta^2, \\ & \text{s.t. } \Phi \mathbf{T}(\mathbf{u}) \Phi^H \geq 0, \end{aligned} \quad (12)$$

where $\|\cdot\|_F^2$ represents the square of Frobenius norm of the matrix, and let $\Delta r = \text{vec}(\mathbf{R}_e - \Phi \mathbf{R} \Phi^H)$, in which $\text{vec}(\bullet)$ is a vectorized operator. It can be obtained from reference [20] that the residuals follow an asymptotic normal distribution, that is,

$$\Delta \mathbf{r} \sim \text{AsN}(0_{M^2}, \mathbf{Q}), \quad (13)$$

where $\mathbf{Q} = \mathbf{R}^T \otimes \mathbf{R}/L$ can be replaced by its approximate estimate $\mathbf{Q}_e = \mathbf{R}_e^T \otimes \mathbf{R}_e/L$, $(\bullet)^T$ represents transpose operation, $\text{AsN}(\mu, \sigma^2)$ represents an asymptotic normal distribution whose mean and variance are μ and σ^2 , respectively, and \otimes refers to the Kronecker inner product of the matrix, and it can be deduced further as follows:

$$\|\mathbf{Q}_e^{-1/2} \Delta \mathbf{r}\|_2^2 \sim \text{As}\chi^2(M^2), \quad (14)$$

where $\text{As}\chi^2(M^2)$ stands for asymptotic chi-square distribution with M^2 degrees of freedom and $\|\cdot\|_2^2$ represents the square of Euclidean norm of the matrix. Combining the properties of matrix traces and vectorized operators, we can obtain

$$\begin{aligned} & \|\mathbf{R}_e^{-1/2} (\mathbf{R}_e - \Phi \mathbf{R} \Phi^H) \mathbf{R}_e^{-1/2}\|_F^2 \\ &= \text{tr}\{(\mathbf{R}_e - \Phi \mathbf{R} \Phi^H) \mathbf{R}_e^{-1/2} (\mathbf{R}_e - \Phi \mathbf{R} \Phi^H) \mathbf{R}_e^{-1/2}\} \\ &= \text{vec}^H(\mathbf{R}_e - \Phi \mathbf{R} \Phi^H) \text{vec}\{\mathbf{R}_e^{-1} (\mathbf{R}_e - \Phi \mathbf{R} \Phi^H) \mathbf{R}_e^{-1}\} \\ &= \text{vec}^H(\mathbf{R}_e - \Phi \mathbf{R} \Phi^H) [\mathbf{R}_e^{-T} \otimes \mathbf{R}_e^{-1}] \text{vec}(\mathbf{R}_e - \Phi \mathbf{R} \Phi^H) \\ &= \|\mathbf{Q}_e^{-1/2} \text{vec}(\mathbf{R}_e - \Phi \mathbf{R} \Phi^H)\|_2^2 = \|\mathbf{Q}_e^{-1/2} \Delta \mathbf{r}\|_2^2. \end{aligned} \quad (15)$$

Let $\mathbf{R}_{w0} = \mathbf{R} - \Phi \mathbf{Q}_e \Phi^H$, then $\mathbf{R}_e - \mathbf{R} = \mathbf{R}_w - \mathbf{R}_{w0}$; it can be further acquired that $\|\mathbf{Q}_e^{-1/2} \text{vec}(\mathbf{R}_w - \mathbf{R}_{w0})\|_2^2$ also follows the chi-square distribution of M^2 . As a result, the value of β becomes simple and convenient via MATLAB function $\text{chi2inv}(1 - \eta, M^2)$ [7], where η is a very small number, which means that qualification in equation (12) is satisfied with $(1 - \eta)$ probability. Thus, a specific energy constraint solution can be obtained. Model (12) can be transformed into the following:

$$\begin{aligned} & \underset{\mathbf{u}}{\text{minimize}} \text{rank}[\mathbf{T}(\mathbf{u})], \\ & \text{s.t. } \|\mathbf{Q}_e^{-1/2} \text{vec}(\mathbf{E})\|_2^2 \leq \beta^2, \\ & \mathbf{T}(\mathbf{u}) \geq 0, \end{aligned} \quad (16)$$

where $\mathbf{E} = \mathbf{R}_w - \Phi \mathbf{T}(\mathbf{u}) \Phi^H$. Same as the previous section, the trace function is also used here to replace the rank function, and as a consequence, model (16) can be equivalent to

$$\begin{aligned} & \underset{\mathbf{u}}{\text{minimize}} \text{trace}[\mathbf{T}(\mathbf{u})], \\ & \text{s.t. } \|\mathbf{Q}_e^{-1/2} \text{vec}(\mathbf{E})\|_2^2 \leq \beta^2, \\ & \mathbf{T}(\mathbf{u}) \geq 0. \end{aligned} \quad (17)$$

The above model can be solved by SDPT3 in the CVX optimization toolbox; after the optimal solution u_e of u is obtained, $\mathbf{T}(\mathbf{u}_e)$ can be used to substitute the estimated value of the noise-free covariance matrix $\mathbf{T}(\mathbf{u})$. Since the rank of $\mathbf{T}(\mathbf{u})$ is equal to the number of incident sources in theory, an estimation of the number of incident sources can be obtained based on the calculated rank of $\mathbf{T}(\mathbf{u}_e)$. However, errors inevitably exist in the actual system, which cause $\mathbf{T}(\mathbf{u}_e)$ usually full rank matrix; the M - K smaller singular

values acquired by the singular value decomposition are not strictly equal to zero. At this time, it is unreasonable to obtain the number of sources based on the number of nonzero singular values, but we can set a threshold to judge

$$\widehat{K} = \{m: \widehat{\lambda}_m \geq \kappa\}, \quad m \in [M], \quad (18)$$

where $\widehat{\lambda}_m$ denotes the m th singular value of the matrix $\mathbf{T}(\mathbf{u}_e)$ and κ is the threshold. Reference [21] proves that the value of κ is preferably equal to $0.05 \widehat{\lambda}_{\max}$ through extensive simulation experiments. Finally, we can possess the estimated values of the arrival angle and power of the incident sources by performing Vandermonde decomposition [8] on $\mathbf{T}(\mathbf{u}_e)$. Besides, since the estimated value of the number of sources is known, subspace-based algorithms (e.g., MUSIC) can also be used to further estimate the direction of the incident signal.

4. Algorithm Analysis

4.1. Estimated Accuracy and Resolution. The proposed gridless DOA estimation algorithm makes use of the diagonal characteristics of the nonuniform noise covariance matrix and the Toeplitz and Hermitian properties of the noise-free signal covariance matrix to effectively improve the estimation accuracy of the algorithm and obtain the number of sources as a byproduct. The array aperture is expanded by using MRA, and the resolution is further improved compared with the conventional uniform linear array.

4.2. Identifiability. It can be seen from Section 3.1 that the proposed algorithm is mainly based on the knowledge that the rank of the correlation matrix of incoherent signals is equal to the number of sources in the stage of removing nonuniform noise; therefore, this algorithm is no longer applicable when the sources are coherent. In addition, the number of signal sources should be as small as possible than the number of sensors to ensure the accuracy of the noise power estimation. Empirically, the number of sources that can be identified by the algorithm is $M/2$.

4.3. Computational Complexity. This article mainly measures the computational complexity of the algorithm by comparing the running time of the CPU. When the proposed algorithm is solved with CVX, in the scenario of experiment 6, the number of iterations is basically about 13, while IL1-SRACV needs about 28 iterations under the same error tolerance. Compared with SPA, the proposed algorithm requires a longer running time due to the two-step operation, but in return, the estimation accuracy is higher.

All the experimental processes were completed on a desktop computer with Win10, 3.6 GHz, 8-core processor, and the MATLAB software version used was R2019b.

4.4. Deterministic CRBs. As we all know, the Cramer-Rao bound (CRB) provides a lowest lower bound for arbitrary unbiased parameter estimation [22, 23]. The CRB derivation used in the subsequent simulation is mainly based on

reference [24], and the specific formula can be written as follows:

$$\text{CRB} = \frac{\sigma^2}{2L} \left\{ \text{Re} \left[\left(\tilde{\mathbf{D}}^H \mathbf{P}_A^\perp \tilde{\mathbf{D}} \right) \odot \hat{\mathbf{P}}^T \right] \right\}^{-1}, \quad (19)$$

where $\tilde{\mathbf{A}} = \mathbf{Q}^{-1/2} \Phi \mathbf{A}_1(\theta)$, $\mathbf{D} = [(\mathbf{d}\mathbf{a}_1(\theta)/\theta)|_{\theta=\theta_1}, (\mathbf{d}\mathbf{a}_1(\theta)/\theta)|_{\theta=\theta_2}, \dots, (\mathbf{d}\mathbf{a}_1(\theta)/\theta)|_{\theta=\theta_k}]$, $\tilde{\mathbf{D}} = \mathbf{Q}^{-1/2} \Phi \mathbf{D}$, $\hat{\mathbf{P}} = (1/N) \sum_{i=1}^N \mathbf{s}(i) \mathbf{s}(i)^H$, \mathbf{P}_A^\perp represents the orthogonal projection of matrix $\tilde{\mathbf{A}}$ on \mathbf{P} , and \odot means the Hadamard product of a matrix.

5. Numerical Simulations

In this part, we conducted simulation experiments to test the performance of the proposed two-stage method and compared it with subspace-based method RTM, sparse representation-based method IL1-SRACV, and gridless method SPA. To be fair, we extend the algorithms listed above to MRA. Unless other specified, we assume that the incident sources are independent with the same power p , the array is the MRA with 8 elements, and the relative position of MRA is $D = [0, 1, 4, 10, 16, 18, 21, 23] \times d$. The covariance matrix of nonuniform noise satisfies

$$\mathbf{Q} = \text{diag}\{10.0, 2.0, 8.5, 10.5, 5.0, 10.0, 10.5, 3.0\}. \quad (20)$$

The SNR is defined as follows [22]:

$$\text{SNR} = 10 \log_{10} \left[\frac{p}{M} \times \sum_{m=1}^M (1/q_m) \right] \text{dB}. \quad (21)$$

5.1. Experiment 1. We assume four independent sources from the direction of $\theta = [-5.0^\circ, 0^\circ, 5.0^\circ, 10.0^\circ]$. The snapshot number $L = 300$, SNR = 0 dB, and $\eta = 0.001$. Figure 2 presents the spatial spectrum of the proposed algorithm, SPA, and RTM. It is easy to see that the proposed method has a relatively sharp peak and is easier to distinguish under the same conditions.

5.2. Experiment 2. Let two independent sources are relatively close, where $\theta = [-1.0^\circ, 1.0^\circ]$; other experimental conditions are consistent with experiment 1. Figure 3 shows the spatial spectrum of the proposed algorithm in ULA and MRA composed of 8 array elements. As can be seen from Figure 3, the spatial spectrum of the proposed method in MRA can better distinguish two sources that are closer together. In other words, the adoption of MRA can effectively improve the resolution.

5.3. Experiment 3. Let $\theta = [-3.41^\circ, 6.37^\circ]$ and $L = 500$; the change of the SNR is increased from -10 dB in steps of 2 dB to 10 dB. 300 Monte Carlo experiments were conducted to reduce the contingency of the experiment. The estimation accuracy of the algorithm is mainly measured by root mean square error (RMSE), which can be expressed as follows:

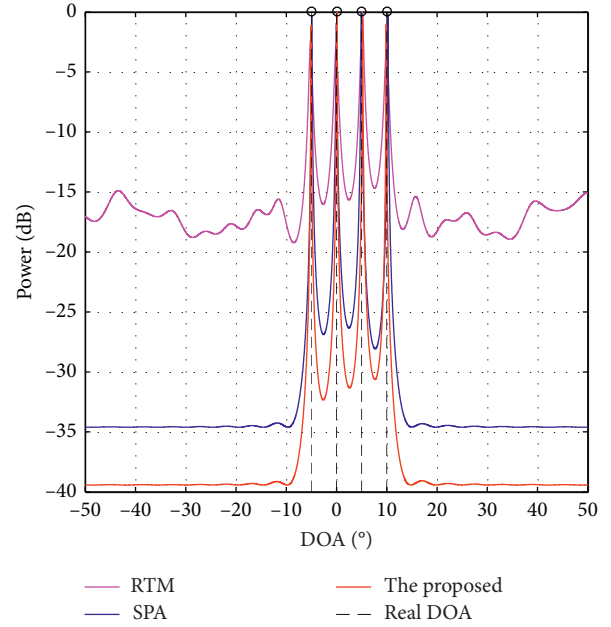


FIGURE 2: Spatial spectrum of the proposed method ($M=8$, SNR=0 dB, $L=300$, and $\theta = [-5.0^\circ, 0^\circ, 5.0^\circ, 10.0^\circ]$).

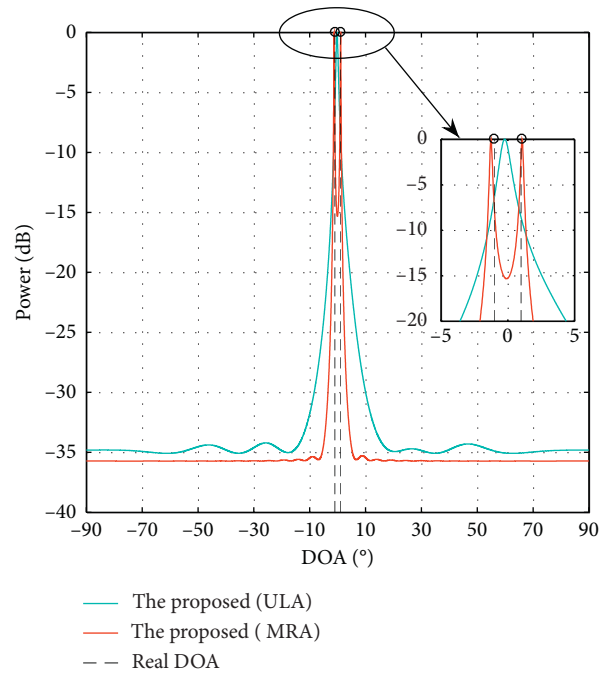


FIGURE 3: Spatial spectrum of the proposed method ($M=8$, SNR=0 dB, $L=300$, and $\theta = [-1.0^\circ, 1.0^\circ]$).

$$\text{RMSE} = \sqrt{\frac{\sum_{l=1}^L \sum_{k=1}^K (\hat{\theta}_k(l) - \theta_k)^2}{L \times K}}. \quad (22)$$

Figure 4 shows the plot of estimation error and success probability with SNR, where Figure 4(a) shows the change curve of RMSE and Figure 4(b) shows the change curve of success probability. Here, the success probability refers to the ratio of the number of experiments with the error

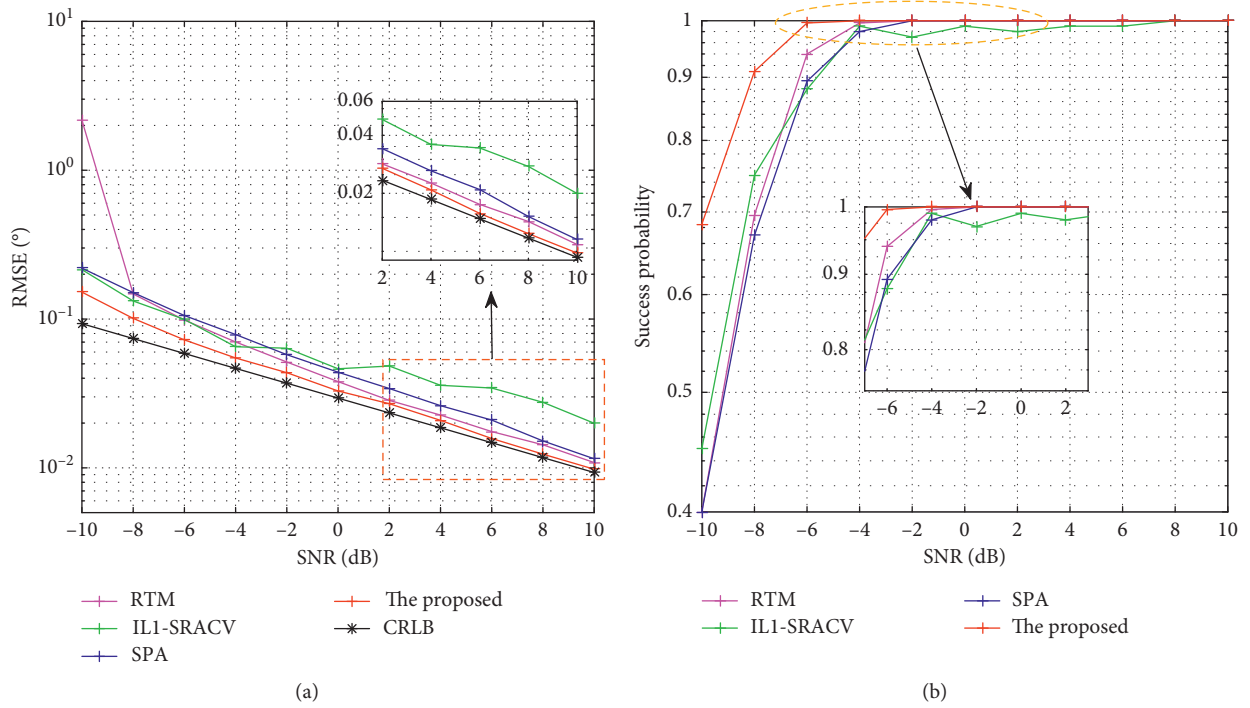


FIGURE 4: The RMSE and the success probability of different methods vary with SNR ($M = 8$ and $L = 500$). (a) The change curve of RMSE. (b) The change curve of success probability.

between the estimated angles and the real angles not more than 0.2° and the total number of Monte Carlo experiments. It can be seen from Figure 4(a) that the RMSEs of all methods decrease with the increase of SNR. Compared with other algorithms, the proposed method has the smallest RMSE and gradually fits to the CRB with the increase of SNR. As can be seen from Figure 4(b), the proposed method can guarantee the estimation error within 0.2° at $SNR = -6$ dB. From the above results, we can conclude that the proposed method has obvious advantages over other methods in estimation accuracy.

5.4. Experiment 4. We set the SNR to 0 dB, and the number of snapshots increased from 100 to 1000 with an interval of 100, and $\theta = [-3.41^\circ, 5.37^\circ]$. 300 independent Monte Carlo experiments were also conducted. Figure 5 shows the change curve of RMSE with the number of snapshots. It can be summarized from the figure that the estimation error of the proposed method is smaller than that of other algorithms overall. With the increase in the number of snapshots, the RMSE of the proposed algorithm is closer to the CRB low bound.

5.5. Experiment 5. Let $L = 500$; other experimental conditions are the same as experiment 4, and the change of the SNR is increased from -10 dB in steps of 2 dB to 10 dB. Figure 6 shows the success rate of the source estimation of the proposed algorithm compared with that of Akaike's information criterion (AIC), minimum description length

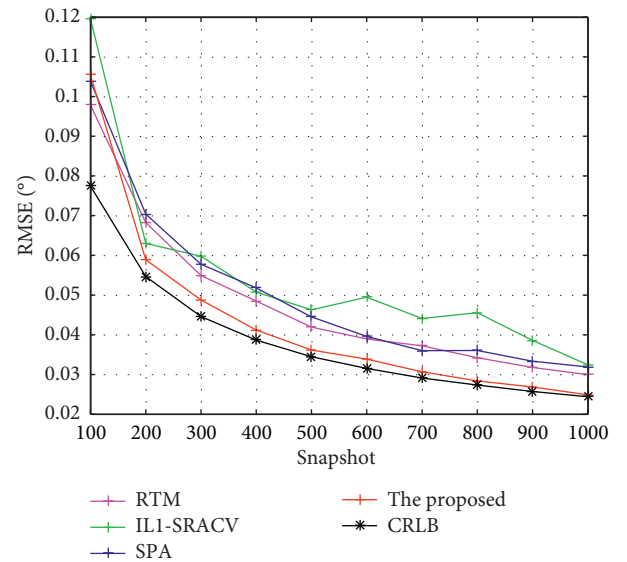


FIGURE 5: The RMSE of different methods varies with snapshot ($M = 8$ and $SNR = 0$ dB).

(MDL) [25], and Gershgorin disk estimator (GDE) [26]. The success rate is defined as the ratio of the number of accurate estimations of all sources to the total number of Monte Carlo experiments. It can be summarized from Figure 6 that the proposed method has better estimation accuracy than other

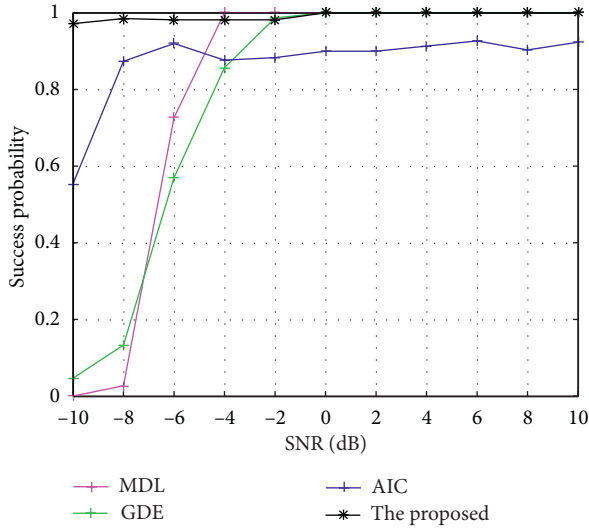


FIGURE 6: The success probability of sources varies with SNR ($M = 8$ and $L = 500$).

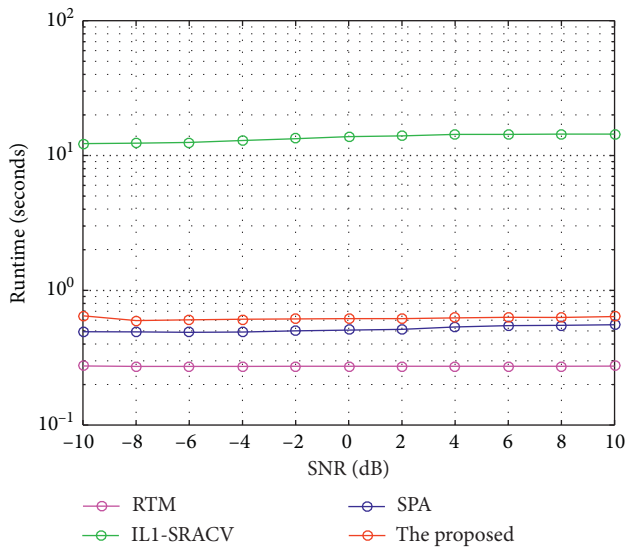


FIGURE 7: The average running time varies with SNR ($M = 8$ and $L = 400$).

algorithms under low SNR and has a higher success probability overall.

5.6. Experiment 6. Let $\theta = [-4.78^\circ, 2.56^\circ]$ and $L = 400$; other experimental conditions are the same as experiment 3. Figure 7 shows the curve of the average running time of different algorithms versus SNR. It can be seen from the figure that RTM has low computational complexity and takes the shortest time. The running time of the proposed algorithm is much lower than that of IL1-SRACV and slightly higher than that of SPA. The average running time of the algorithms increases slightly with the increase of the SNR.

6. Conclusions

This paper proposes a two-stage gridless DOA estimation algorithm for MRA in nonuniform noise. The proposed method can not only effectively eliminate the effect of nonuniform noise but also further improve the estimation accuracy and resolution. Moreover, the number of signals is also able to be acquired as a byproduct. Simulation experiments prove the performance of the proposed method.

Data Availability

The data used to support the findings of this study are included within the article.

Conflicts of Interest

The authors declare that there are no conflicts of interest regarding the publication of this paper.

Acknowledgments

This study was supported by the National Natural Science Foundation of China (nos. 61871218, 61801211, 61701046, and 61671241), the Fundamental Research Funds for the Central University, China (grant nos. 3082019NC2019002, NG2020001, and 3082017NP2017421), and the Open Research Fund of State Key Laboratory of Space-Ground Integrated Information Technology (grant no. 2018_SGIIT_KFJJ_AI_03).

References

- [1] D. Meng, X. Wang, M. Huang, L. Wan, and B. Zhang, "Robust weighted subspace fitting for DOA estimation via block sparse recovery," *IEEE Communications Letters*, vol. 24, no. 3, pp. 563–567, 2020.
- [2] F. Wen, Z. Zhang, K. Wang, G. Sheng, and G. Zhang, "Angle estimation and mutual coupling self-calibration for ULA-based bistatic MIMO radar," *Signal Processing*, vol. 144, pp. 61–67, 2018.
- [3] H. Chen, W. Wang, and W. Liu, "Augmented quaternion ESPRIT-type DOA estimation with a crossed-dipole array," *IEEE Communications Letters*, vol. 24, no. 3, pp. 548–552, 2020.
- [4] Y. Li and Y. Chi, "Off-the-grid line spectrum denoising and estimation with multiple measurement vectors," *IEEE Transactions on Signal Processing*, vol. 64, no. 5, pp. 1257–1269, 2016.
- [5] F. Wen and J. Shi, "Fast direction finding for bistatic EMVS-MIMO radar without pairing," *Signal Processing*, vol. 173, 2020.
- [6] Z.-Q. He, Z.-P. Shi, and L. Huang, "Covariance sparsity-aware DOA estimation for nonuniform noise," *Digital Signal Processing*, vol. 28, pp. 75–81, 2014.
- [7] J. Yin and T. Chen, "Direction-of-arrival estimation using a sparse representation of array covariance vectors," *IEEE Transactions on Signal Processing*, vol. 59, no. 9, pp. 4489–4493, 2011.
- [8] Z. Yang, L. Xie, and C. Zhang, "A discretization-free sparse and parametric approach for linear array signal processing,"

- IEEE Transactions on Signal Processing*, vol. 62, no. 19, pp. 4959–4973, 2014.
- [9] P. Stoica, P. Babu, and J. Li, “SPICE: a sparse covariance-based estimation method for array processing,” *IEEE Transactions on Signal Processing*, vol. 59, no. 2, pp. 629–638, 2011.
- [10] B. Recht, M. Fazel, and P. A. Parrilo, “Guaranteed minimum-rank solutions of linear matrix equations via nuclear norm minimization,” *SIAM Review*, vol. 52, no. 3, pp. 471–501, 2010.
- [11] B. Liao, L. Huang, C. Guo, and H. C. So, “New approaches to direction-of-arrival estimation with sensor arrays in unknown nonuniform noise,” *IEEE Sensors Journal*, vol. 16, no. 24, pp. 8982–8989, 2016.
- [12] A. Moffet, “Minimum-redundancy linear arrays,” *IEEE Transactions on Antennas and Propagation*, vol. 16, no. 2, pp. 172–175, 1968.
- [13] P. Pal and P. P. Vaidyanathan, “Nested arrays: a novel approach to array processing with enhanced degrees of freedom,” *IEEE Transactions on Signal Processing*, vol. 58, no. 8, pp. 4167–4181, 2010.
- [14] P. P. Vaidyanathan and P. Pal, “Sparse sensing with co-prime samplers and arrays,” *IEEE Transactions on Signal Processing*, vol. 59, no. 2, pp. 573–586, 2011.
- [15] J. Leech, “On the representation of $1, 2, \dots, n$ by differences,” *Journal of the London Mathematical Society*, vol. s1–31, no. 2, pp. 160–169, 1956.
- [16] G. Tang, B. N. Bhaskar, P. Shah, and B. Recht, “Compressed sensing off the grid,” *IEEE Transactions on Information Theory*, vol. 59, no. 11, pp. 7465–7490, 2013.
- [17] L. Wan, X. Kong, and F. Xia, “Joint range-doppler-angle estimation for intelligent tracking of moving aerial targets,” *IEEE Internet of Things Journal*, vol. 5, no. 3, pp. 1625–1636, 2018.
- [18] X. Wang, L. Wang, X. Li, and G. Bi, “Nuclear norm minimization framework for DOA estimation in MIMO radar,” *Signal Processing*, vol. 135, pp. 147–152, 2017.
- [19] M. Grant and S. Boyd, “CVX: matlab software for disciplined convex programming, version 2.1,” 2014, <http://cvxr.com/cvx>.
- [20] B. Ottersten, P. Stoica, and R. Roy, “Covariance matching estimation techniques for array signal processing applications,” *Digital Signal Processing*, vol. 8, no. 3, pp. 185–210, 1998.
- [21] X. Wu, W.-P. Zhu, and J. Yan, “A toeplitz covariance matrix reconstruction approach for direction-of-arrival estimation,” *IEEE Transactions on Vehicular Technology*, vol. 66, no. 9, pp. 8223–8237, 2017.
- [22] H. Chen, Y. Liu, Q. Wang, W. Liu, and G. Wang, “Two-dimensional angular parameter estimation for noncircular incoherently distributed sources based on an L-shaped array,” *IEEE Sensors Journal*, vol. 99, p. 1, 2020.
- [23] F. Wen, J. Wang, J. Shi, and G. Gui, “Auxiliary vehicle positioning based on robust DOA estimation with unknown mutual coupling,” *IEEE Internet of Things Journal*, vol. 7, no. 6, pp. 5521–5532, 2020.
- [24] M. Pesavento and A. B. Gershman, “Maximum-likelihood direction-of-arrival estimation in the presence of unknown nonuniform noise,” *IEEE Transactions on Signal Processing*, vol. 49, no. 7, pp. 1310–1324, 2001.
- [25] M. Wax and T. Kailath, “Detection of signals by information theoretic criteria,” *IEEE Transactions on Acoustics, Speech, and Signal Processing*, vol. 33, no. 2, pp. 387–392, 1985.
- [26] H. T. Wu, J. F. Yang, and F. K. Chen, “Source number estimators using transformed Gerschgorin radii,” *IEEE Transactions on Signal Processing*, vol. 43, no. 6, pp. 1325–1333, 1995.

Review Article

Wireless Localization Based on Deep Learning: State of Art and Challenges

Yun-Xia Ye,^{1,2} An-Nan Lu,^{1,2} Ming-Yi You ,^{1,2} Kai Huang ,^{1,2} and Bin Jiang^{1,2}

¹Science and Technology on Communication Information Security Control Laboratory, Jiaxing, Zhejiang 314033, China

²No. 36 Research Institute of CETC, Jiaxing, Zhejiang 314033, China

Correspondence should be addressed to Ming-Yi You; youmingyi@126.com

Received 15 July 2020; Revised 15 September 2020; Accepted 6 October 2020; Published 19 October 2020

Academic Editor: Jian Feng Li

Copyright © 2020 Yun-Xia Ye et al. This is an open access article distributed under the Creative Commons Attribution License, which permits unrestricted use, distribution, and reproduction in any medium, provided the original work is properly cited.

The problem of position estimation has always been widely discussed in the field of wireless communication. In recent years, deep learning technology is rapidly developing and attracting numerous applications. The high-dimension modeling capability of deep learning makes it possible to solve the localization problems under many nonideal scenarios which are hard to handle by classical models. Consequently, wireless localization based on deep learning has attracted extensive research during the last decade. The research and applications on wireless localization technology based on deep learning are reviewed in this paper. Typical deep learning models are summarized with emphasis on their inputs, outputs, and localization methods. Technical details helpful for enhancing localization ability are also mentioned. Finally, some problems worth further research are discussed.

1. Introduction

The attribute of target position is as important as its identity attribute. The target position is a core element in communications, logistics, and military field. Localization can be either self-positioning (e.g., target localization based on Global Positioning System (GPS)) or positioning interested objects (e.g., interference source positioning). We can either transmit a signal actively to locate the target or receive the signal from the target to determine its position. The target localization can be based on image data or signal data.

With the development of machine learning and artificial intelligence technology, some scholars began to pay attention to target localization by machine learning technology. In recent years, the powerful modeling capabilities of deep neural networks are attracting a large number of scholars to study effective use of deep learning techniques to solve the difficult problems in the field of target localization. The indoor localization problem is one of the most difficult problems. Due to the problems such as wall occlusion, the indoor localization accuracy based on GPS signals is not desirable, and sometimes the localization function is interrupted if the signal is very weak.

On the other hand, with the development of the Internet of Things, robots, etc., it is desirable to obtain higher localization accuracy even in indoor environment. Therefore, it becomes valuable and interesting to solve the problem of accurate target localization in indoor environment with large dynamics, multiple reflections, and occlusion by deep learning technology. In addition, some scholars used some deep learning techniques for outdoor large-scale sensor network localization [1], TDOA localization [2], and target tracking [3,4].

While deep learning technology is gradually applied in the field of wireless localization, a work systematically summarizing, classifying, and discussing related results has not yet been reported to our best knowledge. For the application of deep learning technology in the field of wireless localization, the main purpose of this paper is to propose some problems solved by deep learning technology, summarize the typical deep learning models, explore the input forms and localization methods, and pay attention to the technical details in literature which can help to improve localization performance. Besides, we raise some problems that need further study on the wireless localization problem.

2. Wireless Indoor Localization Technology Based on Deep Learning

The serious multipath transmission environment in indoor wireless localization poses great challenges for localization modeling. The powerful modeling ability of deep neural networks provides a powerful tool to deal with this problem. In view of the wide application and urgent research on indoor localization (e.g., there are international conferences on indoor localization), the research studies on indoor localization are very abundant and the methods are very various. There are many elements of wireless indoor localization technology based on deep learning that can be classified. Indoor localization technology is divided into device-oriented indoor localization and device-free indoor localization according to whether the target carries equipment or not in this paper. Certainly, these methods can also be divided from network type, feature type, and localization method. In addition, some localization issues for sound source which are similar to the wireless indoor localization issues are also introduced.

2.1. Device-Oriented Indoor Localization. Device-oriented indoor localization means that a device carried by the target is used in positioning process. This device either receives the environmental signal as a receiver to position itself (the basic model is shown in Figure 1) or transmits a signal as a transmitter, and this signal is received by peripheral sensors to estimate the target position (the basic model is shown in Figure 2).

2.1.1. Self-Positioning. In 2014, Zhang et al. [5] proposed an indoor localization method based on the received wireless LAN WiFi signal strength using Deep Neural Network (DNN) and Hidden Markov Model (HMM), which modeled the indoor localization problem as a classification problem. Firstly, the received signal strengths of multiple hotspots are casted in a four-layer DNN to obtain a coarse estimate of the position. Then, a precise estimate of the position is obtained from the multiple coarse estimates by HMM processing.

In 2016, Félix et al. [6] proposed a fingerprinting indoor localization algorithm based on DNN, Deep Belief Network, and Gauss-Bernoulli Deep Belief Network Regression model by the characteristics of received signal strength. The simulation results show that the accuracy of DNN is the highest.

In 2016, Huang et al. [7] developed an indoor localization research based on deep neural networks with WiFi, iBeacon signals, geomagnetic signals, and other signals and compared the accuracy of localization algorithms with single source data and fusion of multisource data.

In 2017, Xiao et al. [8] proposed two learning algorithms, namely, a deep learning architecture for regression and Support Vector Machine (SVM) for classification, to estimate the target position from the measured signal fingerprint which is the received signal strength from each transmitter, and particularly mentioned that the technique of data enhancement based on random perturbation (the order of signal strength from different transmitter is

independent of position) can improve the localization accuracy by 10%.

In 2017, Zhang et al. [9] proposed a new indoor fingerprinting localization system based on deep learning, combining received signal strength of WiFi and pervasive magnetic field to obtain richer fingerprinting, and investigated the indoor localization method based on deep neural networks in the form of classification and regression. At the same time, the effects of different types of neural networks, different mesh sizes, and different data on localization performance were described.

In 2018, Aikawa et al. [10] introduced an indoor localization method based on deep learning and WLAN signal. The method uses the received signal strengths of multiple WLAN access points as features to construct a six-layer neural network model. An experiment was conducted in an underground shopping center in Himeji City in Japan to validate the effectiveness of their approach. Experiment results show that the method is finer than the traditional least square method when the training time is sufficient.

In 2018, Lin et al. [11] proposed an indoor localization method based on a multitask learning network to handle the poor similarity of received signal strengths using WiFi signals in adjacent locations. The network mainly includes three parts. Firstly, a neural network is used for extracting robust regional features based on the received signal strength of adjacent locations (this paper considers 5 adjacent locations). Then, a neural network is used for learning consistent features to deal with the similarity inconsistency problem. Finally, the position is estimated based on a regression model.

In 2018, Liu et al. [12] pointed out that, although the current fingerprinting localization technology can obtain room level accuracy, the time-varying property of received signal strength caused a large position estimation error. Therefore, an autoencoder adopted to preprocess the noisy received signal strength is designed to improve localization accuracy. The method includes offline phase and online phase. In the offline phase, a deep autoencoder is trained to denoise the data. In the online phase, the fingerprint characteristics of received signal strength are obtained based on the weights after the autoencoder training, and the fingerprint characteristics are the input of three machine learning algorithms, which are random forest regression, multilayer perception classification, and multilayer perception regression. The final estimated position can be obtained by averaging over the results of three algorithms.

In 2018, De Vita and Bruneo [13] presented an indoor user localization method based on WiFi received signal strength and introduced the fingerprint data collection method in detail. The indoor user position is estimated by a DNN classification model using the Media Access Control (MAC) addresses as feature labels and using the corresponding received signal strengths as the feature value.

In 2018, Wu and Tseng [14] proposed a DNN-based indoor localization method using unsupervised preprocessing of channel state information (CSI) to extract richer features of CSI at different reference points. Then, the output of DNN which is the probabilities of received

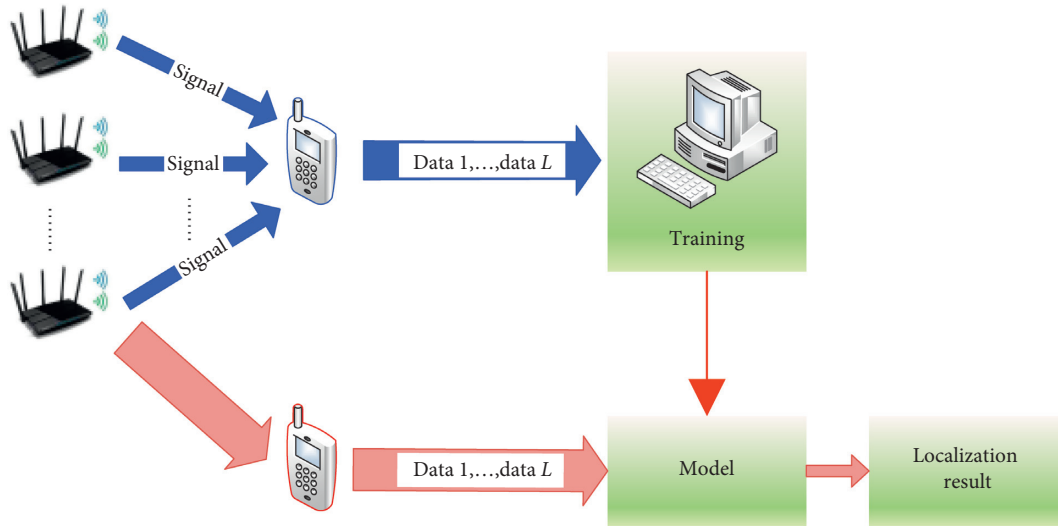


FIGURE 1: Basic model of self-positioning.

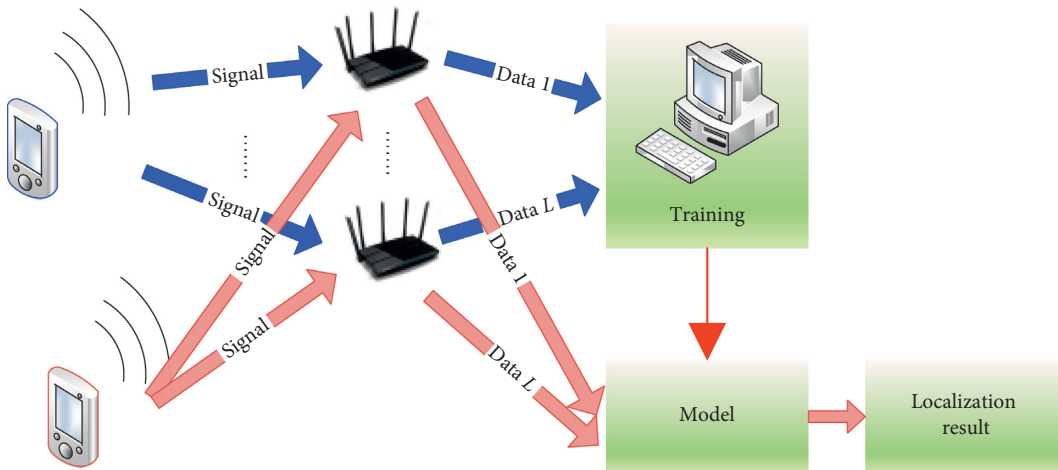


FIGURE 2: Basic model of passive positioning.

position at the reference points can be used for estimating the weighted average position of the receiver.

In 2018, Hsu et al. [15] proposed an adaptive indoor localization scheme based on WiFi signal strengths. The scheme can adaptively adopt the proper fingerprint database built by the crossentropy algorithm or the mean squared algorithm according to the noise level of the received signals. The Bayesian probability algorithm is used for position estimation. Experimental results show that the scheme has lower localization error whether in the noise-free environment or in the noisy environment.

In 2018, Le et al. [16] proposed a WLAN-fingerprint-based indoor localization method using unsupervised deep feature learning for the problem of small training samples. Firstly, a large number of unlabeled received signal strengths are used for extracting the deep features by the Deep Belief Network training. Then, a small number of labeled samples are used for training the shallow supervised learning algorithms (such as SVM). The experimental results show that

the localization method based on a large number of unlabeled fingerprints and a small number of labeled fingerprints with deep feature learning can obtain the same localization accuracy as counterpart based on the same number of entirely labeled fingerprints with shallow feature learning.

In 2018, Khatab et al. [17] also studied on the indoor localization in wireless sensor networks based on the received signal strength. Aiming at the problem that the deep neural networks are training slowly, a deep extreme learning machine is proposed for training. To deal with the dynamic environment which leads to the time-varying characteristics of the received signal strength, they increased the number of training data and used high-level features by autoencoder to train the model.

In 2018, Dou et al. [18] pointed out that WiFi fingerprints localization technology based on the received signal strength is widely used in vast indoor localization systems due to the low cost and high localization accuracy. However, the fluctuation of wireless signal will cause a great fluctuation

on received signal strength, which poses great challenges to indoor localization based on WiFi fingerprints. Dou et al. proposed a top-down searching method based on deep reinforcement learning to deal with the dynamic environment in WiFi fingerprints indoor localization. The localization method based on deep reinforcement learning has three advantages. Firstly, the method can be readily applied to the fluctuation in received signal strength due to dynamic environment. Secondly, the learning process can be online to realize real-time positioning. Thirdly, it is not necessary to require the prior knowledge of floor plan.

In 2019, Elbes et al. [19] presented an indoor localization approach based on WiFi received signal strengths and Long Short-Term Memory (LSTM) Neural Networks. The experimental results show that the localization approach is effective in corridors of the L-shaped floor.

In 2019, Ebuchi and Yamamoto [20] described a smart parking system based on a small number of beacon devices. The system uses the beacon signal strength measured by the smartphones to locate vehicles and pedestrians, and then the gateway broadcasts the position information to all smartphones in the parking lot so that contact accidents can be avoided. A full connected layer DNN and Convolutional Neural Network classification model is used for locating vehicles and pedestrians. The experimental results show that estimation accuracy of the vehicle's position is higher than 98%, and estimation accuracy of the pedestrian's position is about 70%.

In 2019, Jiang et al. [21] proposed fingerprinting-based radio-frequency identification (RFID) indoor localization algorithm based on deep belief network. The collected received signal strength data is input into a deep belief network to extract deep features and then the target is located by the similarity comparison with the deep features.

In 2019, Bae and Choi [22] proposed an indoor localization method based on LSTM Neural Network using continuous geomagnetic data. The localization accuracy of LSTM Neural Network is higher than that of classical recurrent neural network and the existing RF-based fingerprinting techniques.

In 2019, Rizk et al. [23] pointed out that WiFi-based indoor localization technology relies on WiFi chips which limit wide application of the technology. In addition, technologies based on inertial sensors such as accelerometers, gyroscopes, and compasses are only available on high-end phones. Therefore, they proposed an indoor localization method based on cellular signals received by mobile phones. And they proposed two training data augmentation techniques: random augments and lower-bound cropper.

In 2019, Abbas et al. [24] pointed out that many indoor localization systems have been proposed relying on WiFi fingerprinting due to the wide use of indoor WiFi. However, due to the inherent noise and instability of wireless signals, the localization accuracy usually degrades. So, they proposed a deep learning-based indoor localization system called WiDeep to obtain high accuracy and robustness. An autoencoder is trained for the signal strength of each access point separately, and the position estimation is obtained by a probabilistic fusion algorithm based on the output of latent

features from these autoencoders. It is worth noting that Abbas et al. [24] also introduce two techniques adding stochastic noise to the input training data in order to improve the robustness of WiDeep in noisy environments.

In 2017, Takeda and Komatani [25] investigated a sound source localization method based on deep neural networks when sound source is at an unknown position in unknown reverberant environments. The sound source localization accuracy can be improved by using unsupervised adaption of parameters and early stopping of the parameter update.

In 2019, He et al. [26] pointed out that the DNN became the main approaches for sound source localization and directions of arrival estimation, but these approaches still have two major drawbacks: (1) these approaches require a large amount of training data for specific devices and it is particularly difficult to obtain the true sound source positions, and (2) these methods are very sensitive to the mismatch between the training and test conditions. To address the problems, they have studied two domain adaptation methods and their combination for multiple sound source localization: weak supervision and domain adversarial training. The weak supervision regularizes the output of neural network and makes it closer to the possible output space based on the inexact labels. The domain adversarial training aims to find domain-invariant features. The experimental results show that the neural network model adapted with the weak supervision has been significantly improved, but the domain adversarial training does not further improve the performance of the model.

In 2019, Xu et al. [27] proposed a biologically inspired binaural sound localization system for reverberant environments. This sound source localization system uses a convolutional neural network to analyze the 2-D correlation matrix generated by the stereo cochlear system. The system can obtain a lower average absolute error in the -90° to 90° range.

2.1.2. Passive Positioning. In 2017, Xue et al. [28] proposed a localization algorithm based on deep learning and asynchronous time difference of arrival (TDOA) data, measurement errors, and missing data. The algorithm determines the target state first and then predicts the asynchronous TDOAs with measurement errors or missing data. Finally, the target is located based on the predicted TDOA data.

In 2018, Berruet et al. [29] proposed an indoor localization method based on CSI and convolutional neural network in Internet of Things context. This method uses different subcarriers and different receiving antenna CSI to form a two-dimensional matrix as the input of the neural network and uses the target position as the output (regression model). In this method, the receiver is a gateway with multiple antenna elements, while the transmitter is a device with one antenna element, so only one receiver is needed to estimate the target position.

In 2019, Chen et al. [30] used the WiFi routers to scan smartphones so that a large amount of received signal strengths can be collected. Then, they extracted the local

features by consecutive received signal strength features for each router. The LSTM network is leveraged to learn high-level representations from the extracted local features and indoor localization was realized by a regression model.

2.2. Device-free Indoor Localization. Device-free indoor localization means that the located target does not carry any receiving or transmitting equipment (basic model is shown as Figure 3). The localization system achieves the location estimate by utilizing the target's influence on the environment (e.g., communication channel).

In 2016, Wang et al. [31] proposed PhaseFi, an indoor localization system based on calibrated CSI phase information. In PhaseFi, firstly, the raw phase information is extracted from the multiple antennas and multiple subcarriers of the IEEE802.11n network interface card. Then, a linear transformation is applied to extract the calibrated phase information. In the offline phase, a three-layer neural network is designed to train the calibrated phase information, and the weights of the neural network are used as fingerprint features. In the online phase, a probabilistic method based on radial basis functions is used for estimating the target position.

Wang et al. [32,33] studied an indoor localization scheme based on CSI information instead of CSI phase information [28].

In 2017, Wang et al. [34] proposed an indoor localization method (CiFi) based on deep convolutional neural networks. The method uses one transmitter and some receivers consisting of three direction-finding antennas. The AOA (angle of arriving) values of different subcarriers of WiFi signal are used for forming CSI AOA images, and the images are used as the input of the neural network.

In 2017, in order to improve the localization accuracy, Wang et al. [35] used bimodal CSI including AOA and CSI amplitude to estimate indoor position. At the same time, in order to reduce the training time and data storage requirement, a deep residual sharing learning network was used for model training. The input of the network includes two channels, and each input tensor of each signal includes three images: two of them are AOA-time images obtained from three antennas and the other is a CSI amplitude-time image from one antenna. Experimental results show that the localization accuracy of this method is significantly improved.

In 2019, Abdul Samadh et al. [36] pointed out that the advantages of device-free indoor localization methods include the following: (1) they can be used for tracking targets that cannot be controlled directly, (2) they can be used for locating in unexpected circumstances, and (3) they are comparatively cost-effective with minimal infrastructure setup requirements. They studied the localization method based on CSI amplitude and convolutional neural network (classification model) and also studied the impact of CSI time-varying characteristics on localization accuracy. The results show that CSI time-varying characteristics have a greater influence on localization accuracy using CSI amplitude information only.

In 2019, Hsieh et al. [37] formulated the indoor localization as a classification problem, and developed four indoor localization methods based on multilayer perceptron, one-dimensional convolutional neural network, received signal strength, and CSI. The localization method based on one-dimensional convolutional neural network is proposed for the first time. The experimental results show that the one-dimensional convolutional network using CSI information achieves excellent localization performance with much lower network complexity.

In 2019, Liu et al. [38] pointed out that deep neural networks have shown great potential in indoor high-precision localization, but the inner principles are not adequately understood. So, they provide quantitative and visual explanations for the deep learning process and the important features learnt by deep neural network during the learning process. Several visualization techniques are proposed including dimensionality reduction visualization, visual analysis, and information visualization.

3. Wireless Outdoor Localization Technology Based on Deep Learning

Compared with the indoor localization problem, there are even more issues associated with outdoor localization. The multipath effect is greatly reduced in outdoor localization, so the contradiction of localization modeling is not as serious as that of indoor localization. Therefore, while paying attention to the methods, we should also pay attention to the motivation and purpose of the research. Basic models of outdoor localization are the same as those for indoor localization, as shown in Figures 1–3.

In 2017, Houégnigan et al. [39] pointed out that, although underwater range can be standardly estimated by widely spaced sensors in the higher frequency ranges and assuming direct path, opportunistically estimated using surface and bottom reflection or using modal decomposition at certain low frequencies, and it remains a big challenge to develop a general system based on a single sensor or a small-aperture array that can be adapted to real time. They introduced the early results of their ongoing underwater localization and sound source range estimation based on a single sensor and the experimental results of range estimation using shallow and deep neural networks by a single sensor. The deep neural networks used in [39] are AlexNet, VGG-16, and VGG-19.

In 2019, Chang [40] proposed a threshold adaptive varied method for tracking based on deep learning to improve Extended Kalman Filter (EKF) algorithm because the tracking threshold is difficult to update adaptively which may lead to a divergence when tracking a high-speed target. This method uses a recurrent neural network model. The model inputs include current and previous position estimation, and the model output is the target region. If the target region estimation of improved EKF is inconsistent with the neural network model, the tracking threshold should be adjusted until they are consistent.

Existing telecommunication-based localization methods suffer from the challenges of either high localization errors or requiring intensive data samples or high sensitivity

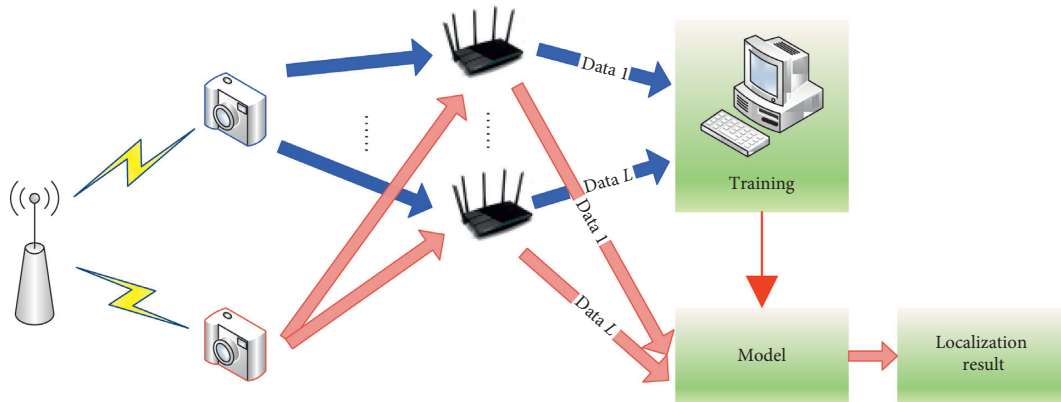


FIGURE 3: Basic model of device-free indoor localization.

towards noisy Measurement Record (MR) data. To address the challenges, Zhang [41] proposed a telecommunication localization framework. The framework mainly includes three main parts: a localization model, a method overcoming the data scarcity issue, and a method repairing noisy MR samples. The localization models include single-point-based localization model and sequence-based localization model. The idea of transfer learning is adopted to overcome the data scarcity issue. In addition, a confidence level method is proposed to detect those MR samples with high localization errors by confidence levels and then repair the predicted positions.

In 2019, Shen et al. [42] proposed a relative localization method of high-density RFID tags via phase and received signal strength indication (RSSI) based on deep learning with convolutional neural networks.

4. Discussion and Conclusion

At present, the core elements of indoor localization technology based on deep learning include the following. (1) Application signal types: WiFi, WLAN, iBeacon, geomagnetic signals, base station cellular signals, etc. (2) Feature types: received signal strength, CSI (amplitude and phase), angle of arrival etc. (3) Preprocessing methods: normalization, adding noise, training data increase, high-level feature learning based on autoencoder, etc. (4) Network frameworks: convolutional neural networks, LSTM neural networks, fully connected networks, etc. (5) Localization methods: classification methods based on neural networks, regression methods based on neural networks, probability methods based on higher-level features, etc. Although there are research results, it is difficult to evaluate the localization performance of various methods based on a unified standard at present. Therefore, further research on the optimal combination of these will be a valuable research direction.

The major challenges of indoor localization are the environmental interference and the time-varying characteristics of the channel, so the transfer function between position and position-sensitive parameters cannot be

established. However, the nonideal model can be solved by deep learning because of the high-dimensional modeling capabilities. At present, a mount of methods based on increasing the training samples, extracting higher-level features, and using deep reinforcement learning have been proposed. It is necessary to compare the cost and performance of the methods with unified data and to find better approaches.

The complex environment in indoor localization greatly promotes the application and research on deep learning technology in indoor localization. In outdoor localization, the first thing that deep learning needs to solve is the application requirement. Although a few researches have been carried out, it is difficult to conclude whether the application of deep learning technology is the best choice in these problems.

At present, most research studies on deep learning-based localization problems focus on two-dimensional problems. For three-dimensional localization problems, the cost of collecting training samples will greatly increase. Therefore, it is of great significance to research on how to reduce the demand of training samples for three-dimensional localization.

Compared with the indoor wireless environment, the complexity of the underwater environment is increased. Making full use of the technical achievements on indoor localization, deep learning technology may be a powerful tool to deal with underwater precise localization.

This article focuses on the application of deep learning technology in the field of wireless localization, the problems solved by deep learning technology, the common deep learning models, the input form, and the methods. And we discuss the need for further research on wireless localization. With the advance and development of big data and deep learning technology, better performance and results are expected to be obtained from wireless localization systems in complex practical application environments.

Conflicts of Interest

The authors declare that they have no conflicts of interest.

Acknowledgments

This work was supported by No. 36 Research Institute of CETC under the project no. CX05.

References

- [1] B. G. Maciel-Pearson, S. Akçay, A. Atapour-Abarghouei, C. Holder, and T. P. Breckon, "Multi-task regression-based learning for autonomous unmanned aerial vehicle flight control within unstructured outdoor environments," *IEEE Robotics and Automation Letters*, vol. 4, no. 4, pp. 4116–4123, 2019.
- [2] F. Carrino, A. Janka, O. Abou Khaled, and E. Mugellini, "LoRaLoc: machine learning-based fingerprinting for outdoor geolocation using LoRa," in *Proceedings of the 2019 6th Swiss Conference on Data Science (SDS)*, pp. 82–86, Bern, Switzerland, June 2019.
- [3] G. Yang and Z. Chen, "Pedestrian tracking algorithm for dense crowd based on deep learning," in *Proceedings of the 2019 6th International Conference on Systems and Informatics (ICSAI)*, pp. 568–572, Shanghai, China, November 2019.
- [4] L. Li and S. Qin, "A synthetic integrative algorithm of fast concurrent detection-recognition with effective tracking of aerial objects based on deep learning of CNN," in *Proceedings of the IEEE 4th Advanced Information Technology, Electronic and Automation Control Conference (IAEAC)*, pp. 1187–1194, Chengdu, China, December 2019.
- [5] W. Zhang, K. Liu, W. Zhang, Y. Zhang, and J. Gu, "Wi-Fi positioning based on deep learning," in *Proceedings of the 2014 IEEE International Conference on Information and Automation (ICIA)*, pp. 1176–1179, Hailar, China, July 2014.
- [6] G. Félix, M. Siller, and E. N. Álvarez, "A fingerprinting indoor localization algorithm based deep learning," in *Proceedings of the 2016 Eighth International Conference on Ubiquitous and Future Networks (ICUFN)*, pp. 1006–1011, Vienna, Austria, July 2016.
- [7] L. Huang, X. Gan, S. Li, H. Zhang, Y. Li, and R. Zhu, "Indoor positioning technology based on deep neural networks," in *Proceedings of the 2018 Ubiquitous Positioning, Indoor Navigation and Location-Based Services (UPINLBS)*, pp. 1–6, Wuhan, China, March 2018.
- [8] L. Xiao, A. Behboodi, and R. Mathar, "A deep learning approach to fingerprinting indoor localization solutions," in *Proceedings of the 2017 27th International Telecommunication Networks and Applications Conference (ITNAC)*, pp. 1–7, Melbourne, Australia, November 2017.
- [9] W. Zhang, R. Sengupta, J. Fodero, and X. Li, "Deep-Positioning: intelligent fusion of pervasive magnetic field and Wi-Fi fingerprinting for smartphone indoor localization via deep learning," in *Proceedings of the 2017 16th IEEE International Conference on Machine Learning and Applications*, pp. 7–13, Cancun, Mexico, December 2017.
- [10] S. Aikawa, S. Yamamoto, and M. Morimoto, "WLAN fingerprint localization using deep learning," in *Proceedings of the 2018 IEEE Asia-Pacific Conference on Antennas and Propagation (APCAP)*, pp. 541–542, Auckland, New Zealand, August 2018.
- [11] W. Lin, C. Huang, N. Duc, and H. Manh, "Wi-Fi indoor localization based on multi-task deep learning," in *Proceedings of the 2018 IEEE 23rd International Conference on Digital Signal Processing (DSP)*, pp. 1–5, Shanghai, China, November 2018.
- [12] J. Liu, N. Liu, Z. Pan, and X. You, "AutLoc: deep autoencoder for indoor localization with RSS fingerprinting," in *Proceedings of the 2018 10th International Conference on Wireless Communications and Signal Processing (WCSP)*, pp. 1–6, Hangzhou, China, October 2018.
- [13] F. De Vita and D. Bruneo, "A deep learning approach for indoor user localization in smart environments," in *Proceedings of the 2018 IEEE International Conference on Smart Computing (SMARTCOMP)*, pp. 89–96, Taormina, Italy, June 2018.
- [14] G. Wu and P. Tseng, "A deep neural network-based indoor positioning method using channel state information," in *Proceedings of the 2018 International Conference on Computing, Networking and Communications (ICNC)*, pp. 290–294, Maui, HI, USA, March 2018.
- [15] C. Hsu, Y. Chen, T. Juang, and Y. Wu, "An adaptive Wi-Fi indoor localization scheme using deep learning," in *Proceedings of the 2018 IEEE Asia-Pacific Conference on Antennas and Propagation (APCAP)*, pp. 132–133, Auckland, New Zealand, August 2018.
- [16] D. V. Le, N. Meratnia, and P. J. M. Havinga, "Unsupervised deep feature learning to reduce the collection of fingerprints for indoor localization using deep belief networks," in *Proceedings of the 2018 International Conference on Indoor Positioning and Indoor Navigation (IPIN)*, pp. 1–7, Nantes, France, September 2018.
- [17] Z. E. Khatab, A. Hajihoseini, and S. A. Ghorashi, "A fingerprint method for indoor localization using autoencoder based deep extreme learning machine," *IEEE Sensors Letters*, vol. 2, no. 1, pp. 1–4, 2018.
- [18] F. Dou, J. Lu, Z. Wang, X. Xiao, J. Bi, and C. Huang, "Top-down indoor localization with Wi-Fi fingerprints using deep Q-network," in *Proceedings of the 2018 IEEE 15th International Conference on Mobile Ad Hoc and Sensor Systems (MASS)*, pp. 166–174, Chengdu, China, October 2018.
- [19] M. Elbes, E. Almaita, T. Alrawashdeh, T. Kanan, S. AlZu'bi, and B. Hawashin, "An indoor localization approach based on deep learning for indoor location-based services," in *Proceedings of the 2019 IEEE Jordan International Joint Conference on Electrical Engineering and Information Technology (JEEIT)*, pp. 437–441, Amman, Jordan, April 2019.
- [20] T. Ebuchi and H. Yamamoto, "Vehicle/pedestrian localization system using multiple radio beacons and machine learning for smart parking," in *Proceedings of the 2019 International Conference on Artificial Intelligence in Information and Communication (ICAIIIC)*, pp. 86–91, Okinawa, Japan, February 2019.
- [21] H. Jiang, C. Peng, and J. Sun, "Deep belief network for fingerprinting-based RFID indoor localization," in *Proceedings of the ICC 2019—2019 IEEE International Conference on Communications (ICC)*, pp. 1–5, Shanghai, China, May 2019.
- [22] H. J. Bae and L. Choi, "Large-scale indoor positioning using geomagnetic field with deep neural networks," in *Proceedings of the ICC 2019—2019 IEEE International Conference on Communications (ICC)*, pp. 1–6, Shanghai, China, May 2019.
- [23] H. Rizk, M. Torki, and M. Youssef, "CellinDeep: robust and accurate cellular-based indoor localization via deep learning," *IEEE Sensors Journal*, vol. 19, no. 6, pp. 2305–2312, 2019.
- [24] M. Abbas, M. Elhamshary, H. Rizk, M. Torki, and M. Youssef, "WiDeep: WiFi-based accurate and robust indoor localization system using deep learning," in *Proceedings of the 2019 IEEE International Conference on Pervasive Computing and Communications (PerCom)*, pp. 1–10, Kyoto, Japan, March 2019.

- [25] R. Takeda and K. Komatani, "Unsupervised adaptation of deep neural networks for sound source localization using entropy minimization," in *Proceedings of the 2017 IEEE International Conference on Acoustics, Speech and Signal Processing (ICASSP)*, pp. 2217–2221, New Orleans, LA, USA, March 2017.
- [26] W. He, P. Motlicek, and J. Odobez, "Adaptation of multiple sound source localization neural networks with weak supervision and domain-adversarial training," in *Proceedings of the ICASSP 2019—2019 IEEE International Conference on Acoustics, Speech and Signal Processing (ICASSP)*, pp. 770–774, Brighton, UK, May 2019.
- [27] Y. Xu, S. Afshar, R. K. Singh, T. J. Hamilton, and A. van Schaik, "A machine hearing system for binaural sound localization based on instantaneous correlation," in *Proceedings of the 2018 IEEE International Symposium on Circuits and Systems (ISCAS)*, Florence, Italy, May 2018.
- [28] Y. Xue, W. Su, H. Wang, D. Yang, and Y. Jiang, "DeepTAL: deep learning for TDOA-based asynchronous localization security with measurement error and missing data," *IEEE Access*, vol. 7, pp. 122492–122502, 2019.
- [29] B. Berruet, O. Baala, A. Caminada, and V. Guillet, "DelFin: a deep learning based CSI fingerprinting indoor localization in IoT context," in *Proceedings of the 2018 International Conference on Indoor Positioning and Indoor Navigation (IPIN)*, pp. 1–8, Nantes, France, September 2018.
- [30] Z. Chen, H. Zou, J. Yang, H. Jiang, and L. Xie, "Wi-Fi fingerprinting indoor localization using local feature-based deep LSTM," *IEEE Systems Journal*, vol. 14, no. 2, pp. 3001–3010, 2019.
- [31] X. Wang, L. Gao, and S. Mao, "CSI phase fingerprinting for indoor localization with a deep learning approach," *IEEE Internet of Things Journal*, vol. 3, no. 6, pp. 1113–1123, 2016.
- [32] X. Wang, L. Gao, S. Mao, and S. Pandey, "DeepFi: deep learning for indoor fingerprinting using channel state information," in *Proceedings of the 2015 IEEE Wireless Communications and Networking Conference (WCNC)*, pp. 1666–1671, New Orleans, LA, USA, March 2015.
- [33] X. Wang, L. Gao, S. Mao, and S. Pandey, "CSI-based fingerprinting for indoor localization: a deep learning approach," *IEEE Transactions on Vehicular Technology*, vol. 66, no. 1, pp. 763–776, 2016.
- [34] X. Wang, X. Wang, and S. Mao, "CiFi: deep convolutional neural networks for indoor localization with 5 GHz Wi-Fi," in *Proceedings of the 2017 IEEE International Conference on Communications (ICC)*, pp. 1–6, Paris, France, May 2017.
- [35] X. Wang, X. Wang, and S. Mao, "ResLoc: deep residual sharing learning for indoor localization with CSI tensors," in *Proceedings of the 2017 IEEE 28th Annual International Symposium on Personal, Indoor, and Mobile Radio Communications (PIMRC)*, pp. 1–6, Montreal, Canada, October 2017.
- [36] S. Abdul Samadh, Q. Liu, X. Liu, N. Ghourchian, and M. Allegue, "Indoor localization based on channel state information," in *Proceedings of the 2019 IEEE Topical Conference on Wireless Sensors and Sensor Networks (WiSNet)*, pp. 1–4, Orlando, FL, USA, January 2019.
- [37] C. Hsieh, J. Chen, and B. Nien, "Deep learning-based indoor localization using received signal strength and channel state information," *IEEE Access*, vol. 7, pp. 33256–33267, 2019.
- [38] S. Liu, R. Y. Chang, and F. Chien, "Analysis and visualization of deep neural networks in device-free Wi-Fi indoor localization," *IEEE Access*, vol. 7, pp. 69379–69392, 2019.
- [39] L. Houégnigan, P. Safari, C. Nadeu, M. André, and M. van der Schaar, "Machine and deep learning approaches to localization and range estimation of underwater acoustic sources," in *Proceedings of the 2017 IEEE/OES Acoustics in Underwater Geosciences Symposium (RIO Acoustics)*, pp. 1–6, Rio de Janeiro, Brazil, July 2017.
- [40] S. Chang, "A deep learning approach for localization systems of high-speed objects," *IEEE Access*, vol. 7, pp. 96521–96530, 2019.
- [41] Y. Zhang, "Outdoor localization framework with telco data," in *Proceedings of the 2019 20th IEEE International Conference on Mobile Data Management (MDM)*, pp. 395–396, Hong Kong, China, June 2019.
- [42] L. Shen, Q. Zhang, J. Pang, H. Xu, and P. Li, "PRDL: relative localization method of RFID tags via phase and RSSI based on deep learning," *IEEE Access*, vol. 7, pp. 20249–20261, 2019.

Research Article

Object Detection from the Video Taken by Drone via Convolutional Neural Networks

Chenfan Sun, Wei Zhan , Jinhiu She, and Yangyang Zhang

School of Computer Science, Yangtze University, Jingzhou, Hubei, China

Correspondence should be addressed to Wei Zhan; zhanwei814@yangtzeu.edu.cn

Received 23 July 2020; Revised 12 September 2020; Accepted 25 September 2020; Published 13 October 2020

Academic Editor: Liangtian Wan

Copyright © 2020 Chenfan Sun et al. This is an open access article distributed under the Creative Commons Attribution License, which permits unrestricted use, distribution, and reproduction in any medium, provided the original work is properly cited.

The aim of this research is to show the implementation of object detection on drone videos using TensorFlow object detection API. The function of the research is the recognition effect and performance of the popular target detection algorithm and feature extractor for recognizing people, trees, cars, and buildings from real-world video frames taken by drones. The study found that using different target detection algorithms on the “normal” image (an ordinary camera) has different performance effects on the number of instances, detection accuracy, and performance consumption of the target and the application of the algorithm to the image data acquired by the drone is different. Object detection is a key part of the realization of any robot’s complete autonomy, while unmanned aerial vehicles (UAVs) are a very active area of this field. In order to explore the performance of the most advanced target detection algorithm in the image data captured by UAV, we have done a lot of experiments to solve our functional problems and compared two different types of representative of the most advanced convolution target detection systems, such as SSD and Faster R-CNN, with MobileNet, GoogleNet/Inception, and ResNet50 base feature extractors.

1. Introduction

An object recognition system uses a priori known object model to find real-world pairs from images of the world [1, 2]. Human beings can perform object detection very easily and effortlessly, but this problem is amazingly difficult for machines.

The need for object detection systems is increasing due to the ever-growing number of digital images in both public and private collections. Object recognition systems are important for reaching higher-level autonomy for robots [3]. Applying computer vision (CV) and machine learning (ML), it is a hot area of research in robotics. Drones are being used more and more as robotic platforms. The research in this article is to determine how to use existing object detection systems and models can be used on image data from a drone. One of the advantages of using a drone to detect objects in a scene may be that the drone can move close to objects compared to other robots [4], for example, a wheeled robot. However, there are difficulties with UAVs because of top-down view angles [5] and the issue to combine with a deep

learning system for compute-intensive operations [6]. When a drone navigates a scene in search for objects, it is of interest for the drone to be able to view as much of its surroundings as possible [7, 8]. However, images taken by UAVs or drones are quite different from images taken by using a normal camera. For that reason, it cannot be assumed that object detection algorithms normally used on “normal” images perform well on taken by drone images. Previous works on this stress that the images captured by a drone often are different from those available for training, which are often taken by a hand-held camera. Difficulties in detecting objects in data from a drone may arise due to the positioning [9, 10] of the camera compared to images taken by a human, depending on what type of images the network is trained on.

In the previous research, the aim of work was to show whether a network trained on normal camera images could be used on images taken by a drone with satisfactory results. They have used a fish-eye camera and conducted several experiments on three kinds of datasets such as images from a normal camera, images from a fish-eye camera, and rectified images from a fish-eye camera. The result shows that using

drone’s fish-eye camera, we can detect many objects—some of the extra number of detected objects compared to the normal camera and the outside field of the view can cause different image quality. [11, 12]. They have done some experiments to prove that more objects can be detected from a closer viewpoint, and the result proved the hypothesis. The result of research work shows that the number of detected object instance and accuracy of detection very depend on the angle of the camera. Their observation tells that it is important to use the same camera angle as in the training dataset. However, different types of objects in the training data are generally photographed from different angles. For example, many images of cups are taken from the side while many images of keyboards are taken from above [9]. Therefore, each object type has an optimal viewing angle depending on the training data. However, as the camera on our drone is assumed to be in a fixed position and the drone itself cannot tilt, one viewing angle has to be chosen. That is why, in our project, we retrained the model using images taken by the drone, and it helped to improve the accuracy of detection.

Other recent studies have used real-time [13, 14] identification of pedestrians, trees, and different types of vehicles and ships from real-world videos of the Caffe framework [15], which are captured with UAVs. In that work, they have observed several experiments to derive the optimal batch size, iteration count, and learning rate for the model to converge [16].

In our experiment, we used TensorFlow object detection API to realize object detection of UAV videos. In our observation, we compared SSD and Faster R-CNN object detection systems depending on speed of detection for frame per second (FPS) and accuracy. In our project, we use Single Shot Detector (SSD) and Faster R-CNN topology as our detection components. We have used them to assess the frame rate and accuracy of several videos we have taken with drones [11].

Section 2 represents TensorFlow object detection API and transfer learning. Section 3 describes design of solution, methods, and network architecture. Section 4 presents the analysis and experiments and shows the results. Section 5 closes the study with a conclusion.

2. Why Choose TensorFlow Object Detection API

If you want to train a complete CNN from scratch, it will take much time and requires very large image datasets [17, 18]. There is a solution to this problem: the solution is to use the advantages of migration learning [12, 19] and TensorFlow’s object detection API, which we can use to train, build, and deploy object detection models. Fortunately, API has some pretrained models. Some concepts of transfer learning are described below.

Transfer learning [19] is mainly performed to extract the best solution from another task, and after that, it is applied for the different but related tasks. In deep learning, there are three main ways to use it.

First method, we can use convolutional neural networks as a fixed feature extractor [20], but we change the last fully

connected layer of it, and the front part is used as the fixed feature extractor for our new image dataset.

The second way is fine-tuning the CNNs, which is almost the same as the first method, but there is a difference. This method uses continuous back propagation to fine-tune the weights of the pretrained network.

The last is pretrained models. In order to have a new CNN structure, it may take much time if we train it from scratch. Fortunately, TensorFlow model zoo has several pretrained models. Researchers usually open source the checkpoint files of the CNNs [21] they finally trained, so we can use the network for fine-tuning.

In our experiments, we applied transfer learning method on a pretrained GoogleNet/Inception V3 model (trained on Microsoft COCO dataset). The last fully connected layer of the network will be initialized with random weights (or zeroes), so when we input new data to train our model, the final layer’s weights will be readjusted. Some of the initial features such as edges and curves have been learned in the topology basic layers. We can apply these initial features [22] for our model to new problems, and this is the main concept of transfer learning. In conclusion, the weight of the fully connected layers will be changed according to the specific tags trained in the dataset of the problem we want to solve.

3. Meta-architectures

Convolutional neural networks (ConvNets) are the most advanced artificial neural networks [23] used for high-accuracy object detection in this decade. Most recently published papers in the areas of ConvNets and computer vision come after this default boxes approach and then reduce a regression loss and associated classification [17, 23] that is explained below. According to default box d , we catch paired ground truth box g (if it exists). If there are pairs, we tag d as “positive” and attach a class label $y_d \in \{1, \dots, K\}$ and box’s vector encoding g with respect to default box d (called the box encoding $\varphi(g_d; d)$). In the case of no pairs, we mark d as “negative” and set the class label to zero. If we suppose box encoding for default box d $f_{\text{loc}}(I; d, \theta)$ and equivalent class $f_{\text{cls}}(I; d, \theta)$, where I represents the image and θ is the model parameters, then the loss of d and the loss of classification are as follows:

$$L(d, I; \theta) = \alpha l_{\text{loc}}(\varphi(g_d; d) - f_{\text{loc}}(I; d, \theta)) + \beta l_{\text{cls}}(y_d, f_{\text{cls}}(I; d, \theta)), \quad (1)$$

where α and β weights are adjust localization and classification losses [24]. Equation (1) is averaged in default boxes and minimized with respect to parameters θ for training our model.

3.1. Single Shot Detector (SSD). The SSD approach discretizes the output space of bounding boxes into a set of default boxes over different aspect ratios and scales per feature map location [8]. At prediction time, the network generates scores for the presence of each object category in each default box and produces adjustments to the box to better match the object shape [13]. Additionally, the network combines predictions from multiple feature maps with different resolutions [25–27] to naturally handle objects of

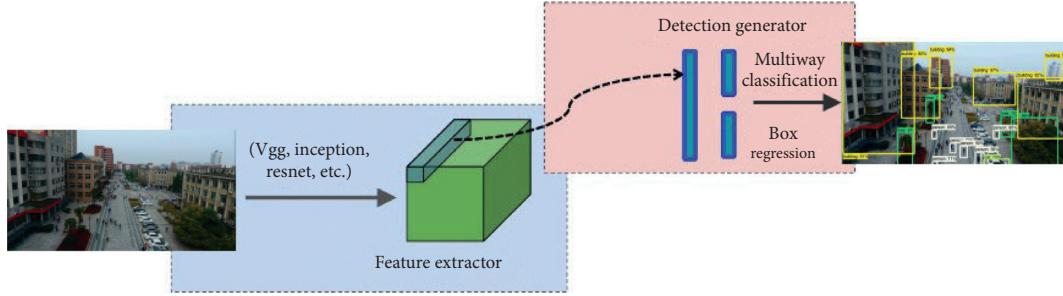


FIGURE 1: High-level diagram of SSD object detection system.

various sizes. SSD is simple and relative to methods that require object proposals [28] because it eliminates proposal generation and subsequent pixel or feature resampling stages and encapsulates all computation in a single network (Figure 1). This makes SSD easy to train and straightforward to integrate into systems that require a detection component.

The SSD training method is obtained from the MultiBox method but can accommodate multiple object classes. Suppose $x_{i,j}^p = \{1, 0\}$, an indicator for pairing the i -th default box to the j -th ground truth box of class p . From the pairing method above, we can write $\sum_i x_{i,j}^p \geq 1$. The long-term loss function is a weighted sum of the localization loss (loc) and the confidence loss (conf):

$$L(x, c, l, g) = \frac{1}{N} (L_{\text{conf}}(x, c) + \alpha L_{\text{loc}}(x, l, g)), \quad (2)$$

where N is the number of paired default boxes. If $N = 0$, set the loss to 0.

$$L_{\text{loc}}(x, l, g) = \sum_{i \in \text{Pos}} \sum_{m \in \{cx, cy, w, h\}} x_{i,j}^p \text{smooth}_{L1}(l_i^m - \hat{g}_j^m),$$

$$\hat{g}_j^{cx} = \frac{g_j^{cx} - d_i^{cx}}{d_i^{cx}},$$

$$\hat{g}_j^{cy} = \frac{g_j^{cy} - d_i^{cy}}{d_i^{cy}},$$

$$\hat{g}_j^w = \log\left(\frac{g_j^w}{d_i^w}\right),$$

$$\hat{g}_j^h = \log\left(\frac{g_j^h}{d_i^h}\right). \quad (3)$$

The loss of confidence is the softmax on multiclass confidence (c):

$$L_{\text{conf}}(x, c) = - \sum_{i \in \text{Pos}} x_{i,j}^p \log(\hat{c}_i^p) - \sum_{i \in \text{Neg}} \log(\hat{c}_i^0), \quad (4)$$

where

$$\hat{c}_i^p = \frac{\exp(c_i^p)}{\sum_p \exp(c_i^p)}, \quad (5)$$

and the weight term α is set to one through crossvalidation.

3.2. Faster Region-Based Convolutional Neural Networks (Faster R-CNN). In the Faster R-CNN [13] model, the detection process is divided into two stages (Figure 2). The first stage is called as region proposal network (RPN), images are processed by a feature extractor (in our case, GoogleNet/Inception V3), and features at some selected intermediate level (e.g., “conv5”) are used to predict class-agnostic box proposals. The last stage is to crop features from these box proposals, and then it is fed to the remainder of the feature extractor (e.g., “fc6” followed by “fc7”). We will get the predict from each proposal (a class and class-specific box refinement) [28]. What we need to know is that the running time depends on the number of regions proposed by the RPN network [13] because a part of the computation must be run in each region, but it does not crop proposals directly from the image and rerun crops through the feature extractor [11], and this is repeated.

3.3. GoogleNet/Inception Module. GoogleNet devised a module called inception module [13, 29] that approximates a sparse CNN with a normal dense construction (shown in the Figure 3), which uses convolutions of varied sizes to capture details at different scales, and the width/number of convolutional filters which have special kernel size is small just because only a little neurons are efficient.

One of the salient points about the module is that it has a so-called bottleneck layer (1×1 convolutions in Figure 3). Bottleneck layers help in massive decrease of the computation requirement as explained here.

We know the first inception module of GoogleNet, which the input has 192 channels. This module has $128 \ 3 \times 3$ kernel size filters and $32 \ 5 \times 5$ size filters, and the calculation order of 5×5 filter is $25 \times 32 \times 192$. When the width of the network and the number of 5×5 filters increase further, it will explode as we go deep into the network [23]. In order to

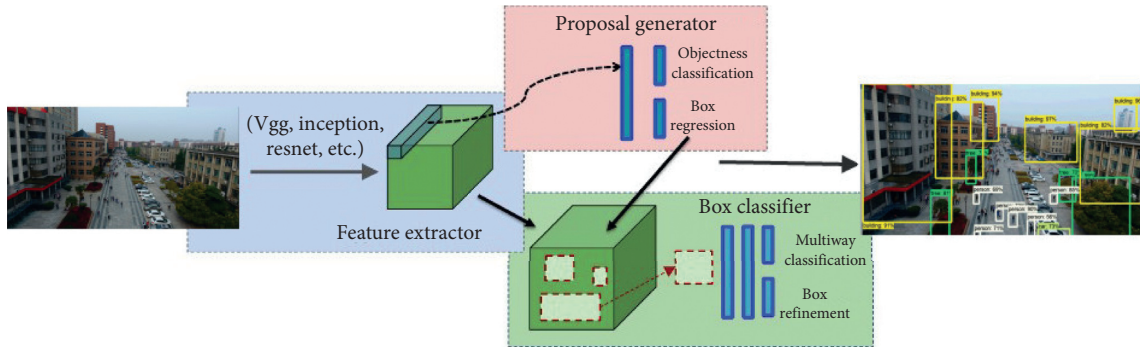


FIGURE 2: High-level diagram of Faster R-CNN object detection system.

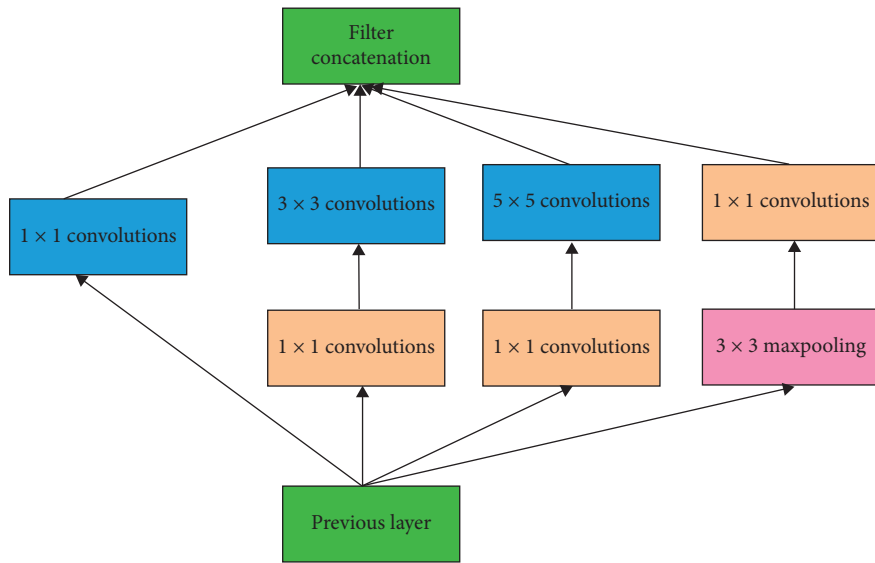


FIGURE 3: Inception modules.

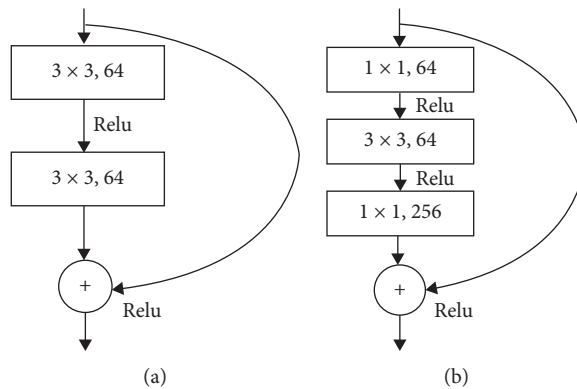


FIGURE 4: Residual blocks. (a) 64-d, (b) 256-d.

solve this problem, we need to use 1×1 convolution to reduce the channel dimension of the input image before we apply the larger size kernels and then feed them into these larger convolution kernels. Therefore, the input of

the inception module is first fed to a filter with only $16 \ 1 \times 1$ convolutions and then fed to a 5×5 convolution. As a result, these changes allow the network to have a greater width and depth.

3.4. *ResNet*. ResNet, or residual networks [30, 31], is one of the deepest networks to this day, and this network won the 2015 ILSVRC.

For any network model we design, we need to calculate the error gradient and then use the back propagation technology to improve the network model. When we use gradient descent (back propagation) to calculate the gradient error, we will use the chain rule of multiplication to calculate the gradient error. Whence, multiplication of many things less than one in the long chain will lead the result to be very small. It will affect the earlier layers in a deep architecture because it cannot update parameters. This will cause the training to become very slow, and the effect is not good; if the gradient becomes zero, the early training parameters cannot be updated.

What will happen if we use back propagation via the identity function? In that case, the gradient would be multiplied by one, and the gradient will not be missed. ResNet stacks residual blocks together [32, 33], which uses the identity function to maintain the gradient [19] (Figure 4).

Residual blocks are very simple to explain. We concatenate the result of applying some functions to the original input with the original input to ensure that the gradient is not less than 1, and no gradient disappears.

Mathematically, we can represent the residual block as follows:

$$H(x) = F(x) + x. \quad (6)$$

We can see from equation (1) that the gradient is unlikely to become zero and we can propagate all gradients backwards. These residual connections are just like a “gradient highway” because the gradient distributes evenly at sums in a computation graph [34].

These residual blocks are very powerful, which can make our network structure deeper. The deepest variant of ResNet was ResNet151 [31]. In our experiments, we have used ResNet50 as a feature extractor.

After revolution of ResNets, now researchers can use skip connections to create a deeper network architecture [32]. Example of ResNet architecture is shown in Figure 5.

4. Experiment Results

In this section, we analyse the results of detections and compare Single Shot Multibox Detector and Faster Region- [31, 32] based convolutional neural network object detection systems for accuracy, speed of detection on GPU and CPU, and memory usage. We organized three sets of experiments to explore object detection on videos captured by the drone. The first and second sets of experiments are focused on testing accuracy of object detection via Faster R-CNNs, and specially, reality of our idea is to apply object recognition systems for drone [35, 36] videos. The third experiment is done using the SSD object detection system.

4.1. Analyses

4.1.1. *Accuracy and Time*. In the scatter plot (Figure 6), the average mAP of each meta-architecture is visualized. Each

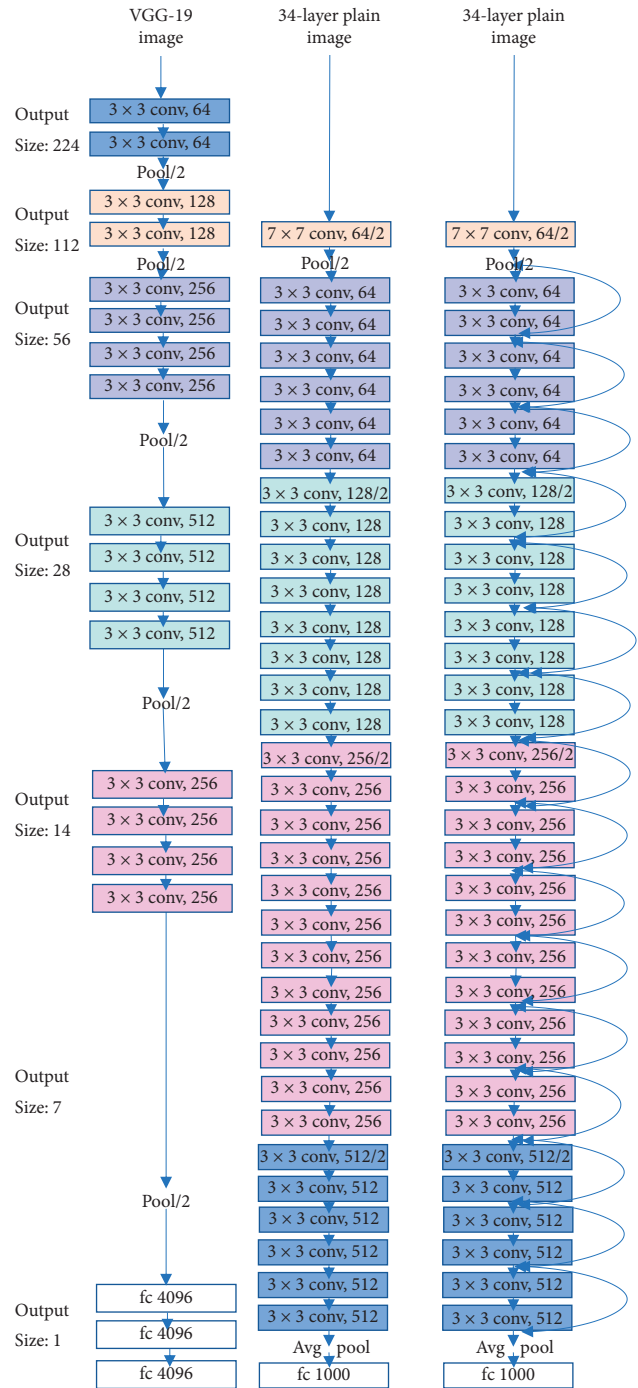


FIGURE 5: Example ResNet architecture.

image average running time is shown in the figure; it goes from a few hundreds milliseconds to 200 milliseconds. In general, our experiment shows that SSD meta-architectures are faster but with lower accuracy, and Faster R-CNN meta-architectures are more accurate; however, it requires at least 130 milliseconds for one image.

4.1.2. *The Effect of the Feature Extractor*. To explore the effect of feature extractors, in Table 1, we show some well-known feature extractors that have been used in other works.

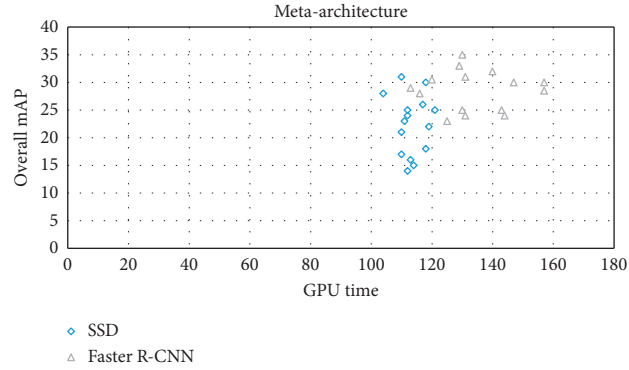


FIGURE 6: Accuracy and time. Overall mAP and average GPU time.

TABLE 1: Convolutional detection models.

Paper	Meta-architecture	Feature extractor	Matching	Box encoding φ (;)	Location loss functions
Szegedy et al.	SSD	Inception V3	Bipartite	$[x_0, y_0, x_1, y_1]$	L_2
Redmon et al.	SSD	R-CNN	Box centre	$[x_c, y_c, \sqrt{w}, \sqrt{h}]$	L_2
Ren et al.	Faster R-CNN	VGG	Argmax	$[(x_c/w_d), (y_c/h_d), \log w, \log h]$	Smooth L_1
He et al.	Faster R-CNN	ResNet101	Argmax	$(x_c/w_d), (y_c/h_d), \log w, \log h$	Smooth L_1
Liu et al.	SSD	Inception V3	Argmax	$[x_0, y_0, x_1, y_1]$	L_2
Liu et al. v1, v2	SSD	VGG	Argmax	$[(x_c/w_d), (y_c/h_d), \log w, \log h]$	Smooth L_1

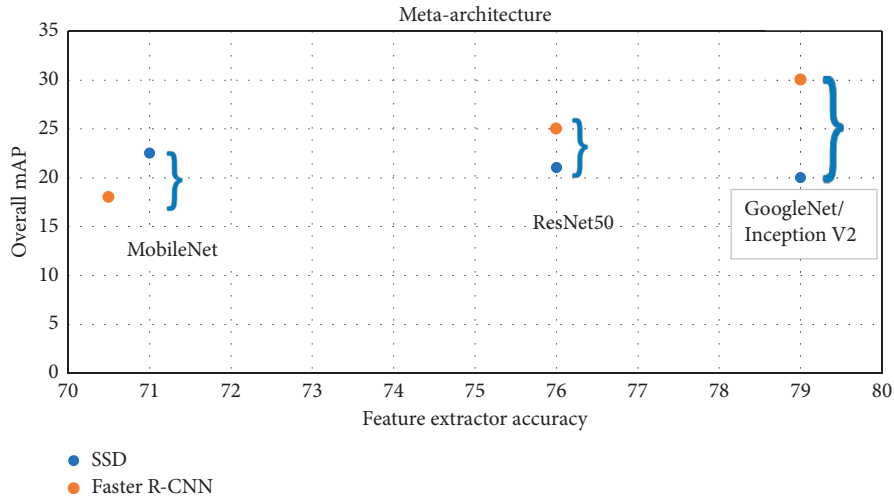


FIGURE 7: The effect of feature extractors for the overall mAP.

Stronger performance on detection is positively connected with stronger performance on classification, and Figure 7 shows such an overall ratio relationship between classification and detection performance really exists.

4.1.3. The Effect of Image Size. Image resolution can hugely affect object detection accuracy, and it has been shown in many other state-of-the-art researches. Our experiments show that decreasing image dimensions coherently decreases accuracy

(by 18% on average) and reduces average running time by a relative factor of 23%. So high-resolution images can solve the problem of small objects, just as Figure 8 shows.

4.1.4. Memory Analysis. In our experiments, the image resolution is 300. We have measured total usage of alternate peak usage for the memory benchmarking. Figure 9 shows the memory usage of different meta-architecture and feature

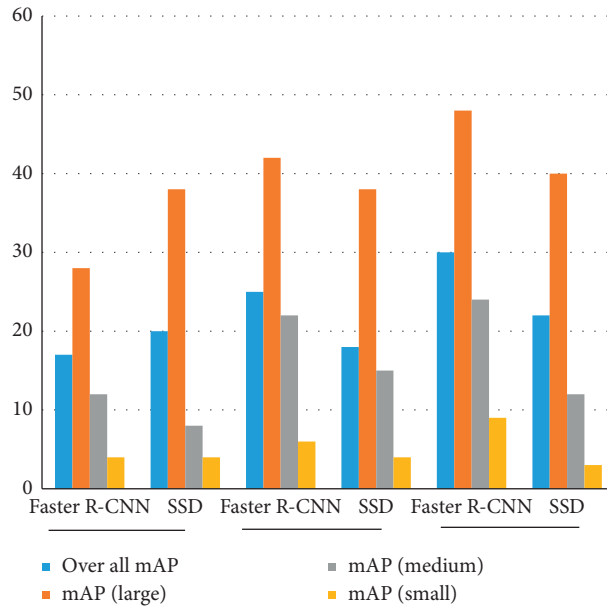


FIGURE 8: The influence of different object sizes, meta-architectures and feature extractors on accuracy.

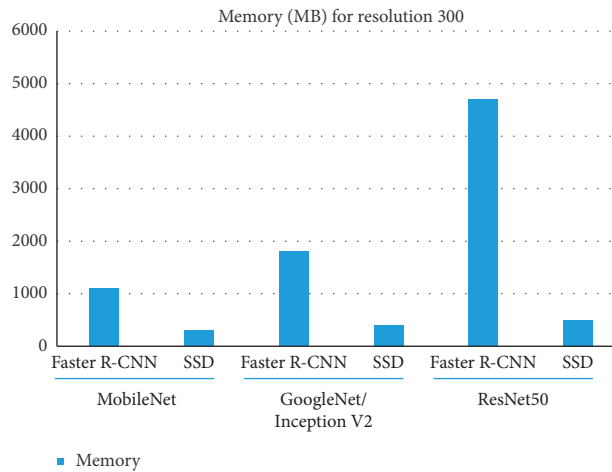


FIGURE 9: Memory usage for each model.

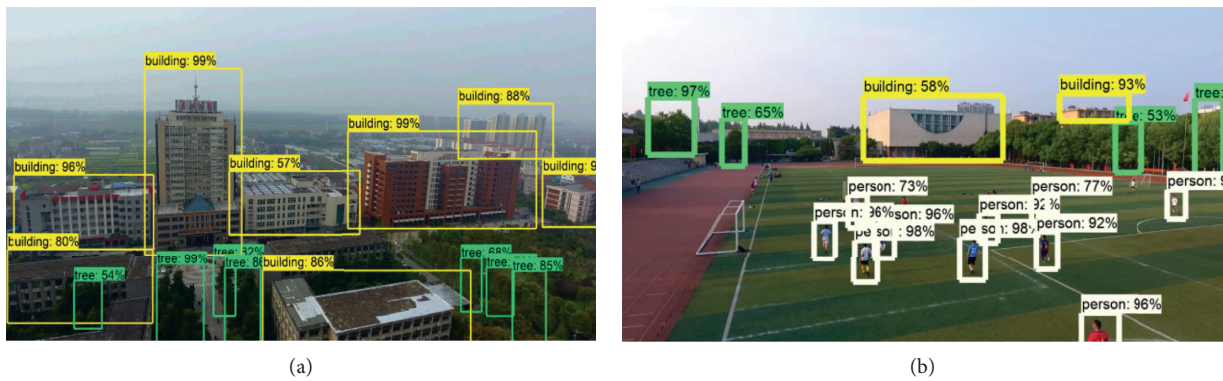


FIGURE 10: Continued.

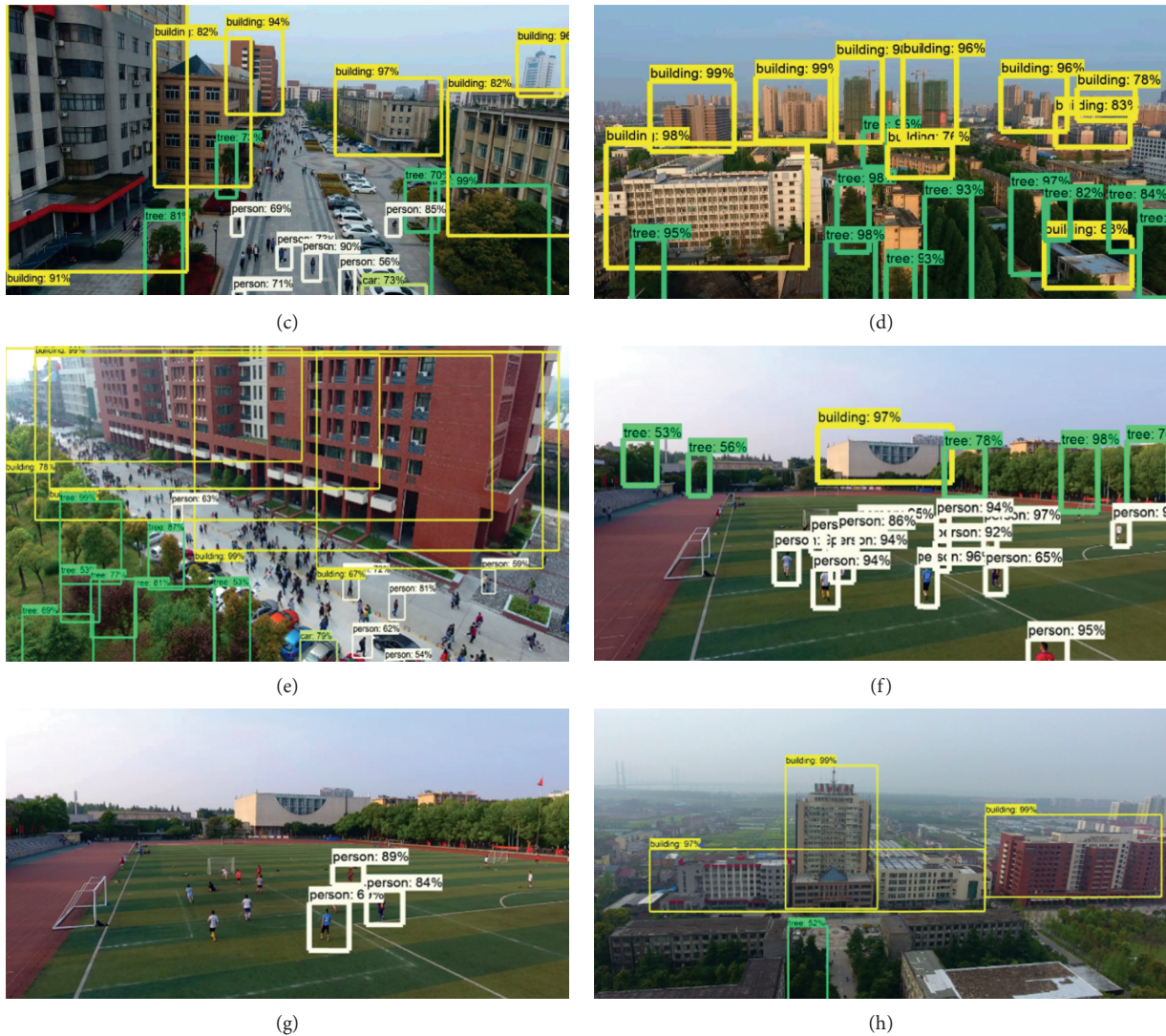


FIGURE 10: Example detections from different models and feature extractors. (a) Result of detection with Faster R-CNN base on GoogleNet/Inception V3. (b) Result of detection with Faster R-CNN base on GoogleNet/Inception V3. (c) Result of detection with Faster R-CNN base on GoogleNet/Inception V3. (d) Result of detection with Faster R-CNN base on ResNet50. (e) Result of detection with Faster R-CNN base on ResNet50. (f) Result of detection with Faster R-CNN base on ResNet50. (g) Result of detection with SSD base on GoogleNet/Inception V3. (h) Result of detection with SSD base on GoogleNet/Inception V3.

extractors. Generally, experiments show that larger and powerful feature extractors take much more memory.

We can see that Mobilenet requires the least memory, even less than 1 Gb (almost) in almost all settings.

5. Conclusion

This research is based on object detection from the video taken by the drone via convolutional neural network [37]. In this research, we put forward for consideration to use CNNs to allow drones to recognize some of object types such as building, car, tree, and person [38]. Convolutional neural networks are computationally expensive [39]; even so, we use the method transfer learning to train our neural networks with smaller image datasets. In our project, we use

TensorFlow's powerful object detection API, and it helped us to easily construct a new model and deploy for detection.

From the results, we observed that the detection accuracy of the two models for buildings, trees, cars, and people is very high, with an average of more than 85% and a maximum of 99%. We have done some experimental comparison of two modern object detectors for memory usage, speed, and accuracy. SSD models pay more attention to scale, aspect ratio and predictions sampling location than Faster R-CNN, the average time of each frame is 115 ms, but the target detection rate is low. However, Faster R-CNN is more accurate and finds more objects from scene, almost 95% of all objects in the image can be recognized, but the average time of each frame is at least 140 ms. In general, our experiments show that the SSD model is faster on average. On the contrary, Faster R-CNN is relatively slower but more

accurate. But one way to speed up the Faster R-CNN model is to limit the number of proposed regions. In our experiment, we tested the memory and runtime requirements of MobileNet, ResNet50, and GoogleNet/Inception V2. MobileNet requires the least memory, which is less than 1 GB, and ResNet50 has nearly 5 GB of memory on Faster R-CNN, while the memory required by GoogleNet/Inception V2 is in the middle, less than 2 GB. In general, we obtained high correlation with running time and memory between the model and the feature extractors.

The detection results shown in Figure 10 were obtained after implementation on a video captured by a drone.

Hopefully, these experimental results help other researchers to choose a suitable algorithm when selecting object detection for deployment in the real world. The experiment shows that viewing small objects from close is important in order to detect as many objects as possible. This proposes the usage of a drone can be assumed for detecting as many objects as possible as a drone is designed flexible.

Data Availability

The raw/processed data required to reproduce these findings cannot be shared at this time as the data also form part of an ongoing study.

Conflicts of Interest

The authors declare that there are no conflicts of interest regarding the publication of this paper.

Acknowledgments

This paper was supported by the 2018 Jingzhou Science and Technology Development Plan Project “Research and Development of New Methods of UAV Visual Data Deep Learning Identification Technology in Urban Management” and the 2019 Yangtze University 12th batch of college students innovation and entrepreneurship project “Implementation of Real-Time Body Gesture Tracking Algorithm on Android Mobile Terminal under the Framework of TensorFlow Lite.”

References

- [1] Z. Zhang, W. Zhan, Z. He, and Y. Zou, “Application of spatio-temporal context and convolution neural network (CNN) in grooming behavior of *Bactrocera minax* (Diptera: tetryptidae) detection and statistics,” *Insects*, vol. 11, no. 9, p. 565, 2020.
- [2] W. Zhan, I. Ramatov, W. Cui et al., “Survey of deep learning target detection algorithms based on candidate regions,” *Journal of Yangtze University*, vol. 16, no. 5, pp. 108–115, 2019.
- [3] X. Hui, B. Jiang, Y. Yu, X. Zhao, and M. Tan, “A novel autonomous navigation approach for UAV power line inspection,” in *Proceedings of the 2017 IEEE International Conference on Robotics and Biomimetics (ROBIO)*, Macau, China, December 2017.
- [4] R. Jain, R. Kasturi, and B. G. Schunck, *Object Recognition*, Machine Vision, McGraw-Hill, NY, USA, 1995.
- [5] F. Wen, Z. Zhang, K. Wang, G. Sheng, and G. Zhang, “Angle estimation and mutual coupling self-calibration for ULA-based bistatic MIMO radar,” *Signal Processing*, vol. 144, pp. 61–67, 2018.
- [6] F. Wen and J. Shi, “Fast direction finding for bistatic EMVS-MIMO radar without pairing,” *Signal Processing*, vol. 173, Article ID 107512, 2020.
- [7] J. C. van Gemert, C. R. Verschoor, P. Mettes, K. Epema, L. P. Koh, and S. Wich, “Nature conservation drones for automatic localization and counting of animals,” *Computer Vision/ECCV 2014 Workshops*, vol. 8925, pp. 255–270, 2015.
- [8] P. Rudol and P. Doherty, “Human body detection and geolocation for UAV search and rescue missions using color and thermal imagery,” in *Proceedings of the 2008 IEEE Aerospace Conference*, Big Sky, MT, USA, March 2008.
- [9] L. Grip, “Vision based indoor object detection for a drone,” M.Sc. thesis dissertation, KTH, Stockholm, Sweden, 2017.
- [10] J. Zheng, T. Yang, H. Liu, T. Su, and L. Wan, “Accurate detection and localization of UAV swarms-enabled MEC system,” *IEEE Transactions on Industrial Informatics*, pp. 1–1, 2020.
- [11] C. Szegedy, S. Reed, D. Erhan, D. Anguelov, and S. Ioffe, “Scalable, high-quality object detection,” 2014, <https://arxiv.org/abs/1412.1441>.
- [12] C. N. Truong, N. Q. H. Ton, H. P. Do, and S. P. Nguyen, “Digit detection from digital devices in multiple environment conditions,” in *Proceedings of the 2020 RIVF International Conference on Computing and Communication Technologies (RIVF)*, Ho Chi Minh City, Vietnam, October 2020.
- [13] S. Ren, K. He, R. Girshick, and J. Sun, “Faster R-CNN: towards real-time object detection with region proposal networks,” *IEEE Transactions on Pattern Analysis and Machine Intelligence*, vol. 39, no. 6, pp. 1137–1149, 2017.
- [14] J. Redmon, S. Divvala, R. Girshick, and A. Farhadi, “You only look once: unified, real-time object detection,” in *Proceedings of the IEEE International Conference on Robotics and Automation (ICRA)*, Washington State Convention Center, Seattle, WA, USA, pp. 1316–1322, May 2015.
- [15] R. A. (Intel), Krishnaprasad T. (Intel), Object detection on drone videos using caffe framework, 2018, http://icml.cc/2016/?page_id=97.
- [16] A. G. Howard, M. Zhu, B. Chen et al., “MobileNets: efficient convolutional neural networks for mobile vision applications,” 2017, <https://arxiv.org/abs/1704.04861>.
- [17] K. Bregar and M. Mohorcic, “Improving indoor localization using convolutional neural networks on computationally restricted devices,” *IEEE Access*, vol. 6, pp. 17429–17441, 2018.
- [18] V. Viitaniemi and J. Laaksonen, “Techniques for image classification, object detection and object segmentation,” *Visual Information Systems. Web-Based Visual Information Search and Management, Lecture Notes in Computer Science*, pp. 231–234, 2008.
- [19] J. Yosinski, J. Clune, Y. Bengio, and H. Lipson, “How transferable are features in deep neural networks?” in *Proceedings of the 27th International Conference on Neural Information Processing Systems*, vol. 27, Montreal, Canada, December 2014.
- [20] L. Wan, X. Kong, and F. Xia, “Joint range-Doppler-angle estimation for intelligent tracking of moving aerial targets,” *IEEE Internet of Things Journal*, vol. 5, no. 3, pp. 1625–1636, 2018.
- [21] X. Wang, L. Wang, X. Li, and G. Bi, “Nuclear norm minimization framework for DOA estimation in MIMO radar,” *Signal Processing*, vol. 135, pp. 147–152, 2017.
- [22] A. S. Razavian, H. Azizpour, J. Sullivan, and S. Carlsson, “CNN features off-the-shelf: an astounding baseline for

- recognition,” in *Proceedings of the 2014 IEEE Conference on Computer Vision and Pattern Recognition Workshops*, pp. 512–519, Columbus, OH, USA, June 2014.
- [23] C. Szegedy, W. Liu, Y. Jia et al., “Going deeper with convolutions,” in *Proceedings of the 2015 IEEE Conference on Computer Vision and Pattern Recognition*, pp. 1–9, Boston, MA, USA, June 2015.
- [24] A. Krizhevsky, I. Sutskever, and G. E. Hinton, “ImageNet classification with deep convolutional neural networks,” *Communications of the ACM*, vol. 60, no. 6, pp. 84–90, 2017.
- [25] J. Wang and L. Perez, “The effectiveness of data augmentation in image classification using deep learning,” 2017, https://www.researchgate.net/publication/335844785_DATA_AUGMENTATION_APPROACHES_FOR_SATELLITE_IMAGE_SUPER-RESOLUTION.
- [26] J. Wu, Y. Yu, C. Huang, and K. Yu, “Deep multiple instance learning for image classification and auto-annotation,” in *Proceedings of the 2015 IEEE Conference on Computer Vision and Pattern Recognition (CVPR)*, pp. 3460–3469, Boston, MA, USA, June 2015.
- [27] V. Mnih and G. Hinton, “Learning to detect roads in high-resolution aerial images,” in *Proceedings of the 11th European conference on Trends and Topics in Computer Vision*, pp. 1–14, Heraklion, Greece, September 2010.
- [28] I. Mansour, R. Hoffman, O. Rawashdeh, and B. Seifert, “A proposed heterogeneous convolutional neural network for embedded automotive vision algorithms,” in *Proceedings of the 2018 IEEE International Conference on Electro/Information Technology (EIT)*, Rochester, MI, USA, May 2018.
- [29] C. Szegedy, V. Vanhoucke, S. Ioffe, J. Shlens, and Z. Wojna, “Rethinking the inception architecture for computer vision,” 2015, <https://arxiv.org/abs/1512.00567>.
- [30] H. Kaiming, “Deep residual networks: deep learning gets way deeper,” in *Proceedings of the ICML 2015 32nd International Conference on Machine Learning*, Lille, France, July 2015.
- [31] F. Wang, M. Jiang, C. Qian et al., “Residual attention network for image classification,” in *Proceedings of the 2017 IEEE Conference on Computer Vision and Pattern Recognition (CVPR)*, vol. 1, pp. 3156–3164, Honolulu, HI, USA, July 2017.
- [32] A. B. Makar, K. E. McMartin, M. Palese, and T. R. Tephly, “Formate assay in body fluids: application in methanol poisoning,” *Biochemical Medicine*, vol. 13, no. 2, pp. 117–126, 1975.
- [33] S. Wu, S. Zhong, and Y. Liu, “Deep residual learning for image steganalysis,” *Multimedia Tools and Applications*, pp. 1–17, 2017.
- [34] J. Huang, V. Rathod, C. Sun et al., “Speed/accuracy trade-offs for modern convolutional object detectors,” in *Proceedings of the 2017 IEEE Conference on Computer Vision and Pattern Recognition (CVPR)*, vol. 2017, pp. 3296–3305, Las Vegas, NV, USA, July 2017.
- [35] F. J. C. Condessa, “Robust image classification with context and rejection,” *IEEE GRSS Workshop Hyperspectral Image Signal*, 2015.
- [36] P. Chen, Y. Dang, R. Liang, W. Zhu, and X. He, “Real-time object tracking on a drone with multi-inertial sensing data,” *IEEE Transactions on Intelligent Transportation Systems*, vol. 19, no. 1, pp. 131–139, 2018.
- [37] W. Cui, W. Zhan, J. Yu, C. Sun, and Y. Zhang, “Face recognition via convolutional neural networks and siamese neural networks,” in *Proceedings of the International Conference on Intelligent Computing, Automation and Systems (ICICAS)*, pp. 746–750, Chongqing, China, December 2019.
- [38] V. Lempitsky and A. Zisserman, “Learning to count objects in images,” *Advances in Neural Information Processing Systems*, pp. 1324–1332, MIT Press, Cambridge, MA, USA, 2010.
- [39] T. Liu, F. Wen, J. Shi, Z. Gong, and H. Xu, “A computationally economic location algorithm for bistatic EVMS-MIMO radar,” *IEEE Access*, vol. 7, pp. 120533–120540, 2019.

Research Article

Flexible MIMO Radar Antenna Selection for Vehicle Positioning in IIOT Based on CNN

Yang Xiong  and Ke Wang 

School of Electronic and Information, Yangtze University, Jingzhou, China

Correspondence should be addressed to Ke Wang; kwangs@sina.com

Received 21 July 2020; Accepted 20 August 2020; Published 1 October 2020

Guest Editor: Liangtian Wan

Copyright © 2020 Yang Xiong and Ke Wang. This is an open access article distributed under the Creative Commons Attribution License, which permits unrestricted use, distribution, and reproduction in any medium, provided the original work is properly cited.

Unmanned vehicles are widely used in industrial scenarios; their positioning information is vital for emerging the industrial internet of thing (IIOT); thus, it has aroused considerable interest. Cooperative vehicle positioning using multiple-input multiple-output (MIMO) radars is one of the most promising techniques, the core of which is to measure the direction-of-arrival (DOA) of the vehicle from various viewpoints. Owing to power limitations, the MIMO radar may be unable to utilize all the antenna elements to transmit/receive (Tx/Rx) signal. Consequently, it is necessary to deploy a full array and select an optimal Tx/Rx solution. Owing to the industrial big data (IBD), it is possible to obtain a massive labeled dataset offline, which contains all possible DOAs and the array measurement. To pursuit fast and reliable Tx/Rx selection, a convolutional neural network (CNN) framework is proposed in this paper, in which the antenna selection is formulated as a multiclass-classification problem. Herein, we assume the DOA of the vehicle has been known as a prior, and the optimization criterion is to minimize the Cram er-Rao based on DOA estimation when we use the selected Tx/Rx subarrays. The proposed framework is flexible and energy friendly. Simulation results verify the effectiveness of the proposed framework.

1. Introduction

Industrial internet of thing (IIOT) is acknowledged as the trend of the manufacturing industry [1], which aims to promote product innovation, improve operation level, and expand novel business models. In industrial logistics, unmanned vehicles are widely used. For safe driving purpose, it is important to enable the vehicles to the internet-of-vehicle (IOV). IOV is an important branch of IIOT [1]. Vehicle positioning is one of the most important tasks in IOV that has gained extensive attention in the past decades. Several frameworks have been put forward, the most commonly used method rely on the global positioning system (GPS). However, the high latency reduces the implementation potential of GPS technique for the IOV. Moreover, the line-of-sight transmission property of the GPS signal makes it unavailable in tunnels, and it may fail to work due to cloud cover. To develop a robust and reliable vehicle positioning system, some advanced sensors have been investigated, for

instance, cameras, lidars, and radars [2]. On the basis of comprehensive consideration of cost, latency, and reliability, the radar approaches are promising. Generally, the vehicle position can be measured from four principles in the radar approaches [3, 4], i.e., radio-signal strength (RSS), time-of-arrival (TOA), time-difference-of-arrival (TDOA), and direction-of-arrival (DOA). Nevertheless, the RSS techniques are difficult to accurately obtain vehicle position due to the complexity of the wireless channel. The TOA and TDOA approaches rely on latency measurement, but it is usually very hard to obtain high-accuracy time difference. The DOA approaches are appearing, since the DOA measurement has adequate accuracy by exploiting an antenna array [5].

The concept of DOA is shown in Figure 1, in which the radar nodes measure the angle of the incoming radio signal from various viewpoints. To achieve super angle resolution, an antenna array is employed to transmit/receive (Tx/Rx) signal at the radar node. Usually, antenna elements are placed into uniform sharps, e.g., uniform linear array,

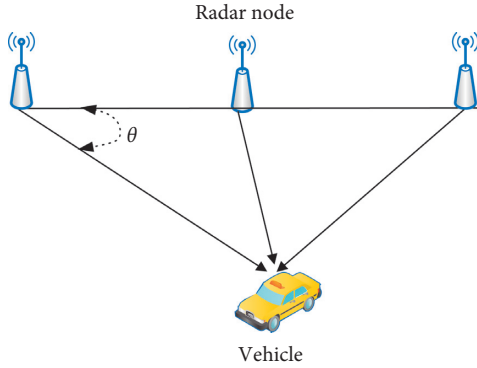


FIGURE 1: Illustration of DOA-based positioning techniques.

uniform circular array, and uniform rectangular array, thus spatial Nyquist sampling is available. By cooperating with the existing estimation algorithms [6], e.g., multiple signal classification (MUSIC), the estimation method of signal parameters via the rotational invariance technique (ES-PRIT), tensor estimator, the DOA can be easily achieved. As is known to us, angular resolution of a uniform array can be improved by increasing the array aperture at the expensive of higher cost, larger physical area, and additional computational burden. To mitigate this issue, several nonuniform alternatives have been proposed, such as minimum redundancy arrays, coprime array, and nested array. These arrays declare to achieve more degree-of-freedom, but the antenna elements are fixed. To pursuit radar cognition, reconfigurable circuitry is required, e.g., waveform agility and array adaptively. To this end, the compressive sensing concept was introduced [7], in which Tx/Rx is randomly chosen from a full array. The DOA can be accurately recovered with high probability via solving an optimization problem, i.e., DOA estimation can be linked to the popular sparse representation methods, e.g., [8]. Nonetheless, such approach is hard to achieve an optimal array manifold since it is agnostic to current target scenario. A adaptive framework was investigated in [9–11], the goal of which is to minimize the determinant of the estimation error covariance matrix, and it was treated as a convex optimization problem. In [12], the sensors were dynamically adjusted via minimizing the Cramér–Rao bound (CRB) on parameter estimation, and the greedy search algorithm was adopted. Another reconfigurable receive array selection framework was addressed in [13], in which the conditional Bobrovski–Zakai bound (BZB) on DOA estimation was chosen as a performance metric. A reconfigurable Tx/Rx pair methodology was proposed for the multiple-input multiple-output (MIMO) radar [14]. Similarly, the selection task is solved via greedy search algorithm. A common feature the approaches in [9, 14] share is that a mathematical optimization problem needs to be solved, which is time-consuming.

With the explosive growth of industrial sensors, tremendous complex real-time data can be obtained from the physical and man-made environments, which leads to industrial big data (IBD). The IBD provides an unprecedented opportunity to facilitate data-driven prediction techniques

for array selection. A few works have interpreted the antenna selection problem to multiclass-classification learning. To realize different type classifications, various classifiers are available, e.g., support vector machine (SVM), k-nearest neighbor (KNN), decision tree (DT), multilayer perception (MLP). In [15], a SVM architecture was presented, which links antenna selection to the supervised machine learning. Inspired by the artificial neural networks, the convolutional neural networks (CNN) become the most popular generative models in machine learning [16, 17]. CNN is a powerful tool, since it is skilled in automatic feature extraction from massive data. It has been proven that its superiority is in extensive aspects, such as text and voice recognition, image processing, and industrial manufacture. More recently, the deep learning network was adopted for antenna selection in [18]. In their work, a CNN is trained offline, in which the real part, the image part, and the angle of the covariance matrix were used as the input of the CNN; the object function is to minimize the error bound on DOA estimation (e.g., BZB and CRB). Compared with the SVM approach, the CNN method provides more accurate and faster classification performance. Similar to [18], the CNN approaches have been exploited for Tx/Rx selection in MIMO communications [19]. Unlike MIMO communications, MIMO radars illuminate an area of interest via emitting diversity waveforms and receive the echoes using multiple antennas. Owing to the noncooperative operation mode, a MIMO radar needs much more transmit power than a MIMO communication system. In practical IOV network, however, most of the radar nodes are far away from the power grid. Usually, the radars are powered by solar panels. Therefore, the transmit power of the radar system is limited. The closest prior study to our work is [18], but it is only suitable for receiving antenna selection in passive radars. Moreover, the training of CNN is inefficient.

In this paper, we investigated the problem of optimal Tx/Rx selection for vehicle positioning in IIOT. The object is to minimize the CRB on MIMO radar DOA estimation error with limited transmit power. The Tx/Rx selection issue is treated as a multiclass-classification problem, and a CNN-auxiliary framework is proposed. Instead of inputting the real part, the image part and the angle of the covariance matrix, the amplitude values and phase values of the covariance matrix are identified as the input of the CNN. Simulation results show the proposed framework offer faster and more accuracy selection performance. The main contributions of this paper are illustrated as follows:

- (a) A cooperative vehicle positioning architecture relying on DOA estimation is presented. The core is to measure the DOA of the vehicle via MIMO radar nodes. Combined with the location information of the nodes, vehicle position can be accurately recovered. Unlike the RSS approaches, the TOA approaches, and the TDOA approaches, the DOA approaches are insensitive to the environment. Benefiting from the virtual aperture of the MIMO radar, high-precision DOA estimation can be easily obtained.

- (b) A practical scenario that the MIMO radar with limited power is considered. We assume the target vehicles are slow-moving so that their DOA information area is prior to the radar nodes. To pursuit efficient and high-accuracy vehicle positioning, we need to choose an optimal Tx/Rx pair from a full array. The antenna selection is transformed into a multiclass classification
- (c) A CNN-auxiliary framework is proposed for fast classification. To obtain the training data, the greedy search strategy is adopted; the optimal Tx/Rx pair is accepted if the minimum CRB is obtained. Thereafter, the upper triangle measurement of the array covariance matrices is designated as the input of CNN to indicate the well-chosen Tx/Rx pairs. Finally, the CNN is utilized to Tx/Rx selection online.

The paper is organized as follows. In Section 2, the problem of vehicle positioning using the colocated MIMO radar is formulated. In Section 3, the derivation of CRB is given. In Section 4, the details of the proposed CNN framework are described. In Section 5, the simulation results are outlined. Finally, a brief conclusion is given in Section 6.

Notations. Lowercase italic letters, e.g., a , boldface lowercase letters, e.g., \mathbf{a} , and boldface capital letters, e.g., \mathbf{A} , are reserved for scalars, vectors, and matrices, respectively; the superscripts $(\mathbf{X})^T$, $(\mathbf{X})^H$, $(\mathbf{X})^{-1}$, and $(\mathbf{X})^+$ stand for the operations of transpose, Hermitian transpose, inverse and pseudoinverse, respectively; \otimes , \odot , and \circledast represent, respectively, the Kronecker product and the Khatri-Rao product and the Hadamard product; $\mathbf{E}\{\cdot\}$ is to get the mathematical expectation; $\text{vec}(\cdot)$ denotes the vectorization operation; \mathbf{I}_M denotes the $M \times M$ identity matrix; C_M^r denotes the combination of selecting r terms out of M . $\text{blkdiag}\{\cdot\}$ accounts for the block diagonal matrix with the diagonal blocks in the bracket.

2. Problem Formulation

The architecture of the proposed vehicle positioning system is illustrated in Figure 2. The MIMO radar nodes are fixed at the roadside with known position, and they are connected with the cloud platform using low-latency optical fiber. The position of the target vehicle barely changes during consecutive scans. In the first scan, a full Tx/Rx array is utilized to detect the vehicle position. The covariance matrix of the MIMO radar node is fed to a CNN to find an optimal Tx/Rx pair for the next scans. All the nodes are well synchronized, and the measured DOAs are uploaded to the cloud to calculate the vehicle position.

Now, we consider a colocated MIMO radar scenario, as depicted in Figure 3. Each radar node is equipped with M transmit antennas and N receive antennas, both of which are uniform linear arrays (ULA) with the same interelement distance d . Taking the first Tx/Rx antenna as reference element, the position sets of the Tx/Rx are given by

$$\begin{aligned}\Omega_t &= \{0, d, 2d, \dots, (M-1)d\}, \\ \Omega_r &= \{0, d, 2d, \dots, (N-1)d\}.\end{aligned}\quad (1)$$

Due to power limitation, we can only choose M_1 transmit antennas and N_1 receive antennas from a full Tx/Rx array (the reference elements are enforced to be chosen). Thus, the position sets corresponding to the selected Tx/Rx are Ω'_t and Ω'_r , respectively. Suppose that K target vehicles are appearing the far-field of the radar nodes, thus they can be regarded as point targets. Let θ_k denote the k -th DOA of the vehicle, and let $\mathbf{a}_t(\theta_k) \in \mathbb{C}^{M_1 \times 1}$ and $\mathbf{a}_r(\theta_k) \in \mathbb{C}^{N_1 \times 1}$ denote the steering vectors corresponding to the selected transmit array and the selected receive array, respectively. The m -th ($m = 1, 2, \dots, M_1$) element of $\mathbf{a}_t(\theta_k)$ and the n -th ($n = 1, 2, \dots, N_1$) entity of $\mathbf{a}_r(\theta_k)$ are respectively given by

$$\begin{aligned}\mathbf{a}_m(\theta_k) &= \exp\left\{\frac{-j2\pi x_m \sin(\theta_k)}{\lambda}\right\}, \\ \mathbf{a}_n(\theta_k) &= \exp\left\{\frac{-j2\pi x_n \sin(\theta_k)}{\lambda}\right\},\end{aligned}\quad (2)$$

where λ denotes the carrier wavelength and x_m and x_n are the m -th and n -th entities of Ω'_t and Ω'_r , respectively. Assume that the selected transmit antennas emit mutual orthogonal pulse waveforms $\{p_m(t)\}_{m=1}^{M_1}$. For any $m_1, m_2 \in \{1, 2, \dots, M_1\}$, there exists

$$\int_{T_p} p_{m_1}(t) p_{m_2}^*(t) dt = \delta(m_1 - m_2), \quad (3)$$

where t accounts for the fast time index, T_p denotes the pulse duration, and $\delta(\cdot)$ stands for the Kronecker delta. The echoes received by the array can be written as

$$\mathbf{r}(t, \tau) = \sum_{k=1}^K s_k(\tau) \mathbf{a}_r(\theta_k) \mathbf{a}_t^T(\theta_k) \mathbf{P}(t) + \mathbf{w}(t, \tau), \quad (4)$$

where τ is the pulse index, $s_k(\tau)$ denotes the reflection coefficient of the k -th vehicle, $\mathbf{P}(t) = [p_1(t), p_2(t), \dots, p_M(t)]^T$ denotes the transmit waveform vector, and $\mathbf{w}(t, \tau)$ is the noise vector, which is the Gaussian white with variance σ^2 , i.e.,

$$\mathbf{E}\{\mathbf{w}(t_1, \tau) \mathbf{w}^H(t_2, \tau)\} = \sigma^2 \mathbf{I} \cdot \delta(t_1 - t_2). \quad (5)$$

Matching $\mathbf{r}(t, \tau)$ with $\mathbf{P}(t)$ yields

$$\begin{aligned}y(\tau) &= \text{vec}\left(\int_{T_p} \mathbf{r}(t, \tau) \mathbf{P}^H(t) dt\right) \\ &= \sum_{k=1}^K [\mathbf{a}_t(\theta_k) \otimes \mathbf{a}_r(\theta_k)] s_k(\tau) + \mathbf{e}(\tau) = \mathbf{A} \mathbf{s}(\tau) + \mathbf{n}(\tau),\end{aligned}\quad (6)$$

where $\mathbf{A} = [\mathbf{a}(\theta_1), \mathbf{a}(\theta_2), \dots, \mathbf{a}(\theta_K)] \in \mathbb{C}^{M_1 N_1 \times K}$ is the virtual response matrix with the k -th virtual vector given by $\mathbf{a}(\theta_k) = \mathbf{a}_t(\theta_k) \otimes \mathbf{a}_r(\theta_k)$ and $\mathbf{s}(\tau) = [s_1(\tau), s_2(\tau), \dots, s_K(\tau)]^T$ is the reflection coefficient vector. $\mathbf{n}(\tau) = \text{vec}\left(\int_{T_p} \mathbf{w}(t, \tau) \mathbf{P}^H(t) dt\right)$ denotes the matched array

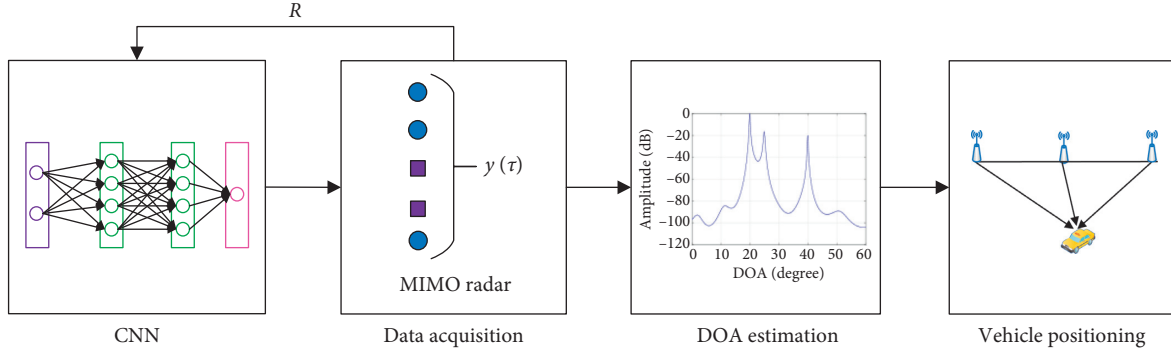


FIGURE 2: The architecture of the proposed vehicle positioning system.

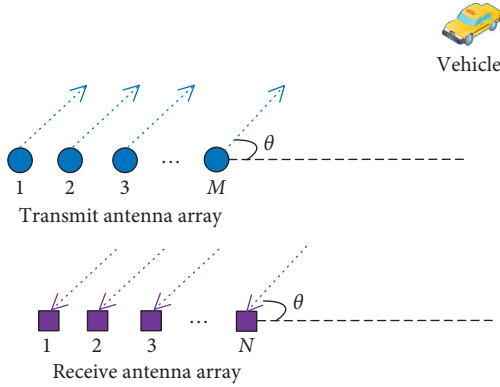


FIGURE 3: DOA estimation model for the colocated MIMO radar.

noise. According to [6], $n(\tau)$ is still a Gaussian white with variance σ^2 , i.e.,

$$\mathbf{R}_n = E\{n(\tau)n^H(\tau)\} = \sigma^2 \mathbf{I}_{M_1 N_1}. \quad (7)$$

Consequently, the covariance matrix of $y(\tau)$ can be expressed as

$$\mathbf{R} = E\{y(\tau)y^H(\tau)\} = \mathbf{A}\mathbf{R}_s\mathbf{A}^H + \mathbf{R}_n, \quad (8)$$

where $\mathbf{R}_s = E\{s(\tau)s^H(\tau)\}$ accounts for the covariance matrix of the reflection coefficient. In the presence of L samples $y(\tau_1), y(\tau_2), \dots, y(\tau_L)$, \mathbf{R} can be estimated via

$$\hat{\mathbf{R}} = \frac{1}{L} \sum_{l=1}^L y(\tau_l)y^H(\tau_l). \quad (9)$$

To estimate the DOA from $y(\tau)$ or its covariance matrix \mathbf{R} , thousands of estimations are available. Typical algorithms include MUSIC, ESPRIT, PM, and tensor-aware approaches [20–24]. Besides, additional information can be exploited to improve the estimation accuracy [25–30]. How to estimate the DOA is an interesting topic, but beyond the scope of this paper. Once DOA of the target vehicle is obtained, the position information can be accurately recovered via solving an inverse problem [3]. In this paper, we only focus on how to select the optimal Tx/Rx pair.

3. CRB Derivation

CRB provides a lower bound for unbiased parameter estimation. It is usual to evaluate the parameter estimation accuracy. In what follows, we will show how it is derived. Firstly, we rewrite (6) as

$$x_l = \mathbf{A}s_l + n_l, \quad l = 1, 2, \dots, L, \quad (10)$$

where $x_l = x(l)$, $s_l = s(l)$, and $n_l = n(l)$. Next, we construct a vector $y = [x_1^T, x_2^T, \dots, x_L^T]^T \in \mathbb{C}^{M_1 N_1 L \times 1}$. Suppose that $s_l = (l = 1, 2, \dots, L)$ are deterministic but unknown to the MIMO system. Then, the mean $\mu \in \mathbb{C}^{M_1 N_1 L \times 1}$ and covariance matrix $\Gamma \in \mathbb{C}^{M_1 N_1 L \times M_1 N_1 L}$ of y are

$$\mu = \begin{bmatrix} \mathbf{A}s_1 \\ \vdots \\ \mathbf{A}s_L \end{bmatrix} = \mathbf{H}\mathbf{S}, \quad (11)$$

$$\Gamma = \text{blkdiag} \left\{ \underbrace{\sigma^2 \mathbf{I}_{M_1 N_1}, \sigma^2 \mathbf{I}_{M_1 N_1}, \dots, \sigma^2 \mathbf{I}_{M_1 N_1}}_L \right\},$$

where $\mathbf{H} \triangleq \text{blkdiag} \{ \underbrace{\mathbf{A}, \mathbf{A}, \dots, \mathbf{A}}_L \} \in \mathbb{C}^{M_1 N_1 L \times LK}$,

$\mathbf{S} \triangleq [s_1^T, s_2^T, \dots, s_L^T]^T \in \mathbb{C}^{LK \times 1}$. Next, let us define the following vectors $\theta \triangleq [\theta_1, \theta_2, \dots, \theta_K]$, $\gamma = [\text{Re}\{S^T\}, \text{Im}\{S^T\}] \in \mathbb{R}^{1 \times 2LK}$. The unknown parameter vector can be formulated as $\zeta = [\alpha, \gamma]^T$. According to [31], the CRB matrix for ζ is given by

$$\text{CRB} = \frac{\sigma_n^2}{2} [\text{Re}\{\Psi^H \Psi\}]^{-1}, \quad (12)$$

where $\Psi = [\partial\mu/\partial\alpha, \partial\mu/\partial\gamma]$.

We now focus on each part of Ψ . Firstly, it is to find that

$$\frac{\partial\mu}{\partial\gamma} = [\mathbf{H}, j\mathbf{H}] \in \mathbb{C}^{ML \times 2LK}. \quad (13)$$

Step further, we have $\partial\mu/\partial\theta = \Delta \in \mathbb{C}^{M_1 N_1 L \times K}$ with

$$\Delta = \begin{bmatrix} \frac{\partial a(\theta_1)}{\partial \theta_1} s_{1,1}, \dots, \frac{\partial a(\theta_K)}{\partial \theta_K} s_{K,1} \\ \vdots & \ddots & \vdots \\ \frac{\partial a(\theta_1)}{\partial \theta_1} s_{1,L}, \dots, \frac{\partial a(\theta_K)}{\partial \theta_K} s_{K,L} \end{bmatrix}, \quad (14)$$

where $s_{k,l}$ is the k th element of s_l . Therefore, $\partial\mu/\partial\zeta^T = [\Delta, \mathbf{H}, j\mathbf{H}]$. Furthermore, we can obtain

$$J = \text{Re}\{\Psi^H \Psi\} = \text{Re}\left\{\begin{bmatrix} \Delta^H \\ \mathbf{H}^H \\ -j\mathbf{H}^H \end{bmatrix} [\Delta, \mathbf{H}, j\mathbf{H}]\right\}. \quad (15)$$

Since we are only interested in the CRB on DOA estimation, by means of diagonalization, we can extract those counterparts from \mathbf{J} . Define

$$P_\Delta = (\mathbf{H}^H \mathbf{H})^{-1} \mathbf{H}^H \Delta \in \mathbb{C}^{L \times K}, \quad (16)$$

thanks to the nonsingular property of $\mathbf{H}^H \mathbf{H}$, P_Δ^{-1} is valid. Now, we define

$$\mathbf{V} \triangleq \begin{bmatrix} \mathbf{I}_K & 0 & 0 \\ -\text{Re}\{P_\Delta\} & \mathbf{I} & 0 \\ -\text{Im}\{P_\Delta\} & 0 & \mathbf{I} \end{bmatrix}. \quad (17)$$

It can be found that

$$[\Delta, \mathbf{H}, j\mathbf{H}]\mathbf{V} = [(\Delta - \mathbf{H}P_\Delta), \mathbf{H}, j\mathbf{H}]. \quad (18)$$

Define $\Pi(1/H)$ as the orthogonal projection of \mathbf{H}^H onto null space

$$\Pi \frac{1}{H} \triangleq \mathbf{I}_{M_1 N_1 L} - \mathbf{H}(\mathbf{H}^H \mathbf{H})^{-1} \mathbf{H}^H. \quad (19)$$

Obviously, $\mathbf{H}^H \Pi(1/H) = 0$. Then, we have

$$\begin{aligned} \mathbf{V}^H \mathbf{J} \mathbf{V} &= \text{Re}\left\{\begin{bmatrix} \Delta^H \Pi \frac{1}{H} \\ \mathbf{H}^H \\ -j\mathbf{H}^H \end{bmatrix} \begin{bmatrix} \Pi \frac{1}{H} \Delta, \mathbf{H}, j\mathbf{H} \end{bmatrix}\right\} \\ &= \text{Re}\left\{\begin{bmatrix} \nabla & 0 & 0 \\ 0 & \tilde{\mathbf{H}} & j\tilde{\mathbf{H}} \\ 0 & -j\tilde{\mathbf{H}} & \tilde{\mathbf{H}} \end{bmatrix}\right\}, \end{aligned} \quad (20)$$

with $\nabla = \Delta^H \Pi(1/H)\Delta$, $\tilde{\mathbf{H}} = \mathbf{H}^H \mathbf{H}$. Based on the properties of a partitioned diagonal matrix, we obtain

$$\begin{aligned} \mathbf{J}^{-1} &= \mathbf{V}(\mathbf{V}^H \mathbf{J} \mathbf{V})^{-1} \mathbf{V}^T = \begin{bmatrix} \mathbf{I} & 0 \\ \times & \mathbf{I} \end{bmatrix} \cdot \begin{bmatrix} \text{Re}\{\nabla\} & 0 \\ 0 & \times \end{bmatrix}^{-1} \begin{bmatrix} \mathbf{I} & \times \\ 0 & \mathbf{I} \end{bmatrix} \\ &= \begin{bmatrix} \text{Re}\{\nabla\} & 0 \\ 0 & \times \end{bmatrix}^{-1}, \end{aligned} \quad (21)$$

where \times stands for the irrelevant part. Inserting (21) and (15) in (12) and removing all the unaffected parts, we can get the CRB on DOA estimation as

$$\text{CRB} = \frac{\sigma^2}{2} [\text{Re}\{\nabla\}]^{-1}. \quad (22)$$

Define $\mathbf{D} = [\partial a(\theta_1)/\partial\theta_1, \partial a(\theta_2)/\partial\theta_2, \dots, \partial a(\theta_K)/\partial\theta_K]$, and let $\mathbf{F} = [s_1, s_2, \dots, s_L]^T$. Recalling (14), we can find that Δ can be rewritten as $\Delta = \mathbf{D} \otimes \mathbf{s}$. Thus, we have

$$\Pi \frac{1}{H} \Delta = \left[\Pi \frac{1}{A} d_1 \otimes f_1, \Pi \frac{1}{A} d_2 \otimes f_2, \dots, \Pi \frac{1}{A} d_K \otimes f_K \right], \quad (23)$$

where d_k and f_k account for the k -th column of \mathbf{D} and \mathbf{F} , respectively. Hence, ∇ can be expressed as

$$\begin{aligned} \nabla &= \begin{bmatrix} d_1^H \otimes f_1^H \\ d_2^H \otimes f_2^H \\ \vdots \\ d_K \otimes f_K \end{bmatrix} \Pi \frac{1}{H} \Delta \\ &= L \cdot \begin{bmatrix} d_1^H \Pi \frac{1}{A} d_{1,R_{1,1}} & \dots & d_1^H \Pi \frac{1}{A} d_{K,R_{1,K}} \\ \vdots & \ddots & \vdots \\ d_K^H \Pi \frac{1}{A} d_{1,R_{K,1}} & \dots & d_K^H \Pi \frac{1}{A} d_{K,R_{K,K}} \end{bmatrix} \\ &= L \cdot \left(\mathbf{D}^H \Pi \frac{1}{A} \mathbf{D} \right) \oplus \hat{\mathbf{R}}_s^T, \end{aligned} \quad (24)$$

where $R_{m,n}$ denotes the (m,n) -th element of $\hat{\mathbf{R}}_s$ and $\hat{\mathbf{R}}_s = (1/L) \cdot \mathbf{F}^H \mathbf{F}$. Finally, we can get the CRB on DOA estimation as

$$\text{CRB} = \frac{\sigma^2}{2L} \left[\text{Re}\left\{ \mathbf{D}^H \Pi \frac{1}{A} \mathbf{D} \oplus \hat{\mathbf{R}}_s^T \right\} \right]^{-1}. \quad (25)$$

4. The Proposed TX/RX Selection Framework

4.1. The Proposed CNN Architecture. The CNN model that utilized in this paper is depicted in Figure 4. It consists of four parts: input layer, convolutional layer, fully-connected layer, and output layer. The output of the CNN can be formulated as the nonlinear mapping of the input. Among which the activation function is a key point of each neuron, and it is linear for input and output layers and sigmoid for hidden layers. The Input layer contains a dataset with samples and associate labels. The convolutional layer is to extract features of the input. Herein, two convolutional layers are depicted. The convolutional kernel size is a key issue in CNN, and it should be designed according to input data. The fully-connected layer is fundamentally a classifier, and three dense layers are shown here. The output layer is a probability distribution, which contains the possibility of each Tx/Rx pair.

Rectified linear unit (ReLU) acts as a role of activation function following behind each available layer before the last

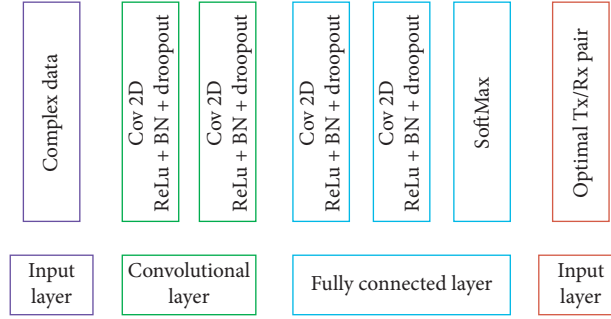


FIGURE 4: The architecture of a general CNN model.

TABLE 1: Part of the selected Tx/Rx results.

	$M = 8$	$N = 10$	$M_1 = 3$	$N_1 = 4$	
DOAs	{13.6°, 1.2°}	{13.6°, 41.2°}	{43.6°, 61.2°}	{53.6°, 81.2°}	{3.6°, 21.4°}
Tx	{1, 4, 5, 8}	{1, 2, 7, 8}	{1, 2, 7, 8}	{1, 3, 7, 8}	{1, 2, 6, 8}
Rx	{1, 2, 3, 9, 10}	{1, 2, 4, 9, 10}	{1, 2, 5, 9, 10}	{1, 2, 7, 9, 10}	{1, 2, 4, 6, 8, 12}
DOAs	$M = 8$ {15.2°, 67.9°}	$N = 10$ {10°, 30°}	$M_1 = 3$ {15°, 25°}	$N_1 = 4$ {20°, 35°}	{30°, 50°}
Tx	{1, 2, 7, 8}	{0, 3, 4, 7}	{0, 1, 6, 7}	{0, 3, 4, 7}	{0, 1, 6, 7}
Rx	{1, 2, 3, 10, 11, 12}	{0, 1, 7, 8, 9}	{0, 4, 1, 8, 9}	{0, 1, 2, 8, 8}	{0, 1, 4, 8, 9}

dense layer. In the dense layer, SoftMax is applied. Let n_i be the output of the i -th neuron in a given layer, then the function with respect to ReLU and SoftMax can be formulated as

$$RLU(n_i) = \max\{0, n_i\}, \quad (26a)$$

$$\text{Soft max}(n_i) = \frac{\exp\{n_i\}}{\sum_j \exp\{n_j\}} \quad (26b)$$

4.2. Training Data Generation. To pursuit the optimal Tx/Rx pair, the CRB on DOA estimation is adopted to evaluate the selection result. The CRBs on the DOAs can be achieved from the diagonal elements of the CRB matrix. For multiple targets scenario, the optimal Tx/Rx selection criterion is defined by minimizing the average CRBs.

In order to train the CNN, we need enough labeled training data. To this end, the spatial domain is firstly discretized into Q grids, and we assume that all possible DOAs are on the grid. For different DOA combinations, we calculate the CRBs corresponding to various Tx/Rx pairs, and pick up the optimal Tx/Rx pair corresponding to min CRB. The antenna selection problem can be interpreted as a problem of permutation and combination; the optimal Tx/Rx pair can be obtained by greedy searching. Since the reference antenna must be chosen, there needs $C_{M-1}^{M-1} \times C_{N-1}^{N-1}$ searches. To alleviate the search burden, the random strategy can be adopted [32]. The labeled data include two essential factors: DOA pair and Tx/Rx indexes. Some of the selected results are shown in Table 1, in which the signal-to-noise ratio (SNR) is set to -10 dB, and $L = 200$ snapshots are considered; all the results are obtained from 100 independent trails. Some of the above details are shown in Figures 5 and 6.

Before we train the CNN using the optimal Tx/Rx pair, we need to label the dataset. According to the CRB expression, one should know the SNR and target number in the training. Therefore, it is necessary for us to preprocess the matched data, i.e., to estimate the target number K and the noise power σ^2 . Thereafter, labeled datasets can be generated via the preprocessing results. Finally, all the datasets can be divided into two subsets: the training datasets and the test datasets. The training datasets are utilized to get the weight values of the CNN, while the test datasets to evaluate the classification results.

It should be noticed that the array data is complex valued. However, only real-valued datasets are acceptable in typical CNN. So, it is necessary for us to convert the complex values to real ones. A common way is to extra the real part, the image part, and the angle of the covariance matrix, as illustrated in [18]. In this paper, however, instead of inputting these counterparts, the amplitude values and phase values of the covariance matrix are identified as the input of the CNN. The detailed steps of training CNN are depicted in Table 2.

5. Simulation Results

To verify the effectiveness of the improved CNN-based Tx/Rx selection framework for the MIMO radar (marked with CNN-MIMO), computer simulations have been carried out. In the simulation, we consider a monostatic MIMO radar setup, which is configured with M transmit elements and N receive elements in total, both of which are ULAs with half-wavelength spacing. Suppose there are K uncorrelated sources, the reflection coefficients of which fulfill the Swerling II model and L snapshots are available. For power

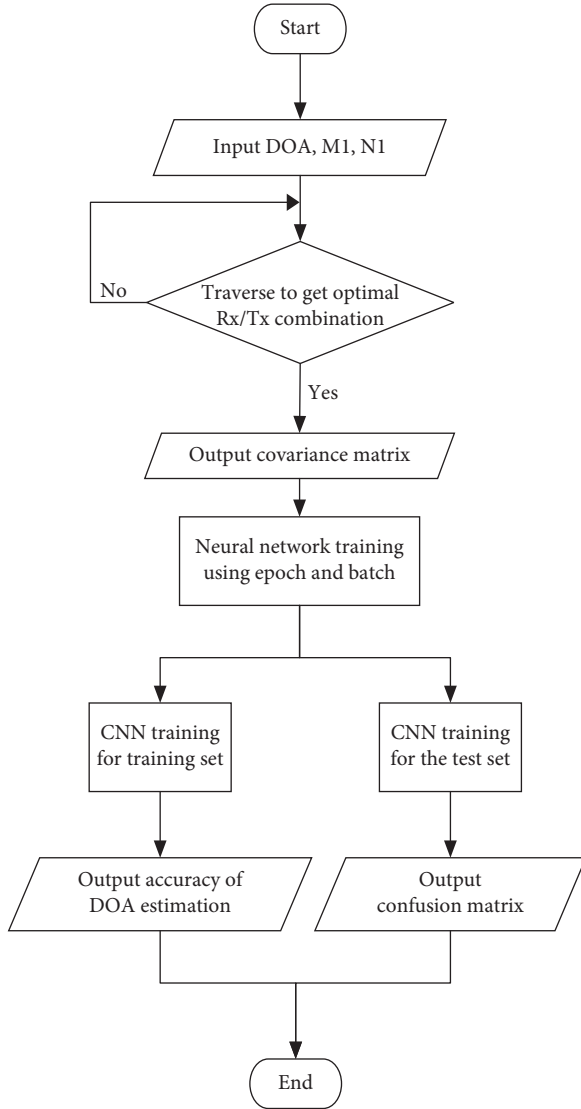


FIGURE 5: System program flow chart.

saving purpose, M_1 Tx and N_1 Rx are chosen from the transmit array and the receive array, respectively.

In the first example, we test the estimation performance of the CNN-MIMO and the CS-MIMO framework in [7]. The root mean square error (RMSE) is defined as

$$\text{RMSE} = \frac{1}{K} \sum_{k=1}^K \sqrt{\frac{1}{T} \sum_{i=1}^T (\hat{\theta}_{i,k} - \theta_k)^2}, \quad (27)$$

where T denotes the total number of trail, θ_k and $\hat{\theta}_{i,k}$ represent the k th DOA and its estimate for the i -th Monte Carlo trial. Herein, we assume there are two DOAs at directions 65.7° and 76.9° , respectively. $M_1 = 3$, $N_1 = 4$, and $L = 200$ are fixed in the simulation. Figure 7 illustrates the RMSE performance of the CNN-MIMO framework and the CS-MIMO method. Obviously, the proposed CNN framework provides much better estimation performance than the CS-MIMO method.

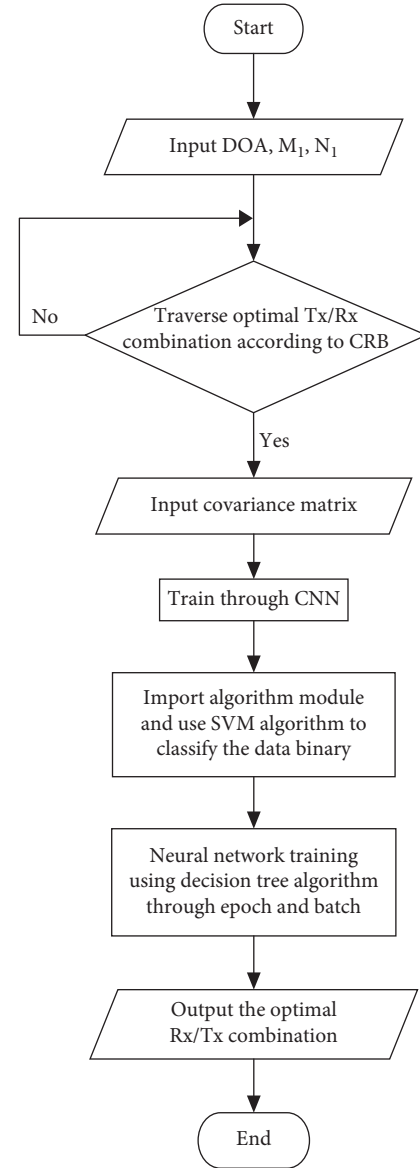


FIGURE 6: CNN training application map.

In the second example, we evaluate the DOA estimate performance of both methods with various snapshot numbers L , where SNR is set to 0 dB; other simulation conditions are the same to that in the first example. In Figure 8, similar to the previous result, the performance of all the methods gradually improved with L increasing. Besides, The CNN-MIMO framework offers much better RMSE performance than the CS-MIMO method. The above improvement benefits from the fact that the CNN-MIMO framework always brings the optimal Tx/Rx pair, while the array geometry of the CS-MIMO method is randomly generated.

In the third example, we give the loss function of the proposed CNN-MIMO framework in one training duration. Figure 9 shows that the loss function is quickly decreased at the first few iterations. However, once the iteration step reaches a threshold, the loss function is slowly decreased

TABLE 2: The proposed CNN-based Tx/Rx selection method.

Input: Tx/Rx pair, DOAs
 Output: generalized CNN
 Step one: generate the matched data model according to (6) with $SNR \in [-10 \text{ dB}, 20 \text{ dB}]$ with interval 5 dB
 Step two: mix all the datasets proportionally and randomly divide the mixed datasets into training datasets and validation datasets by 10 : 2
 Step three: construct the CNN according to Figure 4. Set learning rate to 0.001
 Step four: train the CNN on training dataset and update the corresponding weight values until validation loss is not improved
 Return: generalized CNN

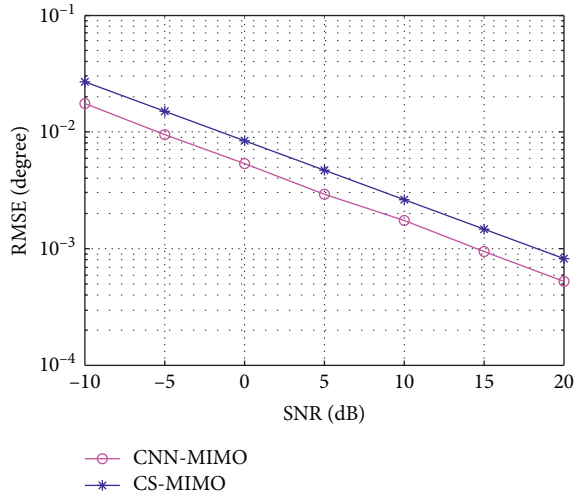


FIGURE 7: Performance comparison of CNN-MIMO and CS-MIMO at different SNRs.

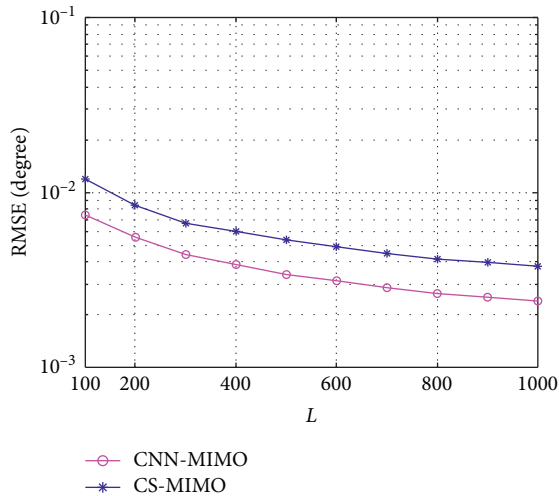


FIGURE 8: Performance comparison of CNN-MIMO and CS-MIMO with various snapshot numbers (L).

with iterative steps increasing. Finally, it can reach the given threshold and all the weight values will accomplished temporally. After all, the training sets have been finished, and the weight values will be fixed.

In the last example, we present the confusion matrices with respect to the CNN framework and the traditional SVM method, in which only ten optimal array configurations have been utilized. Herein, 10000 datasets have been used.

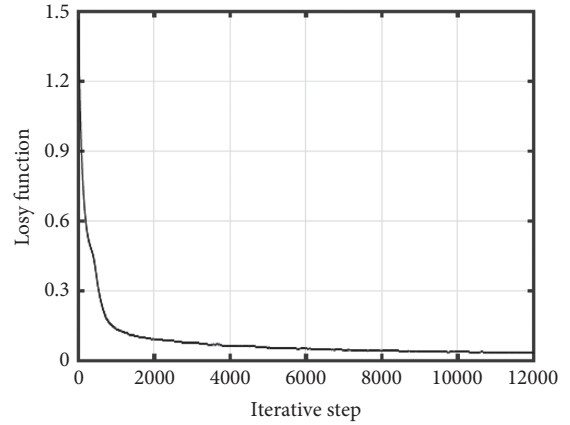


FIGURE 9: Loss function of the CNN-MIMO framework. The training sets have been finished, the weight values will be fixed.

Class0	1000	0	0	0	0	0	0	0	0
Class1	0	1000	0	0	0	0	0	0	0
Class2	0	0	1000	0	0	0	0	0	0
Class3	0	0	0	1000	0	0	0	0	0
Class4	0	0	0	0	1000	0	0	0	0
Class5	0	0	0	0	0	1000	0	0	0
Class6	0	0	0	0	0	3	997	0	0
Class7	0	0	0	0	0	0	0	1000	0
Class8	0	0	0	0	0	0	0	0	1000
Class9	0	0	0	0	0	0	0	0	1000

FIGURE 10: The confusion matrix of the CNN-MIMO framework.

Figure 10 summarizes the prediction results with respect to the CNN framework and the SVM method. Each row of the confusion matrix shows the accuracy of right shot and wrong shot with the test set. From this, we observe that the proposed framework provides better accuracy than the SVM scheme, especially in class 4.

6. Conclusions

In this paper, we considered a realistic scenario in IIOV, in which the MIMO sensor is with limited power to calculate the vehicle position. To this end, the MIMO sensor needs to get the optimal Tx/Rx pair with limited number of Tx/Rx.

From all possible Tx/Rx pairs, which can be formulated as a multiclass-classification problem, a CNN-based framework is proposed for this issue. Firstly, the optimal Tx/Rx pair is calculated at the cost of finding the minimum CRB on DOA estimation. Thereafter, DOAs are classified into various pairs, and the optimal Tx/Rx combinations are one-to-one mapped to the DOAs. Then, 1200 sets are randomly generated associated to each DOA pair, in which 200 groups are used for training and the remainder are utilized for testing. The CNN is trained by the training set for learning the best weight values. After this, the CNN can be utilized to quickly determine the best array configuration once it gets the matched array measurement. The proposed framework provides much better performance than the existing CS-based method; it may get a bright prospect in future IIOV applications.

Data Availability

The data used to support the findings of this study are included within the article.

Conflicts of Interest

The authors declare that they have no conflicts of interest.

References

- [1] L. Sun, L. Wan, K. Liu, and X. Wang, "Cooperative-evolution-based WPT resource allocation for large-scale cognitive industrial IoT," *IEEE Transactions on Industrial Informatics*, vol. 16, no. 8, pp. 5401–5411, 2020.
- [2] S. Kuutti, S. Fallah, K. Katsaros, M. Dianati, F. Mccullough, and A. Mouzakitis, "A survey of the state-of-the-art localization techniques and their potentials for autonomous vehicle applications," *IEEE Internet of Things Journal*, vol. 5, no. 2, pp. 829–846, 2018.
- [3] H. Wang, L. Wan, M. Dong, K. Ota, and X. Wang, "Assistant vehicle localization based on three collaborative base stations via SBL-based robust DOA estimation," *IEEE Internet of Things Journal*, vol. 6, no. 3, pp. 5766–5777, 2019.
- [4] F. Wen, J. Wang, J. Shi, and G. Gui, "Auxiliary vehicle positioning based on robust DOA estimation with unknown mutual coupling," *IEEE Internet of Things Journal*, vol. 7, no. 6, pp. 5521–5532, 2020.
- [5] J. Zheng, H. Liu, and Q. H. Liu, "Parameterized centroid frequency-chirp rate distribution for LFM signal analysis and mechanisms of constant delay introduction," *IEEE Transactions on Signal Processing*, vol. 65, no. 24, pp. 6435–6447, 2017.
- [6] B. Liao, "Fast angle estimation for mimo radar with non-orthogonal waveforms," *IEEE Transactions on Aerospace and Electronic Systems*, vol. 54, no. 4, pp. 2091–2096, 2018.
- [7] M. Rossi, A. M. Haimovich, and Y. C. Eldar, "Spatial compressive sensing for MIMO radar," *IEEE Transactions on Signal Processing*, vol. 62, no. 2, pp. 419–430, 2014.
- [8] Z. Lai, W. K. Wong, Y. Xu, J. Yang, and D. Zhang, "Approximate orthogonal sparse embedding for dimensionality reduction," *IEEE Transactions on Neural Networks and Learning Systems*, vol. 27, no. 4, pp. 723–735, 2016.
- [9] S. Joshi and S. Boyd, "Sensor selection via convex optimization," *IEEE Transactions on Signal Processing*, vol. 57, no. 2, pp. 451–462, 2009.
- [10] J. Zheng, T. Yang, H. Liu, and T. Su, "Efficient data transmission strategy for IIoTs with arbitrary geometrical array," *IEEE Transactions on Industrial Informatics*, vol. 2020, p. 1, 2020.
- [11] J. Zheng, T. Yang, H. Liu, T. Su, and L. Wan, "Accurate detection and localization of UAV swarms-enabled MEC system," *IEEE Transactions on Industrial Informatics*, vol. 2020, p. 1, 2020.
- [12] H. Godrich, A. P. Petropulu, and H. V. Poor, "Sensor selection in distributed multiple-radar architectures for localization: a knapsack problem formulation," *IEEE Transactions on Signal Processing*, vol. 60, no. 1, pp. 247–260, 2012.
- [13] J. Tabrikian, O. Isaacs, and I. Bilik, "Cognitive antenna selection for DOA estimation in automotive radar," in *Proceedings of the 2016 IEEE Radar Conference*, pp. 1–5, Philadelphia, PA, USA, May 2016.
- [14] H. Nosrati, E. Aboutanios, and D. B. Smith, "receiver-transmitter pair selection in mimo phased array radar," in *Proceedings of the 2017 IEEE International Conference on Acoustics, Speech and Signal Processing (ICASSP)*, pp. 3206–3210, New Orleans, LA, USA, March 2017.
- [15] J. Joung, "Machine learning-based antenna selection in wireless communications," *IEEE Communications Letters*, vol. 20, no. 11, pp. 2241–2244, 2016.
- [16] C. Szegegy, W. Liu, Y. Jia, P. Sermanet, S. Reed et al., "Going deeper with convolutions," in *Proceedings of the 2015 IEEE conference on computer vision and pattern recognition 2015*, pp. 1–9, Boston, MA, USA, 2015.
- [17] H. Huang, J. Yang, H. Huang, Y. Song, and G. Gui, "Deep learning for super-resolution channel estimation and DOA estimation based massive MIMO system," *IEEE Transactions on Vehicular Technology*, vol. 67, no. 9, pp. 8549–8560, 2018.
- [18] A. M. Elbir, K. V. Mishra, and Y. C. Eldar, "Cognitive radar antenna selection via deep learning," *IET Radar, Sonar & Navigation*, vol. 13, no. 6, pp. 871–880, 2019.
- [19] A. M. Elbir and K. V. Mishra, "Joint antenna selection and hybrid beamformer design using unquantized and quantized deep learning networks," *IEEE Transactions on Wireless Communications*, vol. 19, no. 3, pp. 1677–1688, 2019.
- [20] F. Wen, C. Mao, and G. Zhang, "Direction finding in MIMO radar with large antenna arrays and nonorthogonal waveforms," *Digital Signal Processing*, vol. 94, pp. 75–83, 2019.
- [21] F. Wen, J. Shi, and Z. Zhang, "Direction finding for bistatic MIMO radar with unknown spatially colored noise," *Circuits, Systems, and Signal Processing*, vol. 39, no. 5, pp. 2412–2424, 2020.
- [22] F. Wen and J. Shi, "Fast direction finding for bistatic EMVSMIMO radar without pairing," *Signal Process.* vol. 173, Article ID 107512, 2020.
- [23] X. Wang, W. Wang, J. Liu, Q. Liu, and B. Wang, "Tensor-based real-valued subspace approach for angle estimation in bistatic MIMO radar with unknown mutual coupling," *Signal Processing*, vol. 116, pp. 152–158, 2015.
- [24] F. Wen, Z. Zhang, K. Wang, G. Sheng, and G. Zhang, "Angle estimation and mutual coupling self-calibration for ULA-based bistatic MIMO radar," *Signal Processing*, vol. 144, pp. 61–67, 2018.
- [25] X. Wang, L. Wan, M. Huang, C. Shen, and K. Zhang, "Polarization channel estimation for circular and non-circular signals in massive MIMO systems," *IEEE Journal of Selected Topics in Signal Processing*, vol. 13, no. 5, pp. 1001–1016, 2019.
- [26] F. Wen, J. Shi, and Z. Zhang, "Joint 2D-DOD, 2D-DOA and polarization angles estimation for bistatic EMVS-MIMO radar via PARAFAC analysis," *IEEE Transactions on Vehicular Technology*, vol. 69, no. 20, pp. 1626–1638, 2020.

- [27] L. Wan, X. Kong, and F. Xia, "Joint range-doppler-angle estimation for intelligent tracking of moving aerial targets," *IEEE Internet of Things Journal*, vol. 5, no. 3, pp. 1625–1636, 2018.
- [28] L. Wan, L. Sun, X. Kong, Y. Yuan, K. Sun, and F. Xia, "Task-driven resource assignment in mobile edge computing exploiting evolutionary computation," *IEEE Wireless Communications*, vol. 26, no. 6, pp. 94–101, 2019.
- [29] D. Meng, X. Wang, M. Huang, L. Wan, and B. Zhang, "Robust weighted subspace fitting for DOA estimation via block sparse recovery," *IEEE Communications Letters*, vol. 24, no. 3, pp. 563–567, 2020.
- [30] X. Wang, L. Wang, X. Li, and G. Bi, "Nuclear norm minimization framework for DOA estimation in MIMO radar," *Signal Processing*, vol. 135, pp. 147–152, 2017.
- [31] P. Stoica and A. Nehorai, "Performance study of conditional and unconditional direction-of-arrival estimation," *IEEE Transactions on Acoustics, Speech, and Signal Processing*, vol. 38, no. 10, pp. 1783–1795, 1990.
- [32] A. Bilal, A. Jourabloo, M. Ye, X. Liu, and L. Ren, "Do convolutional neural networks learn class hierarchy?" *IEEE Transactions on Visualization and Computer Graphics*, vol. 24, no. 1, pp. 152–162, 2018.

Research Article

Direction of Arrival Based on the Multioutput Least Squares Support Vector Regression Model

Kai Huang ^{1,2} Ming-Yi You ^{1,2} Yun-Xia Ye,^{1,2} Bin Jiang,^{1,2} and An-Nan Lu^{1,2}

¹Science and Technology on Communication Information Security Control Laboratory, Jiaxing 314033, Zhejiang, China

²No. 36 Research Institute of CETC, Jiaxing 314033, Zhejiang, China

Correspondence should be addressed to Ming-Yi You; youmingyi@126.com

Received 14 July 2020; Revised 15 September 2020; Accepted 19 September 2020; Published 30 September 2020

Academic Editor: Liangtian Wan

Copyright © 2020 Kai Huang et al. This is an open access article distributed under the Creative Commons Attribution License, which permits unrestricted use, distribution, and reproduction in any medium, provided the original work is properly cited.

The interferometer is a widely used direction-finding system with high precision. When there are comprehensive disturbances in the direction-finding system, some scholars have proposed corresponding correction algorithms, but most of them require hypothesis based on the geometric position of the array. The method of using machine learning that has attracted much attention recently is data driven, which can be independent of these assumptions. We propose a direction-finding method for the interferometer by using multioutput least squares support vector regression (MLSSVR) model. The application of this method includes the following: the construction of MLSSVR model training data, training and construction of the MLSSVR model, and the estimation of direction of arrival. Finally, the method is verified through numerical simulation. When there are comprehensive deviations in the system, the direction-finding accuracy can be effectively improved.

1. Introduction

Direction of arrival (DOA) estimation is a widely studied problem in various fields, including wireless communications [1], radar detection [2–4], target localization, and tracking [5, 6]. Various methods have been proposed to estimate DOA of emitters, such as interferometer [7, 8] and array processing [9–11].

The interferometer estimates the DOA based on the phase difference of different direction-finding baselines. The accuracy of interferometer is sensitive to the phase difference of baselines. In engineering applications, there may be various deviations, such as phase inconsistency between channels, mutual coupling between the antennas, and antenna location deviations. In order to achieve optimal direction-finding performance, the methods including correlation-coefficient [12], weighted least squares [13], and parameter estimation [14] are always used. To facilitate method implementation, simplified models are established to describe the effects of various deviations, and autocalibration processes are proposed to improve DOA estimation precision [15–21]. Most of the simplifications on array

deviations are made from mathematical perspectives approximately with various additional assumptions, such as uniform linearity or circularity array geometries [15–17], constrained antennas location deviations within a particular line or plane [18, 19], and intersensor independence of gain and phase errors [20, 21].

However, the effect of comprehensive disturbances, which probably exist in practical systems, is much more difficult to be modeled precisely and calibrated automatically. The multiple deviations have a great influence on the amplitude and phase of each receiving channel, which greatly affects the performance of the interferometer direction-finding system. The commonly used method to reduce the effect of multiple deviations is the external field calibration method; i.e., for the different directions of incoming signal with a large signal-to-noise ratio, the measured values of the phase difference from baselines are directly recorded and saved together with the known calibration directions [22]. In the application of the direction-finding system, the DOA is calculated by least squares between the measured value of each phase difference with the saved values from the external field. The external field

calibration method is simple in principle and easy to operate and has been widely used in engineering. Due to the influence of multiple deviations, even if there are different gains of each antenna, the external field calibration method always uses the equal-weight least squares method. The influence of the inconsistency between the antennas on the direction-finding accuracy has not been fully considered, i.e., the external field calibration method fails to maximize the effectiveness of the direction-finding system.

Recently, some scholars have used machine learning to solve the DOA estimation with comprehensive disturbances [23–31]. Machine learning have significant advantages over traditional methods based on array geometries and least square in solving direction-finding problems in complicated scenarios with multiple deviations, such as radial basis function (RBF) [23], least squares support vector classification (LSSVC) [24], support vector regression (SVR) [25–29], and deep neural networks (DNN) [30, 31]. These methods are data driven and do not rely on preassumptions about array geometries and whether they are calibrated or not. Despite its potential usefulness, the standard formulation of the LS-SVR cannot cope with the multioutput case [32]. Therefore, with the angles around 0° and 360° , the accuracy has not been effectively improved. The DNN for direction finding requires large samples to perform well, resulting in too long model training time, and if the samples size is insufficient, this method cannot effectively perform. This paper proposes a direction-finding method for the interferometer based on the multioutput least squares support vector regression (MLSSVR) model. The multioutput mode can avoid large errors in the single-output mode around 0° and 360° , and it is expected to achieve higher direction-finding accuracy within the angle range. Due to the MLSSVR model, the model training time can be greatly shortened. The application of this method includes the following: (1) the construction of MLSSVR model training data, (2) training and construction of the MLSSVR model, and (3) the estimation of direction of arrival.

The organization of the rest of the paper is as follows. Section 2 formulates the array output model with complicated deviations. Section 3 presents the process of the MLSSVR model for DOA estimation. Section 4 carries out simulations to verify the validity of the method. Section 5 concludes this work.

The main notation used in this paper is listed in Table 1.

2. Problem Formulation

Assume that the waveform of signal is $s(t)$ and direction of signal is α . Then, the antenna output is

$$\mathbf{x}(t) = \mathbf{a}(\alpha)s(t) + \mathbf{v}(t). \quad (1)$$

When the comprehensive disturbances exist in the direction-finding system, such as phase inconsistency between channels, mutual coupling between the antennas, and antenna location deviations, these disturbances cause deviations to $\mathbf{a}(\alpha)$, and the actual antenna output is

$$\tilde{\mathbf{x}}(t) = \mathbf{a}(\alpha, e)s(t) + \mathbf{v}(t). \quad (2)$$

$\mathbf{a}(\alpha, e)$ is the direction vector of array with comprehensive disturbances.

The phase difference between the antennas may be far away from the theoretical value. Obviously, at this time, high-precision direction finding cannot be performed according to the theoretical geometry of the antennas. In this case, the external field calibration method can be used generally. We propose the MLSSVR model to achieve higher-precision direction finding, and this method is data driven and do not rely on preassumptions about array geometries and whether they are calibrated or not.

3. MLSSVR Model for DOA Estimation

3.1. Construction Training Data of the MLSSVR Model.

For the MLSSVR model, the training data are constructed as a matrix comprising phase differences of baselines and their corresponding vectors related to the direction of incoming signal, which is

$$[\boldsymbol{\Phi}_t, \boldsymbol{\eta}_{\text{label}}] = \begin{bmatrix} \boldsymbol{\Phi}_{t1} & \boldsymbol{\Phi}_{t2} & \cdots & \boldsymbol{\Phi}_{tL} \\ \boldsymbol{\eta}_{\text{label}1} & \boldsymbol{\eta}_{\text{label}2} & \cdots & \boldsymbol{\eta}_{\text{label}L} \end{bmatrix}^T, \quad (3)$$

where $\boldsymbol{\Phi}_{ti} = [\varphi_{ti}^{12} \ \cdots \ \varphi_{ti}^{(N-1)N}]^T$, ($i = 1, \dots, L$) is the phase difference vector of the i -th training sample, where T is the transposed symbol, and $\boldsymbol{\eta}_{\text{label}i}$ is the i -th vector which is related to the DOA of the signal. In order to avoid the large direction-finding error around 0° or 360° caused by the unreasonable loss function of the single-output SVR model, we use the dual output form, namely,

$$\boldsymbol{\eta}_{\text{label}i} = [\cos(\alpha_{\text{label}i}) \ \sin(\alpha_{\text{label}i})]^T. \quad (4)$$

Here, $\alpha_{\text{label}i}$ is the DOA corresponding to the i -th training sample.

It should be pointed out that the MLSSVR model is not acquired through only one experiment, and the acquisition of its training data should be carried out under the condition of similar signal-to-noise ratio in the application scenario. On the other hand, in training data of the MLSSVR model, for a given DOA, it is usually necessary to obtain several samples (generally more than 10 [32]). In addition, the DOA of the signal should cover the angle range in the application as much as possible, namely,

$$\alpha_l \leq \alpha_{\text{label}i} \leq \alpha_u. \quad (5)$$

Here, α_u and α_l represent the upper and lower limits of the possible direction of arrival, respectively.

If the directions of adjacent known incoming signal in the training samples are not the same, they will differ by a fixed step $\Delta\alpha_t$, i.e., $\alpha_{\text{label}i+1} = \alpha_{\text{label}i}$ or $\alpha_{\text{label}i+1} = \alpha_{\text{label}i} + \Delta\alpha_t$. The value should generally be less than the requisite accuracy of direction finding in the application. Between α_u and α_l , the number of sample categories is M .

3.2. Train and Build a MLSSVR Model. Given a data set $(\mathbf{x}_i, \mathbf{y}_i)_{i=1}^L$, $\mathbf{x}_i \in \mathbf{R}^d$ and $\mathbf{y}_i \in \mathbf{R}^m$. The purpose of multioutput

TABLE 1: Symbol and notation.

Symbol	Explanation
$s(t)$	Waveform of signal
$\mathbf{a}(\alpha)$	Direction vector of array
$\mathbf{x}(t)$	The theoretical output of antennas
L	The number of training samples
\mathbf{R}^a	a -Dimensional real number space
\mathbf{R}_+	One-dimensional positive real number space
\mathbf{C}	Mutual coupling matrix
φ_{ti}^{kj}	The measured value of phase difference from baselines formed between the k -th antenna and the j -th antenna in the i -th training sample
α	Direction of signal
$\mathbf{v}(t)$	Zero-mean Gaussian noise
$\bar{\mathbf{x}}(t)$	The actually output of antennas
N	The number of antennas
$\mathbf{R}^{a \times b}$	$a \times b$ -Dimensional real number space
$\mathbf{R}_+^{a \times b}$	$a \times b$ -Dimensional positive real number space
φ_t	Phase differences matrix in the training data
η_{label}	The matrix formed by cosine and sine function of DOA in the training data

regression is to give a set of input vectors $\mathbf{x} \in \mathbf{R}^d$ and predict a set of output vectors $\mathbf{y} \in \mathbf{R}^m$. The MLSSVR model solves this problem by finding $\mathbf{W} = (\mathbf{w}_1, \dots, \mathbf{w}_m) \in \mathbf{R}^{n_h \times m}$ and $\mathbf{b} = (b_1, \dots, b_m)^T \in \mathbf{R}^m$ that minimize the following objective function with constraints:

$$\begin{aligned} \min \tau(\mathbf{W}, \Xi) &= \frac{1}{2} \text{trace}(\mathbf{W}^T \mathbf{W}) + \gamma \frac{1}{2} \text{trace}(\Xi^T \Xi) \\ \text{s.t. } \mathbf{Y} &= \mathbf{Z}^T \mathbf{W} + \text{repmat}(\mathbf{b}^T, L, 1) + \Xi. \end{aligned} \quad (6)$$

Here, $\mathbf{Y} = [\mathbf{y}_i] \in \mathbf{R}^{L \times m}$, $\mathbf{Z} = (\delta(\mathbf{x}_1), \dots, \delta(\mathbf{x}_L)) \in \mathbf{R}^{n_h \times L}$, $\delta(\cdot)$ is the mapping function (kernel function) of $\mathbf{R}^d \rightarrow \mathbf{R}^{n_h}$, whose purpose is to transform \mathbf{x}_i into a more distinguishable high-dimensional feature space with n_h dimensions, $\Xi = (\xi_1, \dots, \xi_m) \in \mathbf{R}_+^{L \times m}$, $\xi_i = (\xi_{i1}, \dots, \xi_{im})^T$ and ξ_{ij} is a slack variable; $\text{trace}(\mathbf{A}) = \sum_i A_{ii}$ where \mathbf{A} is a $m \times m$ matrix, and $\gamma \in \mathbf{R}_+$ is a regularization parameter.

In order to achieve the solution of (6), the objective function can be constructed as a heuristic Bayesian architecture. Let $\mathbf{w}_i = \mathbf{w}_0 + \mathbf{v}_i$, where $\mathbf{w}_0 \in \mathbf{R}^{n_h}$ contains common parameter information and $\mathbf{v}_i \in \mathbf{R}^{n_h}$ carries the individual information of each sample. To obtain a solution \mathbf{w}_0 , $\mathbf{V} = (\mathbf{v}_1, \dots, \mathbf{v}_m)$, and \mathbf{b} , the following objective function with constraints can be constructed:

$$\begin{aligned} \min \tau(\mathbf{w}_0, \mathbf{V}, \Gamma) &= \frac{1}{2} \mathbf{w}_0^T \mathbf{w}_0 + \frac{1}{2} \frac{\lambda}{m} \text{trace}(\mathbf{V}^T \mathbf{V}) + \gamma \frac{1}{2} \text{trace}(\Gamma^T \Gamma) \\ \text{s.t. } \mathbf{Y} &= \mathbf{Z}^T \mathbf{W} + \text{repmat}(\mathbf{b}^T, L, 1) + \Gamma. \end{aligned} \quad (7)$$

Among them, $\lambda \in \mathbf{R}_+$ is another regularization parameter.

Equation (7) can be transformed into Lagrange's equation, and then, the optimal solutions \mathbf{w}_0^* , \mathbf{V}^* , and \mathbf{b}^* can be achieved using the Karush–Kuhn–Tucker (KKT) optimization conditions. After that, the corresponding decision function is [32]

$$\begin{aligned} f(\mathbf{x}) &= \delta(\mathbf{x})^T \mathbf{W}^* + \mathbf{b}^{*T} = \delta(\mathbf{x})^T \text{repmat}(\mathbf{w}_0^*, 1, m) \\ &\quad + \delta(\mathbf{x})^T \mathbf{V}^* + \mathbf{b}^{*T}. \end{aligned} \quad (8)$$

3.3. *DOA Estimate.* Given a set of phase difference data φ , based on equation (8), we have

$$\begin{aligned} \boldsymbol{\eta} &= [\cos(\alpha) \quad \sin(\alpha)]^T = \delta(\boldsymbol{\varphi})^T \text{repmat}(\mathbf{w}_0^*, 1, m) \\ &\quad + \delta(\boldsymbol{\varphi})^T \mathbf{V}^* + \mathbf{b}^{*T}. \end{aligned} \quad (9)$$

Based on the result of equation (9), the final DOA is estimated as

$$\alpha = \text{atan2}(\sin(\alpha), \cos(\alpha)) = \text{atan2}(\boldsymbol{\eta}(2, 1), \boldsymbol{\eta}(1, 1)). \quad (10)$$

Here, atan2 is the four-quadrant inverse tangent function.

4. Simulations and Analysis

This section gives a numerical simulation in a typical scenario to demonstrate the effectiveness of the MLSSVR model applied to direction finding. Consider a 5-element uniform circular array with a radius-to-wavelength ratio of 0.4. The radial basis kernel function is adopted to solve formula (8): $\kappa(x, z) = \exp(-p\|x - z\|^2)$ $p > 0$. After multiple trainings, determine the parameters $\gamma = 0.5$ and $\lambda = 4$ in formula (7) and the radial basis function parameter $p = 1$.

4.1. *Phase Inconsistency between Channels.* Assume that the RMSE of phase difference under 10 dB signal-to-noise ratio is 25° , 5° , 5° , 10° , and 15° in 5 channels, respectively. The training data sets consist of phase difference and cosine and sine functions of each angle from 0° to 360° with a step of 1° , and 10 groups of samples are collected per angle, i.e., the number of training data sets $L = 3600$. Under the same signal-to-noise ratio, a total of 3600 testing samples of phase

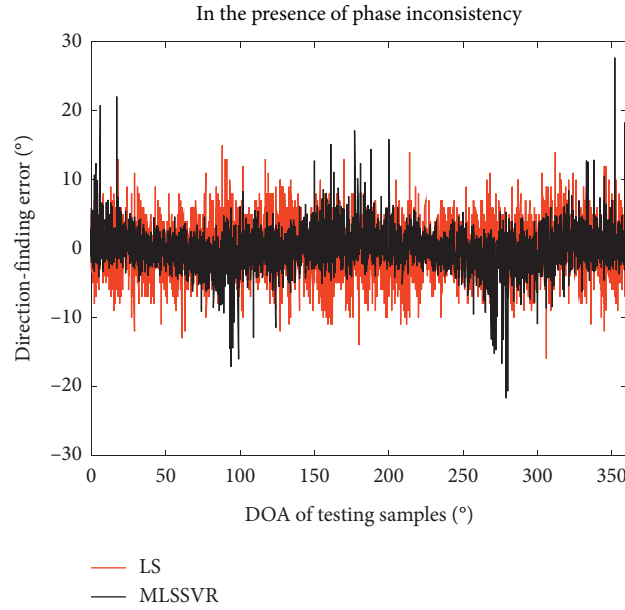


FIGURE 1: Direction-finding error of testing samples with phase inconsistency.

difference are generated from 0° to 360° . As a comparison, the DOA of testing samples is also calculated by using least squares (LS) with training data sets. Figure 1 shows the direction-finding error of testing samples.

4.2. Mutual Coupling between the Antennas. When there is mutual coupling between antennas, assume the mutual coupling matrix as follows:

$$C = \begin{bmatrix} 1 & 0.7821 + 0.2583j & 0.4576 + 0.2469j & 0.4576 + 0.2469j & 0.7821 + 0.2583j \\ 0.7821 + 0.2583j & 1 & 0.7821 + 0.2583j & 0.4576 + 0.2469j & 0.4576 + 0.2469j \\ 0.4576 + 0.2469j & 0.7821 + 0.2583j & 1 & 0.7821 + 0.2583j & 0.4576 + 0.2469j \\ 0.4576 + 0.2469j & 0.4576 + 0.2469j & 0.7821 + 0.2583j & 1 & 0.7821 + 0.2583j \\ 0.7821 + 0.2583j & 0.4576 + 0.2469j & 0.4576 + 0.2469j & 0.7821 + 0.2583j & 1 \end{bmatrix}. \quad (11)$$

Selecting 10 samples for each angle from 0° to 360° , and the training data sets consist of phase difference and cosine and sine functions of each angle. Under the same signal-to-noise ratio and mutual coupling, 3600 groups of phase difference from different DOA are generated as the testing samples. Figure 2 shows the direction-finding error of testing samples.

4.3. Both Phase Inconsistency and Mutual Coupling. In the presence of phase inconsistency and mutual coupling simultaneously, 3600 groups of phase difference and cosine and sine functions of DOA are generated as the training data sets for $0^\circ \sim 360^\circ$ with a step of 1° , and 10 samples are selected for each angle. Under the same signal-to-noise ratio, with the comprehensive disturbances which consist of phase inconsistency and mutual coupling, the testing samples are composed of 3600 groups of phase difference from different DOA. Figure 3 shows the direction-finding error of testing samples.

4.4. Different SNRs. In the presence of phase inconsistency and mutual coupling simultaneously, the training data sets are generated in the same way as mentioned in Section 4.3 under 10 dB SNR, while testing samples are generated under the 5 dB SNR. The number of training data sets and testing samples are both 3600. Figure 4 shows the direction-finding error of testing samples.

Table 2 shows the RMSE of DOA of the testing samples by using LS and MLSSVR, respectively, under different disturbance scenarios. From the results in Table 2, it can be seen that the MLSSVR model can significantly reduce the direction-finding error and obtain high-precision direction-finding results in the full range of 360° .

4.5. Comparison of MLSSVR and Neural Networks. The training data sets and testing samples are generated in the same way as mentioned in Section 4.3. The number of training data sets and the number of testing samples are both 3600. In addition, both phase inconsistency and

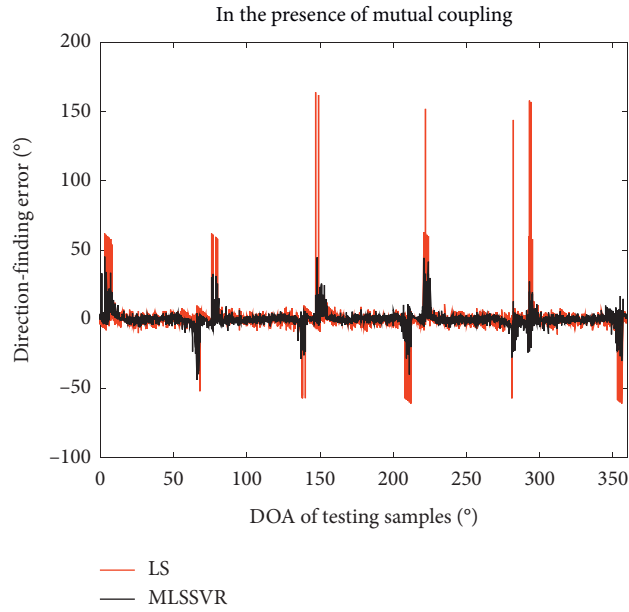


FIGURE 2: Direction-finding error of testing samples with mutual coupling.

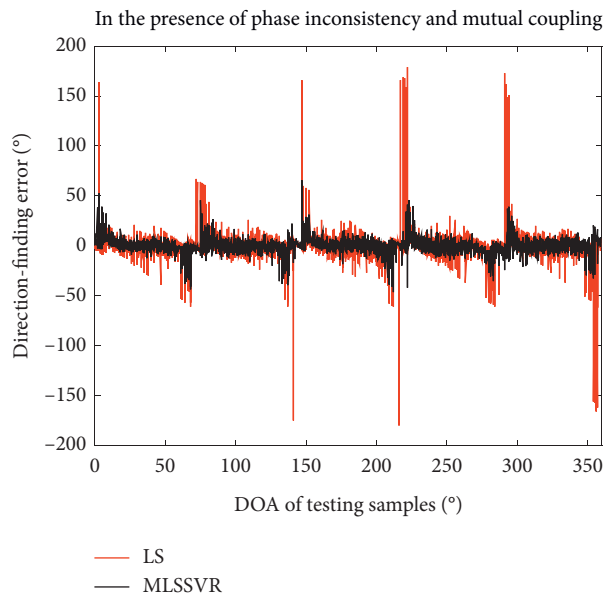


FIGURE 3: Direction-finding error of testing samples with phase inconsistency and mutual coupling.

mutual coupling are still in existence. For the same training data sets and testing samples, the two-layer convolutional neural network is used to estimate the DOA. The MaxEpochs is set to 15 (For the neural network model, it was obvious that the value of MaxEpochs in neural network could be larger to reduce the direction-finding error of the model. Here, a small value was deliberately selected to reduce the training time of neural

network to approximate the training time of MLSSVR model.), so that the training time of the neural network model is close to the MLSSVR model. Figure 5 shows the direction-finding error of testing samples.

Table 3 shows the MLSSVR model is suitable for small training data sets, and compared with neural network model, the MLSSVR model ensures direction-finding accuracy while shortening training time.

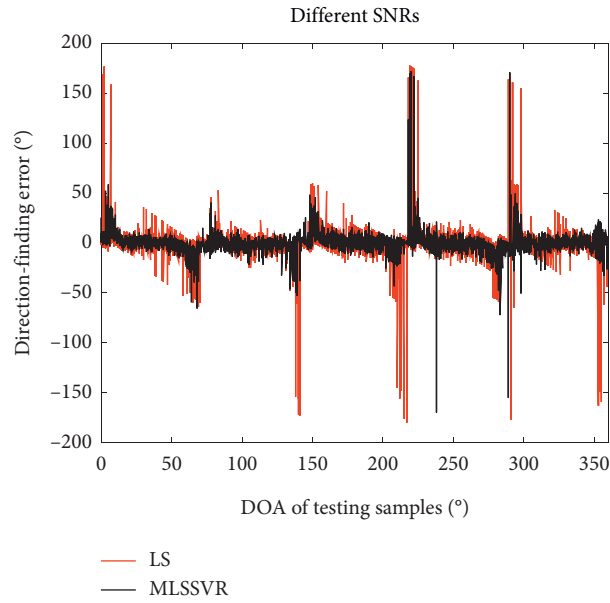


FIGURE 4: Direction-finding error of testing samples with different SNRs.

TABLE 2: RMSE of DOA of the testing samples.

The number of testing samples		Phase inconsistency	Mutual coupling	Phase inconsistency	mutual coupling	Different SNRs
		RMSE of DOA (°)				
LS	3600	4.0870	10.2529	15.9103		20.1085
MLSSVR		2.9695	5.2498	7.9172		11.3850

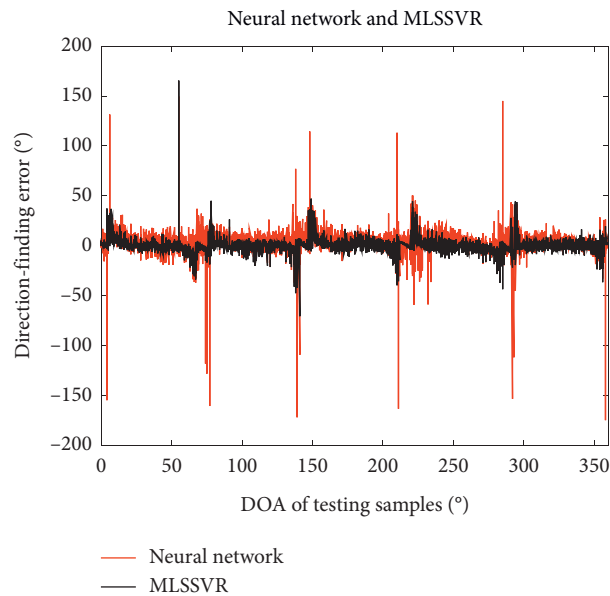


FIGURE 5: Direction-finding error of testing samples.

TABLE 3: RMSE of DOA of the testing samples.

	RMSE of DOA (°)	Training times (s)
Neural network	14.7228	2.531350
MLSSVR	7.7232	2.548054

5. Conclusion

The standard formulation of support vector regression can only deal with the single-output case, and when it is applied to radio direction-finding, there may be a problem that the direction-finding results have large errors around 0° or 360° . This paper applies the MLSSVR model to the field of radio direction-finding; the training data sets consist of phase differences of each baseline and the cosine and sine functions of each angle from 0° to 360° . The DOA is calculated by the sine function and cosine function of the incident angle, thus avoiding a larger case finding the error results in the vicinity of 0° or 360° . In the case of comprehensive disturbances in the direction-finding system, the effectiveness of the MLSSVR model is verified by numerical simulation. And with small training data sets, it can still effectively improve the direction-finding accuracy compared to the LS method.

Data Availability

All training data sets and testing samples used to support the findings of this study are available from the corresponding author upon request.

Conflicts of Interest

The authors declare that they have no conflicts of interest.

Acknowledgments

This work was supported by the No. 36 Research Institute of CETC under the project no. CX05.

References

- [1] L. Wan, L. Sun, X. Kong, Y. Yuan, K. Sun, and F. Xia, "Task-driven resource assignment in mobile edge computing exploiting evolutionary computation," *IEEE Wireless Communications*, vol. 26, no. 6, pp. 94–101, 2019.
- [2] F. Wen, Z. Zhang, K. Wang, G. Sheng, and G. Zhang, "Angle estimation and mutual coupling self-calibration for ULA-based bistatic MIMO radar," *Signal Processing*, vol. 144, pp. 61–67, 2018.
- [3] F. Wen and J. Shi, "Fast direction finding for bistatic EMVS-MIMO radar without pairing," *Signal Process*, vol. 173, 2020.
- [4] X. Wang, L. Wang, X. Li, and G. Bi, "Nuclear norm minimization framework for DOA estimation in MIMO radar," *Signal Processing*, vol. 135, pp. 147–152, 2017.
- [5] L. Wan, X. Kong, and F. Xia, "Joint range-Doppler-angle estimation for intelligent tracking of moving aerial targets," *IEEE Internet of Things Journal*, vol. 5, no. 3, pp. 1625–1636, 2018.
- [6] K. C. Ho and Y. T. Chan, "An asymptotically unbiased estimator for bearings-only and Doppler-bearing target motion analysis," *IEEE Transactions on Signal Processing*, vol. 54, no. 3, pp. 809–822, 2006.
- [7] J.-H. Lee, J.-H. Lee, and J.-M. Woo, "Method for obtaining three- and four-element array spacing for interferometer direction-finding system," *IEEE Antennas and Wireless Propagation Letters*, vol. 15, pp. 897–900, 2016.
- [8] J. H. Lee, J. K. Kim, H. K. Ryu, and Y. J. Park, "Multiple array spacings for an interferometer direction finder with high direction-finding accuracy in a wide range of frequencies," *IEEE Antennas and Wireless Propagation Letters*, vol. 17, no. 4, pp. 563–566, 2018.
- [9] D. Meng, X. Wang, M. Huang, L. Wan, and B. Zhang, "Robust weighted subspace fitting for DOA estimation via block sparse recovery," *IEEE Communications Letters*, vol. 24, no. 3, pp. 563–567, 2020.
- [10] J. Zheng, T. Yang, H. Liu, and T. Su, "Efficient data transmission strategy for IIoTs with arbitrary geometrical array," *IEEE Transactions on Industrial Informatics*, vol. 99, Article ID 2993586, 2020.
- [11] J. Zheng, T. Yang, H. Liu, T. Su, and L. Wan, "Accurate detection and localization of UAV swarms-enabled MEC system," *IEEE Transactions on Industrial Informatics*, vol. 99, Article ID 3015730, 2020.
- [12] C. S. Park and D. Y. Kim, "The fast correlative interferometer direction finder using I/Q demodulator,," in *Proceedings of the Asia-Pacific Conference on Information Processing*, pp. 1–5, Busan, South Korea, 2006.
- [13] G. Zhu, Y. Wang, and S. Mi, "Research on direction finding technique based on the combination of weighted least squares method and MUSIC algorithm," *Rader Science and Technology*, vol. 17, no. 3, pp. 319–323, 2019.
- [14] J. Zheng, H. Liu, and Q. H. Liu, "Parameterized centroid frequency-chirp rate distribution for LFM signal analysis and mechanisms of constant delay introduction," *IEEE Transactions on Signal Processing*, vol. 65, no. 24, pp. 6435–6447, 2017.
- [15] B. Friedlander and A. J. Weiss, "Direction finding in the presence of mutual coupling," *IEEE Transactions on Antennas and Propagation*, vol. 39, no. 3, pp. 273–284, 1991.
- [16] T. Svantesson, "Modeling and estimation of mutual coupling in a uniform linear array of dipole," in *Proceedings of the IEEE International Conference on Acoustics, Speech, and Signal Processing*, IEEE, Phoenix, AZ, USA, pp. 2961–2964, March 1999.
- [17] M. Lin and L. Yang, "Blind calibration and DOA estimation with uniform circular arrays in the presence of mutual coupling," *IEEE Antennas and Wireless Propagation Letters*, vol. 5, no. 1, pp. 315–318, 2006.
- [18] A. J. Weiss and B. Friedlander, "Array shape calibration using eigen-structure methods," *Signal Processing*, vol. 22, no. 3, pp. 251–258, 1991.
- [19] B. P. Flanagan and K. L. Bell, "Array self-calibration with large sensor position errors," *Signal Processing*, vol. 81, no. 10, pp. 2201–2214, 2001.
- [20] A. Paulraj and T. Kailath, "Direction of arrival estimation by eigen-structure methods with unknown sensor gain and phase," *Acoustics, Speech, and Signal Processing*, in *Proceedings of the ICASSP'85. IEEE International Conference on Acoustics, Speech, and Signal Processing*, pp. 640–643, IEEE, Tampa, FL, USA, April 1985.
- [21] Y. Li and M. Er, "Theoretical analyses of gain and phase error calibration with optimal implementation for linear equispaced array," *IEEE Transactions on Signal Processing*, vol. 54, no. 2, pp. 712–723, 2006.
- [22] Q. Zhai, "Research on least square direction-finding method," *Radio Engineering*, vol. 38, no. 3, pp. 55–57, 2008.
- [23] C. S. Shieh and C. T. Lin, "Direction of arrival estimation based on phase differences using neural fuzzy network," *IEEE Transactions on Antennas and Propagation*, vol. 48, no. 7, pp. 1115–1124, 2000.
- [24] C. G. Christodoulou, J. A. Rohwer, and C. T. Abdallah, "The use of machine learning in smart antennas," in *Proceedings of*

- the IEEE Antennas and Propagation Society Symposium*, pp. 321–324, IEEE, Monterey, CA, USA, June 2004.
- [25] J. A. Rohwer, C. T. Abdallah, and C. G. Christodoulou, “Least squares support vector machines for direction of arrival estimation with error control and validation,” in *Proceedings of the GLOBECOM’03. IEEE Global Telecommunications Conference*, pp. 2172–2176, IEEE, San Francisco, CA, USA, December 2003.
- [26] C. A. M. Lima, C. Junqueira, R. Suyama, F. J. V. Zuben, and J. M. T. Romano, “Least-square support vector machines for DOA estimation: a step-by-step description and sensitivity analysis,” in *Proceedings of the International Joint Conference on Neural Networks*, pp. 3226–3231, Montreal, Canada, July 2005.
- [27] S. Vigneshwaran, N. Sundararajan, and P. Saratchandran, “Direction of arrival (DOA) estimation under array sensor failures using a minimal resource allocation neural network,” *IEEE Transactions on Antennas and Propagation*, vol. 55, no. 2, pp. 334–343, 2007.
- [28] M. Dehghanpour, V. T. T. Vakili, and A. Farrokhi, “DOA estimation using multiple kernel learning SVM considering mutual coupling,” in *Proceedings of the 2012 Fourth International Conference on Intelligent Networking and Collaborative Systems*, pp. 55–61, Bucharest, Romania, September 2012.
- [29] R. Wang, B. Wen, and W. Huang, “A support vector regression-based method for target direction of arrival estimation from HF radar data,” *IEEE Geoscience and Remote Sensing Letters*, vol. 15, no. 5, pp. 674–678, 2018.
- [30] Z.-M. Liu, C. Zhang, and P. S. Yu, “Direction-of-arrival estimation based on deep neural networks with robustness to array imperfections,” *IEEE Transactions on Antennas and Propagation*, vol. 66, no. 12, pp. 7315–7327, 2018.
- [31] S. Abeywickrama, L. Jayasinghe, H. Fu, S. Nissanka, and C. Yuen, “RF-based direction finding of UAVs using DNN,” in *Proceedings of the IEEE International Conference on Communication Systems (ICCS)*, December 2018.
- [32] S. Xu, X. An, X. Qiao, L. Zhu, and L. Li, “Multi-output least-squares support vector regression machines,” *Pattern Recognition Letters*, vol. 34, no. 9, pp. 1078–1084, 2013.

Research Article

Partition Selection for Large-Scale Data Management Using KNN Join Processing

Yue Hu ^{1,2}, Ge Peng ¹, Zehua Wang ¹, Yanrong Cui ^{1,2} and Hang Qin ^{1,2}

¹Computer School, Yangtze University, Hubei 434023, China

²Hubei Graduate Workstation with Jingpeng Software Group Co., Ltd., Jingzhou, Hubei, China

Correspondence should be addressed to Hang Qin; 68681700@qq.com

Received 29 May 2020; Accepted 10 August 2020; Published 8 September 2020

Guest Editor: Liangtian Wan

Copyright © 2020 Yue Hu et al. This is an open access article distributed under the Creative Commons Attribution License, which permits unrestricted use, distribution, and reproduction in any medium, provided the original work is properly cited.

For the data processing with increasing avalanche under large datasets, the k nearest neighbors (KNN) algorithm is a particularly expensive operation for both classification and regression predictive problems. To predict the values of new data points, it can calculate the feature similarity between each object in the test dataset and each object in the training dataset. However, due to expensive computational cost, the single computer is out of work to deal with large-scale dataset. In this paper, we propose an adaptive v KNN algorithm, which adopts the Voronoi diagram under the MapReduce parallel framework and makes full use of the advantages of parallel computing in processing large-scale data. In the process of partition selection, we design a new predictive strategy for sample point to find the optimal relevant partition. Then, we can effectively collect irrelevant data, reduce KNN join computation, and improve the operation efficiency. Finally, we use a large number of 54-dimensional datasets to conduct a large number of experiments on the cluster. The experimental results show that our proposed method is effective and scalable with ensuring accuracy.

1. Introduction

In recent years, with the wide deployment of cloud computing, network, and radio, Internet of Things (IOT) products have been widely used in the natural sciences, such as industrial pollution areas [1], mobile devices [2], vehicle communication systems [3], and radar Systems [4]. In the face of complex and diverse signals, the traditional radars have limited performance in DOA estimating [5]. How to enhance useful signals and extract useful information is the focus of current research [6]. With the development of signal processing technology, researchers propose a variety of algorithms to achieve this purpose. Typical algorithms include the multiple signal classification (MUSIC) and its variations [3, 7], ULA-based method [8], reduced-complexity OGSBL [9], PARAFAC decomposition [10], Tensor-based subspace algorithm [11], and NNM [12].

To date, searching for approximate objects from the vast amount of useful data is a very basic and critical operation. With the continuous expansion of network scale, the data scale presents explosive growth with large-volume, complex,

and growing datasets for multiple and autonomous sources. As a result, the k nearest neighbors (KNN) algorithm with high accuracy, insensitive to outliers, and no data input assumptions represents an important paradigm shift in the evolution of partition selection with the trained metric. Existing KNN algorithm-based method assume the classification can be improved by learning a distance metric from labeled examples.

In the classification process, the KNN algorithm calculates the distance (similarity) between the data sample to be classified and the entire known dataset. This method is simple, convenient, and inexpensive for small datasets. When dealing with such large-scale data, the complexity of similarity calculation increases dramatically with the intolerable calculation cost, which directly affects the classification efficiency and accuracy. When the dataset has more attributes, the impact is more evident, and the dimension catastrophes tend to occur to make distances very far when calculated in high-dimensional space. At this point, a natural idea is to introduce the idea of distribution with implementation of data parallel support.

In particular, MapReduce is a distributed parallel programming framework proposed by Google for processing large datasets on large-scale clusters, in terms of a streamlined computational framework to assemble sequential and parallel computation. The programming model via MapReduce was originally designed to simplify large-scale data calculations [13, 14]. In recent years, MapReduce has been studied in many ways [15–18] for large-scale data-intensive computing under data-intensive [19], CPU-intensive, and memory-intensive applications, such as in the fields of smart cities [20], biological data management [21], spatial geometry calculation [22], and distributed computing over a wireless interference network [23].

The goal of this paper is to propose an effective data partitioning strategy. The proposed KNN algorithm designed based on MapReduce framework is mainly used to solve the problem of too much computation and low classification efficiency. With this programming framework, we can divide KNN's computing tasks into several small tasks and assign them to several computing nodes to calculate at the same time for the speedup the operation. Only by dividing the data reasonably and actually reducing the calculation cost practically can the running efficiency of the algorithm be effectively improved.

The contributions of this paper are as follows:

- (1) We introduce the idea of the Voronoi diagram to partition the sample objects and design the partition selection strategy to find the optimal relevant partition for the sample to be tested, thereby avoiding the extracalculation brought by irrelevant data.
- (2) We address the MapReduce framework and propose a vKNN algorithm, which is implemented on the Hadoop cluster with KNN join processing, nearest center points selecting, relevant-partition selecting, and vKNN processing.
- (3) We conduct many experiments using real datasets to study the effects of various parameters on the algorithm. The results show that our proposed algorithm is effective and scalable with the accuracy in relevant-partition selection.

The contents of the paper are structured as follows. Section 2 reviews the related work, Section 3 formally defines the problems to be solved in this paper, Section 4 describes the related technologies involved in this paper, Section 5 details the implementation and improvement of the KNN algorithm based on MapReduce, Section 6 reports the experimental results, and finally Section 7 summarizes the entire study.

2. Related Work

Existing KNN method assumed that the classification algorithm can be widely applied in the field of machine learning and large-scale data analysis. In order to better apply the traditional KNN algorithm, previous studies mainly used two kinds of methods, *i.e.*, speeding up the process of finding k nearest neighbors and eliminating

irrelevant data to reduce the overall computation. For instance, Cui et al. [24] introduced a B^+ -tree method that maps high-dimensional data points in one dimension. The one-dimensional distance computed in the principal component space and the first principal components of the sample points were indexed using a B^+ -tree. At the same time, the principal components were adopted to filter neighboring query points to improve query efficiency. When working with high-dimensional data, most indexing methods cannot scale up well and perform worse than sequential scanning. Xia et al. [25] designed and implemented KNN join algorithm based on block nested join Gorder using a grid-based sorting method, which can effectively assign similar objects to the same grid. Amagata et al. [26] proposed a dynamic set KNN self-join algorithm to trim unnecessary computations using index technology.

However, the processing power of the single processor greatly limits the development of the KNN algorithm, which also makes the application of parallel and distributed compute imperatively. In recent years, MapReduce has been fully practiced in the field of machine learning [27–29]. In order to solve those problems of KNN algorithm, Zhang et al. [30] proposed the HBNJ algorithm implemented by Hadoop and its improved algorithm H-BRJ in document. However, due to the large impact of data size on the efficiency of the algorithm, this research focused more on approximate queries. Moutafis et al. [31] proposed a four-stage algorithm, where three optimization strategies were used to trim distant points, balance the number of reducers, and halve the output, which significantly reduced the computation time. In most studies, people chose to use the first data partitioning to reduce data calculation, such as R-tree, Δ -tree, Quad-Tree, and KDB-Tree [32]. These spatial partitioning-based indexing techniques will dramatically reduce efficiency as dimensions increase. Zhang et al. [30] proposed a Z-value-based partitioning strategy. The result of the algorithm depends to a large extent on the quality of the z -curve, which may cause problems in the processing of high-dimensional data. Ji et al. [33] proposed a distance-based partitioning method. However, this grid-based partitioning method is considered valid only for low-dimensional datasets. We also use a partitioning strategy. In this paper, we introduce the concept of Voronoi diagram because it can be applied to any dimension of data [34]. We use Voronoi diagrams to aggregate similar data so that irrelevant data can be clipped. The Voronoi diagram was proposed with the famous structure of computational geometry. It is widely used in many fields such as geometry, architecture, and geography [35–38]. Voronoi diagrams can partition data into set spaces and are effective in the study of local neighborhoods for each partition [39]. At the same time, Voronoi diagrams can help improve the performance of distance join queries [40].

3. Problem Formulation

In this part, we give the definition of KNN Join with its formulation. Table 1 lists some symbols and their corresponding meanings involved mainly in this paper.

TABLE 1: Symbols and their meanings.

Symbol	Definition
$R(S)$	The d -dimensional dataset
$r(s)$	The data object in $R(S)$
\mathfrak{R}^d	The d -dimensional metric space
$\text{dis}(r, s)$	The distance from r to s
k	The number of nearest neighbors
$\text{knn}(s, R, k)$	The k nearest neighbors of s from R
$\text{knnJ}(R, S)$	The KNN Join of R and S
$\max(\text{knn}(s, R, k))$	The maximum distance from s to its k nearest neighbors from R
N	The number of mappers
N	The number of center points
\mathcal{P}	The set of center points
p_i	The point in \mathcal{P}
P_i	The partition corresponds to p_i
P^x	The partition where x is located
P_i^s	The partition corresponding to the i th center point close to s

Let R and S be two different d -dimensional datasets, and $r(s)$ is the data object in $R(S)$. For the convenience of discussion, we introduce the geometric space to represent them. \mathfrak{R}^d is a d -dimensional geometric space, R and S can be regarded as a sample point set in \mathfrak{R}^d , and the data objects r and s can be viewed as a d -dimensional sample point; then, we have $r \in R (s \in S)$. In order to avoid loss of generality, the distance measurement method adopted in this paper is Euclidean distance. Also, the distance between the data objects r and s , denoted as $\text{dis}(r, s)$, can be calculated as follows:

$$\text{dis}(r, s) = \left(\sum_{l=1}^d |r^l - s^l|^2 \right)^{1/2}, \quad (1)$$

where $\text{dis}(r, s) \geq 0$ and the necessary condition for $\text{dis}(r, s) = 0$ is $r = s$.

The similarity between data objects r and s , denoted as $\text{sim}(r, s)$, is

$$\text{sim}(r, s) = \frac{1}{1 + \text{dis}(r, s)}, \quad (2)$$

where the greater the distance, the greater the difference between objects and the smaller the similarity.

Definition 1 (KNN). Given a sample set R , a newly input sample point s . The KNN operation of them, denoted as $\text{knn}(s, R, k)$, involves the k nearest neighbors of s from R . The formal description is as follows:

$$\text{knn}(s, R, k) = \{z_1, z_2, \dots, z_k \mid z_1, z_2, \dots, z_k \in R\}, \quad (3)$$

for $\forall z_j \in R - \{z_1, z_2, \dots, z_k \mid z_1, z_2, \dots, z_k \in R\}$, and we have

$$d(s, z_j) \geq d(s, z_k) \geq \dots \geq d(s, z_2) \geq d(s, z_1). \quad (4)$$

Definition 2 (KNN Join). Given two sample sets R and S . The KNN join operation denoted as $\text{knnJ}(R, S)$ returns each

object $s \in S$ with its k nearest neighbors from R . The formal description is as follows:

$$\text{knnJ}(R, S) = \{s, \text{knn}(s, R, k) \mid \text{for all } s \in S\}. \quad (5)$$

4. MapReduce for Data Processing under Voronoi-Based KNN Processing

4.1. MapReduce for Flexible Data Processing. MapReduce, a distributed parallel programming framework, is a member of the core designs of Hadoop [41, 42]. It separates the users from the bottom layer of the system. When users write the corresponding programs, they only need to write the *Map* function and *Reduce* function to give what needs to be calculated and how to calculate automatically by the framework. Meanwhile, MapReduce has been extensively used due to its high fault tolerance and scalability.

MapReduce is mainly used for parallel computation of large amounts of data. A MapReduce program contains only two functions: *Map* function and *Reduce* function. The corresponding processing of these two functions can be customized by the user. At the beginning of the calculation task, Hadoop divides the entire job into two sequential phases: *Map* phase and *Reduce* phase. The model first breaks down the computational tasks of large-scale data that need to be processed into many individual tasks. These individual tasks can be run in parallel on a Hadoop server cluster; then, the model combines the results calculated by the cluster and calculates the final result. In the *Map/Reduce* phase, there are multiple instance tasks, which can be executed in parallel on each node. The MapReduce programs save both input and output results in HDFS. They use migration to transfer data to the nearest available node only if the node does not have local data or cannot process local data [43].

Figure 1 shows the specific execution process of MapReduce. The *Client* program divides the file data according to the parameter (m). The *ResourceManager* picks the idle nodes in the cluster and assigns the corresponding compute resources to them. At the same time, the *Job* is assigned the same number of *Map* tasks with the number of file blocks.

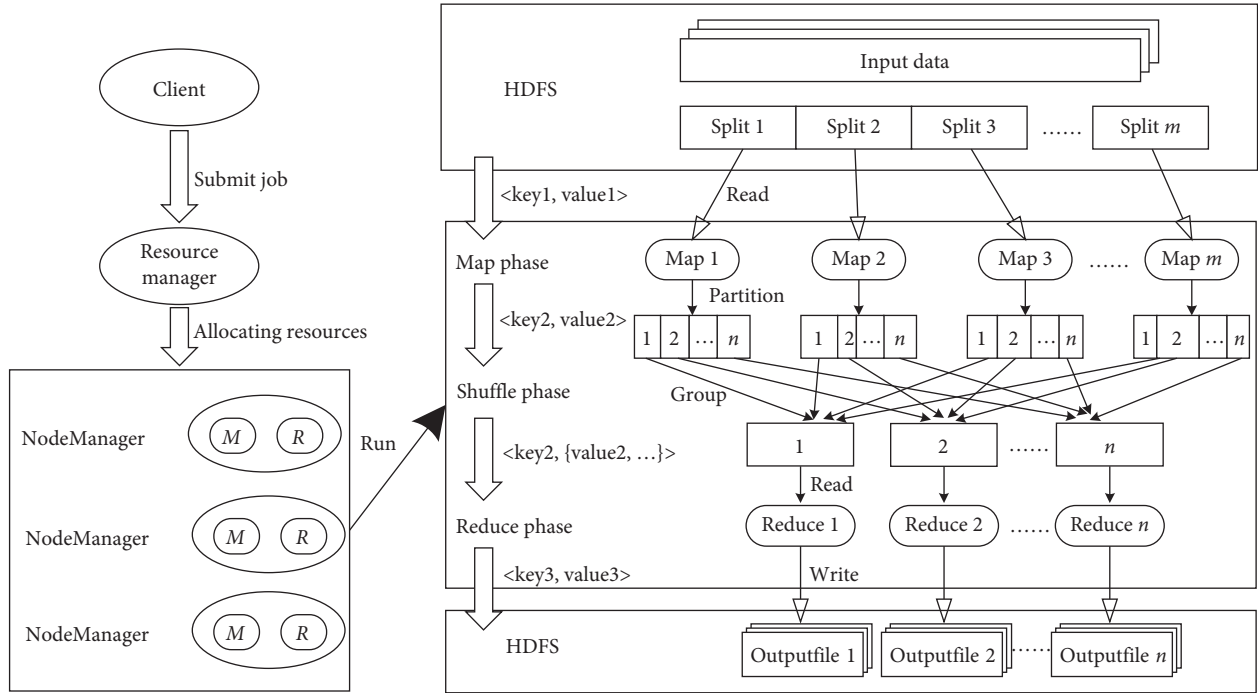


FIGURE 1: The workflow of the MapReduce.

Before starting the *Map* task, the file on the node is read and parsed into $\langle \text{key1}, \text{value1} \rangle$ key-value pairs by line, and then the *Map* function converts it into new $\langle \text{key2}, \text{Value2} \rangle$ key-value pairs. Next, the model uses the *Hash* function to partition and sort $\langle \text{key2}, \text{value2} \rangle$ key-value pairs, and groups them to $\langle \text{key2}, \{\text{value2}, \dots\} \rangle$ according to the *key2*. Finally, the *Reduce* function accepts the data, generates new $\langle \text{key3}, \text{value3} \rangle$ pairs from the corresponding business logic, and saves it in HDFS. When the cluster resources are not sufficient to host all *Map* (*Reduce*) tasks at the same time, the corresponding tasks are started in batches. In addition, the first *Reduce* task can only be started after the last *Map* task has been executed [44].

4.2. Voronoi Diagram with Partition Selection. The Voronoi diagram, also known as Dirichlet diagram, plays an important role in computational geometry. In the field of mathematics, this diagram is a decomposition of a given space, the simplest form to decompose a plane. The division yields that all points in each area are closer to the center of the area than to other centers.

To illustrate this, we can take a two-dimensional plane as an example. Given a dataset R , each object in R can be regarded as a point of \mathfrak{R}^2 . Partitioning using a Voronoi diagram, means selecting n objects as the center points and assigning all objects in R to the partition corresponding to their nearest center points. This divides the entire data space into n partitions, as shown in Figure 2. The large blue circle represents the center points of the Voronoi diagram, and each point represents an object. The green points represent the k nearest neighbors of

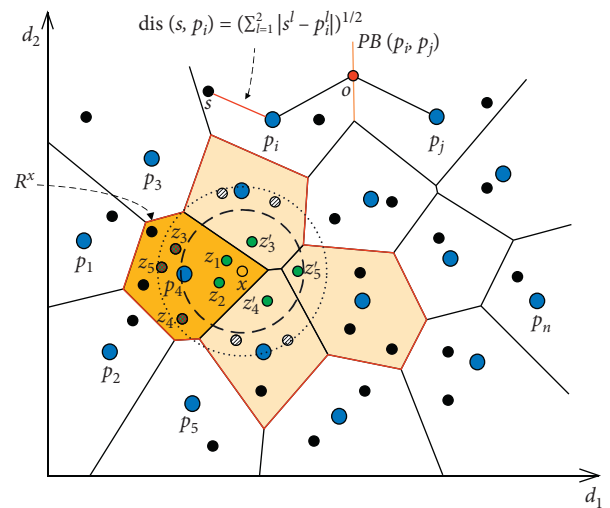


FIGURE 2: Voronoi diagram of the plane.

object x , where the grid points represent the false k nearest neighbors. The orange area is where the area of object x is located, and the region enclosed by the red line is the set of regions, where the true k nearest neighbors of object x are located. The dashed areas correspond to the spatial ranges of the true k nearest neighbors and the false k nearest neighbors, respectively.

For the sake of brevity, let \mathcal{S} be the selected set of center points, where $\mathcal{S} = \{p_1, \dots, p_n\}$. Given two center points p_i and p_j , $PB(p_i, p_j)$ represents the hyperplane dividing the partitions, where p_i and p_j are located for the point o on the hyperplane $PB(p_i, p_j)$, and we have

$$\begin{aligned} \forall o \in PB(p_i, p_j), \\ \text{dis}(o, p_i) = \text{dis}(o, p_j). \end{aligned} \quad (6)$$

According to formula (1), for any sample points s , located in the corresponding subspace of p_i , the distance between s and p_i , denoted as $\text{dis}(s, p_i)$, is

$$\text{dis}(s, p_i) = \left(\sum_{l=1}^d |s^l - p_i^l|^2 \right)^{1/2}, \quad (7)$$

for $\forall p_j \in \mathcal{P} - \{p_i\}$, and we have

$$\text{dis}(s, p_i) < \text{dis}(s, p_j). \quad (8)$$

The distance from s to $PB(p_i, p_j)$, denoted as $\text{dis}(s, PB(p_i, p_j))$, can be calculated as follows:

$$\text{dis}(s, PB(p_i, p_j)) = \frac{(\text{dis}(s, p_j))^2 - (\text{dis}(s, p_i))^2}{2 \times \text{dis}(p_i, p_j)}. \quad (9)$$

Figure 3 shows the distance $\text{dis}(s, PB(p_i, p_j))$. Based on the characteristics of the Voronoi diagram, we can transform the process of finding k nearest neighbors in R in Definition 1 into the process of finding k nearest neighbors in the partition. Now, our work only considers the partition where the sample point is located.

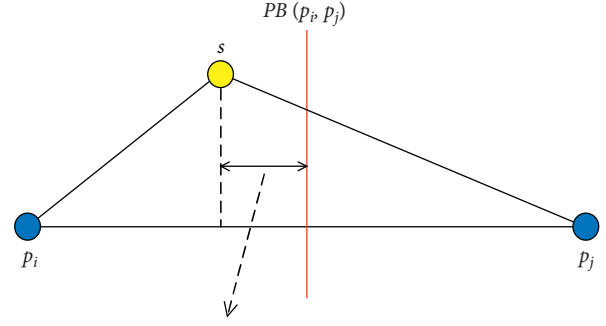
Hypothesis 1 Given a sample set R , perform a KNN operation on the newly input sample point x , that is, find k nearest sample points of x in the partition p^x where x is located. The formal description is as follows:

$$\text{knn}(x, R, k) = \text{knn}(x, p^x, k). \quad (10)$$

In this case, the computational effort of the running process is significantly reduced. However, when x is near the p^x boundary of the partition where it is located, it is easy to produce large errors by roughly limiting the size of the partition involved in the calculation. Suppose $k = 5$, as shown in Figure 2, the sample point x to be measured is located in the partition corresponding to p_4 . According to Hypothesis 1, the k nearest sample points are $\{z_1, z_2, \dots, z_5\}$. And when we look through Figure 2, it is easy to find that the real k nearest sample points are $\{z_1, z_2, z_3', z_4', z_5'\}$, whereas the sample points $\{z_3, z_4, z_5\}$ outside of the partition. This means that, in the actual operation process, only the samples in the partition where x is located may not necessarily yield true results. Consequently, we introduce a new concept: relevant partition, which is given in conjunction with Definition 1 as follows.

Definition 3. (relevant partition). Given the sample set R , the corresponding relevant partition R^x for the newly input sample point x is the partition set of k nearest neighbors. We have

$$R^x = p^{z_1} \cup p^{z_2} \cup \dots \cup p^{z_k}. \quad (11)$$



$$\text{dis}(s, PB(p_i, p_j)) = (\text{dis}(s, p_j))^2 - (\text{dis}(s, p_i))^2 / 2 \times \text{dis}(p_i, p_j)$$

FIGURE 3: The distance from (s) to $PB(p_i, p_j)$.

Therefore, KNN operation on x and R can be converted to finding the k nearest neighbors of x in the relevant partition R^x , and the formal description is as follows:

$$\text{knn}(x, R, k) = \text{knn}(x, R^x, k). \quad (12)$$

5. KNN Algorithm with MapReduce Performance Improvement

5.1. KNN Join Processing. The basic idea of the KNN join algorithm based on MapReduce is in general agreement with that of the KNN algorithm. Firstly, the MapReduce program divides the input test dataset, each node calculates the distance between the test samples in the corresponding slice and each sample in the training dataset, finds out the k nearest neighbors, and selects the label with the largest proportion of these adjacent points. As shown in Algorithm 1, the KNN join processing can be formulated by the following.

In the *Map* function, it first sets the parameter k of the algorithm. Next, it calculates the Euclidean distance between each sample r of the training dataset R and the test sample s and stores the labels of the k nearest training samples into *trainLabel*. The form of the input data $\langle \text{key}, \text{value} \rangle$ is $\langle \text{row number}, \text{sample} \rangle$; the form of the output data $\langle \text{key}, \text{values} \rangle$ is $\langle \text{sample}, \text{the label of adjacent sample} \rangle$. The *Hash* function partitions, sorts, and groups these intermediate results by key values. The *Reduce* function then reads them. The design of the *Reduce* function is relatively simple. Its main task is to obtain the label with the maximum number of k labels and assign it to the test sample. First, iterate through the data passed by the *Map* function in turn, and if the current data exists in the *HashMap*, add 1 to its value. If the current data does not exist in the *HashMap*, mark its value as 1, and add it to the *HashMap*. Finally, the label with the largest value in *HashMap* is used as the prediction label. The form of input data $\langle \text{key}, \text{values} \rangle$ is $\langle \text{sample}, \text{set (the labels of adjacent } k \text{ samples)} \rangle$. The form of output data $\langle \text{key}, \text{value} \rangle$ is $\langle \text{sample}, \text{the prediction label} \rangle$.

Obviously, the method is too expensive. It simply assigns computing tasks to the computing nodes, and each mapper needs to connect a subset from S to the entire dataset R . Considering only the distance calculation to be performed


```

Input:  $k, R, S$ 
Output:  $s.predictLabel$ //prediction label of  $s$ 
map:  $\langle row\ number, s \rangle$ 
  foreach  $r \in R$  do
     $dis = dis(r, s)$ //calculate the Euclidean distance between  $r$  and  $s$ 
    for  $i = 0$  to  $k$  do
      if  $dis < distance[i]$  then//find the minimum  $k$  distances
         $distance[i] = dis$ ;
         $trainLabel[i] = r.label$ ;
        break;
    for  $j = 0$  to  $k$  do
       $output(s, trainLabel[i])$ ;
reduce:  $\langle s, Labels \rangle$ 
   $hmp = new\ HashMap()$ ; //create a HashMap object  $hmp$ 
  foreach  $label \in Labels$  do//count the number of each label
    if  $hmp.get(label) \neq NULL$  then//if the label exists in  $hmp$ 
       $label.value++$ ; //take the value of the label and add 1
       $hmp.put(label) = label.value$ //update the value of the label in  $hmp$ 
    else//if the label does not exist in  $hmp$ 
       $hmp.put(label) = 1$ ; //set the value of the label to 1 and insert to  $hmp$ 
   $predictLabel = hmp.maxvalue$ ; //the label with the largest value as the prediction label
   $output(s, predictLabel)$ ;

```

ALGORITHM 1: KNN join processing.

for each node, the amount of computation reaches $|R| \cdot (|S|/n)$. When the dataset involved in the calculation is large, the amount of computation is still a huge amount in comparison. In addition, the comparison of similarity may exceed the computing capacity of the node, resulting in the task being killed. Therefore, it is unreliable to rely solely on MapReduce to slice computational tasks for efficient classification. A better idea is to reduce the number of samples in R that is involved in the calculation.

5.2. Relevant-Partition Selecting and $vKNN$ Processing.

We consider the Voronoi diagrams for KNN join within the MapReduce framework. The basic idea is to partition the data using the Voronoi diagram and clip the unqualified data to reduce the amount of calculation. There are three main steps as follows.

5.2.1. Preprocessing Step. Input dataset R and partition R using Voronoi diagram. First, randomly select N samples from the dataset R as the initial center point. Then, we use k -means clustering method to analyze the dataset globally to obtain the center points set \mathcal{P} and the corresponding data clusters.

5.2.2. Nearest Center Point Selecting Step. In this step, we use the output of the above processes and dataset S as input objects. Find the k nearest center points of each sample in S and save its index and distance information to help clip the unqualified data.

Algorithm 2 shows the execution of the mappers at this stage. Before the program starts, we can load the preprocess center point data into the main memory of each mapper.

After each mapper reads the sample object s , it traverses each center point and calculates the distance of s from all the center points. In order to reduce the cost of data transmission between nodes, we only save the index and distance information of the k center points nearest to s . We use *TreeMap* to store relevant information so that we can get the first k center points more quickly, where *TreeMap* itself is an ordered set of key values. All elements remain in a specific order and are sorted in ascending order by default by the value of the key. So, we can easily get information about the nearest k center points.

5.2.3. $vKNN$ Processing Step. In this step, we use the output from the previous two processes as input. On the basis of the distance, we can filter out the relevant partition R^s corresponding to each sample s in S to find out the labels of the k nearest neighbors. Finally, reducer counts the labels and outputs the label that appears most often.

In order to ensure the accuracy of the prediction results, the selected relevant partition R^s contains all $knn(s, R, k)$ as minimum as possible. How to determine the relevant partition R^s that will participate in the final calculation is an issue we need to consider now.

Theorem 1. Given a sample point s and a center point p_i , s is located in the partition p_i corresponding to p_i , and we have

$$p_i \in R^s. \quad (13)$$

Proof. As s is located in the partition p_i , s is very similar to the sample points in p_i . This means that the probability of having the nearest neighbors in p_i is greater than that in any

```

Input:  $S, \mathcal{P}$ 
Output:  $\langle s, \{P_1^s, P_2^s, \dots, P_k^s\} \rangle$  //the partitions corresponding to the  $k$  nearest center points of  $s$ 
foreach  $s \in S$  do
  tmp = TreeMap(); //create a TreeMap object tmp
  nearPointSet = [ ]; //create an empty set nearPointSet
  foreach  $p \in \mathcal{P}$  do //insert the distance and index information tmp.put(dis(p, s), p.index);
  for  $i=0$  to  $k$  do //read the first  $k$  center points' information nearPointSet.append(tmp.next()); //put the information to nearPointSet

```

ALGORITHM 2: Nearest center point selecting.

other partition. In other words, p_i are more likely to have the nearest neighbors.

Based on the analysis of Hypothesis 1, we may have errors in predicting using only the sample points within p_i . We can design a selection strategy to determine whether other partitions meet the criteria.

Definition 4. Given two center points p_i and p_j , $PB(p_i, p_j)$ addresses the hyperplane dividing the subspace, where p_i and p_j are located, s is located in the partition p_i corresponding to p_i , and the maximum distance from s to it in its k nearest neighbor samples, denoted as θ , is

$$\theta = \max(\text{knn}(s, p_i, k)). \quad (14)$$

Theorem 2. Given two center points p_i and p_j , $PB(p_i, p_j)$ is the hyperplane dividing the subspace where p_i and p_j are located, s is in the partition p_i corresponding to p_i , and the necessary condition for $p_j \in R^s$ is

$$\text{dis}(s, PB(p_i, p_j)) < \theta. \quad (15)$$

Figure 4(a) shows the case of $\text{dis}(s, PB(p_i, p_j)) > \theta$, and Figure 4(b) shows the case of $\text{dis}(s, PB(p_i, p_j)) < \theta$, respectively. When $\text{dis}(s, PB(p_i, p_j)) > \theta$, there is no intersection between the hypersphere with a radius of θ and the hyperplane $PB(p_i, p_j)$. That is to say, $\forall x \in p_j, \text{dis}(s, x) > \theta$ all hold. At this time, we can directly discard the partition p_j . When $\text{dis}(s, PB(p_i, p_j)) < \theta$, the hypersphere with the radius of θ intersect with the hyperplane $PB(p_i, p_j)$. It means that there is probably a sample point x in the partition p_j , making $\text{dis}(s, x) < \theta$, which also means that the calculated $\text{knn}(s, R^s, k)$ are not the real nearest neighbors. Therefore, we need to add the partition p_j to the relevant partition R^s .

In (Algorithm 3), due to the center point information sorted using TreeMap before, according to Theorem 1, we can get that the initial relevant partition R^s is p_1^s . We calculated k nearest neighbors of s on R^s and saved them in knnDisSet . Next, we judge the subsequent partitions in sequence according to Theorem 2. If the partition p_i^s ($i < k$) makes $\text{dis}(s, PB(p_1, p_i)) < \theta$, then the partition p_i^s may contain the actual k nearest neighbors of s . We need to include the partition p_i^s in R^s and calculate the k nearest neighbors of s in the latest correlation partition. When a certain partition p_i^s ($i < k$) appears where $\text{dis}(s, PB(p_1, p_i)) > \theta$, it means that the partition p_i^s does not

contain the actual k nearest neighbors of s , and we can discard the partition directly. Meanwhile, since the center point of the subsequent partitions are farther away from s , we also believe that they do not contain the actual k nearest neighbors of s , so we do not continue to make judgments and discard them directly. Finally, we can assume that the knnDisSet stores actual k nearest neighbors of s .

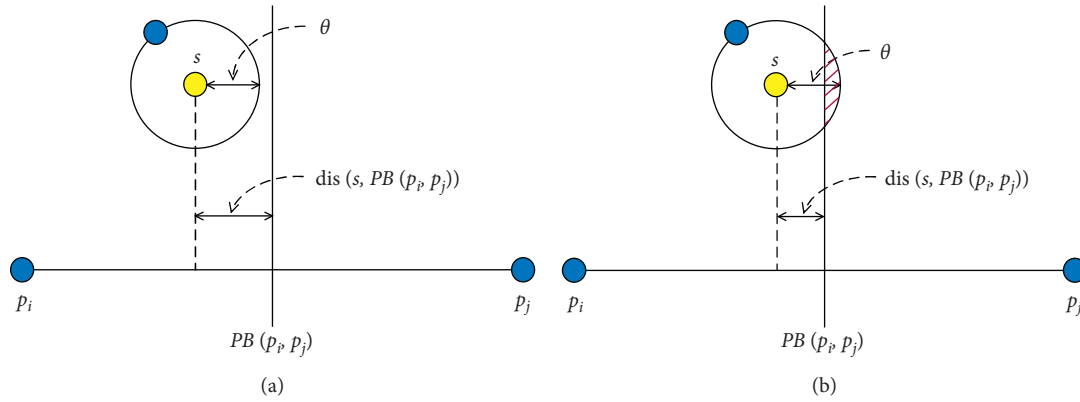
Algorithm 4 describes the specific details of vKNN. Before running the *Map* function, the program loads the center point data. In the *Map* function, call the *selectTrainSet()* function to calculate the k nearest neighbors. After the *selectTrainSet()* function finishes executing, $\text{knnSet}[k]$ accepts the k nearest neighbor samples returned. Meanwhile, the *Map* function creates an array $\text{trainLabel}[k]$ to hold their labels. In the *Reduce* function, we use the *HashMap* to count the labels, find out the label that occur most frequently, and merge the output with s .

In addition, we partition the data, and each partition is roughly the same size, about $|R|/N$. The provided partition selection policy limits the number of filtered partitions. This means that even in the worst case, each sample only needs to be compared with $k \times |R|/N$ training samples to find k nearest neighbors, which greatly reduces the computational effort of the entire KNN join process. Meanwhile, we use k -means clustering in the partitioning process, which makes the sample points in each partition highly similar, and the partition to be filtered is also the most similar to the test sample. Therefore, in theory, we can still maintain a high degree of accuracy while drastically reducing the number of training samples involved in the calculation.

6. Experimental Evaluation

6.1. Experimental Environment and Dataset. The experimental platform used to evaluate the performance of the proposed algorithm is mainly configured as Intel (R) Core (TM) i5-8300H 2.3 GHz processor, 16G memory, and 500G NVMe hard disk. The Hadoop cluster consists of six virtual machines, and each allocating 2G of memory and 40G of hard disk. On each node, we install CentOS 8.0 operating system with Java 1.8.0 and Hadoop 2.10.0. We select one of them as the Master node and the other five as Slave node to be managed through VMware® Workstation 15 Pro. The development environment used in the experiment is Eclipse-2019-12-R-linux-gtk-x86_64.

The experimental data in this study uses the Forest CoverType dataset, a standard dataset in the UCI database.

FIGURE 4: Partition selection. (a) Discard P_j . (b) Reserve P_j .

```

Input:  $s, \{p_1^s, p_2^s, \dots, p_k^s\}$ 
Output:  $\text{knn}(x, R^s, k)$ 
selectTrainSet() {
   $R^s = p_1^s$ ; //determine the initial Relevant-partition
  for  $i=2$  to  $k$  do
     $\text{knn}(x, R^s, k)$ ; //calculate the  $k$  nearest neighbors of  $s$  in  $R^s$ 
     $\theta = \max(\text{knn}(s, R^s, k))$ ; //calculate the maximum distance from  $s$  to its  $k$  nearest neighbors from  $R$ 
     $\text{dis}(s, PB(p_1, p_i)) = (\text{dis}(s, p_i))^2 - (\text{dis}(s, p_1))^2 / 2 \times \text{dis}(p_1, p_i)$ ; //calculate the distance from  $s$  to  $PB(p_1, p_i)$ ,
    if  $(\text{dis}(s, PB(p_1, p_i)) > \theta)$  then //  $p_i^s$  does not belong to  $R^s$ 
      break;
    else //  $p_i^s$  belongs to  $R^s$ 
       $R^s = R^s \cup p_i^s$ ; //add the partition  $p_i^s$  to  $R^s$ 
  }

```

ALGORITHM 3: Relevant partition selecting.

```

Input:  $\{p_1^s, p_2^s, \dots, p_k^s\}, S, k$ 
Output:  $s.\text{predictLabel}$  //prediction label of  $s$ 
map:  $\langle \text{row number}, s \rangle$ 
   $\text{knnSet}[k] \leftarrow \text{selectTrainSet}()$ ; //calculate the  $k$  nearest neighbors
  for  $i=0$  to  $k$  do //fetch the  $k$  nearest neighbors label
     $\text{trainLabel}[i] = \text{knnSet}[i].\text{label}$ ;
  for  $j=0$  to  $k$  do
     $\text{output}(s, \text{trainLabel}[j])$ ;
  reduce:  $\langle s, \text{Labels} \rangle$ 
   $\text{hmp} = \text{new HashMap}()$ ; //create a HashMap object hmp
  foreach  $\text{label} \in \text{Labels}$  do //count the number of each label
    if  $\text{hmp.get}(\text{label}) \neq \text{NULL}$  then //if the label exists in hmp
       $\text{label.value}++$ ; //take the value of the label and add 1
       $\text{hmp.put}(\text{label}) = \text{label.value}$ ; //update the value of the label in hmp
    else //if the label does not exist in hmp
       $\text{hmp.put}(\text{label}) = 1$ ; //set the value of the label to 1 and insert to hmp
   $\text{predictLabel} = \text{hmp.maxvalue}$ ; //the label with the largest value as the prediction label
   $\text{output}(s, \text{predictLabel})$ ;

```

ALGORITHM 4: vKNN processing.

The dataset has 581012 records, each comprising 54-dimensional features (10 quantitative variables, 4 binary wilderness areas, and 40 binary soil type variables) and seven

labels: Spruce/Fir, Lodgepole Pine, Ponderosa Pine, Cottonwood/Willow, Aspen, Douglas-fir, and Krummholz, each represented by a number from 1–7. For simplicity, we first

randomly selected 200,000 data from the dataset as the train set R , and the rest as the test set S .

Consequently, we evaluated the methods mentioned in our experiments. For the two methods described in Section 5, we set the number of reducers to 1 by default.

6.2. Experimental Evaluation Indicators. There are many available evaluation indicators in the classification tasks of machine learning. The two most common types are accuracy and error rate. For a given test set S , the classification error rate is defined as

$$E(S) = \frac{1}{|S|} \sum_{s \in S} I(s_{\text{type}} \neq s_{\text{new_type}}), \quad (16)$$

and the accuracy is defined as

$$\text{Acc}(S) = 1 - E(S) = \frac{1}{|S|} \sum_{s \in S} I(s_{\text{type}} = s_{\text{new_type}}), \quad (17)$$

where s_{type} refers to the actual label of s and $s_{\text{new_type}}$ refers to the label of s predicted by the model.

In addition, we will evaluate the proposed method in terms of the elapsed time and the acceleration ratio. The elapsed time involves the global time for the MapReduce program to run. The acceleration ratio is the ratio of the elapsed time of the original version to the improved version of the relevant parameters:

$$\text{Speedup} = \frac{\text{original_time}}{\text{improved_time}}, \quad (18)$$

where *original_time* is the time when the original version runs and *improved_time* is the time when the program runs after the improved parameter.

6.3. Evaluation of Experimental Results

6.3.1. Effect of Different Center Point Sizes. For our first experiment, we analyze the effect of the number of center points on the performance of vKNN. To further illustrate the situation, the number of mappers is given ($n=4$). Then, we randomly select 600, 800, 1000, 1200, and 1400 pieces of data from the training set in 5 times as the initial center point set. In Figure 5(a), the execution time of Algorithm 2 increases approximately linearly as N increases. This is because when finding the nearest k center points for each element of S , the distance between each element and each center point needs to be calculated with a time complexity of $O(|S| \times N)$. When the center point increases linearly, it means that the computation time will also increase linearly. We adopt the *TreeMap* for sorting distances, so we need not spend any extra time on it. In Figure 5(b), we can see that vKNN execution time decreases as N increases. This is because, as the number of center points increases, the training set is divided more finely when dividing the partitions, *i.e.*, the number of distance calculations needed for each sample decreases accordingly. Also, we notice that the actual reduction is getting smaller as the center point increases. This is because when the partitions are divided more finely, the

probability of occurrence of the scenario shown in Figure 4(b) increases as the set of corresponding partitions is determined. It is shown that some of the samples correspond to a larger set of partitions than before, which also results in increased computation time. Figure 5(c) shows how the accuracy of the algorithm varies from 600 to 1400. As N increases, there is little change in accuracy, which also indicates that the choice of N has no effect on the accuracy of the proposed method.

6.3.2. Effect of the Number of Nearest Neighbors. Next, we study the effect of k on the performance of the two algorithms. Similarly, given the number of mappers ($n=4$). Figure 6 shows the experimental results of k increasing from 3 to 20 gradually.

Figures 6(a) and 6(b) address the operation of two programs of vKNN algorithm. The running time of the algorithm increases approximately with the increase of k value, which means that the vKNN algorithm is not sensitive to the change of the k value. In Algorithm 2, the effect of k is mainly reflected in the following aspects: we added relevant information about k nearest center points of each sample to the training set. The greater the k value, the more information will be added, and the communication cost of data will increase. When the vKNN algorithm is run at the end, the communication cost of the file on HDFS increases accordingly. The increase of k value shows that θ will be larger in the same sample, and the hypersphere with this radius will be larger and easier to cross the hyperplane, as shown in Figure 4(b). At this point, more sample points will be added to the relevant partition, resulting in more computational effort.

Figure 6(c) shows the change of vKNN algorithm accuracy in the process of k increasing from 3 to 20. When k goes from 3 to 5, the algorithm accuracy is improved. As k continued to increase, the accuracy begins to decrease slightly. Explain that the k value of vKNN algorithm is not as large as possible, and we need to select the appropriate k value for the specific situation.

Figure 6(d) shows that vKNN performs better than KNN for the results of the two methods. The execution time of KNN increases linearly with the increase of k . The influence of k value on KNN algorithm is mainly reflected in the selection of the nearest k sample points. However, because the KNN algorithm itself is too computationally intensive when dealing with large datasets, the increase in the amount of computations caused by the increase in k value is less obvious than the amount of computations itself.

6.3.3. Effect of Speedup. Now, we measure the effect of the number of mappers. Given the number of center points ($N=1000$) and the number of nearest neighbors ($k=5$), Figure 7 shows the running time and acceleration ratio of vKNN as the number of mappers gradually increases from 1 to 4. Figure 7(a) shows that the run time decreases as the number of mappers increases. However, the scale is shrinking. This is also reflected in Figure 7(b), where the acceleration ratio gradually stabilizes. It is because

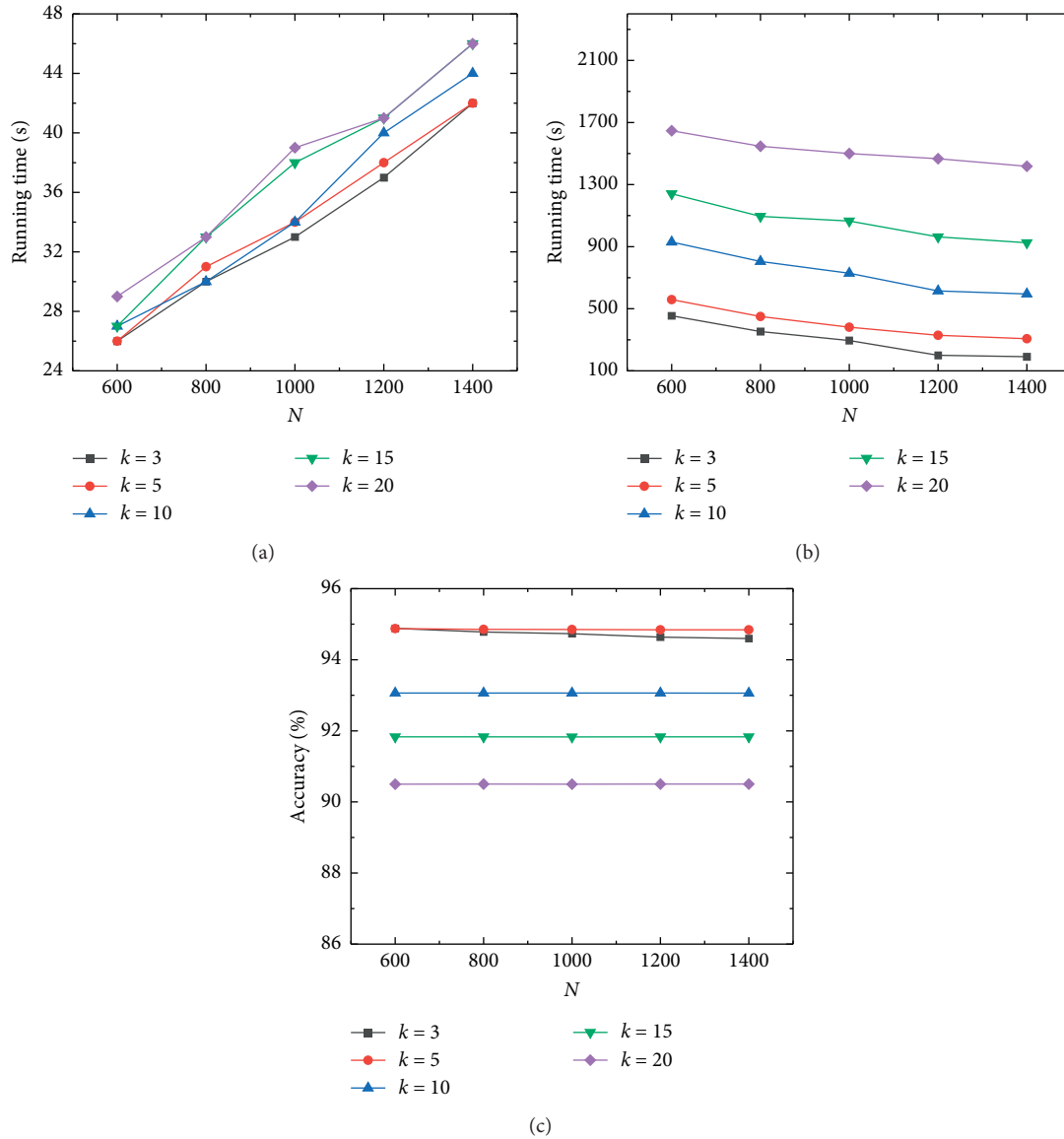


FIGURE 5: Effect of different center point sizes. (a) Running time of nearest center point selecting. (b) Running time of vKNN. (c) Accuracy of vKNN.

increasing the number of mappers means increasing the number of nodes participating in the operation, at which point the amount of computation allocated to each node will also be reduced, so the execution time of the map function on each node will be shortened accordingly. With the increasing number of nodes, the computing resources are larger than the required resources actually needed. At this time, the computing resources are not fully utilized, the execution time decreases less and less obvious, and cluster computing resources are also wasted. On the contrary, each node needs to read files from the HDFS, which increases the corresponding communication costs. When the acceleration effect of computing node growth is insufficient to offset the pressure of increased communication costs, the algorithm execution efficiency will decrease. Therefore, the number of mappers needs to be selected appropriately when facing datasets of different sizes.

6.3.4. Effect of Accuracy. Now, we study the accuracy of the two algorithms. Given the number of center points ($N=1000$) and the number of nearest neighbors ($k=5$). Figure 8 shows the accuracy of the two methods when k is gradually increased from 3 to 20. In general, vKNN is more accurate than KNN. This is because the partitioned data we use is the result of k-means clustering during the preprocessing phase, in which samples with the same characteristics are divided into the same cluster, *i.e.*, the data in the same partition are similar to each other. Subsequently, we search for the center point closest to the sample to be classified. Distance closest represents less difference and more similarity. Therefore, when the vKNN algorithm is executed and compared with other samples, the higher the degree of similarity with the sample to be classified, the smaller the calculation error will be.

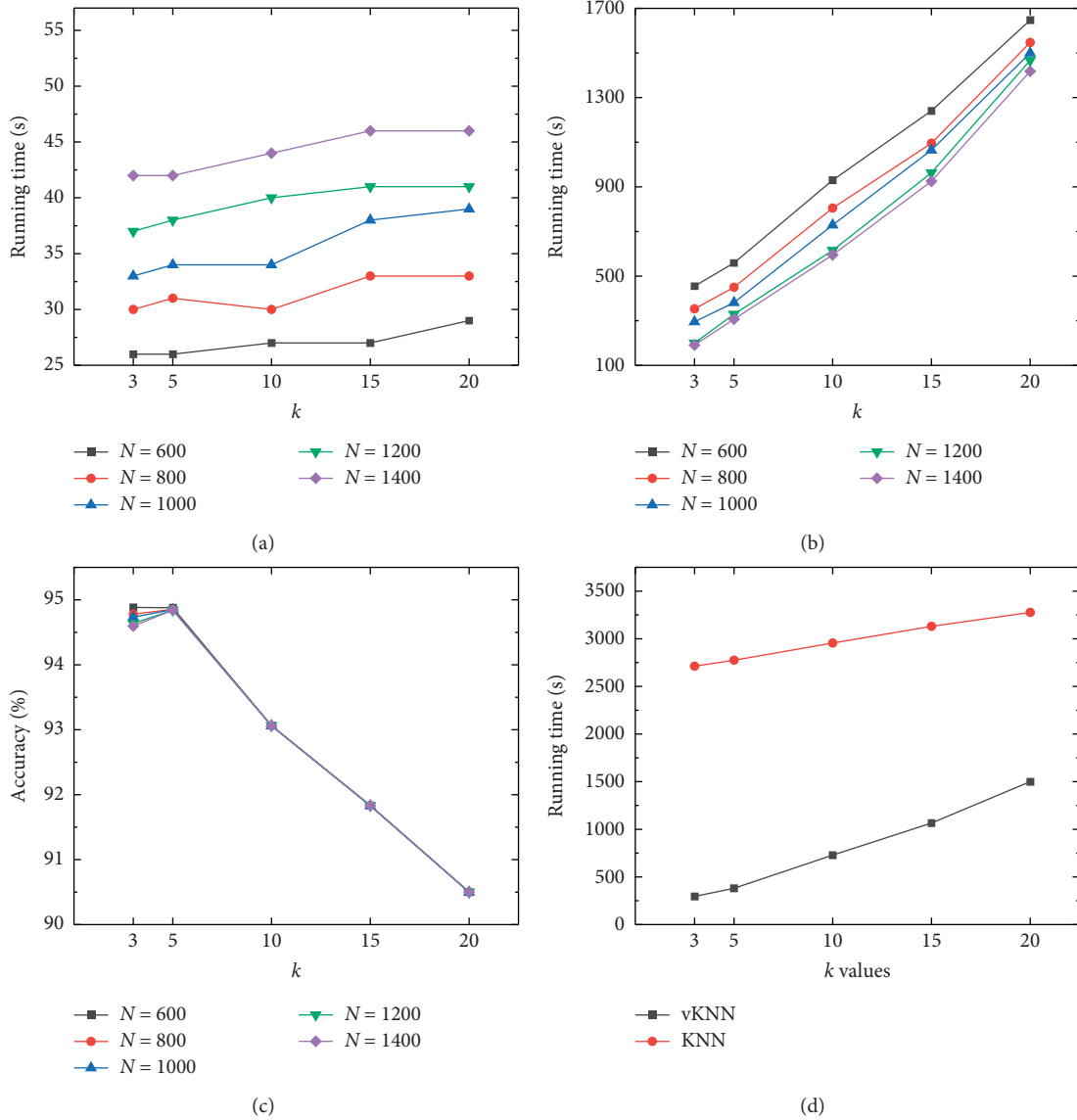


FIGURE 6: Effect of the number of nearest neighbors. (a) Running time of nearest center point selecting. (b) Running time of vKNN. (c) Accuracy of vKNN. (d) Running time comparison of different methods.

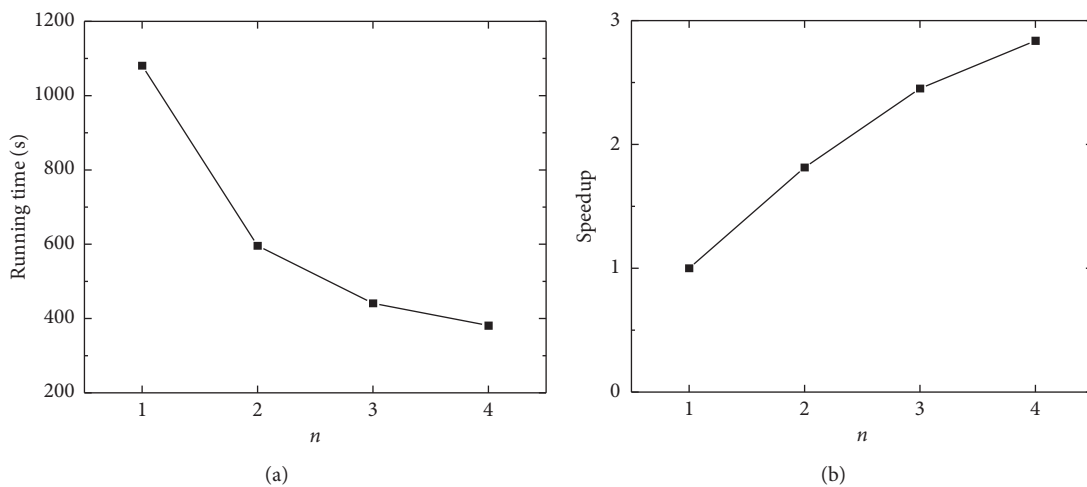


FIGURE 7: (a) Effect of the number of mappers. (b) Speedup.

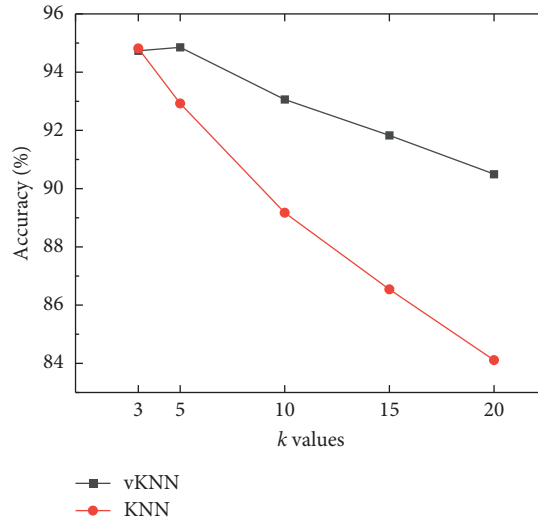


FIGURE 8: Accuracy of different methods.

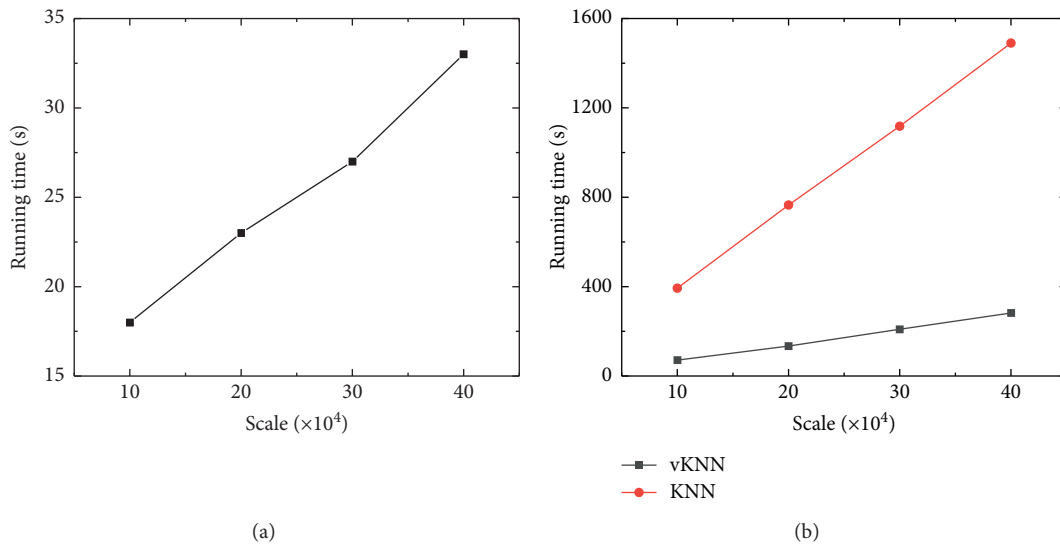


FIGURE 9: Scalability. (a) Running time of nearest center point selecting. (b) Running time of different methods.

6.3.5. Effect of Scalability. In this section, we randomly extract 100,000 pieces of data from the original dataset as a training set. Then, randomly extract 100,000, 200,000, 300,000, and 400,000 pieces of data from the rest of the set four times as a test set. Based on this, the scalability of the proposed method is evaluated. In the experiment, given the number of center points ($N=1000$) and the number of nearest neighbors ($k=5$). Figure 9(a) is the time-consuming result of Algorithm 2, and Figure 9(b) is the time-consuming result of two methods for performing KNN join.

On the whole, the execution time of both methods increases approximately linearly with the increase of training set data size. The reason is that, as the data size increases, the data allocated to each computing node will also increase proportionally, and the computing time of each node will increase in the same proportion. However, when using vKNN algorithm to perform KNN join, the growth is gentler. The average growth time of Algorithm 2 is only 5

seconds, which indicates that the scalability of vKNN algorithm is better than that of KNN algorithm. The time complexity of KNN algorithm is $O(|R| \cdot |S|)$, which is a Cartesian product of the sample set R and S . Obviously, no matter which sample set is increased in size, the effect is enormous. However, vKNN algorithm adopts the idea of partition which alleviates the computational changes caused by the increase of S . Therefore, as the dataset increases, the difference in execution time between the two methods increases.

7. Conclusion

In this paper, we propose a vKNN algorithm based on Voronoi diagram concerning MapReduce-based KNN join scheme. Our algorithm can partition the training set using the idea of Voronoi diagram. Then, we design a partition selection strategy to find the optimal relevant partition for

the sample to be tested, which effectively avoids the enormous amount of computation caused by irrelevant data. This strategy takes full advantage of the parallel processing capabilities of the MapReduce framework and is suitable for large-scale data. A large number of experiments based on real datasets show that our proposed algorithm can accelerate the calculation with good scalability while ensuring accuracy.

Data Availability

The classification data used to support the findings of this study has been taken from the UCI machine learning repository (<http://archive.ics.uci.edu/ml/index.php>).

Conflicts of Interest

The authors declare that there are no conflicts of interest regarding the publication of this paper.

Acknowledgments

This work was partially supported by the Hubei Graduate Workstation with Jingpeng Software Group Co., Ltd.

References

- [1] L. Wan, Y. Sun, I. Lee, W. Zhao, and F. Xia, "Industrial pollution areas detection and location via satellite-based IIOT," *IEEE Transactions on Industrial Informatics*, vol. 12, no. 6, pp. 2353–2364, 2016.
- [2] L. Wan, L. Sun, X. Kong, Y. Yuan et al., "Task-driven resource assignment in mobile edge computing exploiting evolutionary computation," *IEEE Wireless Communications*, vol. 26, no. 6, pp. 94–101, 2019.
- [3] X. Wang, L. Wan, M. Huang, C. Shen, Z. Han, and T. Zhu, "Low-complexity channel estimation for circular and non-circular signals in virtual MIMO vehicle communication systems," *IEEE Transactions on Vehicular Technology*, vol. 69, no. 4, pp. 3916–3928, 2020.
- [4] F. Wen and J. Shi, "Fast direction finding for bistatic EMVS-MIMO radar without pairing," *Signal Process*, vol. 173, p. 107532, 2020.
- [5] L. Wan, X. Kong, and F. Xia, "Joint range-Doppler-angle estimation for intelligent tracking of moving aerial targets," *IEEE Internet of Things Journal*, vol. 5, no. 3, pp. 1625–1636, 2018.
- [6] D. Meng, X. Wang, M. Huang, L. Wan, and B. Zhang, "Robust weighted subspace fitting for DOA estimation via block sparse recovery," *IEEE Communications Letters*, vol. 24, no. 3, pp. 563–567, 2020.
- [7] J. Li, X. Zhang, R. Cao, and M. Zhou, "Reduced-dimension MUSIC for angle and array gain-phase error estimation in bistatic MIMO radar," *IEEE Communications Letters*, vol. 17, no. 3, pp. 443–446, 2013.
- [8] F. Wen, Z. Zhang, K. Wang, G. Sheng, and G. Zhang, "Angle estimation and mutual coupling self-calibration for ULA-based bistatic MIMO radar," *Signal Processing*, vol. 144, pp. 61–67, 2018.
- [9] T. Liu, F. Wen, L. Zhang, and K. Wang, "Off-grid DOA estimation for colocated MIMO radar via reduced-complexity sparse bayesian learning," *IEEE Access*, vol. 7, pp. 99907–99916, 2019.
- [10] F. Wen, X. Xiong, and Z. Zhang, "Angle and mutual coupling estimation in bistatic MIMO radar based on PARAFAC decomposition," *Digital Signal Processing*, vol. 65, pp. 1–10, 2017.
- [11] F. Wen, X. Xiong, J. Su, and Z. Zhang, "Angle estimation for bistatic MIMO radar in the presence of spatial colored noise," *Signal Processing*, vol. 134, pp. 261–267, 2017.
- [12] X. Wang, L. Wang, X. Li, and G. Bi, "Nuclear norm minimization framework for DOA estimation in MIMO radar," *Signal Processing*, vol. 135, pp. 147–152, 2017.
- [13] J. Dean and S. Ghemawat, "MapReduce," *Communications of the ACM*, vol. 51, no. 1, pp. 107–113, 2008.
- [14] J. Dean and S. Ghemawat, "MapReduce," *Communications of the ACM*, vol. 53, no. 1, pp. 72–77, 2010.
- [15] X. Dolev, P. Gupta, Y. Li, S. Mehrotra, and S. Sharma, "Privacy-preserving secret shared computations using MapReduce," *IEEE Transactions on Dependable and Secure Computing*, 2019.
- [16] J. Liu, P. Wang, J. Zhou, and K. Li, "McTAR: a multi-trigger checkpointing tactic for fast task recovery in MapReduce," *IEEE Transactions on Services Computing*, 2019.
- [17] J. Wang, X. Li, R. Ruiz, J. Yang, and D. Chu, "Energy utilization task scheduling for MapReduce in heterogeneous clusters," *IEEE Transactions on Services Computing*, 2020.
- [18] J. Ekanayake, H. Li, B. Zhang et al., "Twister: a runtime for iterative MapReduce," in *Proceedings of the 19th ACM International Symposium on High Performance Distributed Computing*, pp. 810–818, Chicago, IL, USA, June 2010.
- [19] J. Ekanayake and S. Pallickara, "MapReduce for data intensive scientific analyses," in *Proceedings of the 2008 IEEE Fourth International Conference on eScience*, pp. 277–284, IEEE, Indianapolis, IN, USA, December 2008.
- [20] M. Babar, F. Arif, M. A. Jan, Z. Tan, and F. Khan, "Urban data management system: towards big data analytics for internet of things based smart urban environment using customized Hadoop," *Future Generation Computer Systems*, vol. 96, pp. 398–409, 2019.
- [21] J. Liu, Q. Liu, L. Zhang, S. Su, and Y. Liu, "Enabling massive XML-based biological data management in HBase," *IEEE/ACM Transactions on Computational Biology and Bioinformatics*, 2019.
- [22] Y. Li, A. Eldawy, J. Xue, N. Knorozova, M. F. Mokbel, and R. Janardan, "Scalable computational geometry in MapReduce," *The VLDB Journal*, vol. 28, no. 4, pp. 523–548, 2019.
- [23] F. Li, J. Chen, and Z. Wang, "Wireless MapReduce distributed computing," *IEEE Transactions on Information Theory*, vol. 65, no. 10, pp. 6101–6114, 2019.
- [24] J. Cui, Z. An, Y. Guo, and S. Zhou, "Efficient nearest neighbor query based on extended B⁺-tree in high-dimensional space," *Pattern Recognition Letters*, vol. 31, no. 12, pp. 1740–1748, 2010.
- [25] C. Xia, H. Lu, B. C. Ooi, and J. Hu, "Gorder," *Proceedings 2004 VLDB Conference*, vol. 30, pp. 756–767, 2004.
- [26] D. Amagata, T. Hara, and C. Xiao, "Dynamic set kNN self-join," in *Proceedings of the IEEE 35th International Conference on Data Engineering (ICDE)*, pp. 818–829, IEEE, Macao, China, April 2019.
- [27] W. Zhao, H. Ma, and Q. He, "Parallel K-means clustering based on MapReduce," in *Proceedings of the IEEE International Conference on Cloud Computing*, Springer, Beijing, China, pp. 674–679, October 2009.
- [28] J. Santos, T. Syed, M. C. Naldi, R. J. G. B. Campello, and J. Sander, "Hierarchical density-based clustering using MapReduce," *IEEE Transactions on Big Data*, 2019.

- [29] J. Rosen, N. Polyzotis, V. Borkar et al., "Iterative MapReduce for large scale machine learning," 2013, <https://arxiv.org/abs/1303.3517>.
- [30] C. Zhang, F. Li, and J. Jestes, "Efficient parallel kNN joins for large data in MapReduce," in *Proceedings of the 15th International Conference on Extending Database Technology (EDBT)*, pp. 38–49, Berlin, Germany, March 2012.
- [31] P. Moutafis, G. Mavrommatis, M. Vassilakopoulos, and S. Sioutas, "Efficient processing of all- k -nearest-neighbor queries in the MapReduce programming framework," *Data & Knowledge Engineering*, vol. 121, pp. 42–70, 2019.
- [32] J. Yu, Z. Zhang, and M. Sarwat, "Spatial data management in Apache spark: the geospatial perspective and beyond," *Geoinformatica*, vol. 23, no. 1, pp. 37–78, 2019.
- [33] C. Ji, T. Dong, Y. Li et al., "Inverted grid-based KNN query processing with mapreduce," in *Proceedings of the 2012 Seventh ChinaGrid Annual Conference*, IEEE, Beijing, China, September 2012.
- [34] G. Song, J. Rochas, L. E. Beze, F. Huet, F. Magoules et al., "K nearest neighbour joins for big data on mapreduce: a theoretical and experimental analysis," *IEEE Transactions on Knowledge and Data Engineering*, vol. 28, no. 9, pp. 2376–2392, 2016.
- [35] C. Bohler, R. Klein, and C.-H. Liu, "An efficient randomized algorithm for higher-order abstract Voronoi diagrams," *Algorithmica*, vol. 81, no. 6, pp. 2317–2345, 2019.
- [36] C. Song, J. Cha, M. Lee, and D.-S. Kim, "Dynamic Voronoi diagram for moving disks," *IEEE Transactions on Visualization and Computer Graphics*, 2019.
- [37] C.-H. Liu, "A nearly optimal algorithm for the geodesic Voronoi diagram of points in a simple polygon," *Algorithmica*, vol. 82, no. 4, pp. 915–937, 2020.
- [38] F. García-García, A. Corral, L. Iribarne et al., "Improving distance-join query processing with voronoi-diagram based partitioning in SpatialHadoop," *Future Generation Computer Systems*, vol. 111, pp. 723–740, 2019.
- [39] W. Huang, K. Sun, J. Qi, and J. Ning, "Optimal allocation of dynamic var sources using the Voronoi diagram method integrating linear programming," *IEEE Transactions on Power Systems*, vol. 32, no. 6, pp. 4644–4655, 2017.
- [40] F. García-García, A. Corral, L. Iribarne, and M. Vassilakopoulos, "Voronoi-diagram based partitioning for distance join query processing in Spatialhadoop," in *Proceedings of the MEDI Conference*, pp. 251–267, Marrakesh, Morocco, October 2018.
- [41] A. Verma, B. Cho, N. Zea, I. Gupta, and R. H. Campbell, "Breaking the MapReduce stage barrier," *Cluster Computing*, vol. 16, no. 1, pp. 191–206, 2013.
- [42] L. Fan, H. Li, and C. Li, "The improvement and implementation of distributed item-based collaborative filtering algorithm on hadoop," in *Proceedings of the 34th Chinese Control Conference*, pp. 9078–9083, Hangzhou, China, July 2015.
- [43] A. K. Kamn and K. Chitharanjan, "A review on hadoop—HDFS infrastructure extensions," in *Proceedings of the 2013 IEEE Conference on Information & Communication Technologies (ICT)*, pp. 132–137, IEEE, Tamil Nadu, India, April 2013.
- [44] K.-H. Lee, Y.-J. Lee, H. Choi, Y. D. Chung, and B. Moon, "Parallel data processing with MapReduce," *ACM SIGMOD Record*, vol. 40, no. 4, pp. 11–20, 2012.

Research Article

On-Chip Embedded Debugging System Based on Leach Algorithm Parameter on Detection of Wireless Sensor Networks

Wenguang Song ¹, Haiyu Chen ², Qiujuan Zhang,¹ Bingxin Zhang,¹ Hao Wang,¹
and Hao Xu¹

¹School of Computer Science, Yangtze University, Jingzhou 434023, Hubei, China

²Department of Computer, Zhaoqing Medical College, Zhaoqing 526020, Guangdong, China

Correspondence should be addressed to Haiyu Chen; 87626764@qq.com

Received 26 March 2020; Revised 16 June 2020; Accepted 22 July 2020; Published 7 September 2020

Guest Editor: Liangtian Wan

Copyright © 2020 Wenguang Song et al. This is an open access article distributed under the Creative Commons Attribution License, which permits unrestricted use, distribution, and reproduction in any medium, provided the original work is properly cited.

Leach (low energy adaptive clustering hierarchy) algorithm is a self-clustering topology algorithm. Its execution process is cyclical. Each cycle is divided into two phases: cluster building phase and stable data communication phase. In the stage of cluster building, the adjacent nodes cluster dynamically and randomly generate cluster heads. In the data communication phase, the nodes in the cluster send the data to the cluster head, and the cluster head performs data fusion and sends the results to the aggregation node. Because the cluster head needs to complete data fusion, communication with the convergence node and other works, the energy consumption is large. Leach algorithm can ensure that each node acts as cluster head with equal probability, so that the nodes in the network consume energy relatively evenly. The basic idea of Leach algorithm is to randomly select cluster head nodes in a circular way. It evenly distributes the energy load of the whole network to each sensor node in the network. It can reduce network energy consumption and improve network life cycle. Leach repeatedly performs cluster refactoring during its operation. This paper studies the parameter detection of wireless sensor network based on Leach algorithm on the on-chip embedded debugging system. Because the classical low-power adaptive clustering layered protocol (Leach) has the problem of energy imbalance and short node life cycle, this paper uses embedded debugging technology based on Leach algorithm and the residual energy and position of nodes in wireless sensor networks were tested for research. This Leach algorithm uses the concept of wheel. Each round consists of two phases: initialization and stabilization. In the initialization stage, each node generates a random number between 0 and 1. If the random number generated by a node is less than the set threshold $T(n)$, the node publishes a message that it is a cluster head. Through the research on the parameter detection, the simulation results show that the research in this paper has good feasibility and rationality.

1. Research Background

Since entering the 21st century, the development of high and new technology is changing with each passing day. The development and fusion of wireless communication technology, sensor technology, embedded computing technology, and distributed information processing technology promote the generation and development of modern wireless sensor networks. Wireless sensor network is composed of wireless sensor network nodes distributed randomly in a monitoring area, which is used to monitor specific environmental information in a certain area. As a

new technology in fields of communication, automation, and computer, wireless sensor network has the advantages of high monitoring accuracy, good fault tolerance, and wide coverage. It has been widely used in military defense, urban management, environmental monitoring, and hazardous sites. The field of remote control has been widely studied and applied. As the product of various high-tech integrations, wireless sensor network has become an active research branch in computer science and network communication science, which has attracted great attention from academia and industry. It is thought to have a major impact on the 21st century. One of these technologies is also one of the key

research areas during the eleventh five-year plan period [1, 2].

Research into wireless sensor networks began in the late 1990s with the Defense Advanced Research Projects Agency (DAIRPA) funding the Network Embedded Software Technology (NEST) project. The University of California, Berkeley, has developed a wireless sensor network development system called Mote. Since then, DARPA has spent tens of millions of dollars a year on wireless sensor network technology. In early August 2002, the national science foundation (NSF), the defense advanced research projects agency (DARPA), NASA, and other 12 main research institutes at the University of California, Berkeley, jointly organized the “national seminar” on the future sensor system [3] and discussed the future sensor system and its development direction in the engineering application. The meeting discussed the realization of wireless sensor networks and the research of sensor data transmission, analysis, and decision making technologies, which are the same as the new sensor technologies based on nanotechnology and micromachinery, and represent the frontier direction of future sensor research and battlefield information perception. Structural monitoring, homeland security, the war on terrorism, and other applied fields have extremely important research significance.

In the following years, several laboratories at the University of California, Berkeley, continued to conduct in-depth research on wireless sensor networks and made some pioneering studies on wireless sensor networks from different perspectives. Many other American universities and research institutions have done a lot of work and made great progress in wireless sensor networks, for example, CENS (Embedded Network Sensor Center), WINS (wireless integrated network sensor), and NES (Network and Embedded Systems Laboratory)[4]. The Massachusetts Institute of Technology (MIT) is working on low-power wireless sensor networks with DARPA support. SPIN Sensor Protocols for Information via Negotiation is a protocol of MIT [5]. Auburn University has also received DARPA support for extensive research into self-organizing sensor networks. The Computer Systems Research Laboratory of Binghamton University has done a lot of research work in the design of mobile self-organizing network protocol and sensor network system application layer [6]. The Mobile Computing Laboratory at Cleveland State University combines wireless sensor network technology with IP-based mobile networks and ad hoc networks [7]. Meanwhile, American companies such as Intel, Crossbow, Freescale, and Ember have also participated in the research of wireless sensor networks. Some European companies like Philips, Siemens, Ericsson, and Chipcon [8] have studied wireless sensor networks. In March 2004, Japan’s Ministry of Internal Affairs and Communications held a seminar on “ubiquitous wireless sensor networks” [9], which mainly discussed the research and development, standardization, social cognition, and promotion policies of wireless sensor networks. NEC, OKI, and other companies have also launched relevant products and conducted some application tests. In China, the research on wireless sensor networks is mainly led by some

universities and research institutions. Zhejiang University has established the wireless sensor network test group, which is specialized in the hardware implementation of wireless sensor network.

2. Leach Principle

2.1. The Algorithm of Leach. Leach algorithm is a low-power adaptive clustering routing algorithm. The algorithm is executed periodically. Each cycle is defined as a “round,” and each round is divided into two phases: the negotiation phase and the stabilization phase. The negotiation stage is also the formation stage of the cluster, mainly completing the selection of cluster heads and routing of nodes in the cluster, as well as the initialization of the algorithm. After selecting the node as the cluster head, it first sends a broadcast with its OWN ID and other information. The other nodes will receive a large number of broadcasts from different cluster heads. If the cluster head node receives the broadcast information of other cluster head nodes, it will be discarded directly. If the cluster node receives the broadcast information, the judgment signal strength, sure you want to join the cluster. It replies to the corresponding cluster head request to join the packets, after joining cluster nodes in the cluster. The members of the cluster head nodes are in the cluster maintenance information table. The communication time slot for members of the node distribution is in order to avoid confusion in the cluster communication. A time slot is one frame with the same length of time. The stabilization phase is the data communication phase of the cluster. Member nodes in the cluster will collect data and send it to the cluster head node in the way of polling according to the time slot allocated by the cluster head node. The cluster head node will fuse the received data first and then send it to the aggregation node. The longer the stability period is, the more effective the algorithm is. After the data is sent, a new start is made. The implementation is as follows.

The selection of cluster heads in Leach algorithm is random. There are two main factors that determine the cluster head: the number of rounds of the current algorithm and the number of cluster head nodes and the total number of nodes. There are no nodes that play a dominant role in the whole cluster process. Each node is identified by an algorithm, identified by itself, and added to the corresponding cluster. At the beginning of cluster establishment, all sensor nodes in the network are randomly generated into a random number between [0,1]. If the random number is less than threshold $T(n)$, it is compared with threshold $T(n)$, and then the sensor node corresponding to the random number is selected as the cluster head of the round. The broadcast message is then sent to inform other sensor nodes that if the random number is greater than the threshold $T(n)$, it will not be selected as the cluster head. If the selected cluster head node has been selected as the cluster head, the value of $T(n)$ becomes 0, so as to avoid the same node continuously acting as the cluster head, resulting in excessive energy consumption of the node. The formula for calculating threshold $T(n)$ can be expressed as

$$T(n) = \begin{cases} \frac{P}{1 - p * (r \bmod (1/P))}, & \text{if } n \in G, \\ 0, & n \notin G, \end{cases} \quad (1)$$

where P is the percentage of cluster head in all nodes, r is the number of election rounds, $R \bmod (1/P)$ represents the number of nodes selected for cluster head in this round cycle, and G is not the node set selected for cluster head in this round cycle.

As can be seen from the above equation, as the algorithm cycle continues to advance, the number of nodes assigned to the cluster head will increase; that is, the value of $R \bmod (1/P)$ will continue to increase, and the value of $T(n)$ will also increase. Then, the probability of nodes not being chosen as cluster heads will increase. When only one node is not selected as cluster head, $T(n) = 1$; in addition, when $r = 0$ and $r = 1/p$, $T(n)$ has the same value. When $r = 1$ and $r = 1/P + 1$, the result of $T(n)$ is the same. Then, after the algorithm executes a $1/P$ loop, the sensor nodes in the network return to the situation where cluster heads are selected with equal probability, such as repeating the loop. The Leach algorithm allows all nodes in the network to have a cluster head for a period of $1/P$ and only one chance to get the cluster head. After the $1/P$ loop, there is an opportunity to reselect the cluster heads. Therefore, $T(n)$ is also the average probability that a node that does not act as a cluster head is selected in the RTH round.

Suppose that there are altogether N nodes in the sensor network and each time k cluster heads are selected, $P = (N/K)$. The probability of nodes becoming cluster heads in $r + 1$ th cycle is expressed by $T(t)$, so the probability of cluster heads is in $r + 1$ th cycle.

$$E = \sum_{t=1}^N T(t) \times 1 = k. \quad (2)$$

After r rounds, the number of nodes in the current $1/P$ round that have not yet become cluster head is $N - k \times (r \bmod (N/k))$.

If no node is selected as cluster head after r round, the above formula can be obtained. The average probability of $r + 1$ th round node becoming cluster head is $(p / (1 - p * (r \bmod (1/p))))$.

The average probability of $p = (N/K)$ being substituted into the above equation is $(k / (N - K \times (r \bmod (N/k))))$.

Based on the above derivation, the following formula can be obtained:

$$\begin{aligned} E &= \sum_{t=1}^N T(t) \times 1 \\ &= (N - k \times (r \bmod (N/k))) \frac{k}{(N - k \times r \bmod (N/K))} = k. \end{aligned} \quad (3)$$

When a node is selected as a cluster head, a notification message is sent informing the other nodes that they are new cluster heads. The noncluster head node selects the cluster to

be added according to its distance from the cluster head and notifies the cluster head. When the cluster header receives all connection information, it generates a TDMA timing message and notifies all nodes in the cluster. In order to avoid signal interference from nearby clusters, the cluster head can determine the CDMA code used by all nodes in the cluster. The CURRENT phase of the CDMA code is sent with the TDMA timing. When the nodes in the cluster receive the message, they send data in their respective time slots. After a period of data transmission, the cluster head node collects the data sent by the nodes in the cluster, runs the data fusion algorithm to process the data, and sends the results directly to the sink node.

The stabilization phase is the data communication phase. The member nodes communicate according to the time slot allocated by the cluster head node. At the same time, other clusters are also performing intracluster routing. The neighboring nodes of different clusters can then generate cluster crosstalk at the same frequency to reduce crosstalk between clusters. The influence of cluster routing is based on direct sequence spread spectrum (DSSS) mechanism. In this way, the nodes in the cluster treat the non-self-group signal as noise and shield it, thus effectively avoiding the occurrence of signals between adjacent group nodes. Crosstalk: cluster heads communicate with sink nodes according to the CSMA method, and all cluster heads use the same spread spectrum code. Therefore, in the process of establishing a data connection between the cluster head and the sink node, it is first necessary to monitor whether the channel is occupied. If so, the cluster head node that needs to communicate needs to queue until spread spectrum code is not used and can preempt the channel to obtain data communication. Otherwise, the cluster header can use channels to communicate directly with the Sink node.

2.2. Key Technologies of Wireless Sensor Network. The premise of topology control of wireless sensor network is to eliminate unnecessary communication lines between nodes by controlling power and selecting corresponding backbone nodes under the condition of network coverage and connectivity and finally form efficient topology structure of data forwarding network. Excellent network topology control algorithm can effectively improve the efficiency of routing protocol and MAC protocol, provide good support for data fusion, time synchronization, and target positioning, save the energy of nodes, and improve the network life cycle. Topology control is very important for wireless sensor networks with limited energy.

The task realization of wireless sensor network protocol makes each node form a multihop data transmission network. Under the premise of effectively utilizing network energy and improving network life cycle, network bandwidth is effectively utilized to ensure service quality. At present, network layer protocol and data link layer protocol are the focus of research.

Data fusion technology is a combination of multiple data processing processes to make data processing more efficient and more humane process. However, because sensor nodes

are prone to failure, the sensor network still needs data fusion technology to process multiple data comprehensively to improve the accuracy of information. According to the different information content, data fusion can be divided into two types: lossless fusion and lossy fusion. Lossless fusion means to save all the details and remove the redundant information. Lossy integration is when you save storage space and energy by ignoring details or reducing data quality. Data fusion technology can be combined with multiple protocol layers of wireless sensor networks. At present, data fusion technology has been widely used in target tracking and automatic recognition. In the design of wireless sensor networks, targeted data fusion methods are often the most beneficial in application design.

Time synchronization is the key mechanism of wireless sensor networks. When a network system performs some time-sensitive tasks or adopts the time-based MAC protocol, it needs to synchronize the nodes' clocks. Clock synchronization lightweight synchronization and sensor network time synchronization protocol based on receiver and receiver are three basic synchronization mechanisms. The current location includes the location of the node itself and the location of the external target. Positioning accuracy directly affects the effectiveness of data acquisition. Due to the limitations of sensor nodes themselves, the localization mechanism must satisfy the robustness, self-organization, and energy efficiency of network nodes. Generally, nodes are divided into beacon nodes and unknown nodes according to whether the node is determined by its position. Beacon nodes can carry certain positioning equipment to obtain their own accurate position information. Unknown nodes take beacon nodes as reference points and use algorithms such as triangulation, triangulation, and maximum likelihood estimation to determine node position.

2.3. Embedded Debugging Technology. With the continuous improvement of chip integration and the increasingly powerful functions, the requirements for embedded software development are higher and higher, and the embedded debugging technology is also developing constantly. In the development of embedded debugging system, many debugging techniques are developed. There are significant differences between the different debugging techniques and the implementation principles that depend on them. This paper mainly analyzes and introduces the commonly used debugging techniques on chip. With the popularity of SOC technology, on-chip debugging technology began to appear in embedded systems. On-chip debugging techniques embed control modules in the processor. When a trigger condition is met, the processor enters the specified state [10]. In this state, debugging software running on the host can access various resources (registers, memory, and so on) and execute instructions through a specific communication interface outside the processor (the debug support module port). The basic idea of on-chip debugging is to add additional hardware debugging modules inside the processor. The debug software controls the operation and resource access of the processor through the debug module. There are many

different implementations of on-chip debugging techniques. Currently, BDM (background debugging mode) and JTAG (joint test action group) are commonly used on-chip debugging techniques [11]. For users, the two technologies provide similar debugging capabilities, but there are significant differences in implementation principles and debugging standards. Their debugging criteria are described below.

MOTOROLA first recognized the development trend of on-chip debugging technology and implemented the BDM (background debugging mode) debugging interface for the first time on the 68300 series processor. Later, the company applied BDM debugging in a series of processors designed for PowerPC and ColdFire [12].

Taking ColdFire as an example, the implementation mechanism of BDM debugging function is briefly analyzed. ColdFire has many levels of internal buses. The debug module is embedded in the processor and can access the internal bus and CPU kernel information connected to the kernel and on-chip memory. Access to the internal bus allows the debug module to obtain address space and data information in the internal bus that cannot be accessed by external modules. The ColdFire debugging system supports three functions: BDM, real-time debugging, and real-time tracking. The basic principle of BDM (background debugging mode) is that when the processor stops running, the debugging software running on the host machine sends various instructions to the target system through the serial interface of the debugging module to access registers and storage. BDM mainly consists of two control registers: CSR and TDR [13]. The Configuration Status Register (CSR) is used to configure the operations of the processor and on-chip storage and also reflects the state of the processor breakpoint logic. The TDR (trigger definition register) is used to configure and control the operations of the hardware breakpoint logic in the debug module. ABHR (address breakpoint low register) and ABLR (address breakpoint high register) are valid breakpoint address ranges used to define. PBR (program count breakpoint register) and PBMR (program count breakpoint mask register) represent the PC breakpoint register and its mask. The DBR (data breakpoint register) and DBMR (data breakpoint mask register) represent the data breakpoint register and its mask [14].

JTAG (Joint Test Action Group) was established in 1985 and was originally developed by PCB manufacturer (printed circuit board) and IC (integrated circuit) test standards. In 1987, the organization proposed a new testability design method: boundary scan test technology. In 1988, IEEE (Institute of Electrical and Electronics Engineers) and JTAG agreed to jointly develop a boundary scan test architecture. JTAG was approved by IEEE as 1149.1 standard in 1990 and is also known as JTAG boundary scanning standard [15]. The standard defines the boundary scan structure and interface of the standard. At present, JTAG interface has become the standard debugging interface widely used in the world, and most existing microprocessors have JTAG interface. IC designers such as Intel, ARM, MIPS, and TI have implemented JTAG debugging interface.

The JTAG standard provides two main functions:

- (1) It is used for chip electrical characteristic test to detect whether there is a problem with the chip
- (2) For debugging, debugging is the program running on the chip

The JTAG boundary scan standard allows users to test and debug the hardware circuit with the JTAG interface chip. The working mode of the processor based on JTAG is generally divided into normal mode and debug mode. In debugging mode, the debugger stops execution, and the upper debugging software completes various debugging functions by sending debugging commands to the debugging module interface. Examples include setting breakpoints and stepping. When the processor is in normal mode, the processor is running or stopping.

A protocol conversion unit (either a hardware unit or a software implementation) is required between the target and the host. This unit converts the debugger commands into commands that the processor debug interface recognizes. When using JTAG debugging, the debugging interface is provided to the user through debugging software, the commands input by the user are received, and the execution results are given after processing. The JTAG debugger is built into the debugging module of the target chip. Debugging can be regarded as a means to access the target. JTAG debugging has the advantages of small dependency, no change in program operation, stability, and reliability. The debugging system in this paper adopts JTAG debugging standard.

3. Experiment on the Computer Simulation Software

3.1. Data Source. In order to better evaluate the performance of this paper in the field of wireless sensor, this paper conducts experiments on wireless sensor networks based on the classical Leach algorithm and research method. In order to make the experimental data and evaluation results more accurate and objective, the size of the wireless sensor network model was set as $100\text{ M} \times 100\text{ M}$, and 30 nodes were distributed in the region. These nodes are geographically random, randomly generated. The experiment was repeated 50 times and then averaged over all the results to get the final data.

3.2. Experimental Evaluation Criteria. Due to the limited energy of wireless sensor network nodes, the energy of nodes directly affects the life cycle of nodes. When the performance of the judgment research method is getting higher and higher, and it is more and more in line with the requirements of the network, there are several hard standards to judge different research methods.

3.2.1. Time Length of Node Failure. This paper analyzes the lifetime of network from three aspects: initial dead node, half-dead node, and final dead node.

3.2.2. Node Energy Consumption. This paper will record the total energy consumption of nodes in the network in real time and judge whether the corresponding research method is suitable for the network.

3.2.3. Energy Efficiency. When a node in the network transmits data information, we change the packet size and observe the energy utilization rate; the higher the utilization rate is, the more balanced the energy load will be.

3.2.4. Remaining Nodes. At run time, different algorithms have different number of remaining nodes at the same time. The more the nodes there are the less energy the network consumes.

3.2.5. Information Received by the Base Station. Obviously, the more information the base station receives in the end, the more beneficial it is to the work of the observers, thus improving the accuracy of the data.

3.3. Experimental Parameters. The specific parameters of the experiment are shown in Table 1.

3.4. Experimental Data Results. Firstly, the wireless sensor network method based on the classical Leach algorithm is simulated and the data obtained is recorded. Then, on the basis of Leach algorithm, the residual energy and position parameters of nodes are added to optimize the distribution of nodes, and the strategy that the greater the residual energy of nodes, the greater the probability of cluster head selection is adopted. The experimental results are based on the wireless sensor network parameters detection of the embedded debugging system on the chip. The comparison of the number of surviving nodes between the wireless sensor network using the classical Leach algorithm and the wireless sensor network using the research method is shown in Figure 1 with one computer simulation software. The comparison of the remaining energy of the nodes is shown in Figure 2.

After sorting out the experimental data, the node death of wireless sensor network using the classical Leach algorithm and the research method in this paper is shown in Table 2, respectively, and the node energy consumption is shown in Table 3, where the data in the table is the number of cycles.

3.5. Analysis of Experimental Data. Figure 1 shows the relationship between the number of viable wireless sensor network nodes and the number of rounds. When simulating the Leach algorithm, the first death node appears at 580. However, when the first node is present, the method is simulated at 915. The occurrence time of the first dead node is nearly twice longer than that of the classical Leach algorithm. In the comparison of 50% network node death time between the two methods, Leach algorithm takes 1098, but this method extends the time by 53.2% to 1682. In the

TABLE 1: Experimental parameter settings.

Parameter name	Unit	Set parameter value
Number of nodes	\	30
WSN area size	m^2	100 * 100
Transmission data length	k	4000
Energy required for power amplification	$(p^j / (bit.m^4))$	10
Initial energy of the node	J	0.5

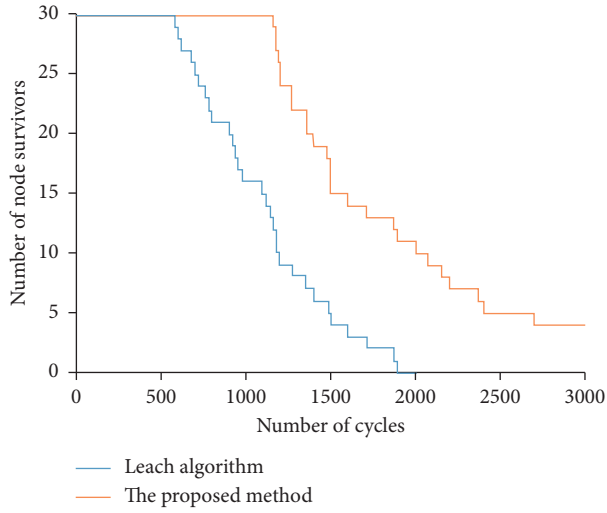


FIGURE 1: Comparison of the number of surviving nodes.

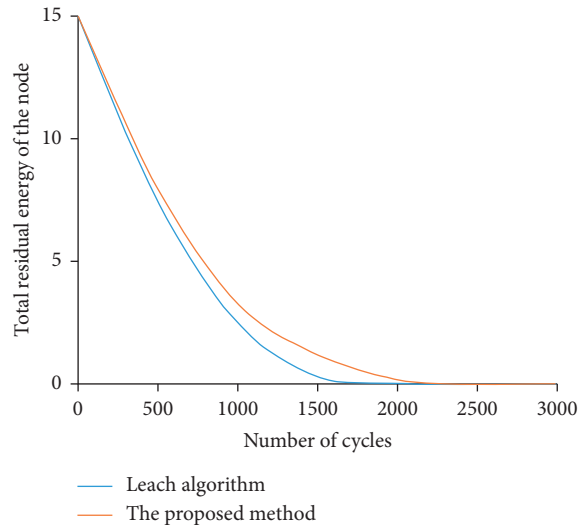


FIGURE 2: Node residual energy comparison chart.

TABLE 2: Comparison of node deaths.

Experiment	First node death	15th node death	15th node death
Leach algorithm	580	1098	1897
Method of this paper	915	1682	2678

TABLE 3: Comparison of node energy consumption.

Experiment	Consumption 33%	Consumption 66%	Exhaust
Leach algorithm	348	705	1896
Method of this paper	382	782	2533

comparison of network lifetime, Leach algorithm's time was 1897. However, the method adopted in this paper takes 2678 times, and the failure time of the whole network is longer than the original. As can be seen from the comparison of simulation results in Figure 1, under the same simulation conditions, the research method has a longer network life cycle than the single Leach algorithm. Figure 2 depicts the relationship between the total residual energy consumption of network nodes and the number of rounds. The life cycle of the whole network is related to the energy consumption of each node. If a node consumes a lot of energy, it will soon fail. If the energy consumption of each node is similar, the network life cycle will be prolonged. The data in Figure 2 demonstrates this. In this paper, the method of residual current energy and maximum current energy ratio as parameters is more reasonable. Parameters are distributed between 0 and 1 and do not decrease with energy consumption.

The node death and residual energy consumption of wireless sensor network can be seen. In this paper, we improve the location of the aggregation nodes and find the nodes with the minimum sum of squares of other nodes in the distribution region. The center of these points acts as a sink node. The positioning method is reasonable. In the improvement of node energy parameters, the higher the probability of nodes is, the larger the residual energy becoming cluster head nodes is. The parameters of each election are more evenly distributed and are always less than or equal to 1. According to the simulation data in Tables 2 and 3, the superiority of the research method is verified, the node mortality is reduced, and the network life is extended.

4. Research Conclusions

Wireless sensor network (WSN) is a new technology, which has broad application prospects in military, environmental, medical, and civil fields. Wireless sensor networks have the characteristics of limited communication capacity, limited node energy, and limited computing capacity. There are many nodes, wide range of distribution, and dynamic network. Therefore, the research on wireless sensor network is of great significance, and the research goal is to improve the performance of wireless sensor network. As wireless routing algorithm is an important topic in wireless sensor network research, its performance directly affects the operation efficiency of the whole network and relates to the lifetime of wireless sensor network. Therefore, this paper first analyzes the Leach algorithm, adding residual energy to the current maximum energy node energy ratio parameter of the classical Leach algorithm and selecting cluster head reasonably. Secondly, the embedded on-chip debugging

technology is used to detect the parameters of wireless sensor network based on Leach algorithm. Finally, the classical Leach algorithm and research method are used to carry out simulation experiments, and the feasibility and effectiveness of the method are verified. The results show that this method can balance the overall energy consumption of network nodes and improve the lifetime of wireless sensor networks.

Data Availability

The data used to support the findings of this study are available from the corresponding author upon request.

Conflicts of Interest

The authors declare that they have no conflicts of interest.

Acknowledgments

This work was supported by Xinjiang Uygur Autonomous Region Innovation Environment (talent, base) Construction Foundation (Xinjiang NSFC Program Foundation 2020D01A132): Research and Implementation of Horizontal Well Inversion Optimization Interpretation Method, Jingzhou Science Technology Foundation (2019EC61-06), Hubei Science and Technology Demonstration Foundation (2019ZYD016), Zhaoqing Science and Technology Innovation Guidance Project (201904030401), and Vertical Research Planning Project of Cloud Computing and Big Data Professional Committee of Higher Vocational College of Guangdong Institute of Higher Education in 2019 (GDJSKT19-18).

References

- [1] J. Li, X. Zhang, R. Cao, and M. Zhou, "Reduced-dimension MUSIC for angle and array gain-phase error estimation in bistatic MIMO radar," *IEEE Communications Letters*, vol. 17, no. 3, pp. 443–446, 2013.
- [2] L. Wan, Y. Sun, I. Lee, W. Zhao, and F. Xia, "Industrial pollution areas detection and location via satellite-based IIOT," *IEEE Transactions on Industrial Informatics*, vol. 19, p. 1, 2020.
- [3] L. Wan, L. Sun, X. Kong, Y. Yuan, K. Sun, and F. Xia, "Task-driven resource assignment in mobile edge computing exploiting evolutionary computation," *IEEE Wireless Communications*, vol. 26, no. 6, pp. 94–101, 2019.
- [4] F. Wen, X. Xiong, and Z. Zhang, "Angle and mutual coupling estimation in bistatic MIMO radar based on PARAFAC decomposition," *Digital Signal Processing*, vol. 65, pp. 1–10, 2017.
- [5] F. Wen, X. Xiong, J. Su, and Z. Zhang, "Angle estimation for bistatic MIMO radar in the presence of spatial colored noise," *Signal Processing*, vol. 134, pp. 261–267, 2017.
- [6] T. Liu, F. Wen, L. Zhang, and K. Wang, "Off-grid DOA estimation for colocated MIMO radar via reduced-complexity sparse bayesian learning," *IEEE Access*, vol. 7, pp. 99907–99916, 2019.
- [7] F. Wen and J. Shi, "Fast direction finding for bistatic EMVS-MIMO radar without pairing," *Signal Processing*, vol. 173, 2020.
- [8] D. Meng, X. Wang, M. Huang, L. Wan, and B. Zhang, "Robust weighted subspace fitting for DOA estimation via block sparse recovery," *IEEE Communications Letters*, vol. 24, no. 3, pp. 563–567, 2020.
- [9] N. Miceli, A. Marino, A. Koroğlu et al., "Comparative study of the phenolic profile, antioxidant and antimicrobial activities of leaf extracts of five Juniperus L. (Cupressaceae) taxa growing in Turkey," *Natural Product Research*, vol. 34, no. 11, 2020.
- [10] Hydrometallurgy, "Report summarizes hydrometallurgy study findings from sichuan university (recovery of vanadium from leach solutions of vanadium slag using solvent extraction with N235)," *Mining & Minerals*, 2020.
- [11] Columbia gas transmission, "LLC; notice of availability of the environmental assessment for the proposed leach xpress project amendment," *The Federal Register/Find*, vol. 85, no. 93, 2020.
- [12] R. M. Dhanunjaya, M. Arunabh, H. Verma, K. Singh Kamalesh, and M. Tilak Raj, "Study to enhance cementation of impurities from zinc leach liquor by modifying the shape and size of zinc dust," *Hydrometallurgy*, vol. 195, 2020.
- [13] Metals Research, "New metals research study results reported from hokkaido university (recovery of lead and zinc from zinc plant leach residues by concurrent dissolution-cementation using zero-valent aluminum in chloride medium)," *Mining & Minerals*, 2020.
- [14] P. Guo, S. Wang, L. Zhang, L. Xu, and W. Sun, "Optimization of the synergy between reduction leaching of manganese anode slime and oxidation pretreatment of refractory gold ore by response surface methodology," *Chemical Papers*, vol. 74, no. 233–235, 2020.
- [15] Chemistry, "New chemistry study findings have been reported by investigators at nuclear materials authority [recovery of uranium(VI) from sulfate leach liquor using modified duo-lite]," *Journal of Technology & Science*, vol. 23, pp. 15–27, 2020.

Research Article

Study on Extraction Methods for Different Components in a Carbonate Digital Core

Xiaoling Xiao,¹ Jiarui Zhang,² Xinyu Li,³ Jing Zhang,³ and Xiang Zhang⁴ 

¹School of Computer Science, Yangtze University, Jingzhou 434023, China

²School of Geosciences, Yangtze University, Wuhan 430100, China

³SiChuan Basin Research Center, Research Institute of Petroleum Exploration and Development, PetroChina, Beijing 100083, China

⁴Key Laboratory of Exploration Technologies for Oil and Gas Resources, Yangtze University, Wuhan 430100, China

Correspondence should be addressed to Xiang Zhang; zhangxiang_wh@163.com

Received 19 July 2020; Revised 11 August 2020; Accepted 17 August 2020; Published 7 September 2020

Guest Editor: Jianfeng Li

Copyright © 2020 Xiaoling Xiao et al. This is an open access article distributed under the Creative Commons Attribution License, which permits unrestricted use, distribution, and reproduction in any medium, provided the original work is properly cited.

It is difficult to carry out petrophysical experiments because of the serious damage caused to cores in the development of fractures and pores in carbonate reservoirs. The development of a three-dimensional digital core in carbonate reservoirs has become a hot topic in rock physics research. Compared with the three-dimensional digital core, including basic rock skeletons and pores in sandstone reservoirs, carbonate reservoirs also include secondary structures such as microfractures. The carbonate contains different components, and extracting these components is a very difficult problem. The resolution on the electrical image log image is high, which can clearly reflect the macrocomponents in various reservoirs. There are some blank areas between electrodes on the electrical image log, which affects the extraction of components in a three-dimensional digital core. Aiming at the serious heterogeneities in the carbonate reservoirs and affecting image inpainting on the electrical image log image, a new method of image inpainting based on a combination of multipoint geostatistics and an interpolation method is put forward. The experimental results show that this method generates faster and better full-bore images than other methods. Due to the multipeak histogram, the maximum interclass variance in the two times method is proposed to extract macrocomponents such as basic rock skeletons, pores, and connected parts. The microfractures can be extracted from the CT scanned images by using image segmentation from the combination of the watershed and OTSU methods. The experimental results prove that using extraction methods for different components enables better results to be obtained.

1. Introduction

Carbonate and other complex reservoirs have become a hot topic in the study of rock physics. It is difficult to carry out petrophysical experiments because of the serious damage caused to cores during development of fractures and pores in carbonate reservoirs. Rock physics numerical simulations play a crucial role. It is necessary to study the three-dimensional digital core method in terms of carbonate reservoirs [1].

Compared with a three-dimensional digital core in sandstone, only two parts of basic rock skeletons and pores are included. In addition to basic rock skeletons and pores of

a digital core in sandstone, the carbonate reservoirs also have secondary structures such as microfractures. The carbonate contains different components. Extracting these components is a very difficult problem [2–7].

Fractures can improve reservoir permeability. The accurate identification and evaluation of fractures are among the important contents in exploration and development [8]. Well logging techniques that are currently used for fracture identification include resistivity logging, sonic logging, radiological logging, dip logging, density logging, compensated neutron logging and electrical image log, and acoustic image log [9–13]. These techniques have limitations when using various conventional well logs to directly identify

fractures, so some methods for identifying fractures by conventional well logs have been proposed [14–19]. For example, the differences between the real resistivity and measured resistivity obtained from the apparent acoustic porosity using rock-electricity by Yang Xue are used to identify fractures in the formation [20]. At present, the majority of hole recognition in carbonate reservoirs is processed based on the OTSU (maximum between-class variance) segmentation algorithm. For example, Jiang has established a chart of fracture-hole recognition based on resistivity response [21]. However, this method does not work well when there are multi-peaks in the histogram of an electrical image log image. Li and others automatically identify the holes using the threshold segmentation algorithm with the contour tracking algorithm after hollowing out the interior point [22]. However, this algorithm is the human fetching threshold, and the influence of human factors is significant. One of the core problems in the interpretation and evaluation of carbonate reservoirs is hole identification. The OTSU method is slow and computationally expensive for hole identification. An image segmentation algorithm based on OTSU and watershed is proposed to effectively extract hole targets from complex backgrounds [23].

There are some blank areas between the electrodes of the electrical image log image. The electrical image log image does not completely cover the stratum around the borehole [24], and the information is relatively small, which affects the extraction of components. Simultaneously, the heterogeneities in the carbonate reservoir are very serious, which affects the image inpainting of the electric imaging image. The incomplete electrical image log image and severe heterogeneity in the carbonate reservoirs are solved by image inpainting, which improves the extraction accuracy of different components in three-dimensional cores.

The resolution on the electrical image log image is high, which can clearly reflect the macrocomponents of various reservoirs. Various macrocomponents (basic rock skeletons, pores, and connected parts) in the carbonate reservoirs can be extracted from the electrical image log image. Some microfractures can be extracted from the CT (computed tomography) scanned images, which can provide microscopic component information of rocks.

In this paper, the full-bore image is first generated from the electrical image log image, and then, the macrocomponents (rock skeletons, pores, and connected parts) are extracted. The CT scanned images can provide the microscopic component information of rocks in the carbonate reservoirs, and the microfractures can be extracted from the CT scanned images. These methods make the extraction of different components more accurate.

2. Method Principle

2.1. Image Inpainting Based on Combining the Multipoint Geostatistics with an Interpolation Method. Image inpainting refers to the process of reconstructing the lost or damaged parts of images and videos [25]. Image inpainting technologies have many goals and applications [26]. The

inpainting steps of the Criminisi image inpainting algorithm are composed of four parts: marking of the area to be repaired, the calculation of priority, searching and filling the best matching blocks, and confidence of updating. Aiming at the defects of the Criminisi algorithm, such as the long period of image inpainting, many researchers have improved the algorithm [27]. Image inpainting is implemented by the Filtersim simulation algorithm based on multipoint geostatistics [28]. The image inpainting method for significant heterogeneities in carbonate reservoirs, which affect inpainting of the electrical image, is proposed based on combining multipoint geostatistics with an interpolation method.

Training: the Filtersim simulation algorithm requires a set of 6 directional filters to filter the training images. Each pattern in the training images is classified according to the filtering scores.

Inpainting: find the nearest pattern in the training filtering scores for the repaired areas, and then, the pattern is chosen for the repaired areas.

The image inpainting method based on multipoint geological statistics has a good effect on homogeneous reservoirs, but when image inpainting is ineffective on large significantly heterogeneous reservoirs, matching of the effects will be uncertain, and the image inpainting results will be abnormal. In view of this situation, the image inpainting method is improved based on multipoint geostatistics [29]. This paper combines multipoint geostatistics with an interpolation method to make full use of the fast interpolation method of quickly inpainting the basic blank areas of the electrical image log image. The preliminary inpainting results are used to filter and match the pattern in the filtering domain to find the optimum matching pattern. After the image inpainting is processed on blanks with serious heterogeneities, using the preliminary image inpainting results and multipoint geostatistics, the amount of information is increased, the uncertainty in matching patterns in this area is reduced, and the image inpainting results are made more reliable.

2.2. Denoising of the Inpainting Image and the CT Scanned Images. First, the SNR (signal-to-noise ratio) of the images is calculated to determine whether there are some noises in the images whose SNR is larger than a certain threshold. Finally, there should be various denoising methods for the noise images, and the image inpainting and CT scanned images should be processed to eliminate some noises.

2.3. Different Methods Are Used to Extract Different Components of the Electrical Image Log Image and the CT Scanned Images. The electrical image log image produces the full-bore image, and different components can be extracted after denoising from the full-bore image and the CT scanned images. The electrical image log image and the CT scanned images contain different components (basic rock skeletons, pores, connected parts, and microfractures). Different components in the carbonate reservoirs have different distributions of gray levels in the electrical image log images

and CT scanned images. Different components are extracted using the improved methods.

After preprocessing of the full-bore images, there are different distributions of gray levels in the basic rock skeletons, pores, and connected parts extracted by the maximum interclass variance in the two times method. Microfractures are extracted using the improved image segmentation between the watershed and OTSU methods.

2.3.1. Different Component Extractions from the Electrical Image Log Image. The method of maximum interclass variance was proposed by Nobuyuki Otsu, a Japanese scholar, in 1979 [30]. This method is an adaptive threshold determination method, also known as the OTSU method, or OTSU for short. OTSU divides an image into two parts, the background and the target, according to the gray level distribution of the images. The larger the variance is between the background and the target, the greater the difference will be between the two parts of the images. When part of the target is misclassified into the background or part of the background is misclassified into the target, the difference between the two parts will decrease. Therefore, maximizing interclass variance minimizes the probability of misclassification. The threshold of the image is obtained by using the maximum interclass variance method [31]. An automatic extraction method of basic rock skeletons, pores, and connected parts based on the maximum interclass variance in the two times method is proposed for the histogram of the electrical image log image. There is one threshold in the maximum interclass variance method:

$$g(i, j) = \begin{cases} \in P & f(i, j) \geq T, \\ \notin P & f(i, j) < T, \end{cases} \quad (1)$$

where $f(i, j)$ is the gray value of the original image, $g(i, j)$ is the gray value of the image after segmentation, and p represents the gray value of the target; (i, j) represents the coordinates of the current location, such as $i \in [0, l]$ and $j \in [0, w]$, l is the length of the image, w is the width of the image, and T is the threshold. There are two thresholds in the interclass maximum variance twice method:

$$g(i, j) = \begin{cases} P_1 & f(i, j) \geq T_1, \\ P_2 & T_2 \leq f(i, j) < T_1, \\ P_3 & f(i, j) < T_2, \end{cases} \quad (2)$$

where $f(i, j)$ is the gray value of the original image, $g(i, j)$ is the gray value of the image after segmentation, (i, j) represents the coordinates of the current location, such as $i \in [0, l]$ and $j \in [0, w]$, l is the length of the image, w is the width of the image, P_1 is the gray value of target 1, P_2 is the gray value of target 2, P_3 is the gray value of target 3, T_1 is the first threshold, and T_2 is the second threshold. The histogram of the measured electrical image log image does not have single peaks but three peaks. The segmentation results cannot be obtained by using the maximum interclass variance. The maximum interclass variance in the two times method is proposed. According to different distribution

characteristics of the gray levels of different components in the electrical image log, two threshold segmentation points with the largest variance and the second largest variance are calculated sequentially to obtain the automatic segmentation of basic rock skeletons, pores, and connected parts.

The maximum interclass variance in the two times method is the maximum interclass variance method for extended classes among three classes segmentation. First, the image is segmented into two classes by using the maximum interclass variance method, which means that the optimal threshold T is determined by the maximum interclass variance method, and the gray level of the full-bore image is segmented into two parts according to the first threshold T . Then, the maximum interclass variance method is also used to calculate the best classifications in each subclass, and the two best thresholds T_1 and T_2 are determined, which means that region P_{11} and region P_{12} are determined from subregion P_1 according to the second threshold T_1 , and region P_{21} and region P_{22} are determined from subregion P_2 according to the third threshold T_2 . The second and third thresholds are determined using the maximum interclass variance among subclass methods. The other optimal threshold T_3 is determined from the two best thresholds T_1 and T_2 . Some components are extracted from the full-bore image using the two best thresholds T_3 and T . The two best thresholds T_3 and T are used to clarify the basic rock skeletons, pores, and connected parts.

2.3.2. Microfracture Extraction from the CT Scanned Images. Generally, strata with microfractures show dark or black features on CT scanned images, which mean that the gray values are much smaller than the background values. However, when the underground situations are complex, the backgrounds of the image become complex, and there will be dark spots similar to the microfractures, which make identification of the microfractures difficult. To effectively separate the targets and backgrounds, the key step is to segment the CT scanned images, and the OTSU method proposed by Japanese scholars is a widely used image segmentation method. However, because of the complexity of the underground strata, there are many dark spots in the backgrounds, and there are many peaks in the gray histogram. The segmentation effects of the OTSU are not ideal in this case. This method divides many backgrounds into the microfractures and enlarges the range of dark spots. There are many burrs in the contour of the microfractures, the boundary is not clear, and the segmentation effects are not good. Therefore, an image segmentation-based method that combines the OTSU and watershed methods is proposed, which can denoise effectively and is suitable for image segmentation with complex backgrounds.

(1) The Principle of the Watershed Segmentation Method. The basic idea of the watershed method is that the image is regarded as a topographic surface [32]. The gray value represents the height of the ground, and each minimum represents a low-lying area where water continuously gushes out and gradually fills the catchment basin related to the low-

lying area. When water from different low-lying areas converges at some points, dams will be built at these points to prevent the water from overflowing. These dams are called watersheds, which divide the whole topographic surface into many areas. The watershed method usually can be divided into three kinds: the rainfall method, the submergence method, and the Vincent–Soille method. The Vincent–Soille method is adopted in this paper.

(2) *The Improved Image Segmentation between the Watershed and OTSU Methods.* The principle of the OTSU method has been introduced in detail in many articles. The specific steps of the combined OTSU and watershed method are as follows: converting the image into a 8-bit pseudocolor image, performing morphological open-close filtering to denoise the image, and converting the image RGB (red-green-blue) into LUV (light-uniform-variation) color space, and then, the watershed is segmented to obtain the 24 true color segmentation image. Additionally, the segmented true color image is converted into an 8-bit gray image, and finally, the final segmentation image is obtained by using the improved image segmentation combining the watershed and OTSU methods. Compared with the traditional OTSU method, this improved image segmentation method that combines the watershed and OTSU methods can effectively extract microfractures, eliminate dark spots in the backgrounds, and reduce the interference of noise. This method is more conducive to microfracture identification and subsequent fusion processing.

3. Example Analysis

3.1. Extraction of Basic Rock Skeletons, Pores, and Connected Parts in the Electrical Image Log Image. Figure 1 is the measured electrical image log image with 5 mm resolution. The electrical logging image was measured by EILog instrument of CPL company. Figure 2 is the full-bore electrical image log image based on the combination of multipoint geostatistics and an interpolation method. Based on Figure 2, compared with the measured image, the full-bore image can be obtained from the inpainting image. Through image inpainting, the amount of information in the image is increased, which is conducive to improve the recognition accuracy of subsequent geological targets. Figure 3 shows extraction of some components of the image segmentation by using the maximum interclass variance in the two times method. Figure 3 shows the extracted macrocomponents such as basic rock skeletons, pores, and connected parts. Blue part represents the extracted pores, green part represents the extracted rock skeleton, and red part represents the extracted connected parts in Figure 3.

3.2. Extraction of Microfractures in the CT Scanned Images. Figure 4 is the CT scanned image with 8 micron resolution. CT images were measured with GE scanner. Figure 5 is the histogram corresponding to Figure 4. Figure 6 is the CT scanned image showing the

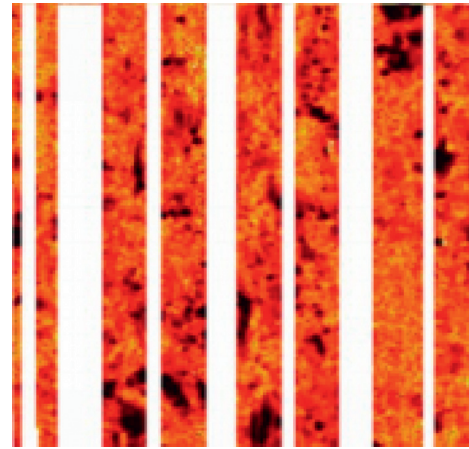


FIGURE 1: The measured electrical image log image.

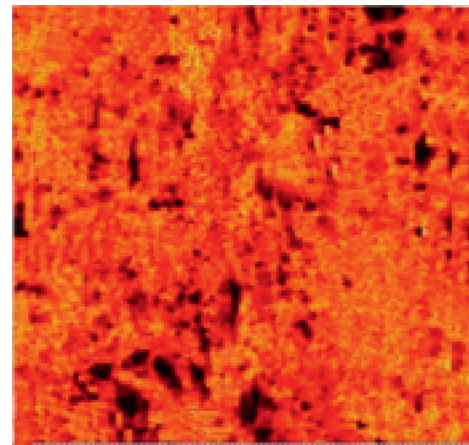


FIGURE 2: The full-bore image after image inpainting.

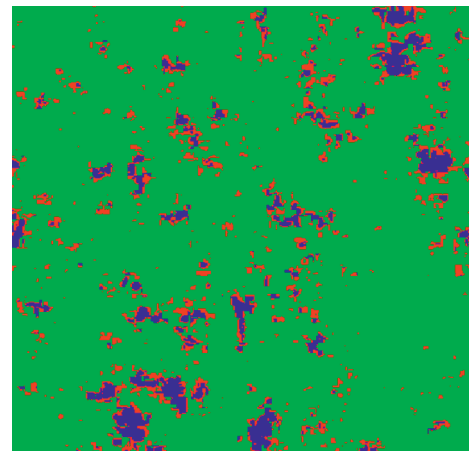


FIGURE 3: Extraction of rock skeletons, pores, and connected parts using the maximum interclass variance in the two times method.

microfractures and some noise. For the single-peak classification problem shown in the histogram of Figure 5, when the basic pixels are the background and the proportion of the foreground pixels is very small, the

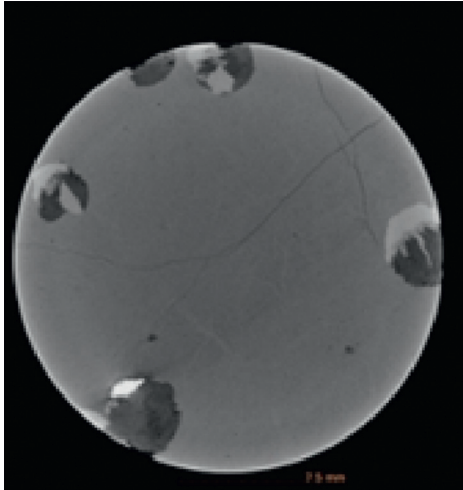


FIGURE 4: The CT scanned image.

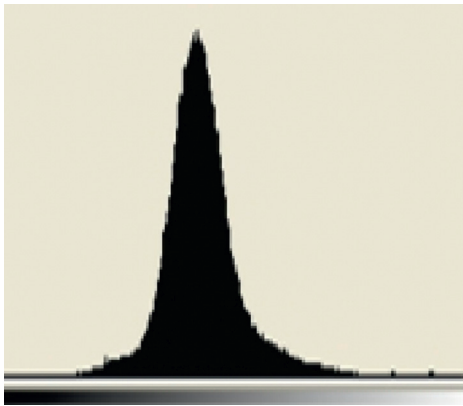


FIGURE 5: The histogram corresponding to Figure 4.

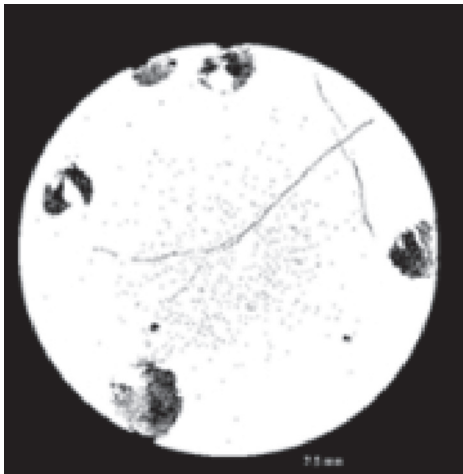


FIGURE 6: The microfractures with some noises.

OTSU and watershed methods are used to classify component from the CT scanned images. After the image noises are removed by filtering, the microcomponents are extracted. Figure 6 shows the microfractures with some noises. Figure 7 shows the final extracted

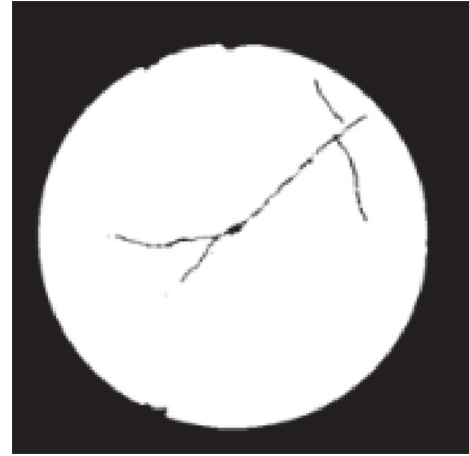


FIGURE 7: The final extracted microfractures.

microcomponents after removing noise. The experimental results prove that using extraction methods for different components enables better results to be obtained.

4. Conclusions

Compared with a three-dimensional digital core in sandstone reservoirs, carbonate reservoirs include secondary structures in addition to the basic rock skeleton and pore components. These different components have different properties. Extracting these different components is a very difficult problem.

Based on generation of the full-bore image, different macroscopic components such as basic rock skeletons, pores, and connected parts are extracted from the full-bore image, and microfractures are extracted from the CT scanned images. The maximum interclass variance in the two times method is proposed in this paper. The macroscopic components with different properties can be calculated from the electrical image log images. The histogram of multipeaks of different macroscopic components can be well processed. The method is proposed to make the extraction of different components with different properties more accurate. The improved image segmentation from the combined watershed and OTSU methods can effectively eliminate black spots and reduce noise interference in the CT scanned images.

Data Availability

The core data are the actual oilfield data and are confidential.

Conflicts of Interest

The authors declare that they have no conflicts of interest.

Acknowledgments

This work was supported in part by the National Natural Science Foundation of China (Grant nos. 41674136 and 41374148).

References

- [1] L. Ji, M. Lin, W. Jiang, and C. Wu, "An improved method for reconstructing the digital core model of heterogeneous porous media," *Transport in Porous Media*, vol. 121, no. 2, pp. 389–406, 2018.
- [2] X. H. Li, Q. Y. Wu, and F. J. Pang, "Building and application of three-mineral rock components identification model for carbonate," *Well Logging Technology*, vol. 41, no. 3, pp. 301–304, 2017.
- [3] Y. Liu, C. Chen, X. C. Shu et al., "The formation model of the carbonatite-syenite complex REE deposits in the east of Tibetan plateau: a case study of Dalucao REE deposit," *Acta Petrologica Sinica*, vol. 33, no. 7, pp. 1978–2000, 2017.
- [4] W. Chen, J. Xie, S. Zu, S. Gan, and Y. Chen, "Multiple-reflection noise attenuation using adaptive randomized-order empirical mode decomposition," *IEEE Geoscience and Remote Sensing Letters*, vol. 14, no. 1, pp. 18–22, 2017.
- [5] W. Chen, H. Song, and X. Y. Chuai, "Fully automatic random noise attenuation using empirical wavelet transform," *Journal of Seismic Exploration*, vol. 28, no. 2, pp. 147–162, 2019.
- [6] F. Wen, Z. Zhang, K. Wang, G. Sheng, and G. Zhang, "Angle estimation and mutual coupling self-calibration for ULA-based bistatic MIMO radar," *Signal Processing*, vol. 144, pp. 61–67, 2018.
- [7] X. Xiao, X. Zhang, J. Zhang, and X. Luo, "Study of three-dimensional digital core reconstruction based on multiple-point geostatistics in a cylindrical coordinate system," *IEEE Access*, vol. 7, pp. 178522–178527, 2019.
- [8] X. M. Ge, Y. R. Fan, J. Li et al., "Experimental studies and investigations on the dual lateral log response of near borehole fractures," *Chinese Journal of Geophysics*, vol. 62, no. 1, pp. 354–360, 2019.
- [9] Z. W. Wang, L. Y. Fu, Y. Zhang, and W. Wei, "The ultrasonic response of numerical simulation and analysis of scattering characteristics in digital core for shale reservoir," *Chinese Journal of Geophysics*, vol. 61, no. 3, pp. 1069–1082, 2018.
- [10] L. Wan, X. Kong, and F. Xia, "Joint range-Doppler-angle estimation for intelligent tracking of moving aerial targets," *IEEE Internet of Things Journal*, vol. 5, no. 3, pp. 1625–1636, 2018.
- [11] D. Meng, X. Wang, M. Huang, L. Wan, and B. Zhang, "Robust weighted subspace fitting for DOA estimation via block sparse recovery," *IEEE Communications Letters*, vol. 24, no. 3, pp. 563–567, 2020.
- [12] L. Wan, L. Sun, X. Kong, Y. Yuan, K. Sun, and F. Xia, "Task-driven resource assignment in mobile edge computing exploiting evolutionary computation," *IEEE Wireless Communications*, vol. 26, no. 6, pp. 94–101, 2019.
- [13] X. Wang, L. Wang, X. Li, and G. Bi, "Nuclear norm minimization framework for DOA estimation in MIMO radar," *Signal Processing*, vol. 135, pp. 147–152, 2017.
- [14] X. L. Xiao, X. J. Jin, X. Zhang, H. L. Liu, and Y. W. Jiang, "Fracture identification based on information fusion of conventional logging and electrical imaging logging," *Oil Geophysical Prospecting*, vol. 50, no. 3, pp. 542–547, 2015.
- [15] X.-Y. Zhang, S. Wang, X. Zhu, X. Yun, G. Wu, and Y. Wang, "Update vs. upgrade: modeling with indeterminate multi-class active learning," *Neurocomputing*, vol. 162, pp. 163–170, 2015.
- [16] X.-Y. Zhang, S. Wang, and X. Yun, "Bidirectional active learning: a two-way exploration into unlabeled and labeled data set," *IEEE Transactions on Neural Networks and Learning Systems*, vol. 26, no. 12, pp. 3034–3044, Feb. 2015.
- [17] L. Yang, W. Chen, W. Liu, B. Zha, and L. Zhu, "Random noise attenuation based on residual convolutional neural network in seismic datasets," *IEEE Access*, vol. 8, no. 1, pp. 30271–30286, 2020.
- [18] F. Wen and J. Shi, "Fast direction finding for bistatic EMVS-MIMO radar without pairing," *Signal Processing*, vol. 173, Article ID 107512, 2020.
- [19] W. Chen, M. Bai, and H. Song, "Seismic noise attenuation based on waveform classification," *Journal of Applied Geophysics*, vol. 167, no. 8, pp. 118–127, 2019.
- [20] X. Yang, Y. Wang, and W. C. Li, "Identify fissure with conventional logging information," *Jilin Geology*, vol. 32, no. 1, pp. 102–105, 2013.
- [21] Y. J. Jiang, "New method of fluid type identification for fracture-vug type reservoirs," *Well Logging Technology*, vol. 41, no. 6, pp. 676–679, 2017.
- [22] X. Y. Li, J. L. Lin, and H. J. Wen, "Automatic recognition of geological aperture in carbonates," *Journal of Daqing Petroleum University*, vol. 29, no. 4, pp. 4–6, 2005.
- [23] Z. H. Li, X. Zhang, L. Luo, Y. X. Mao, and M. Li, "Automatic identification and parameter calculation of carbonate cavities under complex background," *Fault-Block Oil & Gas Field*, vol. 23, no. 3, pp. 314–323, 2016.
- [24] X. Zhang, M. Zhang, X. L. Xiao, L. Luo, Y. Q. Yang, and W. P. Cui, "Image inpainting for fullbore electrical logging in complex formations," *Geophysical Prospecting for Petroleum*, vol. 57, no. 1, pp. 148–153, 2018.
- [25] Q. Fan and L. Zhang, "A novel patch matching algorithm for exemplar-based image inpainting," *Multimedia Tools and Applications*, vol. 77, no. 9, pp. 10807–10821, 2018.
- [26] M. Ghorai, S. Mandal, and B. Chanda, "A group-based image inpainting using patch refinement in MRF framework," *IEEE Transactions on Image Processing*, vol. 27, no. 2, pp. 556–567, 2018.
- [27] A. Tavakoli, P. Mousavi, and F. Zarmehi, "Modified algorithms for image inpainting in Fourier transform domain," *Computational and Applied Mathematics*, vol. 37, no. 4, pp. 5239–5252, 2018.
- [28] X. R. Meng, Y. B. Liang, X. H. Meng, and Q. Yang, "Using FILTERSIM for reservoir faces simulation," *Computer Engineering and Design*, vol. 34, no. 2, pp. 545–549, 2013.
- [29] Y. Wu, C. Lin, L. Ren et al., "Reconstruction of 3D porous media using multiple-point statistics based on a 3D training image," *Journal of Natural Gas Science and Engineering*, vol. 51, pp. 129–140, 2018.
- [30] N. Otsu, "A threshold selection method from gray-level histograms," *IEEE Transactions on Systems, Man, and Cybernetics*, vol. 9, no. 1, pp. 62–66, 1979.
- [31] Q. Li, H. Tang, J. N. Chi, Y. Y. Xing, and H. T. Li, "Gesture segmentation with improved maximum between-cluster variance algorithm," *Acta Automatica Sinica*, vol. 43, no. 4, pp. 528–537, 2017.
- [32] Z. Q. Ma, Y. S. Wang, Z. B. Song, and M. L. Xiao, "The color tread image segmentation based on improved labeled watershed," *Journal of Graphics*, vol. 39, no. 1, pp. 36–42, 2018.

Review Article

A Review on Machine Learning-Based Radio Direction Finding

Ming-Yi You ^{1,2}, An-Nan Lu,^{1,2} Yun-Xia Ye ^{1,2}, Kai Huang ^{1,2} and Bin Jiang^{1,2}

¹Science and Technology on Communication Information Security Control Laboratory, Jiaxing, Zhejiang 314033, China

²No. 36 Research Institute of CETC, Jiaxing, Zhejiang 314033, China

Correspondence should be addressed to Ming-Yi You; youmingyi@126.com

Received 1 July 2020; Accepted 17 August 2020; Published 24 August 2020

Guest Editor: Jianfeng Li

Copyright © 2020 Ming-Yi You et al. This is an open access article distributed under the Creative Commons Attribution License, which permits unrestricted use, distribution, and reproduction in any medium, provided the original work is properly cited.

The research and applications of radio direction-finding technology based on machine learning are reviewed. Detailed application scenarios are summarized with focus on the advantages of machine learning-based direction-finding models. Important elements such as problem formulation and model inputs and outputs are introduced in detail. Finally, some valuable future research topics are discussed.

1. Introduction

Radio direction finding is the measurement of the direction from which a received signal is transmitted. Recently, direction-finding technology has been widely applied in emitter localization, jamming guide, determination of communication relationship, communication network division, cooperative communication, etc. Radio direction finding is essentially an inverse problem of signal reception from a given direction, and the core is the mapping relationship of several signal parameters with its incidence direction.

With the advances in machine learning and artificial intelligence, some researchers gradually began to consider the problem of direction finding using machine learning techniques. The idea of direction finding using machine learning techniques can be dated back to the 1990s. At that time, some researchers considered the application of artificial neural networks (ANNs) to direction finding with fast development in different types of shallow neural networks. At about 2000s, support vector machines (SVMs) achieved satisfactory results in many fields including direction finding. Recently, deep learning techniques greatly improve the modeling capability of neural networks and are attracting more and more researchers and engineers in the field of direction finding.

With wide applications of machine learning techniques to direction finding problems, however, a systematic

overview that collects, organizes, clarifies, and compares the related works has not yet been reported. By this motivation, facing the applications of machine learning techniques in direction finding, the main objective of the paper is to collect and extract the specific problems solved by machine learning models, to summarize the main types of model inputs and outputs, and to raise several problems that deserve further research.

2. Research and Applications of Machine Learning Techniques in Direction Finding

In general, machine learning techniques have special advantages for direction finding in complex scenarios compared with classical approaches such as analytical methods and the least square (LS) method. Such complex scenarios include complex receiving systems, complex channels, and complex signals. In addition, machine learning techniques are usually applied to improve direction finding capabilities such as computing speed and angle resolution. Figure 1 summarizes the direction finding scenarios where machine learning techniques have been utilized. In the following, we will review the research works that could be categorized into the corresponding application scenarios, with focus on the problems to be solved and the model inputs and outputs.

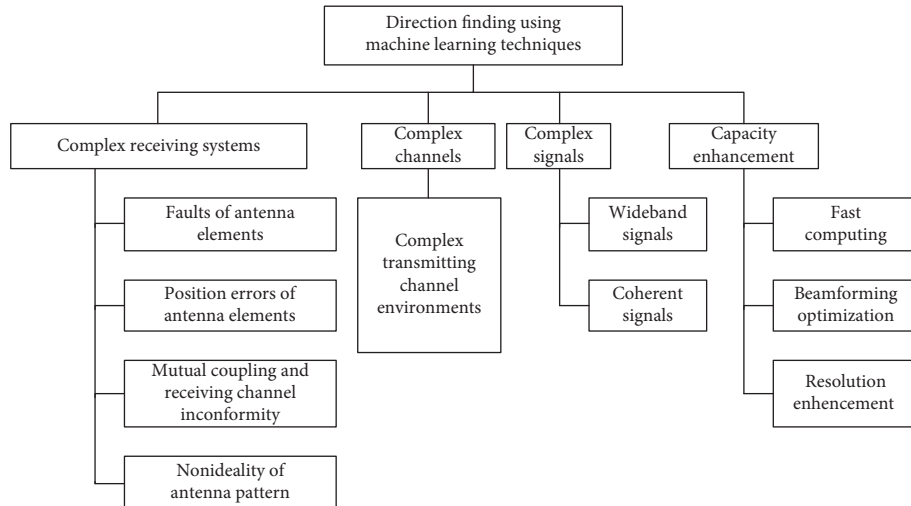


FIGURE 1: Overview of applications of machine learning techniques in direction finding.

2.1. Concrete Scenarios

2.1.1. Complex Receiving Systems. Scenarios of complex receiving systems include the scenarios where there are position errors of antenna elements, the scenarios where there are mutual coupling of antenna elements and receiving channel inconformity, the scenarios of nonideal antenna pattern, and the scenarios where some antenna elements malfunction.

Shieh and Lin [1] pointed out that high resolution methods such as multiple signal classification (MUSIC) were highly sensitive to the structure of the covariance matrix and required excessively large computation effort. The estimation of signal parameters by rotational invariance techniques (ESPRIT) was faster at the expense of increased number of sensors. Both MUSIC and ESPRIT algorithms were very sensitive to imperfections of models of signals and noise. To handle the abovementioned problem, a neural fuzzy scheme was proposed in [1] based on the phase differences from an interferometer. A self-constructing neural fuzzy inference network (SONFIN) was used in [1] which was a general connectionist model of a fuzzy logic system and could find its optimal structure and parameters automatically. In addition, to avoid the discontinuities caused by the input phase transition, a quadrature representation of the phase differences was used as the input of SONFIN. The output of SONFIN is the direction of arrival (DOA). Simulation results showed that the SONFIN always produced DOA estimates close to the desired DOA values, and the required number of parameters of SONFIN was much less than that in classical radial basis function network (RBFN) under the same root mean square error in DOA.

Motivated by the fact that once an antenna is built and placed on a certain platform, changes that affect both the shape of the structure and effectiveness of the materials used to fabricate the antenna may occur. Christodoulou et al. [2] proposed a least square support vector machine (LSSVM) approach to direction finding to make arrays smart so that the beamforming and beamsteering performance of the

array degraded gracefully when one of the antenna elements failed. The LSSVM algorithm was trained with projection vectors generated from the signal subspace eigenvectors and the respective covariance matrices. And the output labels from the multiclass LSSVM system were the DOA estimates. Rohwer et al. [3] adopted a similar approach for DOA estimation. Following the works by Rohwer et al. [3], an extensive sensitivity analysis was carried out in [4] to understand how parameters of the LSSVM formulation affect the performance of the resulting multiclass classifier system, with a clear dependence on the width of the radial basis kernel function.

Motivated by the requirement of not monitoring the failed antenna element and time of failure, S. Vigneshwaran et al. [5] proposed a direction-finding approach based on the minimal resource allocation network (MRAN). The training for MRAN was conducted under no failure and no noise cases and the trained network was then used when there was a failure. To overcome the problem of high direction finding error near $\pm 90^\circ$, Vigneshwaran et al. [5] used the magnitude and phase angles of the elements of the correlation matrix instead of their real and imaginary parts as the network inputs. During the training process, MRAN has larger number of tunable parameters as it tunes the centers, weights, and spread of the neurons, whereas the classical RBFN tunes just the weights. And this leads to higher generalization capability of MARN.

Dehghanpour et al. [6] dealt with direction finding in presence of mutual coupling of antenna elements using a multiple kernel SVM. The normalized elements of the upper triangle part of the correlation matrix were used as the inputs of the multiple kernel SVM, whereas the DOAs are used as the model outputs. Simulation results demonstrated the superiority of the proposed method over classical methods such as MUSIC, single kernel support vector regression (SVR), and smooth SVR.

Wang et al. [7] pointed out that the performance of MUSIC algorithm relied on the precision of the antenna pattern which could be contaminated by nearby

electromagnetic interference and was not easy to measure, and therefore it was meaningful to seek a direction finding approach without the need of precise measurement of the antenna pattern. They developed a SVR-based direction finding method for an M-element radar receiving system. The relative magnitude and phase of signals to those of the reference receiving channel were used as the model input. The field experiments conducted in Pingtan and Liuaio validated that the SVR-based method outperformed the classical MUSIC algorithm.

Liu et al. [8] pointed out that the existing learning-based direction finding methods suffered the following drawbacks: (1) the generalization capability was questionable where the volume of the training set was limited; (2) the existing methods were mainly applicable to the case of single object and could not be applied to a general direction-finding problem when the number of objects was unknown. They proposed a hierarchical framework of deep NNs (DNNs) to deal with the general DOA estimation problem. The framework consists of an autoencoder for spatial filtering and a multiclass classifier for DOA estimation. The normalized elements in the upper triangle part of the correlation matrix were used as the model input. The simulation results showed that the proposed method was applicable to the scenarios when the number of incident directions differed from those of training samples.

2.1.2. Complex Channels. Research on machine learning-based direction finding in complex transmitting channels mainly focuses on indoor direction finding and localization in presence of multipath effect and heavy reverberation.

Xiao et al. [9] pointed out existing direction finding approaches faced either one or a combination of the following problems: high-computational cost, nonrealistic assumptions on signal/noise models, and unreliable performance in real environments. To estimate DOAs in noisy and reverberate environments, they formulated the task of direction finding as a classification problem, extracted features from the generalized cross correlation (GCC) vectors, and used a multilayer perception (MLP) NN to learn the nonlinear mapping from such features to the DOA. Experimental results on simulated data showed that the method performed much better than the LS method.

To address the problem of localization in adverse environments such as high reverberation and low signal-to-noise ratio (SNR), Sun et al. [10] proposed an indoor sound source localization approach with a probabilistic NN (PNN). The GCC features were again used as the network inputs, whereas the space of interest was divided into a number of equal-dimensional rectangular clusters.

Cheng et al. [11] compared the capability of several SVMs and the k-means approach for indoor localization using the magnitudes of ambient FM and DVB-T signals. The comparison results demonstrated the superiority of the SVMs. In addition, Cheng et al. [11] discussed the problem of feature extraction and ensemble learning.

Yue et al. [12] pointed out that traditional signal processing methods could not handle noise and reverberation

effectively and proposed a learning-based approach of DOA estimation in a three-dimensional room space. GCC with phase transform (GCC-PHAT) was used as the input to a convolutional NN (CNN), and it was formulated as a classification problem. Accuracy of single sound source direction detection and compatibility of multiple sound sources were verified by extensive simulations.

Li et al. [13] proposed a method combining CNN and long short-term memory (LSTM) network to address the online DOA estimation in noisy and reverberant environments. The proposed approach used a two-dimensional input matrix spreading over the time and frequency domain for GCC-PHAT. In addition, the feature matrixes for all sensor pairs were summed up for robustness improvement. Experimental results showed that the method was robust to the topologies of microphone array and the trained model could get better performance on a new microphone array structure using only very few new data for adaptation.

Mane et al. [14] proposed a CNN-based classification method for broadband DOA estimation of a single steady sound source in noisy and reverberation conditions. The input to the CNN was given as the short-time Fourier transform (STFT) coefficients of the phase components obtained from the uniform linear array (ULA) of microphones. Similar approach was suggested in [15] with extension to multiple sources with the assumption of disjoint speaker activity in STFT domain.

Khan et al. [16] pointed out that the MUSIC spectrum would not produce a clean outstanding peak in the case of multipath and proposed a NN-based DOA estimation model with the MUSIC spectrum as the input. The performance of the proposed model showed consistent improvement over a range of channel parameters including elevation angles, single-to-noise ratios (SNRs), and channel configuration.

Fahim et al. [17] proposed a multisource DOA estimation technique using a CNN algorithm which learnt the modal coherence patterns of an incident sound field through measured spherical harmonic coefficients. The model was trained with individual time-frequency bins in the STFT spectrum. The proposed model was capable of estimating multiple sound sources on a three-dimensional space using a single-source training set.

2.1.3. Complex Signals. Wideband signals and coherent signals impose special difficulties for accurate direction finding. Recently, some researchers tried to solve the problem of DOA estimation of wideband or coherent signals using machine learning techniques.

A novel class of focusing matrices for coherent signal subspace method was proposed in [18]. These matrices are formed based on a backpropagation (BP) NN and the concept of uniform focusing transformation of the DOA of wideband sources. The proposed DOA estimating procedure is efficient without prior knowledge of the DOAs.

Lizzi et al. [19] presented an approach for DOA estimation of correlated signals based on a SVM classifier and an iterative multiscaling approach (IMSA). The use of SVM guarantees real-time operations, while the IMSA enhances

the angular resolution within the regions of incidence of the incoming signals.

Terabayashi et al. [20] proposed a DOA estimation method using a complex-valued spatiotemporal NN (CVSTNN) for ultrawideband (UWB) systems. The CVSTNN was combined with the power-inversion adaptive array (PIAA) for null steering without the knowledge of incident directions. Simulation and experimental results demonstrated that the CVSTNN showed a higher accuracy than the conventional MUSIC method.

A fast DOA estimation method based on CNN for broadband radio direction finding system was proposed in [21]. The phase component of the covariance matrix was fed into the network, whereas each DOA label was consisted of the sine and cosine values of the angle of arrival (AOA).

Mack et al. [22] extended broadband DOA estimation to broadband signal-aware DOA estimation by focusing on narrow frequency bands dominated by the desired source and removing the spatial information in other bands. The experiments with estimated masks showed the possibility to combine signal-independent DOA with independently trained mask estimators to perform signal-aware DOA estimation.

2.1.4. Capability Enhancement. Capability enhancement is continuously a core topic for research on direction finding systems. With the help of machine learning techniques, researchers have made progress on weight parameter optimization for beamforming, computation acceleration, and direction finding resolution improvement.

The 1st part of capability enhancement is beamforming optimization. Xu et al. [23] proposed a beamforming algorithm using SVM. The sampled signals were used as the model input, whereas the expected signal sequences served as the model output.

Savitha et al. [24] compared the performance of beamforming using the fully complex-valued RBF (FC-RBF) network with the fully complex-valued activation function with the performance of the existing complex-valued RBF network. The received signals were used as the model input and the expected transmitted signals were used as the model output.

One of smart antennas' main functions is adaptive beamforming, which forms a high-gain beam at the desirable signal directions and weakens interference signals in the other directions. However, the real-time calculation of adaptive weighting coefficients is computationally intensive, especially in the case of a large number of antenna array elements. Hence, Pei et al. [25] proposed an efficient method for real-time calculation of beamforming weighting coefficients based on the generalized regression NN. The normalized elements of the upper triangle part of the correlation matrix were used as the model input and the normalized weighting matrix was used as the model output. The simulation results verified the superiority of the proposed method over the minimum variance distortionless response (MVDR) method in terms of computing speed.

Salvati et al. [26] presented a weighted MVDR algorithm for far-field broadband sound source localization in a noisy environment. A machine learning method based on a SVM was used for selecting the narrowband components that positively contributed to the broadband fusion. The skewness measure of response power function was used as the input feature for the supervised SVM learning. Simulations demonstrated the effectiveness of the weighted MVDR in an outdoor noisy environment.

Zaharis et al. [27] introduced the implementation of antenna array beamforming based on a simplified CNN. The inputs to the CNN were the AOAs of signals of interest (SOI) and signals of avoidance (SOA), whereas the output was the expected magnitude and phase of exciting weights. In the proposed NN structure, the first hidden layer was divided into sublayers, and a direct connection between every input and a respective sublayer was performed in order to alleviate the performance degradation due to uncertainties in interference correlation.

The 2nd part of capability enhancement is fast computing. Jha and Durrani [28] pointed out that the maximum likelihood estimator was the optimal estimator of the direction of sources, but it required the minimization of a complex, multimode, and multidimensional cost function. A neural optimization procedure was presented that did not require an initial estimate of the direction of sources, which offered the potential of real-time solutions to the DOA estimation problem by utilizing the fast relaxation properties of the Hopfield network.

In 1998, Zooghyby et al. [29–31] pointed out that super-resolution algorithms for DOA estimation were computationally intensive and hard to implement in real time and proposed a NN-based direction finding approach. The approach was claimed to be able to track any numbers of incident directions with any angle separation without prior knowledge on the emitter number. The approach firstly divided the angle region of interest into several subregions and trained the same number of NNs to judge if the emitter belonged to a given subregion with the normalized upper triangle part of the covariance matrix as the model input. Afterwards, several NNs were trained to accurately estimate the DOAs in each subregion, and each subregion was further divided into N grids. Simulation results demonstrated that the proposed NN could estimate different numbers of DOAs from those of the training samples. They also considered using the DOAs as the NN output directly [32, 33]. Similar inputs are considered in [34, 35], except that Pour et al. [34] used a MLP network along with ant colony optimization for NN training and a BP NN was used in [35]. A similar treatment for a uniform linear array was adopted in [36].

Jeong et al. [37] addressed the problem for the DOA estimation of narrowband emitter signals impinging on an array of sensors by the modified Hopfield NN. They showed that the operation of the NN had an analog with the covariance fit estimator in estimating the DOA.

To reduce the computation complexity, Tong et al. [38] studied satellite interference location through a RBF network. The time averaged and normalized signals were used

as the model input, whereas the DOAs were designed as the model output.

Based on a four-element linear array, Lee [39] compared the performance of three types of NNs for direction finding, namely, a Hopfield NN, a BP NN, and a RBF NN. He pointed out that appropriately choosing the center would accelerate the training process of the RBF NN.

Chen et al. [40] proposed a method for reducing the volume of training samples for two-dimensional direction finding using a uniform circular array. The elevation and azimuth were estimated in two separate NNs, respectively. A similar strategy for two-dimensional DOA estimation was adopted in [41] based on a linear vector quantization (LVQ) NN.

Matsumoto and Kuwahara [42] conducted a direction finding experiment using a RBF NN. To avoid the discontinuity near 0° , the outputs of the NN were designed as $[\sin\alpha, \cos\alpha]$, where α was the AOA. The input of the NN is a vector composed of the normalized elements of the upper triangle part of the covariance matrix.

Raj et al. [43] pointed out that there were two main disadvantages of the direction-finding algorithms such as MUSIC, root-MUSIC, and ESPRIT. Firstly, they are computational intensive. And secondly, they assume that the antenna elements are exactly equal. Raj et al. [43] used a nonlinear SVR approach for direction finding where the fixed number of angles and their corresponding normalized array input vectors were used as the output/input pair.

Gotsis et al. [44, 45] proposed a DOA estimation methodology based on NNs and designed for a switched-beam system. The method incorporated the benefits of NNs and switch-beam systems to achieve DOA estimation in a less complex and expensive way compared to the corresponding widely known super-resolution algorithms. The NN firstly despreads direct sequence code division multiple access (DS-CDMA) signals and the signal amplitudes of multiple beams were used as the model inputs. It was shown that a properly trained NN could accurately find the SOI AOA at the presence of a varying number of mobile users and a varying SOI to interference ratio. Similar inputs were used in [46] to design a compact DOA estimation system which used only four circularly patch elements. NNs were used to firstly classify the antenna signals and then estimate the DOA.

George and Sajjanshetty [47] proposed a technique for the estimation of DOA of moving signals using two architectures of NNs, i.e., feedforward and RBF NNs. A fundamental assumption made was that the number of signals was either known, or could be estimated in priori. The normalized sensor array output was given as the input to the network.

Agatonovic et al. [48–51] proposed a two-level NN for two-dimensional direction finding. The first-level NN classified the AOA into a small subregion, whereas the second-level NN estimated the AOA accurately. The inputs to the two NNs were the normalized elements of the first array of the covariance matrix. To deal with the mutual coupling among antenna elements, similar methods are adopted in [52–54]. Similar features are used in [55] for DOA estimation of a multiple input multiple output

(MIMO) orthogonal frequency division multiplexing (OFDM) radar.

To reduce the real-time computation burden, Stankovic et al. [56–59] proposed a direction-finding approach using a MLP NN. The inputs of the NN are all elements of the covariance matrix and the output are the DOAs. NN training was conducted for the scenarios of one emitter and two emitters with fixed DOA separation.

Chakrabarty and Habets [60] pointed out that the existing NNs used generalized correlation or covariance matrix as model inputs, and even the process of feature extraction was time consuming. They proposed a direction finding approach for wideband signals using only phase of each spectral lines. A classification NN was established for direction finding. The experimental results demonstrated that the NN trained by simulated data could be effectively applied in real signal environments.

Faye et al. [61] demonstrated the ability of a single uniform linear array (ULA) of isotropic elements along with an NN approach to achieve two-dimensional DOA estimation. LVQ NNs were sequentially trained on elevation and azimuth-dependent datasets built from received signal in predefined spatial sectors chosen in accordance with pattern symmetry and radiation intensity.

Efimov et al. [62] presented the approach to the design of AOA estimator for narrowband noise-like signal based on NN to improve the signal processing speed. The signal time delay of each sensor pair was used as the model input and the associated AOA was designed as the model output.

Huang et al. [63] proposed a deep learning based super-resolution DOA estimation model in the uplink MIMO system with the model input and output to be the array received signals and the DOA, respectively. Similar treatment was adopted in [64] for sound source localization and direction finding with a CNN.

The 3rd part of capability enhancement is resolution improvement. Wang and Ma [65] compared the estimation bias and angle resolution of a NN-based direction finding approach with MUSIC when signals were uncorrelated, partially correlated, and correlated.

Chen and Hou [66] proposed a principle component decomposition approach based on a complex-valued NN. The estimated feature vectors from the NN were used for direction finding based on MUSIC to obtain high resolution estimations. Similarly, Chang et al. [67] proposed a high resolution bearing estimation method via unitary decomposition artificial NN.

A DOA estimation method based on a cascaded NN was proposed in [68] for two closely spaced sources. The NN contained two parts: SNR classification network and DOA estimation network. Due to the cascade structure, the method could be applied to a wider range of SNR than other existing algorithms.

3. Summary

Based on the reported studies, Figure 2 summarizes the commonly used inputs, models, and outputs for machine learning-based direction finding.

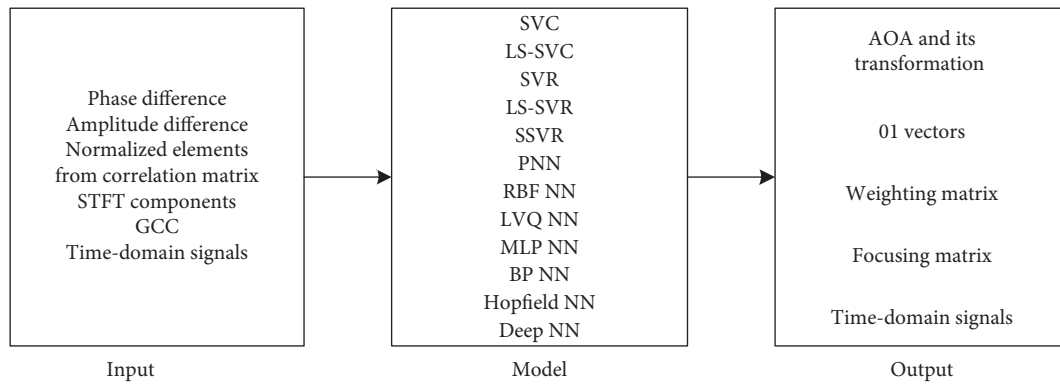


FIGURE 2: Commonly used inputs, models, and outputs for machine learning-based direction finding.

4. Future Challenges

Based on the above review, it is evident that machine learning techniques have been widely used in direction finding. However, there are still many challenges when these intelligent models are applied to practical engineering problems.

The first problem in performing two-dimensional direction finding is the huge volume of training samples which prohibits practical use of NN models of direction finding. Chen et al. [40] has suggested a method for reducing the necessity for training samples for a uniform circular array. However, an effective training method is still an open issue for general array formulations.

Section 2 has summarized the common features for machine learning models. However, it is still unclear which type is most effective. Deep learning techniques may shed light on this problem by feeding original signal samples into a DNN and letting the network learn the feature vectors by itself.

In the application process of machine learning-based direction-finding approaches, more training samples can be collected. It might be interesting to study the incremental learning method for direction finding which could quickly update the model capability without batch processing.

For the scenario where elements of an antenna array fails and the failure time is unknown, Vigneshwaran et al. [5] suggests an MRAN-based method, but the capability loss is still remarkable. In engineering applications, it is common to see failures or degradation of antenna elements, and it would be beneficial to establish a more robust direction-finding system by considering the possibility of element failure even in the training phase of the NN.

In some cases such as field calibration of satellite antennas, the AOAs may even be uncertain to some extent for the training samples, and how to establish the mapping between the extracted features and the AOAs remains an unsolved problem.

To solve the problem of direction finding when the AOAs of a testing sample are different from those in the training samples [8], it is common to use 01 vector as the model output. It is recognized that a NN for general direction finding is necessary to deal with the problem

effectively, but it is still unclear whether there are other effective modeling forms of the NN output.

Most current works consider the case of direction finding for a single central frequency explicitly or implicitly. For practical cases when multiple central frequencies are of interest, the frequency information must be considered which may significantly influence array manifold. Establishing a NN separately for each central frequency may be very time consuming and hard to implement in real time; hence, it is necessary to establish a unified NN which could handle direction finding for multiple central frequencies.

5. Concluding Remarks

The research and applications of machine learning-based direction finding are reviewed and discussed, with focus on application scenarios, concrete problems to be solved, and model inputs and outputs. Some future challenges and interesting research topics are also discussed. It has been twenty years since the initial use of machine learning techniques for direction finding, and it is expected that direction finding systems have better performance in more and more complex application scenarios with rapid development of dig data and deep learning techniques. And this all depends on continuous research on related theories and applications.

Conflicts of Interest

The authors declare that they have no conflicts of interest.

Acknowledgments

This work was support by No. 36 Research Institute of CETC under the project no. CX05.

References

- [1] C.-S. Shieh and C.-T. Lin, "Direction of arrival estimation based on phase differences using neural fuzzy network," *IEEE Transactions on Antennas and Propagation*, vol. 48, no. 7, pp. 1115–1124, 2000.
- [2] C. G. Christodoulou, J. A. Rohwer, and C. T. Abdallah, "The use of machine learning in smart antennas," vol. 1, pp. 321–324, in *Proceedings of the IEEE Antennas and Propagation*

- Society Symposium*, vol. 1, pp. 321–324, IEEE, Monterey, CA, USA, June 2004.
- [3] J. A. Rohwer, C. T. Abdallah, and C. G. Christodoulou, “Least squares support vector machines for direction of arrival estimation with error control and validation,” in *Proceedings of the GLOBECOM 2003*, pp. 2172–2176, San Francisco, CA, USA, December 2003.
 - [4] C. A. M. Lima, C. Junqueira, R. Suyama, F. J. V. Zuben, and J. M. T. Romano, “Least-square support vector machines for DoA estimation: a step-by-step description and sensitivity analysis,” in *Proceedings of International Joint Conference on Neural Networks*, pp. 3226–3231, IEEE, Montreal, Canada, July–August 2015.
 - [5] S. Vigneshwaran, N. Sundararajan, and P. Saratchandran, “Direction of arrival (DoA) estimation under array sensor failures using a minimal resource allocation neural network,” *IEEE Transactions on Antennas and Propagation*, vol. 55, no. 2, pp. 334–343, 2007.
 - [6] M. Dehghanpour, V. T. T. Vakili, and A. Farrokhi, “DoA estimation using multiple kernel learning SVM considering mutual coupling,” in *Proceedings of the 2012 Fourth International Conference on Intelligent Networking and Collaborative Systems*, IEEE, Bucharest, Romania, pp. 55–61, September 2012.
 - [7] R. Wang, B. Wen, and W. Huang, “A support vector regression-based method for target direction of arrival estimation from HF radar data,” *IEEE Geoscience and Remote Sensing Letters*, vol. 15, no. 5, pp. 674–678, 2018.
 - [8] Z.-M. Liu, C. Zhang, and P. S. Yu, “Direction-of-arrival estimation based on deep neural networks with robustness to array imperfections,” *IEEE Transactions on Antennas and Propagation*, vol. 66, no. 12, pp. 7315–7327, 2018.
 - [9] X. Xiao, S. Zhao, X. Zhong, D. L. Jones, E. S. Chng, and H. Li, “A learning-based approach to direction of arrival estimation in noisy and reverberant environments,” in *Proceedings of the ICASSP*, IEEE, Brisbane, Australia, pp. 2814–2818, April 2015.
 - [10] Y. Sun, J. Chen, C. Yuen, and S. Rahardja, “Indoor sound source localization with probabilistic neural network,” *IEEE Transactions on Industrial Electronics*, vol. 65, no. 8, pp. 6403–6413, 2018.
 - [11] Y.-K. Cheng, R. Y. Chang, and L.-J. Chen, “A comparative study of machine-learning indoor localization using FM and DVB-T signals in real testbed environments,” in *Proceedings of the 2017 IEEE 85th Vehicular Technology Conference*, IEEE, Sydney, Australia, pp. 1–7, June 2017.
 - [12] X. Yue, G. Qu, B. Liu, and A. Liu, “Detection sound source direction in 3D space using convolutional neural networks,” in *Proceedings of the First International Conference on Artificial Intelligence for Industries*, IEEE, Laguna Hills, CA, USA, pp. 81–84, September 2018.
 - [13] Q. Li, X. Zhang, and H. Li, “Online direction of arrival estimation based on deep learning,” in *Proceedings of the ICASSP 2018*, IEEE, Calgary, Canada, pp. 2616–2620, April 2018.
 - [14] S. S. Mane, S. G. Mali, and S. P. Mahajan, “Localization of steady sound source and direction detection of moving sound source using CNN,” in *Proceedings of the 10th ICCNT 2019*, IEEE-45670, Kanpur, India, July 2019.
 - [15] S. Chakrabarty and E. A. P. Habets, “Multi-speaker DOA estimation using deep convolutional networks trained with noise signals,” *IEEE Journal of Selected Topics in Signal Processing*, vol. 13, no. 1, pp. 8–21, 2019.
 - [16] A. Khan, S. Wang, and Z. Zhu, “Angle-of-arrival estimation using an adaptive machine learning framework,” *IEEE Communications Letters*, vol. 23, no. 2, pp. 294–297, 2019.
 - [17] A. Fahim, P. N. Samarasinghe, and T. D. Abhayapala, “Multi-source DOA estimation through pattern recognition of the modal coherence of a reverberant soundfield,” *IEEE/ACM Transactions on Audio, Speech, and Language Processing*, vol. 28, pp. 605–618, 2020.
 - [18] D. L. Zhong, X. K. Huang, and S. J. Zhang, “A novel algorithm for wideband DoA estimates based on neural network,” vol. 4, pp. 2167–2170, in *Proceedings of International Conference on Neural Networks*, vol. 4, pp. 2167–2170, IEEE, Houston, TX, USA, June 1997.
 - [19] L. Lizzi, G. Oliveri, P. Rocca, and A. Massa, “Estimation of the directions-of-arrival of correlated signals by means of a SVM-based multi-resolution approach,” in *Proceedings of the 2010 IEEE Antennas and Propagation Society International Symposium*, July 2010.
 - [20] K. Terabayashi, R. Natsuaki, and A. Hirose, “Ultrawideband direction-of-arrival estimation using complex-valued spatio-temporal neural networks,” *IEEE Transactions on Neural Networks and Learning Systems*, vol. 25, no. 9, pp. 1727–1732, 2014.
 - [21] W. Zhu and M. Zhang, “A deep learning architecture for broadband DOA estimation,” in *Proceedings of the 19th IEEE International Conference on Communication Technology*, pp. 244–247, IEEE, Xi’an, China, October 2019.
 - [22] W. Mack, U. Bharadwaj, S. Chakrabarty, and E. A. P. Habets, “Signal-aware broadband DOA estimation using attention mechanisms,” in *Proceedings of the ICASSP 2020*, pp. 4930–4934, Barcelona, Spain, May 2020.
 - [23] N. Xu, C. G. Christodoulou, and M. Martinez-Ramon, “Antenna array processing for radar applications using support vector machines,” in *Proceedings of the Antennas and Propagation Society International Symposium*, pp. 1295–1298, IEEE, Albuquerque, NM, USA, July 2006.
 - [24] R. Savitha, S. Vigneswaran, S. Suresh, and N. Sundararajan, “Adaptive beamforming using complex-valued radial basis function neural networks,” in *Proceedings of the TENCON*, pp. 1–6, IEEE, Singapore, Singapore, January 2009.
 - [25] B. Pei, H. Han, Y. Sheng, and B. Qiu, “Research on smart antenna beamforming by generalized regression neural network,” in *Proceedings of the 2013 IEEE International Conference on Signal Processing, Communication and Computing*, pp. 1–4, IEEE, KunMing, China, August 2013.
 - [26] D. Salvati, C. Drioli, and G. L. Foresti, “On the use of machine learning in microphone array beamforming for far-field sound source localization,” in *Proceedings of the 2016 IEEE International Workshop on Machine Learning for Signal Processing*, pp. 1–6, Vietri sul Mare, Italy, September 2016.
 - [27] Z. D. Zaharis, T. V. Yioultsis, C. Skeberies et al., “Implementation of antenna array beamforming by using a novel neural network structure,” in *Proceedings of the 2016 International Conference on Telecommunications and Multimedia*, pp. 1–5, IEEE, Heraklion, Greece, July 2016.
 - [28] S. Jha and T. Durrani, “Direction of arrival estimation using artificial neural networks,” *IEEE Transactions on Systems, Man, and Cybernetics*, vol. 21, no. 5, pp. 1192–1201, 1991.
 - [29] A. H. E. Zooghby, C. G. Christodoulou, and M. Georgiopoulos, “A neural network-based smart antenna for multiple source tracking,” *IEEE Transactions on Antennas and Propagation*, vol. 48, no. 5, pp. 768–776, 2000.
 - [30] A. H. E. Zooghby, H. L. Southall, and C. G. Christodoulou, “Experimental validation of a neural network direction finder,” vol. 3, pp. 1592–1595, in *Proceedings of the IEEE Antennas and Propagation Society International Symposium 1999 Digest*, vol. 3, pp. 1592–1595, IEEE, Orlando, FL, USA, July 1999.

- [31] A. H. E. Zooghby, C. G. Christodoulou, and M. Georgiopoulos, "Multiple Sources neural network direction finding with arbitrary separations," in *Proceedings of the 1998 IEEE-APS Conference on Antennas and Propagation for Wireless Communications*, pp. 57–60, IEEE, Waltham, MA, USA, November 1998.
- [32] A. H. E. Zooghby, C. G. Christodoulou, and M. Georgiopoulos, "Performance of radial-basis function networks for direction of arrival estimation with antenna arrays," *IEEE Transactions on Antennas and Propagation*, vol. 45, no. 11, pp. 1611–1617, 1997.
- [33] A. H. E. Zooghby, C. G. Christodoulou, and M. Georgiopoulos, "Antenna array signal processing with neural networks for direction of arrival estimation," vol. 4, pp. 2274–2277, in *Proceedings of the IEEE Antennas and Propagation Society International Symposium 1997 Digest*, vol. 4, IEEE, Montreal, Canada, July 1997.
- [34] H. M. Pour, Z. Atlasbaf, A. Mirzaee, and M. Hakkak, "A hybrid approach involving artificial neural network and ant colony optimization for direction of arrival estimation," in *Proceedings of the 2008 Canadian Conference on Electrical and Computer Engineering*, May 2008.
- [35] P. Zhang, "DoA estimation method based on neural network," in *Proceedings of the 2015 10th International Conference on P2P, Parallel Grid, Cloud and Internet Computing*, pp. 828–831, IEEE, Krakow, Poland, November 2015.
- [36] M. F. Unlarsen and E. Yaldiz, "Direction of arrival estimation by using artificial neural networks," in *Proceedings of the 2016 European Modelling Symposium*, IEEE, Pisa, Italy, pp. 242–245, November 2016.
- [37] J. S. Jeong, K. Araki, and J.-I. Takada, "A neural network for direction of arrival estimation under coherent multiple waves," in *Proceedings of the 1998 IEEE Asia-Pacific Conference on Circuits and Systems, Microelectronics and Integrating Systems*, pp. 495–498, IEEE, Chiangmai, Thailand, November 1998.
- [38] X. Tong, H. Wang, and Z. Gan, "Satellite interference location based on RBF neural network method," vol. 1, pp. 445–449, in *Proceedings of the 2000 5th International Conference on Signal Processing*, vol. 1, pp. 445–449, IEEE, Beijing, China, August 2000.
- [39] C. S. Lee, "Non-linear adaptive techniques for DoA estimation: a comparative analysis," in *Proceedings of the Electronic Technology Directions to the Year 2000*, pp. 72–77, IEEE, Adelaide, Australia, May 1995.
- [40] H. Chen, B. Li, and Z. Shen, "Efficient network training method for two-dimensional DoA estimation," in *Proceedings of the the Fourth International Conference on Computer and Information Technology*, pp. 1028–1032, IEEE, Wuhan, China, September 2004.
- [41] J. D. Ndaw, A. Faye, and A. S. Maiga, "Decoupled 2D DOA estimation using LVQ neural networks and UCA arrays," in *Proceedings of the 2016 IEEE Radio and Antenna Days of the Indian Ocean (RADIO)*, pp. 1–2, IEEE, St. Gilles-les-Bains, Reunion, October 2016.
- [42] T. Matsumoto and Y. Kuwahara, "Experiments of direction finder by RBF neural network with post processing," vol. 4A, pp. 10–13, in *Proceedings of the 2005 IEEE Antennas and Propagation Society International Symposium*, vol. 4A, pp. 10–13, IEEE, Washington, DC, USA, July 2005.
- [43] N. C. Raj, P. V. Aswathy, and K. V. Sagar, "Determination of angle of arrival using nonlinear support vector machine regressors," in *Proceedings of the IEEE-ICSCN*, pp. 512–515, IEEE, Chennai, India, February 2007.
- [44] K. A. Gotsis, K. Siakavara, and J. N. Sahalos, "On the direction of arrival (DoA) estimation for a switched-beam antenna system using neural networks," *IEEE Transactions on Antennas and Propagation*, vol. 57, no. 5, pp. 1399–1411, 2009.
- [45] K. A. Gotsis, T. Kaifas, K. Siakavara, and J. Sahalos, "Direction of arrival estimation for a switched-beam DS-CDMA system using neural networks," in *Proceedings of the 2007 19th International Conference on Applied Electromagnetics and Communications*, pp. 1–4, IEEE, Dubrovnik, Croatia, September 2007.
- [46] N. Fonseca, M. Coudyser, J.-J. Laurin, and J.-J. Brault, "On the design of a compact neural network-based DoA estimation system," *IEEE Transactions on Antennas and Propagation*, vol. 58, no. 2, pp. 357–366, 2010.
- [47] K. George and K. S. Sajjanshetty, "Neural network architectures for time-varying direction-of-arrival estimation," in *Proceedings of the 5th International Conference on Industrial and Information Systems*, pp. 69–74, IEEE, Mangalore, India, July-August 2010.
- [48] M. Agatonovic and Z. Stankovic, "Hybrid ANN model for accurate 2D DoA estimation of a radiating source," in *Proceedings of the TELSISKS*, pp. 370–373, IEEE, Nis, Serbia, October 2013.
- [49] M. Agatonovic, Z. Stankovic, and B. Milovanovic, "High resolution two-dimensional DoA estimation using artificial neural networks," in *Proceedings of the 2012 6th European Conference on Antennas and Propagation*, pp. 1–5, IEEE, Prague, Czech Republic, March 2012.
- [50] B. Milovanovic, M. Agatonovic, Z. Stankovic, N. Doncov, and M. Sarevska, "Application of neural networks in spatial signal processing," in *Proceedings of the 11th Symposium on Neural Network Applications in Electrical Engineering*, pp. 5–14, IEEE, Belgrade, Serbia, September 2012.
- [51] M. Agatonovic, Z. Stankovic, B. Milovanovic, and N. Doncov, "DoA estimation using radial basis function neural networks as uniform circular antenna array signal processor," in *Proceedings of the TELSISKS*, pp. 544–547, IEEE, Nis, Serbia, October 2011.
- [52] S. Caylar, "A new neural network DoA estimation technique based on subarray beamforming," in *Proceedings of the 2009 International Conference on Electromagnetics in Advanced Applications*, pp. 732–734, IEEE, Torino, Italy, September 2009.
- [53] S. Caylar, K. Leblebicioglu, and G. Dural, "A neural network method for direction of arrival estimation with uniform circular dipole array in the presence of mutual coupling," in *Proceedings of the 2007 3rd International Conference on Recent Advances in Space Technologies*, pp. 537–540, IEEE, Istanbul, Turkey, June 2007.
- [54] Faye, A. B. Youm, and J. D. Ndaw, "LVQ based DoA estimation," in *Proceedings of the 2013 fifth International Conference on Computational Intelligence, Communication Systems and Networks*, pp. 245–250, Madrid, Spain, June 2013.
- [55] Y. L. Sit, M. Agatonovic, and T. Zwick, "Neural network based direction of arrival estimation for a MIMO OFDM Radar," in *Proceedings of the 2012, Proceedings of the 9th European Radar Conference*, IEEE, Amsterdam, Netherlands, pp. 298–301, October–November 2012.
- [56] Z. Stankovic, N. Doncov, J. Russer, T. Asenov, and B. Milovanovic, "Efficient DoA estimation of impinging stochastic EM signal using neural networks," in *Proceedings of the 2013 International Conference on Electromagnetics in Advanced Applications*, pp. 575–578, IEEE, Torino, Italy, September 2013.
- [57] Z. Stankovic, N. Doncov, B. Milovanovic, and J. Russer, "Neural network approach for efficient DoA determination of

- multiple stochastic EM Sources in far-field,” in *Proceedings of the 2014 International Conference on Numerical Electromagnetic Modeling and Optimization for RF, Microwave, and Terahertz Applications*, pp. 1–4, IEEE, Pavia, Italy, May 2014.
- [58] Z. Stankovic, N. Doncov, I. Milovanovic, and B. Milvanovic, “Neural network model for efficient localization of a number of mutually arbitrary positioned stochastic EM sources in far-field,” in *Proceedings of the 2014 12th Symposium on Neural Network Applications in Electrical Engineering*, November 2014.
- [59] Z. Stankovic, N. Doncov, B. Milovanovic, J. Russer, I. Milovanovic, and M. Agatonovic, “Neural networks-based DoA estimation of multiple stochastic narrow-band EM sources,” vol. 2, pp. 526–529, in *Proceedings of the TELSIKS*, vol. 2, pp. 526–529, IEEE, Nis, Serbia, October 2013.
- [60] S. Chakrabarty and E. A. P. Habets, “Broadband DoA estimation using convolutional neural networks trained with noise signals,” in *Proceedings of the 2017 IEEE workshop on applications of signal processing to audio and acoustics*, pp. 136–140, IEEE, New Paltz, NY, USA, October 2017.
- [61] Faye, J. D. Ndaw, and A. S. Maiga, “Two-dimensional DoA estimation based on a single uniform linear array,” in *Proceedings of the 25th Telecommunications forum*, pp. 1–4, IEEE, Belgrade, Serbia, November 2017.
- [62] E. Efimov, T. Shevgunov, and D. Filimonova, “Angle of arrival estimator based on artificial neural network,” in *Proceedings of the 2016 17th International Radar Symposium*, pp. 1–3, IEEE, Krakow, Poland, May 2016.
- [63] H. Huang, J. Yang, H. Huang, Y. Song, and G. Gui, “Deep learning for super-resolution channel estimation and DOA estimation based massive MIMO system,” *IEEE Transactions on Vehicular Technology*, vol. 67, no. 9, pp. 8549–8560, 2018.
- [64] J. J. Tong and Y. F. Fang, “Robust sound localization of sound sources using deep convolution network,” in *Proceedings of the 2019 ICCA*, pp. 196–200, IEEE, Edinburgh, UK, July 2019.
- [65] Y. M. Wang and Y. L. Ma, “The performance of neural network for high resolution direction-of-arrival estimation,” in *Proceedings of the China 1991 International Conference on Circuit and Systems*, pp. 301–304, IEEE, Shenzhen, China, June 1991.
- [66] Y. Chen and C. Hou, “High resolution adaptive bearing estimation using a complex-weighted neural network,” in *Proceedings of the IEEE International Conference on Acoustics, Speech, and Signal Processing*, pp. 317–320, IEEE, San Francisco, CA, USA, March 1992.
- [67] S.-H. Chang, T.-Y. Lee, and W.-H. Fang, “High-resolution bearing estimation via unitary decomposition artificial neural network (UNIDANN),” in *Proceedings of the IEEE International Conference on Acoustics, Speech, and Signal Processing*, pp. 3607–3610, IEEE, Detroit, MI, USA, May 1995.
- [68] Y. Guo, Z. Zhang, Y. Huang, and P. Zhang, “DOA estimation method based on cascaded neural network for two closely spaced sources,” *IEEE Signal Processing Letters*, vol. 27, pp. 570–574, 2020.

Research Article

Single Snapshot DOA Estimation by Minimizing the Fraction Function in Sparse Recovery

Changlong Wang, Jibin Che , Feng Zhou, Jinyong Hou, and Chen Li

Key Laboratory of Electronic Information Countermeasure and Simulation Technology, Ministry of Education Xidian University, Xi'an, China

Correspondence should be addressed to Jibin Che; chejiben@126.com

Received 6 July 2020; Accepted 27 July 2020; Published 24 August 2020

Guest Editor: Jianfeng Li

Copyright © 2020 Changlong Wang et al. This is an open access article distributed under the Creative Commons Attribution License, which permits unrestricted use, distribution, and reproduction in any medium, provided the original work is properly cited.

Sparse recovery is one of the most important methods for single snapshot DOA estimation. Due to fact that the original l_0 -minimization problem is a NP-hard problem, we design a new alternative fraction function to solve DOA estimation problem. First, we discuss the theoretical guarantee about the new alternative model for solving DOA estimation problem. The equivalence between the alternative model and the original model is proved. Second, we present the optimal property about this new model and a fixed point algorithm with convergence conclusion are given. Finally, some simulation experiments are provided to demonstrate the effectiveness of the new algorithm compared with the classic sparse recovery method.

1. Introduction

The problem of estimating the direction of arrival (DOA) of signals impinging on an array of sensors is widely applied in radar, sonar, and wireless communication systems [1–9]. For fast-moving sources and multipath propagation problems, snapshots are limited, so high resolution adaptive DOA estimation approaches such as MVDR [10], MUSIC [11], and covariance matching methods [12, 13] fail due to inaccurate estimation of the spatial covariance matrix.

As one of the most important methods designed for single snapshot DOA estimation, sparse recovery has its own advantage for single snapshot case [14–17]. By dividing the angle range into grid points, the number of source is much less than that of grid points. By matching the grid points, these methods usually consider to solve the following l_0 -minimization:

$$\begin{aligned} \min \quad & \|x\|_0 \\ \text{s.t.} \quad & Ax = y, \end{aligned} \quad (1)$$

where $\|\cdot\|_0$ stands for the number of nonzero elements. In recent years, many sparse algorithms such as OMP and

l_1 -minimization [18–22] have been applied to solve this problem. Although a lot of work has given the rationality of sparse recovery algorithms [23–25], these conditions not only require the measurement matrix to meet the RIP condition, but also the corresponding RIC constant to meet certain conditions. However, verifying RIP conditions for a given matrix is itself an NP-hard problem, and the current RIP estimation conclusion is only valid for random matrices. However, DOA measurement matrix does not have such a random structure, so it is difficult to directly verify its RIP conditions. Therefore, there is no sufficient guarantee of model theory. In order to overcome these difficulties, we use the following fraction function:

$$g_p(x) = \frac{|x|}{\sqrt{x^2 + p}}, \quad (2)$$

to replace the original 0-norm. In Figure 1, it is easy to get that the new alternative function tends to 0-norm when $p \rightarrow 0$. Therefore, it is reasonable to believe this function is a good choice.

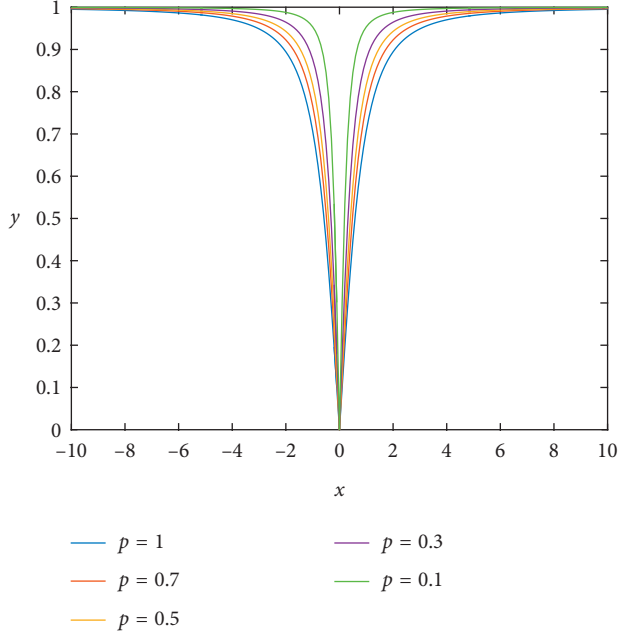


FIGURE 1: The graph of $g_p(x)$ with different p .

1.1. The Existed Main Problems of Classic Sparse DOA Estimation Methods. As the main idea of these methods, the real DOA is recovered by matching the real solution with the grid points. In order to deal with off-grid cases, we have to reduce the spacing between these points and increase the number of grid points. If we do not care about the hardware, the main problem caused by a big number of grid points is the measurement matrix A with high coherence $\mu(A)$ which leads to invalidation of the existed sparse methods, such as l_1 -minimization and OMP.

For a given matrix A , the coherence $\mu(A)$ is defined as

$$\mu(A) = \max_{i \neq j} \frac{A_i^T A_j}{\|A_i\|_2 \|A_j\|_2}. \quad (3)$$

In [24], OMP can recover the real sparse solution as long as the number of sources k satisfies the following inequalities:

$$k < \frac{1}{2} \left(1 + \frac{1}{\mu(A)} \right). \quad (4)$$

Meanwhile, it is obvious that the coherence will increase as long as the number of grid points increases. In Figure 2, the coherence of measurement matrices changes as the number of grid points increases, and it is obvious that OMP only can guarantee one source when the number of grid points is more than ten.

Besides, increasing the number of grid points also lead to the RIP condition deterioration of the measurement matrix. A matrix A is said to satisfy RIP of order $2k$ if and only if there exists a constant $\delta_{2k} \in (0, 1)$ such that

$$(1 - \delta_{2k})\|x\|_2^2 \leq \|Ax\|_2^2 \leq (1 + \delta_{2k})\|x\|_2^2, \quad (5)$$

for any $2k$ sparse vector x . It is obvious that δ_{2k} increases as the number of grid points increases until RIP is no longer

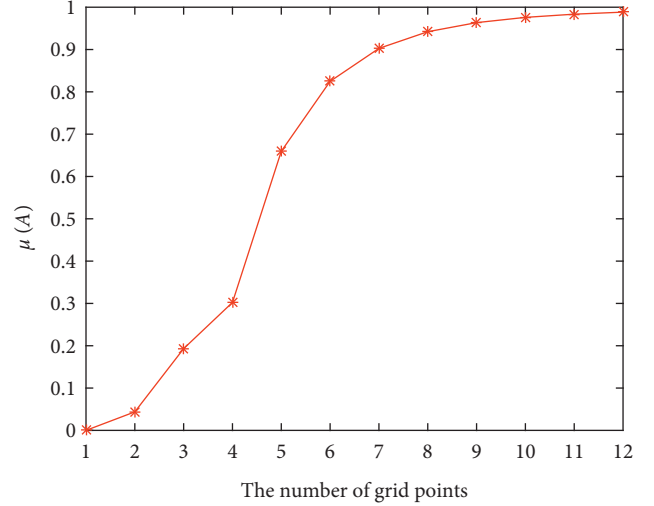


FIGURE 2: The relationship between $\mu(A)$ and the number of grid points.

satisfied. For the alternative method, [25] has proved that k sources can be recovered as long as $\delta_{2k} \leq (\sqrt{2}/2)$, and this condition is theoretical optimal.

Therefore, both greedy algorithms and l_1 -minimization are difficult to deal with situation when the number of grid points increases.

1.2. The Main Contribution of This Paper. To summarize, the main contribution of this paper can be expressed as follows:

- (1) In order to design a reasonable sparse recovery model for solving DOA estimation, we use the alternative function $g_p(\cdot)$ to replace 0-norm and give some theoretical analysis about the new alternative function
- (2) With theoretical guarantee about the new alternative model, we design a fixed iterative algorithm and the convergence conclusion is also given

This paper is organized as follows. In Section 2, we review the model processing of DOA estimation problem and give the upper number of sources that the sparse method can recover. We give a new alternative function $g_p(\cdot)$ for l_0 -minimization and prove the equivalence between the new models and the original sparse model both in noiseless and noise cases. By analysing the optimal property about this new model in Section 3, an algorithm designed for minimizing the fraction function $g_p(\cdot)$ and its convergence are presented. Some simulation experiments are given. Compared to some classic methods, the proposed method has a better result than others.

1.3. Symbols. Through this paper, we use $\theta^* \in \mathbb{R}^K$,

$$\theta^* = \{\alpha_1, \alpha_2, \dots, \alpha_K\}, \quad (6)$$

which stands for the real DOA solution, and use $\Theta \in \mathbb{R}^n$,

$$\Theta = \{\theta_1, \theta_2, \dots, \theta_n\}, \quad (7)$$

which stands for the grid point sets. For convenience, for $x \in \mathbb{R}^n$, its support is defined by $\text{suppt}(x) = \{i: x_i \neq 0\}$ and the cardinality of set Ω is denoted by $|\Omega|$. Let $\text{Ker}(A) = \{x \in \mathbb{R}^n: Ax = 0\}$ be the null space of the matrix A . We define subscript notation x_Ω to be such a vector that is equal to x on the index set Ω and zero everywhere else and use the subscript notation A_Ω to denote a submatrix whose columns are those of the columns of A that are in the set index Ω . Let Ω^c be the complement of Ω . For any positive integer n , we denote $[n] = \{1, 2, 3, \dots, n\}$.

2. Sparse DOA Estimation Model and Some Theory Analysis

2.1. Data Model. Assume that K far-field stationary and narrowband signals impinge on an M -element uniform linear array with DOAs of $\Theta^* = [\theta_1, \theta_2, \dots, \theta_K]$. For a given $\theta \in \mathbb{R}$, define a vector $A(\theta) \in \mathbb{R}^M$,

$$A(\theta)_m = \exp\left(-j2\pi(m-1)\left(\frac{d \cdot \sin \theta}{\lambda}\right)\right), \quad (8)$$

where $m \in [M]$ and where d is the distance between adjacent sensors and λ is the wavelength of the incident signals. Then, the array outputs of N snapshots can be expressed as

$$y(t) = A(\Theta^*)s(t) + n(t), \quad t = 1, 2, \dots, N, \quad (9)$$

where $s(t) = [s_1(t), s_2(t), \dots, s_K(t)]^T$ stands for far-field signals and $n(t)$ stands for the noise vector. $A(\Theta^*)$ is an $M \times K$ array manifold matrix, whose elements

$$A(\Theta^*) = [A(\theta_1), A(\theta_2), \dots, A(\theta_K)]. \quad (10)$$

We consider to recover θ^* from a grid points set $\Omega = \{\alpha_1, \alpha_2, \dots, \alpha_n\} \in \mathbb{R}^n$. If $\Theta^* \subseteq \Theta$, then there exist two mappings $\pi_{\Theta^*, \Omega}: [K] \rightarrow [n]$ and $\mu_{\Theta^*, \Omega}: \Theta^* \rightarrow \Omega$ such that

$$u_{\Theta^*, \Omega}(\theta_i) = \alpha_{\pi_{\Theta^*, \Omega}(i)}. \quad (11)$$

It is obvious that

$$A(\Theta)x^*(t) = y(t), \quad (12)$$

where

$$x^*(t)_i = \begin{cases} s_{\pi_{\Theta^*, \Omega}(i)}(t), & i \in \pi_{\Theta^*, \Omega}([K]), \\ 0, & \text{else.} \end{cases} \quad (13)$$

Once $n \gg M$ and $N = 1$, we can recover Θ^* via the following l_0 -minimization:

$$\begin{aligned} \min_{x \in \mathbb{R}^n} & \|x\|_0 \\ \text{s.t.} & A(\Omega)x = y(t). \end{aligned} \quad (14)$$

Then, we can recover Θ^* by $\text{suppt}(x) = \{i \in [n] \mid \|x_i\|_2 > 0\}$.

2.2. Sparse DOA Estimation via Minimizing Fraction Function. As one of the most important methods designed for single snapshot DOA estimation, the following theorem shows the upper bound on the number of sources by the sparse method.

Theorem 1. For the measurement matrix $A(\Omega) \in \mathbb{C}^{M \times n}$ defined in (10), if $\theta^* \subseteq \Theta$, $K < ((M+1)/2)$ and there is no noise during the measurement; then, the real solution Θ^* of DOA estimation can be recovered by l_0 -minimization (14), i.e.,

$$\Theta^* = \{\alpha_i \mid i \in \text{suppt}(x)\}, \quad (15)$$

where x is the solution of model (14).

Proof. Without loss of generality, we consider the following vector $x^* \in \mathbb{R}^n$:

$$x_i^* = \begin{cases} s_{\pi_{\Theta^*, \Omega}(i)}, & i \in \pi_{\Theta^*, \Omega}([K]), \\ 0, & \text{else.} \end{cases} \quad (16)$$

It is obvious that $A(\Omega)x^* = y$ and $\|x^*\|_0 \leq K$. Therefore, it is enough to prove that x^* is the sparsest solution of $A(\Omega)x^* = y$.

If there exists another solution $z^* \in \mathbb{R}^n$ such that

$$A(\Omega)z^* = y, \quad (17)$$

$$\|z^*\|_0 < \|x^*\|_0 \leq K.$$

Therefore, we can get that $z^* - x^* \in \text{Ker}(A(\Omega))$ and

$$\|z^* - x^*\|_0 \leq \|z^*\|_0 + \|x^*\|_0 \leq 2K \leq M, \quad (18)$$

since $K < M + (1/2)$.

However, for the given Vandermonde matrix $A(\Omega)$, it is obvious that any of its submatrix of order M is a full-rank matrix; i.e., for $\forall S \in [n]$, we have that

$$|A(\Omega)_S| = \prod_{\substack{u, v \in S \\ u < v}} \left(\exp\left(\frac{-j2\pi d \cdot \sin \theta_u}{\lambda}\right) - \exp\left(\frac{-j2\pi d \cdot \sin \theta_v}{\lambda}\right) \right) \neq 0, \quad (19)$$

since $\theta_u \neq \theta_v$, which is contradict conclusion (18).

By Theorem 1, the performance of the sparse recovery method is clearly demonstrated. In practices, we usually consider the following model because of noise:

$$\begin{aligned} \min_{x \in \mathbb{R}^n} & \|x\|_0 \\ \text{s.t.} & \|A(\Omega)x - y\|_f \leq \varepsilon, \end{aligned} \quad (20)$$

where $\|\cdot\|_f$ stand for a certain norm. Similar to discussion above, in this paper, we use the following $l_{g_p}^f(\varepsilon)$ -minimization model instead of (20):

$$\begin{aligned} \min_{x \in \mathbb{R}^n} & \|x\|_{g_p} \\ \text{s.t.} & \|A(\Omega)x - y\|_f \leq \varepsilon. \end{aligned} \quad (21)$$

Before, we prove the equivalence between (20) and (21), some lemmas are needed. The following lemma is easy to get by the definition of $\|\cdot\|_0$, and we leave the proof to the readers. \square

Lemma 1. *If x^* is the solution of l_0 -minimization (22), then the column vectors belong to $\text{supp}(x^*)$ are linearly independent.*

Lemma 2. *If x^* is the solution of $l_{g_p}^f(\varepsilon)$ -minimization (23), then the column vectors belong to $\text{supp}(x^*)$ are linearly independent.*

Proof. If the submatrix $A_{\text{supp}(x^*)}$ is not full rank, then there exists a vector $h \in \text{Ker}(A)$ such that $\text{supp}(h) \subseteq \text{supp}(x^*)$. For such x^* and h , let

$$a = \max_{h_i \neq 0} \frac{|x_i^*|}{|h_i|}. \quad (22)$$

Therefore, it is easy to get that

$$\text{sgn}(x_i^* + ah_i) = \text{sgn}(x_i^* - ah_i) = \text{sgn}(x_i^*), \quad (23)$$

for $\alpha \in [0, a]$ with $x_i^* \neq 0$.

Since $g_p(x)$ is a concave function when $x \geq 0$, it is easy to get that

$$\begin{aligned} g_p(x_i^*) &= g_p\left(\frac{1}{2}x_i^* + ah_i + \frac{1}{2}x_i^* - ah_i\right) \geq \frac{1}{2}g_p(x_i^* + ah_i) \\ &\quad + \frac{1}{2}g_p(x_i^* - ah_i). \end{aligned} \quad (24)$$

Therefore, we can get that

$$g_p(x_i^*) \geq \frac{1}{2}g_p(x_i^* + ah_i) + \frac{1}{2}g_p(x_i^* - ah_i), \quad (25)$$

and it is easy to get that

$$\|x^*\|_{g_p} \geq \frac{1}{2}\|x^* + ah\|_{g_p} + \frac{1}{2}\|x^* - ah\|_{g_p}, \quad (26)$$

which contradicts the assumptions.

In order to extend of application of $g_p(\cdot)$ in sparse recovery, we consider the following models, $F_0(r)$ -minimization and $F_{g_p}(r)$ -minimization. Furthermore, (20) and (21) can be treated as special cases of these two models:

$$\begin{aligned} \min \quad & \|x\|_0 \\ \text{s.t.} \quad & \begin{cases} Ax \leq b, \\ \|x\|_\infty \leq r, \end{cases} \end{aligned} \quad (27)$$

$$\begin{aligned} \min \quad & \|x\|_{g_p} \\ \text{s.t.} \quad & \begin{cases} Ax \leq b, \\ \|x\|_\infty \leq r. \end{cases} \end{aligned} \quad (28)$$

Next, the following theorem shows the equivalence between $F_0(r)$ -minimization and $F_{g_p}(r)$ -minimization. \square

Theorem 2. *For any A, b , and r , there exists a constant $p^*(A, b, r)$ such that the solution of $F_{g_p}(r)$ -minimization (28) also solves $F_0(r)$ -minimization (27) whenever $0 < p < p^*(A, b, r)$.*

Proof. It is easy to get the constraint region in model (27) and model (28) are polygons which is a convex combination of its limited extreme points.

Define a set $V = \{v \in \mathbb{R}^n \mid v_i \in \{-1, 0, 1\}\}$, and $\|\cdot\|_{g_p}$ is a concave function for a given quadrant $\{x \mid \text{sgn}(x) = v, v \in V\}$ so the solution of the following problem must be contained in the extreme points of the convex polygon $\{x \in \mathbb{R}^n \mid \text{sgn}(x) = v, Ax \leq y, \|x\|_\infty \leq r\}$:

$$\begin{aligned} \min_{\text{sgn}(x)=v} \quad & \|x\|_{g_p} \\ \text{s.t.} \quad & \begin{cases} Ax \leq y, \\ \|x\|_\infty \leq r. \end{cases} \end{aligned} \quad (29)$$

Since the number of quadrants in \mathbb{R}^n is limited, so there exists a limited point set \widehat{V} such that model (28) is equal to

$$\begin{aligned} \min_{x \in \widehat{V}} \quad & \|x\|_{g_p} \\ \text{s.t.} \quad & \begin{cases} Ax \leq y, \\ \|x\|_\infty \leq r. \end{cases} \end{aligned} \quad (30)$$

For such limited points set \widehat{V} , define its subset V^* as

$$V^* = \{x \in \widehat{V} \mid \|x\|_0 \leq \|y\|_0, \forall y \in \widehat{V}\}. \quad (31)$$

Since $\|\cdot\|_{g_p}$ is a continuous function and the element number of \widehat{V} is limited, we can define a constant $p^*(A, y, r)$ such that

$$\|x\|_{g_p} < \|y\|_{g_p}, \quad (32)$$

for any $x \in V^*$, $y \in \widehat{V} \setminus V^*$, and $0 < p < p^*(A, y, r)$. Finally, it is obvious that the elements of V^* also solve $F_0(r)$ -minimization (27) since $\|\cdot\|_{g_p}$ is a continuous function.

The proof is completed. \square

Corollary 1. *For the noiseless cases and the measurement matrix $A(\Omega) \in \mathbb{C}^{M \times n}$ defined in (10), if $\Theta^* \subseteq \Omega$ and $K < ((M + 1)/2)$, then there exists a constant $p^*(A, y)$ such that the real solution Θ^* of DOA estimation can be recovered by both model (20) and model (21) whenever $0 < p < p^*(A, y)$.*

Proof. By Lemma 2, it is obvious that both of model (20) and model (21) are equal to the themselves with a bounded constrained $\|x\|_\infty \leq T(A(\Omega), y)$, where

$$T(A(\Omega), y) = \min_{x_i \neq 0} \{x_i \mid A(\Omega)x = y, \text{rank}(A(\Omega)_{\text{supp}(x)}) = \|x\|_0\}. \quad (33)$$

Since the solution x of $Ax = y$ with $A_{\text{supp}(x)} = \|x\|_0$ is limited, it is impossible to calculate $T(A(\Omega), y)$ for given $A(\Omega)$ and y .

By Theorem 1, we can conclude the equivalence between model (27) and model (28), and the proof is completed. \square

Corollary 2. *Let $f = 1$ or $f = \infty$, then there exists a constant $p_f^*(A, b, \varepsilon)$ such that the solution of $l_{g_p}^f(\varepsilon)$ -minimization (28) also solves $l_{g_p}^f(\varepsilon)$ -minimization (27) whenever $0 < p < p_f^*(A, b, \varepsilon)$.*

Proof. By the prove in Theorem 1, it is enough to prove the constraint zone in (27) and (28) are polytopes. By Lemmas 1 and 2 and (33), it is easy to find that the solutions of (27) and (28) are contained in a bounded zone.

When $f = 1$ or $f = \infty$, the constraint zone $\|Ax - y\|_f$ can be rewritten as

$$\begin{aligned} \Delta(Ax - y) &\leq \varepsilon 1, \\ -\varepsilon 1 + y &\leq Ax \leq \varepsilon 1 + y, \end{aligned} \quad (34)$$

where the matrix $\Delta \in \mathbb{R}^{2^n \times n}$ with $\Delta_{i,j} \in \{-1, 1\}$ stands for the whole permutations by $-1, 1$.

The proof is completed. \square

3. A Sparse Recovery Algorithm Designed for DOA Estimation

In Section 2, we show the theoretical performance of DOA sparse methods and the equivalence between the alternative function $g_p(\cdot)$ and the original 0-norm. In this section, we will focus on the algorithm designed for DOA estimation. As the theoretical basis for new algorithm, the following theorem shows us the local property of l_{g_p} -minimization.

Theorem 3. *If $\Theta^* \subseteq \Omega$, $2K < m + 1$, and $0 < p < p^*(A(\Omega), y)$, then x^* is the solution of model (14):*

$$x_i^* = \begin{cases} s_{\pi_{\Theta^*, \Omega}(i)}, & i \in \pi_{\Theta^*, \Omega}([K]), \\ 0, & \text{else,} \end{cases} \quad (35)$$

and x^* satisfies the following equalities:

$$x^* = \Gamma(x^*)A^T(A\Gamma(x^*)A^T)^\dagger y, \quad (36)$$

where $\Gamma(x)$ is a diagonal matrix with $\Gamma(x)_{i,i} = (|x_i| (x_i^2 + p)^{1.5}/p)$.

Proof. Without loss of generality, we assume that $\text{supp}(x) = [K]$ and consider the following problem:

$$\begin{aligned} \min_{t \in \mathbb{R}^s} \quad & \|t\|_{g_p} \\ \text{s.t.} \quad & Bt = y, \end{aligned} \quad (37)$$

where $B = A(\Omega)_{[K]}$. It is obvious that $x_{[K]}$ is the solution of model (37) and there exists a constant η small enough such that the function $\|\cdot\|_{g_p}$ is differentiable at the point $x = x_{[K]}$ when $\|t - x_{[K]}\|_2 \leq \eta$. Therefore, KKT condition can be applied in such area. Define the Lagrange function $L(t, \lambda)$ as follows:

$$L(t, \lambda) = \|t\|_{g_p} - \lambda^T (Bt - y). \quad (38)$$

Therefore, $x_{[K]}$ must be the solution of the following equations:

$$\begin{cases} \left. \frac{\partial L}{\partial x} \right| = 0, \\ Bt = y. \end{cases} \quad (39)$$

To solve equation (39), we can get that

$$\begin{aligned} \lambda^* &= (BF(z)B^T)^{-1}b, \\ x_{[K]} &= \Gamma(x_{[K]})B^T(B\Gamma(x_{[K]})B^T)^{-1}y. \end{aligned} \quad (40)$$

Since $\text{supp}(x^*) = [K]$, it is easy to get that

$$x = \Gamma(x)A(\Omega)^T(A(\Omega)\Gamma(x)A(\Omega)^T)^{-\dagger}y. \quad (41)$$

By analysis expression (36), a fixed point iterative algorithm is presented in Algorithm 1. Next, the following theorem shows the convergence conclusion of this new algorithm. \square

Theorem 4. *The sequence $\{x^k\}$ produced by*

$$x^{k+1} = \Gamma(x^k)A^T(A\Gamma(x^k)A^T)^\dagger y, \quad (42)$$

satisfies the following equality:

$$\|x^{k+1}\|_{g_p} \leq \|x^k\|_{g_p}, \quad (43)$$

and the limit point x^* satisfies equality (36).

Proof. Since $x^{k+1} = \Gamma(x^k)A^T(A\Gamma(x^k)A^T)^\dagger y$, it is obvious that

$$\begin{cases} \Gamma(x^k)^\dagger x^{k+1} = A^T(A\Gamma(x^k)A^T)^\dagger y, \\ Ax^{k+1} = y. \end{cases} \quad (44)$$

Therefore, we can conclude that x^{k+1} is the solution of the following problem:

$$\begin{aligned} \min_x \quad & x^T \Gamma(x^k)^\dagger x \\ \text{s.t.} \quad & Ax = y, \end{aligned} \quad (45)$$

i.e.,

$$\sum_{x_i^k \neq 0} \frac{g_p(x_i^k)}{|x_i^k|} (x_i^{k+1})^2 \leq \sum_{x_i^k \neq 0} g_p(x_i^k) |x_i^k|. \quad (46)$$

By the expression of $g_p(\cdot)$, it is easy to get that

$$g_p(x_i^{k+1}) - \frac{g_p'(x_i^k)(x_i^{k+1})^2}{2|x_i^k|} \leq g_p(x_i^k) - \frac{|x_i^k|g_p'(x_i^k)}{2}. \quad (47)$$

By (46) and (47), we can conclude that

$$\|x^{k+1}\|_{g_p} \leq \|x^k\|_{g_p}. \quad (48)$$


```

Require:  $A \in \mathbb{R}^{m \times n}, b \in \mathbb{R}^n, p, x^1$ 
Ensure:  $x^*$ 
 $F = \Gamma(x^1)$ 
for  $k = 1, 2, \dots$  until convergence do
   $x^{k+1} = FA^T(AFA^T)^\dagger b$ 
   $F = \Gamma(x^{k+1})$ 
   $k = k + 1$ 
end for
 $x^* = x^{k+1}$ 

```

ALGORITHM 1: An sparse recovery algorithms for DOA estimation.

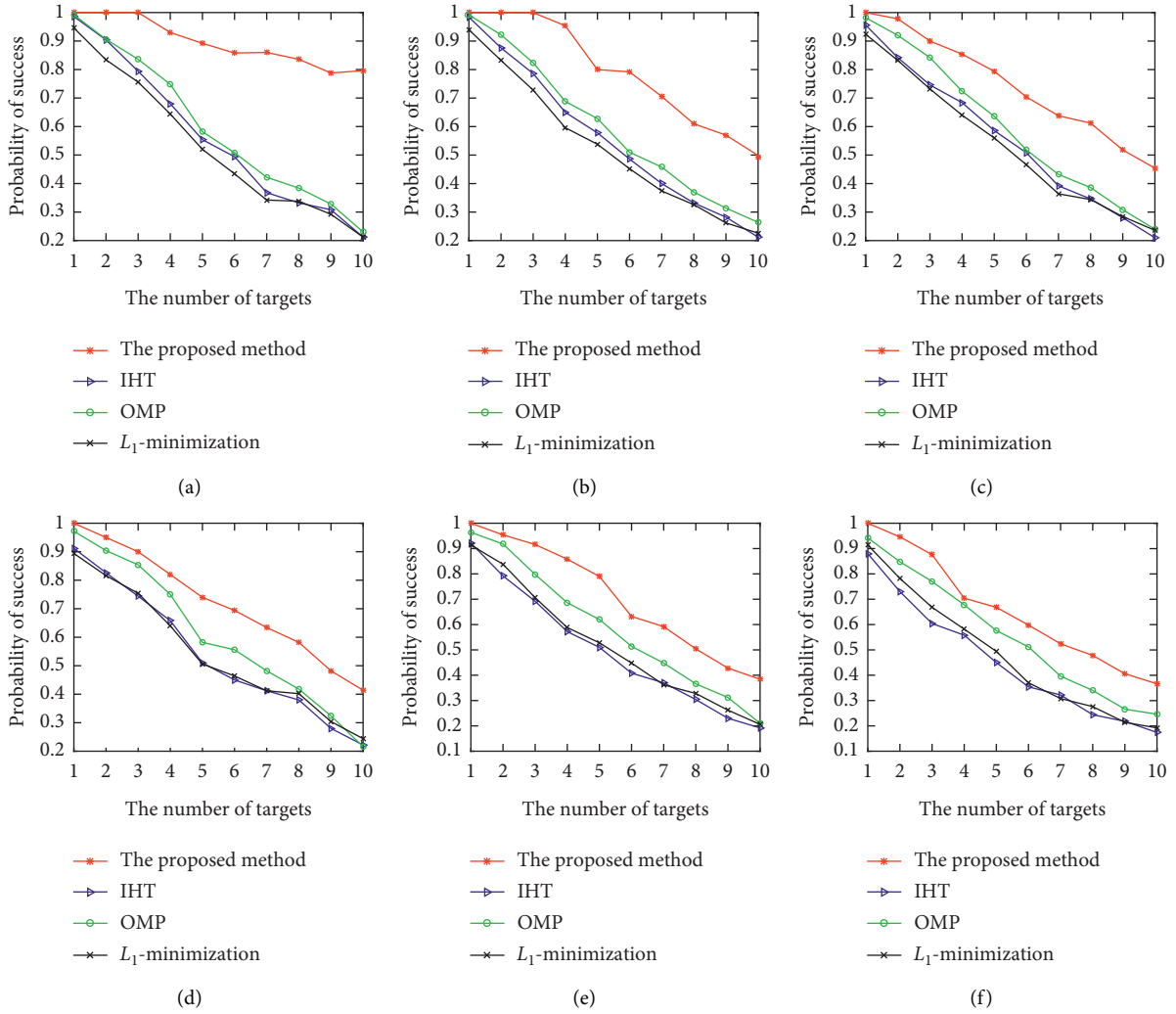


FIGURE 3: The result of the proposed method and classic method: (a) 80 dB, (b) 20 dB, (c) 15 dB, (d) 10 dB, (e) 5 dB, and (f) 0 dB.

Since $\|\cdot\|_{g_p} \geq 0$ and $\|x\|_{g_p} = 0$ if and only if $x = 0$, the sequence $\|x^{k+1}\|_{g_p}$ is convergent and the limit point x^* is the solution of

$$\begin{aligned} \min_x \quad & x^T \Gamma(x^*)^\dagger x \\ \text{s.t.} \quad & Ax = y. \end{aligned} \quad (49)$$

By the Lagrange function of (49), we can get the conclusion of this theorem.

Next, we will give some experiment results to show the effective of the proposed method. In Figure 3, we consider the case when $\Theta^* \subseteq \Omega$. In this experiments, we take $M = 40$ and $n = 180$, and the range of angle is $[-90^\circ, 90^\circ]$. Under different SNR 80 dB, 20 dB, 15 dB, 10 dB, 5 dB, and 0 dB, it is

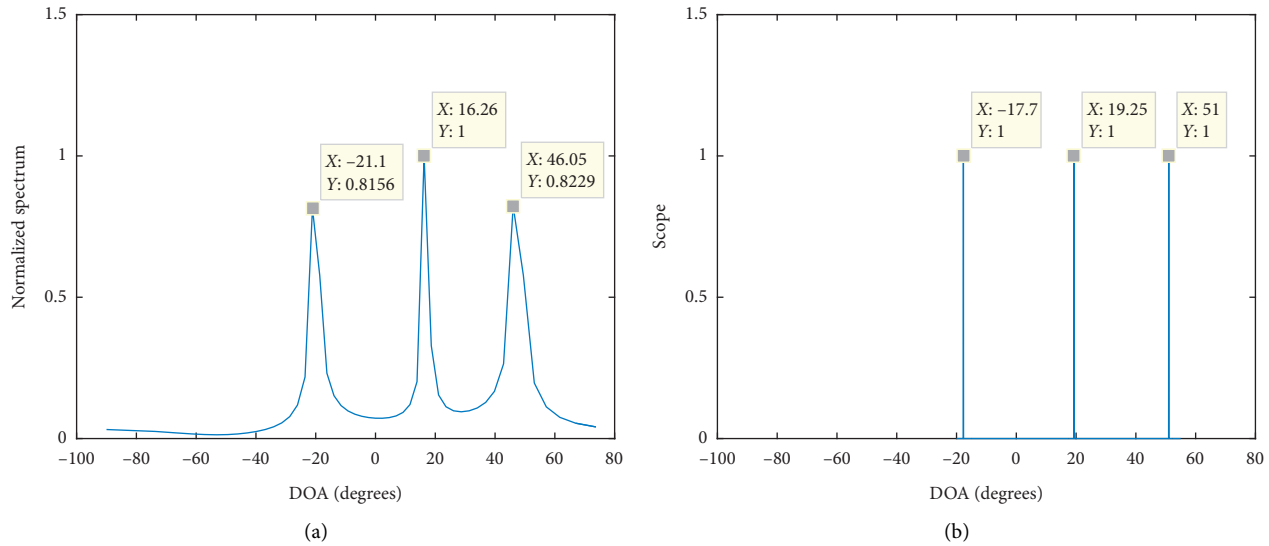


FIGURE 4: The result of the proposed method and classic method: (a) the estimation of real solution and (b) the result of the proposed method.

obvious that the proposed method has a better result than other classic algorithms and it should be emphasized that the proposed method can recover 10 sources which are much closer to theoretical optimal value in Theorem 1. \square

For off-grid case, we give a reasonable estimation of the real solution by FFT [26] and then divide the responding zone to match the real solution by a more nuanced division. In Figure 4, the real DOA solution $\Theta^* = \{-17.7^\circ, 19.25^\circ, 51^\circ\}$, the left one shows us a rough estimation of real solution by FFT, then we divide 200 grid points around -21.1° , 16.26° and 46.05° with a 0.1° interval, the right one shows the result of a more precise segmentation by the estimation.

4. Conclusion

In this paper, we consider the alternative function $g_p(x)$ to replace 0-norm. Furthermore, the equivalence relationship between these two models is presented. Although $g_p(x)$ is not a smooth function, we give an analysis expression of its local optimal solution and a fixed point algorithm. Finally, we use this new alternative function to solve DOA estimation problem. Compared to some classic algorithms, the result of our method is better than the classic algorithms. In conclusion, the authors hope that in publishing this paper, a brick will be thrown out and be replaced with a gem.

Data Availability

The data used to support the findings of this study are available from the corresponding author upon request.

Conflicts of Interest

The authors declare that there are no conflicts of interest regarding the publication of this paper.

Acknowledgments

This paper was funded in part by the China Postdoctoral Science Foundation, grant numbers 2017M613076 and 2016M602775; in part by the National Natural Science Foundation of China, grant numbers 61801347, 61801344, 61522114, 61471284, 61571349, 61631019, 61871459, 61801390, and 11871392; by the Fundamental Research Funds for the Central Universities, grant numbers XJS17070, NSIY031403, and 3102017jg02014; in part by the Aeronautical Science Foundation of China, grant number 20181081003; and by the Science, Technology, and Innovation Commission of Shenzhen Municipality, grant number JCYJ20170306154716846.

References

- [1] L. Wan, G. Han, L. Shu, S. Chan, and T. Zhu, "The application of DOA estimation approach in patient tracking systems with high patient density," *IEEE Transactions on Industrial Informatics*, vol. 12, no. 6, pp. 2353–2364, 2016.
- [2] X. Wang, L. Wan, M. Huang, C. Shen, Z. Han, and T. Zhu, "Low-complexity channel estimation for circular and non-circular signals in virtual MIMO vehicle communication systems," *IEEE Transactions on Vehicular Technology*, vol. 69, no. 4, pp. 3916–3928, 2020.
- [3] H. Wang, L. Wan, M. Dong, K. Ota, and X. Wang, "Assistant vehicle localization based on three collaborative base stations via SBL-based robust DOA estimation," *IEEE Internet of Things Journal*, vol. 6, no. 3, pp. 5766–5777, 2019.
- [4] X. Wang, L. Wan, M. Huang, C. Shen, and K. Zhang, "Polarization channel estimation for circular and non-circular signals in massive MIMO systems," *IEEE Journal of Selected Topics in Signal Processing*, vol. 13, no. 5, pp. 1001–1016, 2019.
- [5] F. Wen and J. Shi, "Fast direction finding for bistatic EMVS-MIMO radar without pairing," *Signal Processing*, vol. 173, Article ID 107512, 2020.
- [6] H. Chen, Y. Liu, Q. Wang, W. Liu, and G. Wang, "Two-dimensional angular parameter estimation for noncircular

- incoherently distributed sources based on an L-shaped array,” *IEEE Sensors Journal*, 2020.
- [7] Z. Zheng, Y. Huang, W.-Q. Wang, and H. C. So, “Direction-of-arrival estimation of coherent signals via coprime array interpolation,” *IEEE Signal Processing Letters*, vol. 27, pp. 585–589, 2020.
- [8] H. Chen, W. Wang, and W. Liu, “Augmented quaternion ESPRIT-type DOA estimation with a crossed-dipole array,” *IEEE Communications Letters*, vol. 24, no. 3, pp. 548–552, 2020.
- [9] Y.-Y. Dong, C.-X. Dong, W. Liu, M.-M. Liu, and Z.-Z. Tang, “Scaling transform based information geometry method for DOA estimation,” *IEEE Transactions on Aerospace and Electronic Systems*, vol. 55, no. 6, pp. 3640–3650, 2019.
- [10] J. Capon, “High-resolution frequency-wavenumber spectrum analysis,” *Proceedings of the IEEE*, vol. 57, no. 8, pp. 1408–1418, 1969.
- [11] J. Li, D. Li, D. Jiang, and X. Zhang, “Extended-aperture unitary root MUSIC-based DOA estimation for coprime array,” *IEEE Communications Letters*, vol. 22, no. 4, pp. 752–755, 2018.
- [12] P. Stoica and P. Babu, “SPICE and LIKES: two hyperparameter-free methods for sparse-parameter estimation,” *Signal Processing*, vol. 92, no. 7, pp. 1580–1590, 2012.
- [13] Y. Wei and X. Guo, “Pair-matching method by signal covariance matrices for 2D-DOA estimation,” *IEEE Antennas and Wireless Propagation Letters*, vol. 13, pp. 1199–1202, 2014.
- [14] C. Zeng, S. Zhu, S. Li, Q. Liao, and L. Wang, “Sparse frame DOA estimations via a rank-one correlation model for low SNR and limited snapshots,” *Applied and Computational Harmonic Analysis*, vol. 41, no. 2, pp. 362–383, 2016.
- [15] A. Chinatto, E. Soubies, C. Junqueira et al., “L0-optimization for channel and DOA sparse estimation,” in *Proceedings of the International Workshop on Computational Advances in Multi-Sensor Adaptive Processing (CAMSAP)*, IEEE, Cancun, Mexico, December 2016.
- [16] J. Cai, D. Bao, P. Li, J. Cai, D. Bao, and P. Li, “DOA estimation via sparse recovering from the smoothed covariance vector,” *Journal of Systems Engineering and Electronics*, vol. 27, no. 3, pp. 555–561, 2016.
- [17] X. Li, Z. X. Wei, and Z. Ye, “DOA estimation based on sparse signal recovery utilizing weighted l_1 -norm penalty,” *IEEE Signal Processing Letters*, vol. 19, no. 3, pp. 155–158, 2012.
- [18] M. Emadi, J. E. Miandji, and J. Unger, “OMP-based DOA estimation performance analysis,” *Digital Signal Processing*, vol. 79, pp. 57–65, 2018.
- [19] X. Zhang, Y. Li, Y. Yuan, T. Jiang, and Y. Yuan, “Low-complexity DOA estimation via OMP and majorization-minimization,” in *Proceedings of the 2018 IEEE Asia-Pacific Conference on Antennas and Propagation (APCAP)*, August 2018.
- [20] Y. Chen, W. Wang, Z. Wang, and B. Xia, “A source counting method using acoustic vector sensor based on sparse modeling of DOA histogram,” *IEEE Signal Processing Letters*, vol. 26, no. 1, pp. 69–73, 2019.
- [21] F. Liu, L. Peng, M. Wei, P. Chen, and S. Guo, “An improved L1-SVD algorithm based on noise Subspace for DOA estimation,” *Progress In Electromagnetics Research C*, vol. 29, pp. 109–122, 2012.
- [22] R. Wei, Q. Wang, and Z. Zhao, “Two-dimensional DOA estimation based on separable observation model utilizing weighted L1-norm penalty and bayesian compressive sensing strategy,” in *Proceedings of the 2017 4th International Conference on Information Science and Control Engineering (ICISCE)*, IEEE, Changsha, China, July 2017.
- [23] J. Peng, S. Yue, and H. Li, “NP/CMP equivalence: a phenomenon hidden among Sparsity models l_0 minimization and l_p minimization for information processing,” *IEEE Transactions on Information Theory*, vol. 61, no. 7, pp. 4028–4033, 2015.
- [24] S. Fourcart and H. Rauhut, *A Mathematical Introduction to Compressive Sensing*, Springer-Verlag, Berlin, Germany, 2013.
- [25] T. T. Cai and A. Zhang, “Sharp RIP bound for sparse signal and low-rank matrix recovery,” *Applied and Computational Harmonic Analysis*, vol. 35, no. 1, pp. 74–93, 2013.
- [26] C. J. Lam and A. C. Singer, “Bayesian beamforming for DOA uncertainty: theory and implementation,” *IEEE Transactions on Signal Processing*, vol. 54, no. 11, pp. 4435–4445, 2006.

Research Article

Sparsity-Based DOA Estimation with Gain and Phase Error Calibration of Generalized Nested Array

Ziang Feng , Guoping Hu, and Hao Zhou

Air and Missile Defence College, Air Force Engineering University, Xi'an 710051, China

Correspondence should be addressed to Ziang Feng; netbigangang@163.com

Received 24 May 2020; Revised 30 June 2020; Accepted 6 July 2020; Published 31 July 2020

Academic Editor: Fangqing Wen

Copyright © 2020 Ziang Feng et al. This is an open access article distributed under the Creative Commons Attribution License, which permits unrestricted use, distribution, and reproduction in any medium, provided the original work is properly cited.

Sparse arrays, which can localize multiple sources with less physical sensors, have attracted more attention since they were proposed. However, for optimal performance of sparse arrays, it is usually assumed that the circumstances are ideal. But in practice, the performance of sparse arrays will suffer from the model errors like mutual coupling, gain and phase error, and sensor's location error, which causes severe performance degradation or even failure of the direction of arrival (DOA) estimation algorithms. In this study, we follow with interest and propose a covariance-based sparse representation method in the presence of gain and phase errors, where a generalized nested array is employed. The proposed strategy not only enhances the degrees of freedom (DOFs) to deal with more sources but also obtains more accurate DOA estimations despite gain and phase errors. The Cramer–Rao bound (CRB) derivation is analyzed to demonstrate the robustness of the method. Finally, numerical examples illustrate the effectiveness of the proposed method from DOA estimation.

1. Introduction

Superresolution direction finding is a key branch of signal processing, which has received much attention in many fields like radar systems, communication, and navigation [1, 2]. In the last decades, the research of direction of arrival (DOA) estimation has successively gone through three stages: adaptive beamforming, subspace decomposition (such as multiple signal classification (MUSIC) [3], estimation of signal parameters via the rotational invariance technique (ESPRIT) [4], etc.), and subspace fitting (such as maximum-likelihood (ML) algorithm [5], weighted subspace fitting (WSF) algorithm [6], etc.). With the development of the algorithms, issues such as aperture expansion, optimization of hardware resource requirements, array structure design, and resolution accuracy improvement [7, 8] have been gradually solved, laying a solid foundation for further broadening the application prospects.

However, the uniform linear array (ULA) is always applied in most of the traditional DOA estimation methods due to modeling and computation convenience. For ULAs, most $N - 1$ sources can be detected with N physical sensors.

Besides, the arrangement of ULAs will make it difficult to achieve in some scenarios and increase the system cost. Several sparse arrays are designed in this context. Nested array [9] and coprime array [10] are the most representative geometries, which can resolve $O(MN)$ sources with only $M + N - 1$ physical sensors. Attracted by the effectiveness of sparse array (e.g., enhancing degrees of freedom, reducing mutual coupling, and eliminating angle ambiguity), a series of DOA estimation algorithms have been developed [11–19]. A spatial smoothing method was proposed in [8], which achieved superresolution direction finding for sparse arrays. However, discrete virtual elements limit the ability to detect more sources by utilizing the spatial smoothing method. In order to improve the utilization of the discrete virtual elements, the multifrequency high-order cumulant algorithms were proposed in [13] and virtual array interpolation methods were introduced to build a nonuniform virtual array by the idea of array interpolation [14, 15]. To achieve better estimation performance, the category of sparse reconstruction algorithms, which can also be utilized to deal with the coherent sources, was extended to sparse arrays [16–19]. Another method of taking advantage of difference

coarray is array geometry optimization method; the super nested array (SNA) and generalized nested array (GNA) were designed in [20, 21]. All the new forms of sparse arrays aimed to construct the optimal array geometry with largest DOFs and least mutual coupling.

However, the foregoing strategies are highly sensitive to the accuracy of the manifold matrix. In practice, the DOA estimation system will suffer from one or more model uncertainties inevitably like gain and phase error, mutual coupling, and sensor location error, which will lead to severe performance degradation or even failure of the direction of arrival estimations [22, 23]. Various corresponding algorithms have been proposed to eliminate the influence of gain and phase error, such as Hadamard product method [24], eigenstructure method [25], and ESPRIT-like method [26]. Unfortunately, most of the calibration strategies were proposed based on the assumption of ULA, which was invalid for sparse arrays in underdetermined cases. Partial Toeplitz structure of the covariance matrix and the sparse total least squares (STLS) method were utilized to estimate the parameters for nested array in [27]. But the prior knowledge of the noise power was required. Tian aimed to calibrate the error in the underdetermined case by applying a partly calibrated nested array and a high-power calibrated source [28]. Though the mathematical derivation and simulations demonstrated the effectiveness of the method, it was difficult to find sensors with accurate calibration in practice.

Motivated by the sparse arrays and the proposed methods, a novel strategy for an underdetermined case is proposed in this paper. Firstly, a GNA is applied to enhance the DOFs which enable us to deal with more sources than traditional sparse arrays. To achieve better DOA estimation performance and reduce the adverse effect of gain and phase error, we transfer the DOA estimation into a sparse reconstruction problem with nonnegativity constraint by exploiting a covariance-based sparse representation method. To further demonstrate the robustness of the strategy, the Cramer–Rao bound is derived subsequently.

The remainder of this paper is organized as follows. In Section 2, the geometry and signal model of GNA are constructed, respectively. Next, it is proved that the traditional eigenstructure method is invalid in the underdetermined case and a covariance-based sparse representation method is introduced in Section 3. In Section 4, we derive the Cramer–Rao bound (CRB) for further demonstration. Numerical results are provided to evaluate the effectiveness of the proposed method in Section 5, and the conclusion is drawn in Section 6.

Notations: throughout this paper, \otimes , \circ , and \circledast represent the Kronecker product, Khatri–Rao product, and convolution product, respectively. $(\cdot)^T$, $(\cdot)^H$, and $(\cdot)^*$ denote the transpose, conjugate transpose, and complex conjugate operations, respectively. $\Re(\cdot)$ and $\Im(\cdot)$ denote the real part and imagery part of a complex number. $\text{diag}(\cdot)$, $\text{vec}(\cdot)$, and $E[\cdot]$ represent the diagonal matrix operation, vectorization operation, and expectation operation, respectively.

2. Problem Formulation

2.1. Generalized Nested Array. Generalized nested array is a flexible sparse array with more DOFs and less mutual coupling. As shown in Figure 1, the GNA is constructed by two concatenated ULAs, where the inner subarray is an N_1 -elements ULA with interelement spacing of αd and the outer is an N_2 -elements array with spacing βd . Herein, d equals $\lambda/2$, where λ represents the wavelength of the signal. Different from the traditional nested array, the element spacings α and β are two arbitrary coprime integers.

Figure 1 indicates that the sensor position set as follows:

$$D_{\text{GNA}} = \{1, 1 + \alpha, \dots, 1 + N_1\alpha, 1 + N_1\alpha + \beta, \dots, 1 + N_1\alpha + (N_2 - 1)\beta\}. \quad (1)$$

According to (1), it is easy to find that the GNA has two special cases. When $\alpha = 1$ and $\beta = N_1 + 1$, the GNA becomes the nested array. When $\alpha = N_2$ and $\beta = N_1$, the GNA can be interpreted as Coprime Array with Displaced Subarrays (CADiS) [19].

Based on the sensor position set D_{GNA} , we can obtain the difference coarray of GNA by the following equation:

$$\begin{aligned} \mathbf{S}_{\text{GNA}} &= \mathbf{S}_{\text{GNA}}^+ \cup \mathbf{S}_{\text{GNA}}^- \\ \mathbf{S}_{\text{GNA}}^+ &= \{n_1\alpha + n_2\beta, n_1 \in [0, N_1], n_2 \in [0, N_2 - 1]\}, \end{aligned} \quad (2)$$

where $\mathbf{S}_{\text{GNA}}^+$ and $\mathbf{S}_{\text{GNA}}^-$ denote the positive and negative part of the difference coarray, respectively. And the values in $\mathbf{S}_{\text{GNA}}^+$ and $\mathbf{S}_{\text{GNA}}^-$ are symmetric to zero.

By analyzing the vectorized covariance matrix, only when $\alpha = 1$ or $\beta = 1$ can the values in difference coarray \mathbf{S}_{GNA} be contiguous. The larger α and β are, the more inconsecutive lags exist. According to the proof in Ref. [13], when $\alpha \in [1, N_2]$ and $\beta \in [1, N_1 + 1]$, the range of contiguous lags in the positive part of $\mathbf{S}_{\text{GNA}}^+$ is $[(\alpha - 1)(\beta - 1), N_1\alpha N_2\beta - \alpha\beta + \alpha - 1]$. In addition, if we define $[f = N_1\alpha + N_2\beta - \alpha\beta + \alpha - 1]$, the number of unique lags in \mathbf{S}_{GNA} can reach $2f + 1$ in the same assumption.

Consider a GNA with $N = N_1 + N_2$ sensors, the DOFs of the array under the constraints of $\alpha \in [1, N_2]$ and $\beta \in [1, N_1 + 1]$ can be obtained by the following equation:

$$f_{\max} = \begin{cases} (N^2 + 2N - 1)/2, & N \text{ is odd, } N_1 = N_2 - 1, \\ (N^2 + 2N - 2)/2, & N \text{ is even, } N_1 = N_2. \end{cases} \quad (3)$$

With the optimal factors of $\alpha = N_2$, $\beta \in [1, N_1 + 1]$, or $\alpha \in [1, N_2]$, $\beta = N_1 + 1$. In that case, the DOFs of GNA are the same as the nested array or SNA.

The nested array and coprime array with the same elements as GNA ($\alpha = 4, \beta = 3$) are selected for direct comparison. Sensors location and DOFs of the three kinds of arrays are listed in Table 1.

Figure 2 shows the coarray location of the sparse arrays. Compared with nested array and coprime array, both the GNA and nested array have the same DOFs, while the coprime array has the least DOFs.

In general, the GNA possesses the advantages of both nested array and coprime array. The GNA not only provides

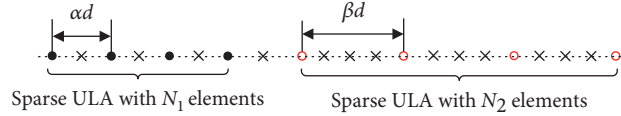


FIGURE 1: Geometry of generalized nested array.

TABLE 1: Sensor location and DOFs of NA, CPA, and GNA.

	NA	CPA	GNA
Sensors location	{1, 2, 3, 4, 5, 10, 15, 20}	{0, 3, 6, 9, 4, 8, 12, 16}	{1, 5, 9, 13, 17, 20, 23, 26}
DOFs	39	27	39

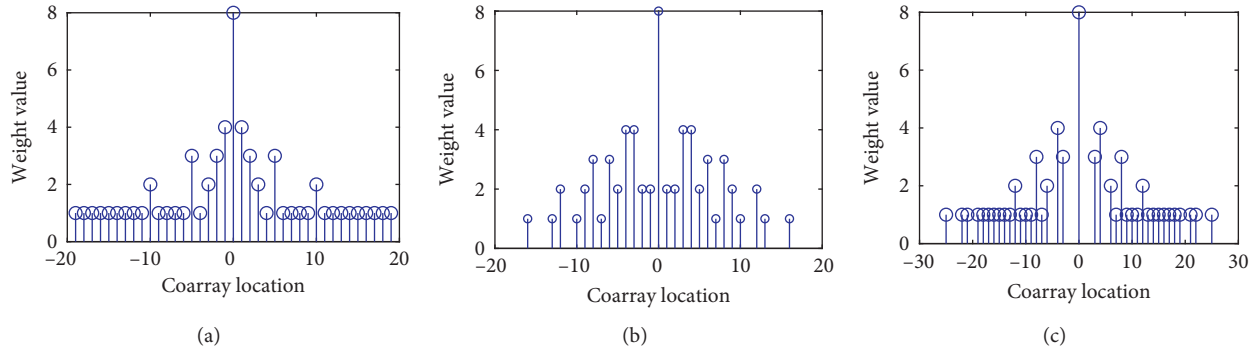


FIGURE 2: Coarray location of the (a) nested array, (b) coprime array, and (c) GNA.

the larger DOFs but also reduces the mutual coupling owing to the large element spacing. However, the large factors lead to short contiguous lags, which makes spatial smoothing MUSIC (SS-MUSIC) algorithm inapplicable. In practice, the compressive sensing (CS) algorithm can be widely utilized to estimate the DOA in this case.

2.2. Array Signal Model. Consider a GNA with $N = N_1 + N_2$ sensors, which receives K uncorrelated far-field narrow-band sources from $\{\theta_1, \theta_2, \dots, \theta_K\}$. Then the received signal under ideal condition is denoted by the following equation:

$$\mathbf{x}(t) = \mathbf{A}\mathbf{s}(t) + \mathbf{n}(t), \quad (4)$$

where $\mathbf{s}(t)$ denotes the signal vector and $\mathbf{A} = [\mathbf{a}(\theta_1), \mathbf{a}(\theta_2), \dots, \mathbf{a}(\theta_K)]^T$ is the manifold matrix. $\mathbf{a}(\theta_k) = [e^{-j2\pi d_1 d \sin \theta_k / \lambda}, \dots, e^{-j2\pi d_N d \sin \theta_k / \lambda}]^T$ represents the steering vector, where d_n ($n = 1, 2, \dots, N$) denotes the n -th sensor's position. $\mathbf{n}(t)$ is the noise vector, which is assumed to follow the Gaussian distribution and uncorrelated with the sources.

Now consider the scenario that each sensor is affected by gain and phase error, then (4) can be rewritten as follows:

$$\mathbf{x}(t) = \widetilde{\mathbf{A}}\mathbf{s}(t) + \mathbf{n}(t) = \mathbf{\Phi}\mathbf{\Psi}\mathbf{A}\mathbf{s}(t) + \mathbf{n}(t), \quad (5)$$

where $\mathbf{\Phi}$ and $\mathbf{\Psi}$ denote the gain error matrix and phase error matrix, respectively. $\mathbf{\Phi}$ and $\mathbf{\Psi}$ are both $N \times N$ diagonal matrices, whose diagonal entries are given by the following equation:

$$[\mathbf{\Phi}]_{ii} = \rho_i, [\mathbf{\Psi}]_{ii} = e^{j\psi_i}, \quad i = 1, 2, \dots, N. \quad (6)$$

Then, we obtain the covariance matrix of the received signal based on (5)

$$\widetilde{\mathbf{R}} = E[\mathbf{x}(t)\mathbf{x}^H(t)] = \mathbf{\Phi}\mathbf{\Psi}\mathbf{A}\mathbf{R}_s\mathbf{A}^H\mathbf{\Psi}^H\mathbf{\Phi}^H + \sigma^2\mathbf{I}_N \approx \frac{1}{L} \sum_{l=1}^L \mathbf{x}(t)\mathbf{x}^H(t), \quad (7)$$

where $\mathbf{R}_s = \text{diag}(\mathbf{p}) = \text{diag}([\sigma_1^2, \sigma_2^2, \dots, \sigma_K^2]^T)$ denotes the source covariance matrix and σ_k^2 represents the power of the k -th source. In addition, σ^2 denotes the power of the noise signal and L is the number of snapshots.

Define the covariance matrix \mathbf{S} without gain and phase error or noise, then we have the following equation:

$$\mathbf{S} = \mathbf{A}\mathbf{R}_s\mathbf{A}^H. \quad (8)$$

Rewriting the relation in (7), it can be obtained as follows:

$$\widetilde{\mathbf{R}} = \mathbf{\Phi}\mathbf{\Psi}\mathbf{S}\mathbf{\Psi}^H\mathbf{\Phi}^H + \sigma^2\mathbf{I}_N. \quad (9)$$

As we all know, gain and phase errors will lead to severe performance degradation or even failure of traditional DOA estimation algorithms. For ULA conditions, the covariance matrix $\widetilde{\mathbf{R}}$ has Toeplitz structure, which makes it easy to correct the model errors. However, the nonuniformity of GNA destroys the Toeplitz structure and increases the difficulty of DOA estimation.

3. DOA Estimation Strategy

Although the Toeplitz structure of the covariance matrix will be destroyed by the nonuniformity of sparse arrays, it still can be utilized to estimate some parameters of the gain and phase error. Define a function $z_{p,q} = d_p - d_q$, $p, q \in [1, N]$ to indicate the positions of the virtual elements.

It is obvious that the (p, q) -th element of \mathbf{S} can be defined as follows:

$$[\mathbf{S}]_{p,q} = \sum_{k=1}^K \sigma_k^2 e^{j2\pi(d_p - d_q)d \sin \theta_k / \lambda}. \quad (10)$$

Then, we rewrite the covariance matrix without noise as follows:

$$\bar{\mathbf{R}} = \tilde{\mathbf{R}} - \sigma^2 \mathbf{I}. \quad (11)$$

σ^2 denotes the noise power, which can be obtained by estimating the minimum eigenvalue of $\bar{\mathbf{R}}$. The element of $\bar{\mathbf{R}}$ can be defined as $\mathbf{r}_{p,q} = [\mathbf{S}]_{p,q} \rho_p \rho_q e^{j(\psi_p - \psi_q)}$.

Considering the gain error, a series of equations can be given by the following equation:

$$\mu_{i,t,p,q} = \ln \left\{ \frac{|\mathbf{r}_{i,t}|}{|\mathbf{r}_{p,q}|} \right\} = \ln \left(\frac{\rho_i \rho_t}{\rho_p \rho_q} \right) + \ln \left\{ \frac{|[\mathbf{S}]_{i,t} e^{j(\psi_i - \psi_t)}|}{|[\mathbf{S}]_{p,q} e^{j(\psi_p - \psi_q)}|} \right\}, \quad (12)$$

where $\mu_{i,t,p,q}$ denotes a quantity determined from $\bar{\mathbf{R}}$.

Similar to the ULA case [27], select the elements which satisfy $d_i - d_t = d_p - d_q$. Therefore, (12) can be simplified as follows:

$$\mu_{i,t,p,q} = \ln \rho_i + \ln \rho_t - \ln \rho_p - \ln \rho_q. \quad (13)$$

In order to estimate the gain error, no less than N equations are required; otherwise, the parameter estimation will be underdetermined. However, by analyzing the

elements of $\tilde{\mathbf{R}}$, the number of equations like (13) is as follows [29]:

$$\sum_{w(n) \geq 2, n \geq 0} \frac{w(n)(w(n)-1)}{2}, \quad (14)$$

where $w(n) = (c \otimes c^-)(n)$ denotes weight function calculated by convolution. $c(n)$ is a conditional function. If there is a virtual element located at $z_n d$, the value of $c(n)$ is 1; otherwise it is 0 and $c^-(n) = c(-n)$. It is obvious that $w(0) = N$ when $n = 0$; thus, the number of equations provided similar to (13) is $(N(N-1)/2)$. That means the gain error can be estimated by an overdetermined equation set.

Taking all the nonredundant relations satisfy $d_i - d_t = d_p - d_q$ and constructing an equation set, it can be described compactly as follows:

$$\mathbf{B}_\rho [\ln \rho_1, \ln \rho_2, \dots, \ln \rho_N]^T = [\dots, \mu_{i,t,p,q}, \dots]^T, \quad (15)$$

where \mathbf{B}_ρ is a $k_\rho \times N$ matrix that the $1 \times N$ row vector $[1, 1, \dots, 1]^T$ is its lone null space spanning vector, k_ρ denotes the result of (14).

However, due to the estimation error of $\mu_{i,t,p,q}$, (15) is not strictly correct. The singular value decomposition (SVD) method can be utilized to obtain the least squares solution.

$$[\ln \rho_1, \ln \rho_2, \dots, \ln \rho_N]^T = \mathbf{B}_\rho^+ [\dots, \mu_{i,t,p,q}, \dots]^T, \quad (16)$$

where \mathbf{B}_ρ^+ represents the pseudoinverse of \mathbf{B}_ρ .

Equation (16) provides a minimum norm least squares solution, and a general solution can be regarded as adding an arbitrary scalar to the null space spanning vector. Then, the gain error can be estimated by an arbitrary multiplicative constant; i.e., $\tilde{\Phi} = e^\varepsilon \Phi$, where ε is an arbitrary scalar.

Hence, the previous conclusion means that the gain error will only affect the amplitude of the spectrum.

For phase error, we utilize a similar strategy. Defining

$$\tau_{i,t,p,q} = \text{angle}(|\mathbf{r}_{i,t}|) - \text{angle}(|\mathbf{r}_{p,q}|) = \text{angle}(|[\mathbf{S}]_{i,t}|) + \psi_i - \psi_t - \text{angle}(|[\mathbf{S}]_{p,q}|) - \psi_p + \psi_q, \quad (17)$$

where $\text{angle}(r) = \arctan(\Im(r)/\Re(r))$ and $\tau_{i,t,p,q}$ is a quantity determined from $\bar{\mathbf{R}}$.

If $d_i - d_t = d_p - d_q$ is satisfied, (17) can be simplified as follows:

$$\tau_{i,t,p,q} = \psi_i - \psi_t - \psi_p + \psi_q. \quad (18)$$

Since the elements in the main diagonal are inapplicable as they have no phase error information, the number of meaningful equations provided by (18) is as follows [29]:

$$\sum_{w(n) \geq 2, n \geq 1} \frac{w(n)(w(n)-1)}{2}. \quad (19)$$

Unfortunately, the large coprime factors of GNA lead to a few repeated virtual sensors, making the number of meaningful equations even less than the estimated parameters. In other words, we cannot construct an overdetermined equation set like (15) to estimate the phase error in most scenarios.

To deal with the situation, a covariance-based sparse representation method is introduced for DOA estimation.

Based on (9) and $\tilde{\Phi} = e^\varepsilon \Phi$, the covariance matrix after gain error calibration can be obtained by the following equation:

$$\tilde{\mathbf{R}}' = \tilde{\Phi}^{-1} (\Phi \Psi \mathbf{S} \Psi^H \Phi^H + \sigma^2 \mathbf{I}_N) \Phi^{-H} = \Psi \frac{\mathbf{S}}{e^{2\varepsilon}} \Psi^H + \sigma^2 \mathbf{I}_N, \quad (20)$$

Then, vectorizing the covariance matrix with calibrated gain error, we have the following:

$$\mathbf{z} = \text{vec}(\tilde{\mathbf{R}}') = \text{vec}\left(\Psi \frac{\mathbf{S}}{e^{2\varepsilon}} \Psi^H + \sigma^2 \mathbf{I}_N\right) = (\tilde{\mathbf{A}}^* \circ \tilde{\mathbf{A}}) \frac{\mathbf{P}}{e^{2\varepsilon}} + \sigma^2 \vec{\mathbf{1}}, \quad (21)$$

where $(\tilde{\mathbf{A}}^* \circ \tilde{\mathbf{A}}) = [\tilde{\alpha}^*(\theta_1) \otimes \tilde{\alpha}(\theta_1), \tilde{\alpha}^*(\theta_2) \otimes \tilde{\alpha}(\theta_2), \dots, \tilde{\alpha}^*(\theta_K) \otimes \tilde{\alpha}(\theta_K)]$ and $\vec{\mathbf{1}} = [\vec{\mathbf{e}}_1^T, \vec{\mathbf{e}}_2^T, \dots, \vec{\mathbf{e}}_N^T]^T$. $\vec{\mathbf{e}}_i$ is a column vector whose i -th element is 1 and the rest elements are all zeros. As there are only N nonzero values in specific positions of $\vec{\mathbf{1}}$, an $N(N-1) \times N^2$ selection matrix to remove the nonzero values can be defined as follows [30]:

$$\mathbf{J}^T = [\mathbf{J}_1, \mathbf{J}_2, \dots, \mathbf{J}_{N-1}], \quad (22)$$

where $\mathbf{J}_n = [\mathbf{e}_{(n-1)(N+1)+2}, \mathbf{e}_{(n-1)(N+1)+3}, \dots, \mathbf{e}_{n(N+1)}] \in R^{N^2 \times N}$, $n = 1, 2, \dots, N-1$. \mathbf{e}_n is an $N^2 \times 1$ column vector of all zeros except a 1 at the n -th position. Therefore, (21) can be rewritten as follows:

$$\bar{\mathbf{z}} = \mathbf{J} \mathbf{z} = \mathbf{J} \left((\tilde{\mathbf{A}}^* \circ \tilde{\mathbf{A}}) \frac{\mathbf{P}}{e^{2\varepsilon}} + \sigma^2 \vec{\mathbf{1}} \right) = \mathbf{J} (\tilde{\mathbf{A}}^* \circ \tilde{\mathbf{A}}) \frac{\mathbf{P}}{e^{2\varepsilon}}. \quad (23)$$

After this arithmetical operation, the noise item can be completely eliminated.

Directions of source signals impinging on the GNA range from $(-\pi/2, \pi/2)$ as the assumption, then the grid sampling over the space domain is utilized. Next, we can construct a grid set $\Theta = \{\theta_1, \theta_2, \dots, \theta_L\}$, $L \gg N(N-1)$ which contains all the origin signal directions.

The equivalent expression of (23) is denoted by the following equation:

$$\bar{\mathbf{z}} = \mathbf{J} (\tilde{\mathbf{A}}^* (\Theta) \circ \tilde{\mathbf{A}} (\Theta)) \frac{\bar{\mathbf{P}}}{e^{2\varepsilon}}, \quad (24)$$

where $\mathbf{J} (\tilde{\mathbf{A}}^* (\Theta) \circ \tilde{\mathbf{A}} (\Theta))$ represents the overcomplete dictionary. $\bar{\mathbf{P}}$ denotes the K -sparse vector whose ℓ_0 -norm is K , and its nonzero values correspond to the exact DOAs in Θ . Based on the analysis, the DOA estimation can be transformed into the recovery of $\bar{\mathbf{P}}$ and the location detection of nonzero values.

For the convenience of calculations, it would be better to transform the high-computation ℓ_0 -norm minimization problem into the ℓ_1 -norm minimization problem. Thus, the equivalent expression is represented as follows:

$$\min_{\bar{\mathbf{P}}} \|\bar{\mathbf{P}}\|_1 \quad (25)$$

$$\text{s.t. } \bar{\mathbf{z}} = \mathbf{J} (\tilde{\mathbf{A}}^* (\Theta) \circ \tilde{\mathbf{A}} (\Theta)) \frac{\bar{\mathbf{P}}}{e^{2\varepsilon}}, \quad [\bar{\mathbf{P}}]_i \geq 0,$$

where $[\bar{\mathbf{P}}]_i$ denotes the i -th elements of $\bar{\mathbf{P}}$.

However, as the number of snapshots is limited, the estimated covariance matrix cannot be equal to the exact covariance matrix, and the error exists. The relations can be expressed by the following:

$$\Delta \mathbf{z} = \hat{\mathbf{z}} - \mathbf{z}, \quad \Delta \bar{\mathbf{z}} = \hat{\bar{\mathbf{z}}} - \bar{\mathbf{z}} = \mathbf{J} \Delta \mathbf{z}. \quad (26)$$

Therefore, we can transform (25) into the following optimization problem:

$$\min_{\bar{\mathbf{P}}} \|\bar{\mathbf{P}}\|_1 \quad (27)$$

$$\text{s.t. } \|\hat{\bar{\mathbf{z}}} - \mathbf{J} (\tilde{\mathbf{A}}^* (\Theta) \circ \tilde{\mathbf{A}} (\Theta)) \frac{\bar{\mathbf{P}}}{e^{2\varepsilon}}\|_2^2 \leq \xi, \quad [\bar{\mathbf{P}}]_i \geq 0,$$

where ξ denotes the threshold parameter on the upper bound of $\Delta \mathbf{z}$. By applying the Orthogonal Matching Pursuit (OMP) algorithm or other sparse reconstruction algorithms like L1-SVD algorithm [31], the optimal solution is obtained, and the DOA can be estimated accurately. It should be noted that $e^{2\varepsilon}$ has no influence on the locations of nonzero value in $\bar{\mathbf{P}}$.

4. The Cramer–Rao Bound

The Cramer–Rao bound provides a theoretical lower bound on the variance of any unbiased estimation, which can be applied for the evaluation of the optimal performance of the estimation algorithms. However, traditional mathematical derivations are based on the assumption of the overdetermined system (the number of sensors is more than sources), which may be invalid for underdetermined cases like a nested array, coprime array, and GNA.

Assuming that the signal model is unconditional, we derive the CRB for DOAs based on the Ref. [32,33], the expression is shown as follows:

$$\text{CRB}_\theta = \frac{1}{L} (\mathbf{M}_\theta \mathbf{\Pi}_{M_G}^\perp \mathbf{M}_\theta)^{-1},$$

$$\mathbf{\Pi}_{M_G}^\perp = \mathbf{I} - \mathbf{M}_G (\mathbf{M}_G^H \mathbf{M}_G)^{-1} \mathbf{M}_G,$$

$$\mathbf{M}_\theta = \left(\tilde{\mathbf{R}}^T \otimes \tilde{\mathbf{R}} \right)^{-1/2} \mathbf{N}_\theta,$$

$$\mathbf{M}_G = \left(\tilde{\mathbf{R}}^T \otimes \tilde{\mathbf{R}} \right)^{-1/2} \mathbf{N}_G,$$

$$\mathbf{N}_\theta = \tilde{\mathbf{A}}_d' \mathbf{R}_S, \quad \mathbf{N}_G = [\tilde{\mathbf{A}}_\rho' \mathbf{R}_S, j \tilde{\mathbf{A}}_\psi' \mathbf{R}_S],$$

$$\tilde{\mathbf{A}}_d' = \tilde{\mathbf{A}}^{*'} \circ \tilde{\mathbf{A}} + \tilde{\mathbf{A}}^* \circ \tilde{\mathbf{A}}', \quad \tilde{\mathbf{A}}' = \left[\frac{\partial \tilde{\mathbf{a}}(\theta_1)}{\partial \theta_1}, \frac{\partial \tilde{\mathbf{a}}(\theta_2)}{\partial \theta_2}, \dots, \frac{\partial \tilde{\mathbf{a}}(\theta_K)}{\partial \theta_K} \right],$$

$$\tilde{\mathbf{A}}_\rho' = \left[\frac{\partial (\tilde{\mathbf{A}} \circ \tilde{\mathbf{A}})}{\partial \rho_1}, \frac{\partial (\tilde{\mathbf{A}} \circ \tilde{\mathbf{A}})}{\partial \rho_2}, \dots, \frac{\partial (\tilde{\mathbf{A}} \circ \tilde{\mathbf{A}})}{\partial \rho_N} \right],$$

$$\tilde{\mathbf{A}}_\psi' = \left[\frac{\partial (\tilde{\mathbf{A}} \circ \tilde{\mathbf{A}})}{\partial \psi_1}, \frac{\partial (\tilde{\mathbf{A}} \circ \tilde{\mathbf{A}})}{\partial \psi_2}, \dots, \frac{\partial (\tilde{\mathbf{A}} \circ \tilde{\mathbf{A}})}{\partial \psi_N} \right], \quad (28)$$

where $\mathbf{\Pi}_{M_G}^\perp$ represents the orthogonal projection matrix of \mathbf{M}_G .

The detailed derivation is presented in the Appendix.

5. Simulation Results

In order to verify the DOA estimation performance of the proposed strategy, several numerical simulations are provided in this section. For DOA estimation performance comparison, the nested array and coprime array are utilized. Meanwhile, sparse total least squares (STSL) algorithm and CRB are provided for error calibration performance comparison. Throughout the experiments, we assume that the physical sensors of GNA are 8 and the coprime factors are $\alpha = 4$ and $\beta = 3$, respectively. Further, the noise term satisfies zero-mean Gaussian distribution.

5.1. Effect of Gain and Phase Error on DOA Estimation.

In this simulation, we study the effect of gain error and phase error, respectively. In the first case, only gain error exists. Similarly, only phase error affects in the second case. Assume that the gain error matrix and phase error matrix are $\Phi = \text{diag}([1, 0.95, 1.2, 0.75, 0.81, 1.36, 1.14, 0.9])$ and $\Psi = \text{diag}([1, e^{j\pi/6}, e^{-j\pi/3}, e^{j\pi/15}, e^{j\pi/4}, e^{-j\pi/8}, e^{-j\pi/6}, e^{j\pi/5}])$, respectively. We choose 9 sources ranging from -40° to 40° , with a step 10° . The snapshot number is $L = 200$. Simulation results when SNR = 0dB are given by Figure 3. In the following figures, the dotted red line represents the real DOAs.

Compared with Figures 3(a) and 3(b), it can be found that only phase error affects the performance of DOA estimation, leading to large performance degradation or even failure, while the gain error only leads to influence on the amplitude of the spectrum.

5.2. DOA Estimation Performance under Gain and Phase Error Condition.

Firstly, assume that the gain error matrix and phase error matrix in this experiment are the same as the matrices in Section 1. Then, we plot the CS spectrum [34] of GNA in Figure 4. We observe that the effect of gain and phase error can be eliminated and all the sources can be identified by the proposed method at the same time.

For further evaluations, we discuss the effect of SNR and snapshot numbers on DOA estimation performance. Therefore, the root mean square error (RMSE) is introduced for quantitative analysis. The STSL algorithm is selected as a comparison for DOA estimation performance simulations under the gain and phase error. In this section, it is assumed that two uncorrelated sources impinge on the array from directions of 10° and 20° . Then, we provide the estimation performance curves versus SNR and snapshot numbers by fixing snapshot numbers or SNR, respectively. The RMSE via 200 Monte Carlo trails is denoted by the following equation:

$$\text{RMSE} = \sqrt{\frac{1}{200K} \sum_{q=1}^{200} \sum_{k=1}^K (\hat{\theta}_k^q - \theta_k)^2}, \quad (29)$$

where $\hat{\theta}_k^q$ represents the estimated value of θ_k in the q -th trail.

Firstly, assume that SNR ranges from -10 dB to 10 dB, while the snapshot number is 200. The DOA estimation performances of two strategies and CRB versus SNR under gain and phase error condition are shown in Figure 5. Similarly, the SNR is set to 0 dB and the snapshot number varies from 20 to 400. Then, we obtain the DOA estimation performance of three strategies and CRB versus snapshot numbers under the influence of gain and phase error as shown in Figure 6. It can be found from Figures 5 and 6 that the DOA estimation of each strategy will be more accurate as SNR or snapshot number increasing. However, compared with the STSL method, the proposed method in this paper has the lower RMSE curve and becomes closest to the CRB.

6. Conclusions

This paper investigates into sparsity-based strategy for DOA estimation in the case of gain and phase errors via generalized nested array. With the advantage of sparsity, the generalized nested array is utilized to enhance the degrees of freedom and decrease the influence of mutual coupling firstly. Then, the signal model and error model are established, and a covariance-based sparse representation method is provided to estimate the DOAs. Besides, the Cramer–Rao bound is derived, and the robustness of DOA estimation is analyzed. Although the covariance matrix no longer has the Toeplitz structure in the case of gain and phase errors, which makes DOA estimation become an underdetermined problem, the proposed strategy still has excellent parameter estimation performance. Numerical simulations verify the advantages and effectiveness of the theoretical analysis.

Appendix

CRB for DOA

Under the assumption of unconditional signal model assumption, a parameter vector can be defined as follows:

$$\boldsymbol{\eta} = [\theta_1, \theta_2, \dots, \theta_K, \rho_1, \rho_2, \dots, \rho_N, \psi_1, \psi_2, \dots, \psi_N]^T. \quad (\text{A.1})$$

Thus, the entries of the Fisher Information Matrix (FIM) is formulated by the following equation:

$$\text{FIM}_{i,j} = L \text{tr} \left[\frac{\partial \tilde{\mathbf{R}}}{\partial \boldsymbol{\eta}_i} \tilde{\mathbf{R}}^{-1} \frac{\partial \tilde{\mathbf{R}}}{\partial \boldsymbol{\eta}_j} \tilde{\mathbf{R}}^{-1} \right] = L \left[\frac{\partial \tilde{\mathbf{r}}}{\partial \boldsymbol{\eta}_i} \right] \left(\tilde{\mathbf{R}}^T \otimes \tilde{\mathbf{R}} \right)^{-1} \frac{\partial \tilde{\mathbf{r}}}{\partial \boldsymbol{\eta}_j}, \quad (\text{A.2})$$

where $\tilde{\mathbf{r}} = \text{vec}(\tilde{\mathbf{R}})$, $\text{tr}[\cdot]$ represents the trace of a matrix, η_i is the i -th element of the vector $\boldsymbol{\eta}$, and η_j is the j -th element, respectively.

Assume that

$$\frac{\partial \tilde{\mathbf{r}}}{\partial \boldsymbol{\eta}} = \left[\frac{\partial \tilde{\mathbf{r}}}{\partial \theta_1}, \dots, \frac{\partial \tilde{\mathbf{r}}}{\partial \theta_K}, \frac{\partial \tilde{\mathbf{r}}}{\partial \rho_1}, \dots, \frac{\partial \tilde{\mathbf{r}}}{\partial \rho_N}, \frac{\partial \tilde{\mathbf{r}}}{\partial \psi_1}, \dots, \frac{\partial \tilde{\mathbf{r}}}{\partial \psi_N} \right] = [\tilde{\mathbf{A}}_d' \mathbf{R}_S, \tilde{\mathbf{A}}_\rho' \mathbf{R}_S, j \tilde{\mathbf{A}}_\psi' \mathbf{R}_S] = [\mathbf{N}_\theta, \mathbf{N}_G], \quad (\text{A.3})$$

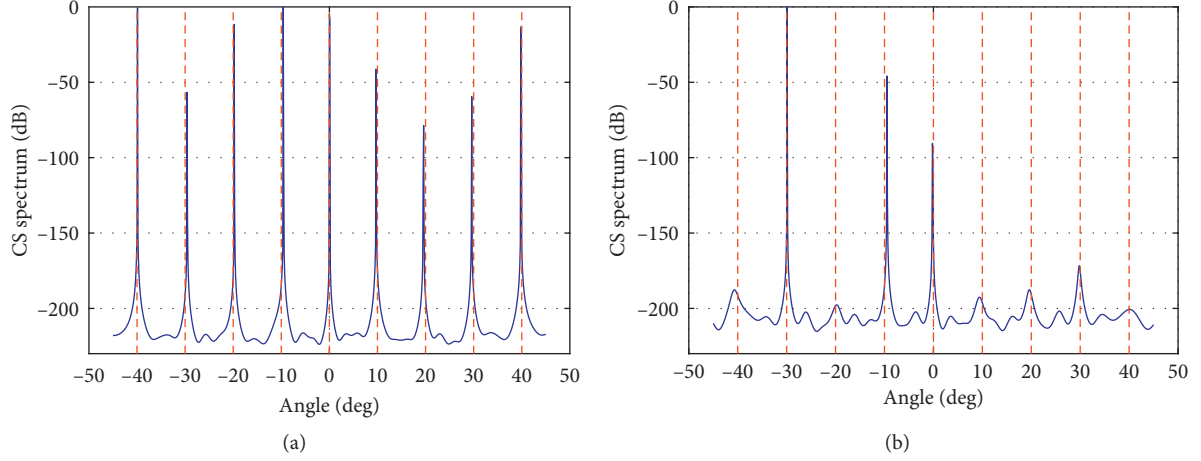


FIGURE 3: The effect of only (a) gain error and (b) phase error on DOA estimation.

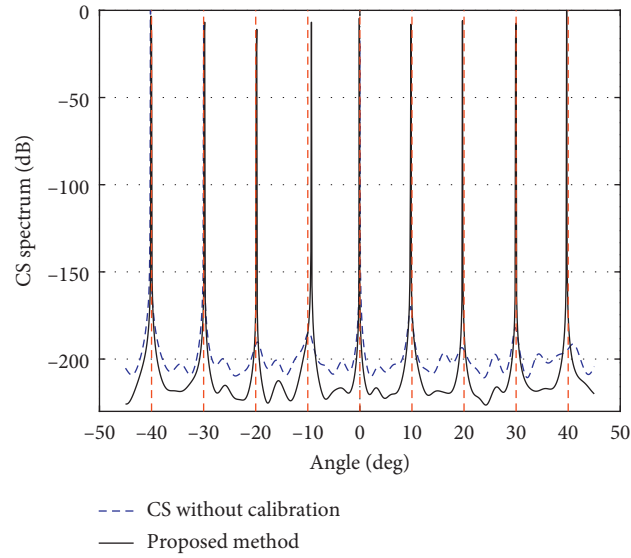


FIGURE 4: CS spectrum of GNA in the presence of gain and phase error.

where

$$\begin{aligned}\tilde{\mathbf{A}}'_d &= \tilde{\mathbf{A}}'^* \circ \tilde{\mathbf{A}} + \tilde{\mathbf{A}}^* \circ \tilde{\mathbf{A}}', \\ \tilde{\mathbf{A}}' &= \left[\frac{\partial \tilde{\mathbf{a}}(\theta_1)}{\partial \theta_1}, \frac{\partial \tilde{\mathbf{a}}(\theta_2)}{\partial \theta_2}, \dots, \frac{\partial \tilde{\mathbf{a}}(\theta_K)}{\partial \theta_K} \right], \\ \tilde{\mathbf{A}}'_\rho &= \left[\frac{\partial (\tilde{\mathbf{A}} \circ \tilde{\mathbf{A}})}{\partial \rho_1}, \frac{\partial (\tilde{\mathbf{A}} \circ \tilde{\mathbf{A}})}{\partial \rho_2}, \dots, \frac{\partial (\tilde{\mathbf{A}} \circ \tilde{\mathbf{A}})}{\partial \rho_N} \right], \\ \tilde{\mathbf{A}}'_\psi &= \left[\frac{\partial (\tilde{\mathbf{A}} \circ \tilde{\mathbf{A}})}{\partial \psi_1}, \frac{\partial (\tilde{\mathbf{A}} \circ \tilde{\mathbf{A}})}{\partial \psi_2}, \dots, \frac{\partial (\tilde{\mathbf{A}} \circ \tilde{\mathbf{A}})}{\partial \psi_N} \right].\end{aligned}\quad (\text{A.4})$$

Then, (A.3) can be further transferred to the following equation:

$$\text{FIM} = L \left[\frac{\partial \tilde{\mathbf{r}}}{\partial \boldsymbol{\eta}} \right] \left(\tilde{\mathbf{R}}^T \otimes \tilde{\mathbf{R}} \right)^{-1} \frac{\partial \tilde{\mathbf{r}}}{\partial \boldsymbol{\eta}} \quad (\text{A.5})$$

Since $\tilde{\mathbf{R}}$ is positive semidefinite, it is easy to obtain that the FIM is positive semidefinite.

Therefore, we can obtain the following:

$$\text{FIM} = L \begin{bmatrix} \mathbf{M}_\theta^H \mathbf{M}_\theta & \mathbf{M}_\theta^H \mathbf{M}_G \\ \mathbf{M}_G^H \mathbf{M}_\theta & \mathbf{M}_G^H \mathbf{M}_G \end{bmatrix}, \quad (\text{A.6})$$

where

$$\mathbf{M}_\theta = \left(\tilde{\mathbf{R}}^T \otimes \tilde{\mathbf{R}} \right)^{-1/2} \mathbf{N}_\theta, \quad (\text{A.7})$$

$$\mathbf{M}_G = \left(\tilde{\mathbf{R}}^T \otimes \tilde{\mathbf{R}} \right)^{-1/2} \mathbf{N}_G. \quad (\text{A.8})$$

According to (A.8), the CRB for DOAs can be calculated by the following:

$$\text{CRB}_\theta = \frac{1}{L} \left(\mathbf{M}_\theta \boldsymbol{\Pi}_{\mathbf{M}_G}^+ \mathbf{M}_\theta \right)^{-1}, \quad (\text{A.9})$$

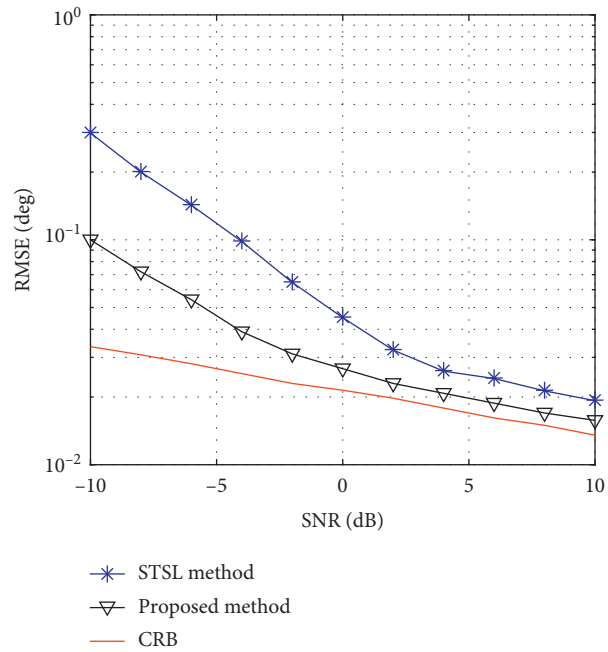


FIGURE 5: RMSE curves of DOA estimation versus SNR under gain and phase error condition.

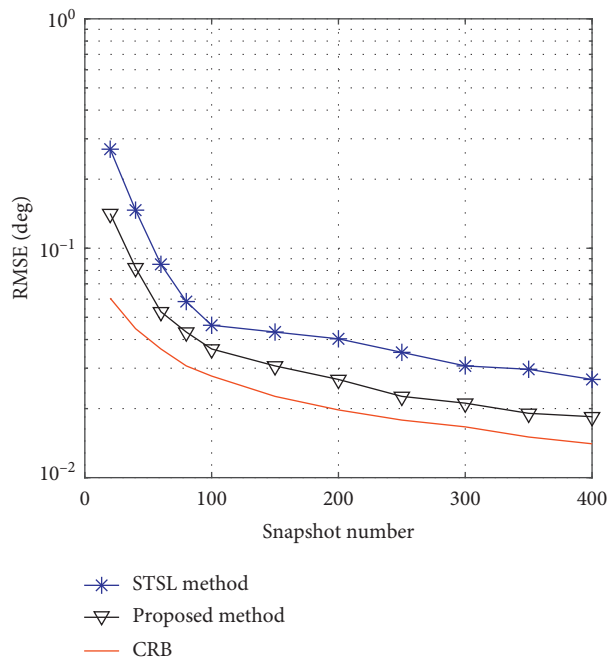


FIGURE 6: RMSE curves of DOA estimation versus snapshot number under gain and phase error condition.

where $\Pi_{M_G}^\perp$ denotes the orthogonal projection matrix of M_G .

Data Availability

The data sources from the references are all marked in this paper. The parameters designed are all described in this paper. Therefore, the data in this paper have been fully covered and can be obtained.

Conflicts of Interest

The authors declare that there are no conflicts of interest regarding the publication of this paper.

Acknowledgments

This research was funded by the National Natural Science Foundation of China (grant no. 61601504).

References

- [1] I. Bekkerman and J. Tabrikian, "Target detection and localization using MIMO radars and sonars," *IEEE Transactions on Signal Processing*, vol. 54, no. 10, pp. 3873–3883, 2006.
- [2] F. Wen and J. Shi, "Fast direction finding for bistatic EMVS-MIMO radar without pairing," *Signal Processing*, vol. 173, Article ID 107512, 2020.
- [3] R. Schmidt, "Multiple emitter location and signal parameter estimation," *IEEE Transactions on Antennas and Propagation*, vol. 34, no. 3, pp. 276–280, 1986.
- [4] R. Roy, A. Paulraj, and T. Kailath, "ESPRIT—A subspace rotation approach to estimation of parameters of cisoids in noise," *IEEE Transactions on Acoustics, Speech, and Signal Processing*, vol. 34, no. 5, pp. 1340–1342, 1986.
- [5] I. Ziskind and M. Wax, "Maximum Likelihood localization of multiple sources by alternating projection," *IEEE Transactions on Acoustics, Speech, and Signal Processing*, vol. 36, no. 10, pp. 1553–1560, 1988.
- [6] M. Viberg, B. Ottersten, and T. Kailath, "Detection and estimation in sensor arrays using weighted subspace fitting," *IEEE Transactions on Signal Processing*, vol. 39, no. 11, pp. 2436–2449, 1991.
- [7] L. Tao and N. Arye, "Maximum likelihood direction finding in spatially colored noise fields using sparse sensor arrays," *IEEE Transactions on Signal Processing*, vol. 59, no. 3, pp. 1048–1062, 2011.
- [8] B. R. Jackson, S. Rajan, B. J. Liao, and S. Wang, "Direction of arrival estimation using directive antennas in uniform circular arrays," *IEEE Transactions on Antennas and Propagation*, vol. 63, no. 2, pp. 736–747, 2015.
- [9] P. Pal and P. P. Vaidyanathan, "Nested arrays: a novel approach to array processing with enhanced degrees of freedom," *IEEE Transactions on Signal Processing*, vol. 58, no. 8, pp. 4167–4181, 2010.
- [10] P. P. Vaidyanathan and P. Pal, "Sparse sensing with co-prime samplers and arrays," *IEEE Transactions on Signal Processing*, vol. 59, no. 2, pp. 573–586, 2011.
- [11] C. Zhou, Z. Shi, Y. Gu et al., "DECOM: DOA estimation with combined MUSIC for coprime array," in *Proceedings of the International Conference on Wireless Communications & Signal Processing (ICWCSP)*, pp. 1–5, Hangzhou, China, October 2013.
- [12] C. Zhou and J. Zhou, "Direction-of-Arrival estimation with coarray ESPRIT for coprime array," *Sensors*, vol. 17, no. 8, pp. 1779–1795, 2017.
- [13] H. Zhou, G. Hu, J. Shi, and Z. Feng, "Multi-frequency based direction-of-arrival estimation for 2q-level nested radar & sonar arrays," *Sensors*, vol. 18, no. 10, pp. 3385–3401, 2018.
- [14] C. Zhou, Y. Gu, X. Fan, Z. Shi, G. Mao, and Y. D. Zhang, "Direction-of-arrival estimation for coprime array via virtual array interpolation," *IEEE Transactions on Signal Processing*, vol. 66, no. 22, pp. 5956–5971, 2018.
- [15] C. Zhou, Y. Gu, Z. Shi, and Y. D. Zhang, "Off-grid direction-of-arrival estimation using coprime array interpolation," *IEEE Signal Processing Letters*, vol. 25, no. 11, pp. 1710–1714, 2018.
- [16] T. Liu, F. Wen, L. Zhang, and K. Wang, "Off-grid DOA estimation for colocated MIMO radar via reduced-complexity sparse bayesian learning," *IEEE Access*, vol. 7, pp. 99907–99916, 2019.
- [17] C. Zhou, Y. Gu, Y. D. Zhang, Z. Shi, T. Jin, and X. Wu, "Compressive sensing-based coprime array direction-of-arrival estimation," *IET Communications*, vol. 11, no. 11, pp. 1719–1724, 2017.
- [18] J. Shi, G. Hu, X. Zhang, F. Sun, and H. Zhou, "Sparsity-based two-dimensional DOA estimation for coprime array: from sum-difference coarray viewpoint," *IEEE Transactions on Signal Processing*, vol. 65, no. 21, pp. 5591–5604, 2017.
- [19] Z. Shi, C. Zhou, Y. Gu, N. A. Goodman, and F. Qu, "Source estimation using coprime array: a sparse reconstruction perspective," *IEEE Sensors Journal*, vol. 17, no. 3, pp. 755–765, 2017.
- [20] C.-L. Liu and P. P. Vaidyanathan, "Super nested arrays: linear sparse arrays with reduced mutual coupling-Part I: Fundamentals," *IEEE Transactions on Signal Processing*, vol. 64, no. 15, pp. 3997–4012, 2016.
- [21] J. Shi, G. Hu, X. Zhang, and H. Zhou, "Generalized nested array: optimization for degrees of freedom and mutual coupling," *IEEE Communications Letters*, vol. 22, no. 6, pp. 1208–1211, 2018.
- [22] A. J. Weiss and B. Friedlander, "Eigenstructure methods for direction finding with sensor gain and phase uncertainties," *Circuits, Systems, and Signal Processing*, vol. 9, no. 3, pp. 271–300, 1990.
- [23] F. Wen, Z. Zhang, K. Wang, G. Sheng, and G. Zhang, "Angle estimation and mutual coupling self-calibration for ULA-based bistatic MIMO radar," *Signal Processing*, vol. 144, pp. 61–67, 2018.
- [24] S. Cao, Z. Ye, D. Xu, and X. Xu, "A hadamard product based method for DOA estimation and gain-phase error calibration," *IEEE Transactions on Aerospace and Electronic Systems*, vol. 49, no. 2, pp. 1224–1233, 2013.
- [25] A. Liu, G. Liao, C. Zeng, Z. Yang, and Q. Xu, "An eigenstructure method for estimating DOA and sensor gain-phase errors," *IEEE Transactions on Signal Processing*, vol. 59, no. 12, pp. 5944–5956, 2011.
- [26] B. Liao and S. C. Chan, "Direction finding with partly calibrated uniform linear arrays," *IEEE Transactions on Antennas and Propagation*, vol. 60, no. 2, pp. 922–929, 2012.
- [27] K. Han, P. Yang, and A. Nehorai, "Calibrating nested sensor arrays with model errors," *IEEE Transactions on Antennas and Propagation*, vol. 63, no. 11, pp. 4739–4748, 2015.
- [28] Y. Tian, Y. Wang, and B. Shi, "Gain-phase errors calibration of nested array for underdetermined direction of arrival estimation," *AEU—International Journal of Electronics and Communications*, vol. 108, pp. 87–90, 2019.
- [29] A. Paulraj and T. Kailath, "Direction of arrival estimation by eigenstructure methods with unknown sensor gain and phase," in *Proceedings of the ICASSP '85. IEEE International Conference on Acoustics, Speech, and Signal Processing*, pp. 640–643, Tampa, FL, USA, April 1985.
- [30] Z.-Q. He, Z.-P. Shi, and L. Huang, "Covariance sparsity-aware DOA estimation for nonuniform noise," *Digital Signal Processing*, vol. 28, pp. 75–81, 2014.
- [31] D. A. Linebarger, I. H. Sudborough, and I. G. Tollis, "Difference bases and sparse sensor arrays," *IEEE Transactions on Information Theory*, vol. 39, no. 3, pp. 716–721, 1993.
- [32] A. Koochakzadeh and P. Pal, "Cramér-rao bounds for underdetermined source localization," *IEEE Signal Processing Letters*, vol. 23, no. 7, pp. 919–923, 2016.
- [33] C. L. Liu and P. P. Vaidyanathan, "New Cramér-Rao Bound Expressions for Coprime and Other Sparse Arrays," in *Proceedings of the 2016 IEEE Sensor Array and Multichannel Signal Processing Workshop (SAM)*, pp. 1–5, Rio de Janeiro, Brazil, July 2016.
- [34] C. Zhou, Y. Gu, S. He, and Z. Shi, "A robust and efficient algorithm for coprime array adaptive beamforming," *IEEE Transactions on Vehicular Technology*, vol. 67, no. 2, pp. 1099–1112, 2018.

Research Article

Key-Frame Detection and Super-Resolution of Hyperspectral Video via Sparse-Based Cumulative Tensor Factorization

Ruofei Zhou ¹, Gang Wang ¹, Bo Li ¹, Jinlong Wang,¹ Tianzhu Liu,^{1,2}
and Chungang Liu³

¹School of Electronics and Information Engineering, Harbin Institute of Technology, Harbin 150001, China

²Heilongjiang Province Key Laboratory of Space-Air-Ground Integrated Intelligent Remote Sensing, Harbin 150001, China

³College of Career Technology, Hebei Normal University, Shijiazhuang 050000, China

Correspondence should be addressed to Gang Wang; gwang51@hit.edu.cn

Received 11 May 2020; Revised 25 May 2020; Accepted 5 June 2020; Published 14 July 2020

Guest Editor: Liangtian Wan

Copyright © 2020 Ruofei Zhou et al. This is an open access article distributed under the Creative Commons Attribution License, which permits unrestricted use, distribution, and reproduction in any medium, provided the original work is properly cited.

Thanks to the rapid development of hyperspectral sensors, hyperspectral videos (HSV) can now be collected with high temporal and spectral resolutions and utilized to handle invisible dynamic monitoring missions, such as chemical gas plume tracking. However, using such sequential large-scale data effectively is challenged, because the direct process of these data requires huge demands in terms of computational loads and memory. This paper presents a key-frame and target-detecting algorithm based on cumulative tensor CANDECOMP/PARAFAC (CP) factorization (CTCF) to select the frames where the target shows up, and a novel super-resolution (SR) method using sparse-based tensor Tucker factorization (STTF) is used to improve the spatial resolution. In the CTCF method, the HSV sequence is seen as cumulative tensors and the correlation of adjacent frames is exploited by applying CP tensor approximation. In the proposed STTF-based SR method, we consider the HSV frame as a third-order tensor; then, HSV frame super-resolution problem is transformed into estimations of the dictionaries along three dimensions and estimation of the core tensor. In order to promote sparse core tensors, a regularizer is incorporated to model the high spatial-spectral correlations. The estimations of the core tensor and the dictionaries along three dimensions are formulated as sparse-based Tucker factorizations of each HSV frame. Experimental results on real HSV data set demonstrate the superiority of the proposed CTCF and STTF algorithms over the comparative state-of-the-art target detection and SR approaches.

1. Introduction

Hyperspectral imaging has been one of the most popular research fields due to its ability of identifying the materials from very high spectral resolution and coverage. In the last decade, researchers focused on the processing and application of hyperspectral image (HSI), such as denoising [1, 2], feature extraction [3, 4], classification [5–11], detection [12–14], and super-resolution (fusion) [15–18]. In this section, researching of the latter two fields which are related to this paper will be briefly introduced.

Basically, target detection is a kind of binary classifier with the purpose of labeling every image pixel as a target or background. In HSIs, pixels with a significantly different spectral signature from their neighboring background pixels are defined as spectral anomalies. Anomaly detectors are

statistical or pattern recognition methods used to detect distinct pixels that differ from the background. It is worth mentioning that, in spectral anomaly detection approaches [19–22], such as Reed-Xiao (RX) algorithm [23], no prior information of the target spectral signature is assumed or used. However, we focus on the detection of invisible gas plumes in this paper, and the prior knowledge of the desired targets spectral characteristics is assumed to be known. In such cases, signature-based target detection algorithms are presented instead of anomaly detection. In these algorithms, the spectral characteristics of the target can be represented by a target subspace or a single target spectrum [24]. Likewise, the characteristics of background can be statistically expressed by a Gaussian distribution or a subspace defining the local or whole background statistics. As for this category, the matched subspace detector (MSD) method [25]

is one of the most typical algorithms. In the MSD, the target pixel vectors are represented by a linear combination of the target spectral signature and the background spectral signature, which stand for the subspace target spectra and the subspace background spectra, respectively. Then, the generalized likelihood ratio test (GLRT) is applied, using projection matrices associated with the background subspace and the target-and-background subspace. At last, the comparison between the output of GLRT and a preset threshold makes a final decision about whether the target is absent or present. From pixel level to subpixel level, a single pixel may contain several distinct pure materials (endmembers), also known as the mixed pixel. The presence of mixed pixels is a tough problem caused by the low spatial resolution of HSIs. Accordingly, some unmixing approaches [26–28] have been designed to compute fractional abundance of endmembers. In [29], a hyperspectral unmixing approach based on constrained matrix factorization (CMF) was proposed. Unlike conventional methods, each column vector of endmember matrix is represented as a nonnegative linear combination of pixel spectra. After endmember matrix and the corresponding fractional abundance matrix are obtained by solving optimization problems, abundance map of the target endmember shows the detection result.

As mentioned before, the HSIs often suffered from low spatial resolution. To acquire an HSI, the number of sun photons in each spectral band has to be greater than a minimum value, and the number of spectral bands is so huge in an HSI that the spatial resolution has to be sacrificed. Therefore, super-resolution (SR) techniques have aroused great interest in the last decade. Generally, the SR methods of HSI can be classified into four categories: Bayesian [30], component analysis [31], deep learning [32], and sparse representation. Due to the limited length of this paper, we focus on the introduction of sparse-based algorithms. In such HSI super-resolution schemes, images are expressed by dictionaries and corresponding sparse coefficients. On the basis of the spatial-spectral sparsity in the HSIs, the dictionaries and sparse coefficients are estimated jointly [33]. Huang et al. [34] introduced a fusion method of multispectral images (MSIs) with different spectral and spatial resolutions based on sparse matrix factorization. Akhtar et al. [35] presented an MSI-HSI fusion approach using sparse coding and Bayesian dictionary learning. Moreover, some algorithms based on matrix factorization [36–38] or unmixing [39] can also be regarded as the sparse representation schemes because the source images are decomposed into some basis and the corresponding coefficients. Yokoya et al. proposed a couple nonnegative matrix factorization (CNMF) [40] algorithm, where the unmixing techniques are employed to yield the endmember matrices and the high-resolution (HR) abundance matrices of HSI. In [41], Lanaras et al. suggested a joint scheme to solve the spectral unmixing problems. In [42], Zhang et al. fused the low-resolution (LR) HSI and HR-MSI based on the group spectral embedding and low-rank factorization.

However, the matrix factorization based schemes cannot fully exploit the spatial-spectral correlations of the HSIs. It is believed that considering HSIs as tensors is better because an HSI can be naturally expressed as a third-order tensor. In this paper, a detection algorithm based on cumulative tensor CP factorization (CTCF) is proposed. The sequential HSV data is expressed as a four-dimensional (4D) cumulative tensor; factor matrices are obtained by decomposing original 4D tensor using CP factorization. When a new frame presents and is added to the time dimension of the original tensor, this 4D cumulative tensor is updated together with the factor matrices. Consequently, a CP tensor approximation of the new frame is computed by updated factor matrices and the fitness between the new frame and the approximation is calculated. After comparing the fitness to a preset threshold, we can make the decision that whether the new frame continues to be used to update the cumulative tensor or the new frame is the key-frame where the target presents. CTCF-based method exploits not only the spatial-spectral correlations of the HSIs by applying tensor model, but also the temporal correlation between adjacent frames of the HSV.

On the other hand, tensor-based analysis has also been widely used in HSI super-resolution [43–45]. To the best of our knowledge, most of the SR algorithms enhance spatial resolution by fusing high-resolution MSI (HR-MSI) and low-resolution HSI (LR-HSI) from the same scene. Unfortunately, it is less practical in real application. In some situations, LR-HSI is the only data we have rather than both. In this paper, we suggest an SR algorithm using sparse-based tensor Tucker factorization (STTF). Inspired by the Tucker factorization and its related works, the HSV frames are represented as third-order tensors, which are approximated by the multiplication of the dictionaries along three dimensions (i.e., the dictionaries of the height mode, the width mode, and the spectral mode: they are named “three modes dictionaries” for short in the rest of this paper) and a core tensor. Then, the problem of SR is transformed into the estimations of the three modes dictionaries and estimation of the core tensor. Specifically, the spatial information is represented by the height mode dictionary and the width mode dictionary, the spectral information is represented by the spectral mode dictionary, and the correlations of the three modes dictionaries are modeled by the core tensor. HSIs are generally self-similar so that a sparse prior can be imposed on the core tensor; then, the estimations of the core tensor and three modes dictionaries are formulated as the STTF of the LR and HR HSV frames. In the iteration of STTF, core tensor and dictionaries are all updated and accurate estimates are yielded when convergence is achieved.

The remainder of this paper is organized as follows. Section 2 presents the materials and methods, including the basic notations and preliminaries of tensor and tensor factorization, the proposed CTCF approach for key-frame detection, and the proposed STTF method for key-frame super-resolution problem. In Section 3, experimental results on real HSV and the discussions are given. The paper is

summarized in Section 4 with ideas for future work along the path presented here.

2. Materials and Methods

2.1. Tensor Notations and Preliminaries

2.1.1. Tensor Notations. In this paper, vectors are denoted by boldface lowercase letters ($\mathbf{a}, \mathbf{b}, \mathbf{c}, \dots$), matrices are denoted by boldface capital letters ($\mathbf{A}, \mathbf{B}, \mathbf{C}, \dots$), and tensors are denoted by bold Euler script letters ($\mathbf{A}, \mathbf{B}, \mathbf{C}, \dots$). Generally, a tensor is a kind of multidimensional array, denoted by $\mathbf{A} \in \mathbb{R}^{I_1 \times I_2 \times \dots \times I_N}$. Here, tensor \mathbf{A} is an N th-order tensor and I_n ($1 \leq n \leq N$) is the dimension of the n th mode. Obviously, vectors are first-order tensors and matrices are second-order tensors. We use $\mathbf{A}(i_1, \dots, i_{n-1}, :, i_{n+1}, \dots, i_N)$ to denote the mode- n fiber, which are vectors yielded from tensor \mathbf{A} by changing index i_n with other indexes fixed. The mode- n unfolding matrix of tensor \mathbf{A} is generated by placing all the mode- n fibers in a matrix as columns, denoted by $\mathbf{A}_{(n)} \in \mathbb{R}^{I_n \times I_1 \times \dots \times I_{n-1} \times I_{n+1} \times \dots \times I_N}$.

An important calculation between a tensor and a matrix is the n -mode product, which is defined as

$$\mathbf{F} = \mathbf{A} \times_n \mathbf{B}, \quad (1)$$

where $\mathbf{B} \in \mathbb{R}^{I_n \times I_n}$ and $\mathbf{F} \in \mathbb{R}^{I_1 \times \dots \times I_{n-1} \times J_n \times I_{n+1} \times \dots \times I_N}$. The elements of \mathbf{A} are denoted by $a_{i_1 i_2 \dots i_N}$, so the elements of \mathbf{F} are computed by

$$f_{i_1, \dots, i_{n-1}, j_n, i_{n+1}, \dots, i_N} = \sum_{i_n} a_{i_1, \dots, i_{n-1}, i_n, i_{n+1}, \dots, i_N} b_{j_n i_n}. \quad (2)$$

Given the definition of n -mode product, we can obtain

$$\mathbf{F} = \mathbf{A} \times_n \mathbf{B} \Leftrightarrow \mathbf{F}_{(n)} = \mathbf{B} \mathbf{A}_{(n)}. \quad (3)$$

For continuous multiplication of a tensor and matrices in distinct modes, the result is not affected by the multiplication order, described by

$$\mathbf{A} \times_n \mathbf{B} \times_m \mathbf{C} = \mathbf{A} \times_m \mathbf{C} \times_n \mathbf{B} \quad (m \neq n). \quad (4)$$

If the modes are equivalent, equation (4) is transformed into

$$\mathbf{A} \times_n \mathbf{B} \times_n \mathbf{C} = \mathbf{A} \times_n (\mathbf{C} \mathbf{B}). \quad (5)$$

Suppose that $\mathbf{E}_n \in \mathbb{R}^{J_n \times I_n}$ ($1 \leq n \leq N$) is a collection of matrices; we define tensor $\mathbf{G} \in \mathbb{R}^{J_1 \times J_2 \times \dots \times J_N}$ as

$$\mathbf{G} = \mathbf{A} \times_1 \mathbf{E}_1 \times_2 \mathbf{E}_2 \cdots \times_N \mathbf{E}_N. \quad (6)$$

The matricization form of equation (6) is presented by

$$\mathbf{g} = (\mathbf{E}_N \otimes \mathbf{E}_{N-1} \otimes \cdots \otimes \mathbf{E}_1) \mathbf{a}, \quad (7)$$

where $\mathbf{g} = \text{vec}(\mathbf{G}) \in \mathbb{R}^J$ ($J = \prod_{n=1}^N J_n$) and $\mathbf{a} = \text{vec}(\mathbf{A}) \in \mathbb{R}^I$ ($I = \prod_{n=1}^N I_n$) are vectors yielded by arranging the mode-1 fibers of the tensors \mathbf{G} and \mathbf{A} . The Kronecker product is denoted by symbol " \otimes ."

Moreover, given the tensor \mathbf{A} , $\|\mathbf{A}\|_0$ represents the ℓ_0 -norm which equals the number of nonzero elements of \mathbf{A} , $\|\mathbf{A}\|_1 = \sum_{i_1, i_2, \dots, i_N} |a_{i_1 i_2, \dots, i_N}|$ denotes the ℓ_1 -norm, and $\|\mathbf{A}\|_F = \sqrt{\sum_{i_1, i_2, \dots, i_N} |a_{i_1 i_2, \dots, i_N}|^2}$ denotes the Frobenius norm.

The definition of rank-one tensor is introduced at last. The N th-order tensor \mathbf{A} is rank-one if it can be written as the outer product of N vectors, i.e., $\mathbf{A} = \mathbf{a}_1 \circ \mathbf{a}_2 \circ \dots \circ \mathbf{a}_N$. The symbol " \circ " denotes the vector outer product [46].

2.1.2. Tensor Factorizations. CANDECOMP/PARAFAC (CP) factorization decomposes a tensor into a sum of component rank-one tensors [47]. For example, given a third-order tensor $\mathbf{X} \in \mathbb{R}^{I \times J \times K}$, we may formulate it as

$$\mathbf{X} \approx \sum_{r=1}^R \mathbf{a}_r \circ \mathbf{b}_r \circ \mathbf{c}_r, \quad (8)$$

where R is a positive integer and $\mathbf{a}_r \in \mathbb{R}^I$, $\mathbf{b}_r \in \mathbb{R}^J$, and $\mathbf{c}_r \in \mathbb{R}^K$ ($r = 1, 2, \dots, R$). The element of tensor \mathbf{X} can be computed by

$$x_{ijk} \approx \sum_{r=1}^R a_{ir} b_{jr} c_{kr}, \quad i = 1, \dots, I, j = 1, \dots, J, k = 1, \dots, K. \quad (9)$$

CP factorization is illustrated in Figure 1.

The factorization result can be expressed by factor matrices of three dimensions. Factor matrices refer to the combination of the vectors from the rank-one components; i.e.,

$$\begin{aligned} \mathbf{A} &= [\mathbf{a}_1, \mathbf{a}_2, \dots, \mathbf{a}_R], \\ \mathbf{B} &= [\mathbf{b}_1, \mathbf{b}_2, \dots, \mathbf{b}_R], \\ \mathbf{C} &= [\mathbf{c}_1, \mathbf{c}_2, \dots, \mathbf{c}_R]. \end{aligned} \quad (10)$$

Following [48], the CP model can be concisely represented as

$$\mathbf{X} \approx \llbracket \mathbf{A}, \mathbf{B}, \mathbf{C} \rrbracket \equiv \sum_{r=1}^R \mathbf{a}_r \circ \mathbf{b}_r \circ \mathbf{c}_r. \quad (11)$$

On the basis of factor matrices, the mode- n unfolding matrices $\mathbf{X}_{(n)}$ ($n = 1, 2, 3$) of \mathbf{X} can be represented as

$$\begin{aligned} \mathbf{X}_{(1)} &\approx \mathbf{A} (\mathbf{C} \circ \mathbf{B})^T, \\ \mathbf{X}_{(2)} &\approx \mathbf{B} (\mathbf{C} \circ \mathbf{A})^T, \\ \mathbf{X}_{(3)} &\approx \mathbf{C} (\mathbf{B} \circ \mathbf{A})^T, \end{aligned} \quad (12)$$

where the symbol " \circ " denotes the Khatri-Rao product [49]. In this way, loss functions can be modeled as the approximation of the mode- n unfolding matrices; then the factor matrices of CP factorization can be obtained by solving the corresponding optimization problem.

Tucker factorization is another popular tensor decomposing approach [50]. It decomposes a tensor into a core tensor multiplied by a matrix along each mode. Thus, in the same case as above where $\mathbf{X} \in \mathbb{R}^{I \times J \times K}$, the factorization can be described as

$$\mathbf{X} \approx \mathbf{Z} \times_1 \mathbf{A} \times_2 \mathbf{B} \times_3 \mathbf{C} = \sum_{p=1}^P \sum_{q=1}^Q \sum_{r=1}^R z_{pqr} \mathbf{a}_p \circ \mathbf{b}_q \circ \mathbf{c}_r, \quad (13)$$

where $\mathbf{A} \in \mathbb{R}^{I \times P}$, $\mathbf{B} \in \mathbb{R}^{J \times Q}$, and $\mathbf{C} \in \mathbb{R}^{K \times R}$ are factor matrices which can be regarded as the principal components in each mode. Therefore, Tucker factorization is a form of higher-

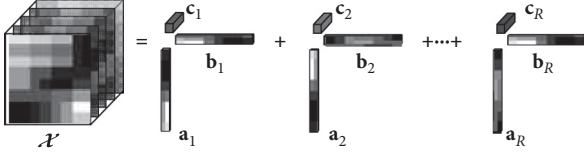


FIGURE 1: CP factorization of a third-order tensor.

order principal component analysis (PCA). Tensor $\mathbf{Z} \in \mathbb{R}^{P \times Q \times R}$ is the core tensor and its elements stand for the correlation level between the different components. Similar to (11), the Tucker model can be concisely represented by $\mathbf{X} \approx \llbracket \mathbf{Z}; \mathbf{A}, \mathbf{B}, \mathbf{C} \rrbracket$. Elementwise equation (13) can be represented as

$$x_{ijk} \approx \sum_{p=1}^P \sum_{q=1}^Q \sum_{r=1}^R z_{pqr} a_{ip} b_{jq} c_{kr}, \quad i = 1, \dots, I, j = 1, \dots, J, k = 1, \dots, K. \quad (14)$$

The Tucker factorization is illustrated in Figure 2.

2.2. The Proposed CTCF-Based Detection Method. In this subsection, the optimization problem of updating factor matrix is presented, followed with the proposed cumulative tensor CP factorization (CTCF) of third-order tensors. It is then extended to N th-order tensors. The CTCF-based detection method is described in the end of this subsection with its flowchart shown in Figure 3.

2.2.1. CP Tensor Approximation by Factor Matrices. Similar to equation (12), the mode- n unfolding matrix of $\mathbf{X} \in \mathbb{R}^{I_1 \times I_2 \times \dots \times I_N}$ can be approximated by factor matrices; i.e.,

$$\begin{aligned} \mathbf{X}_{(n)} &\approx \mathbf{A}^{(n)} \left(\mathbf{A}^{(N)} \odot \dots \odot \mathbf{A}^{(n+1)} \odot \mathbf{A}^{(n-1)} \odot \dots \odot \mathbf{A}^{(1)} \right)^T \\ &= \mathbf{A}^{(n)} \left(\odot_{i \neq n}^N \mathbf{A}^{(i)} \right)^T, \end{aligned} \quad (15)$$

where the factor matrices $\mathbf{A}^{(1)}, \dots, \mathbf{A}^{(N)}$ are obtained by CP factorization. The corresponding loss function is

$$\mathcal{L} = \frac{1}{2} \left\| \mathbf{X}_{(n)} - \mathbf{A}^{(n)} \left(\odot_{i \neq n}^N \mathbf{A}^{(i)} \right)^T \right\|^2. \quad (16)$$

The Alternating Least Squares (ALS) algorithm is often applied to obtain factor matrices by solving the following optimization problem:

$$\mathbf{A}^{(n)} = \arg \min_{\mathbf{A}^{(n)}} \frac{1}{2} \left\| \mathbf{X}_{(n)} - \mathbf{A}^{(n)} \left(\odot_{i \neq n}^N \mathbf{A}^{(i)} \right)^T \right\|^2. \quad (17)$$

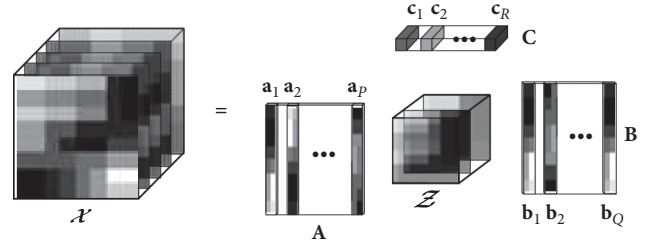


FIGURE 2: Tucker factorization of a third-order tensor.

When the tensor updates, the new tensor can be computed by the updated factor matrices which are given by equation (17).

2.2.2. CTCF of Third-Order Tensor. Generally, an image is a second-order tensor; then sequential images form a third-order tensor, i.e., a video, adding a temporal dimension on two spatial dimensions. When a new video frame presents and is added to the time dimension of the original tensor, it is defined as a three-dimensional (3D) cumulative tensor. With the number of new frames increasing, the 3D cumulative tensor updates frame by frame.

In conventional CP tensor approximation, whenever a new frame of image is added in the time dimension, ALS algorithm needs to be reused to approximate the new cumulative tensor, which is a time consuming process. In addition, the temporal correlation between neighboring frames is not exploited in the decomposition of the cumulative tensor. This paper proposes CTCF to update the CP factorization of original cumulative tensor, obtain the updated factor matrices, and approximate the new frame.

Given an original 3D cumulative tensor $\mathbf{X}_{\text{ori}} \in \mathbb{R}^{I \times J \times T_{\text{ori}}}$, the result of CP factorization is denoted by $\mathbf{X}_{\text{ori}} \approx \llbracket \mathbf{A}_{\text{ori}}, \mathbf{B}_{\text{ori}}, \mathbf{C}_{\text{ori}} \rrbracket$. When a new tensor $\mathbf{X}_{\text{new}} \in \mathbb{R}^{I \times J \times T_{\text{new}}}$ is added in the time dimension, the updated cumulative tensor is $\mathbf{X} \in \mathbb{R}^{I \times J \times (T_{\text{ori}} + T_{\text{new}})}$, of which the CP factorization appears as $\mathbf{X} \approx \llbracket \mathbf{A}, \mathbf{B}, \mathbf{C} \rrbracket$. We focus on obtaining \mathbf{A} , \mathbf{B} , and \mathbf{C} by updating \mathbf{A}_{ori} , \mathbf{B}_{ori} , and \mathbf{C}_{ori} .

The updating process is operated in an alternating way. Firstly, temporal dimensional factor matrix \mathbf{C} is computed while factor matrices \mathbf{A} and \mathbf{B} are fixed; i.e.,

$$\begin{aligned} \mathbf{C} &= \arg \min_{\mathbf{C}} \frac{1}{2} \left\| \mathbf{X}_{(3)} - \mathbf{C} (\mathbf{B} \odot \mathbf{A})^T \right\|^2 = \arg \min_{\mathbf{C}} \frac{1}{2} \left\| \begin{bmatrix} \mathbf{X}_{\text{ori}(3)} \\ \mathbf{X}_{\text{new}(3)} \end{bmatrix} - \begin{bmatrix} \mathbf{C}^{(1)} \\ \mathbf{C}^{(2)} \end{bmatrix} (\mathbf{B} \odot \mathbf{A})^T \right\|^2 \\ &= \arg \min_{\mathbf{C}} \frac{1}{2} \left\| \begin{bmatrix} \mathbf{X}_{\text{ori}(3)} - \mathbf{C}^{(1)} (\mathbf{B} \odot \mathbf{A})^T \\ \mathbf{X}_{\text{new}(3)} - \mathbf{C}^{(2)} (\mathbf{B} \odot \mathbf{A})^T \end{bmatrix} \right\|^2, \end{aligned} \quad (18)$$

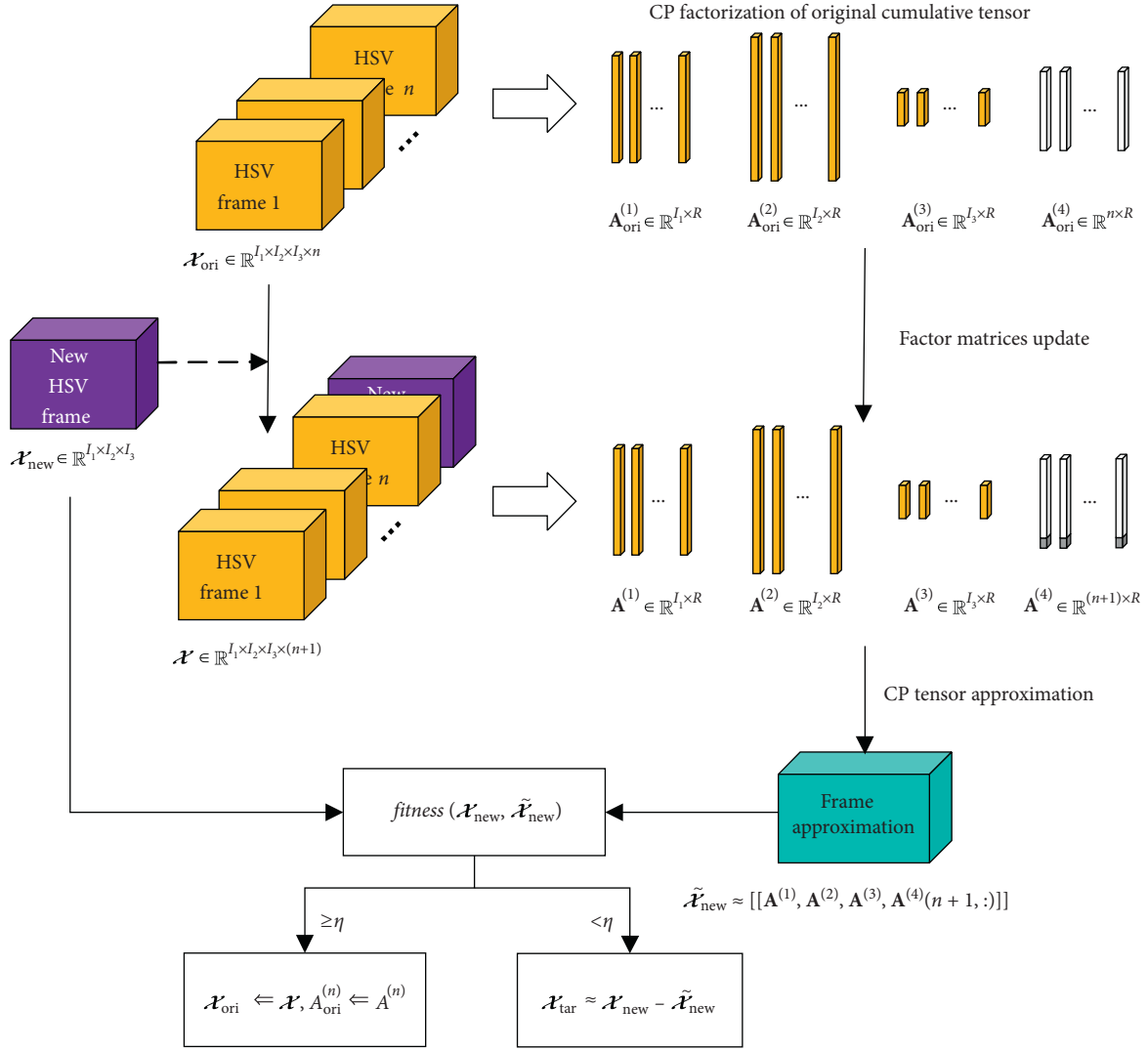


FIGURE 3: Flowchart of CTCF-based detection method.

where \mathbf{C} is divided into two terms. For \mathbf{A} and \mathbf{B} are fixed as \mathbf{A}_{ori} and \mathbf{B}_{ori} , the first row of (18) will be minimized if $\mathbf{C}^{(1)} = \mathbf{C}_{\text{ori}}$. To minimize the second row, according to (12), the optimal solution of $\mathbf{C}^{(2)}$ is $\mathbf{X}_{\text{new}(3)} ((\mathbf{B} \odot \mathbf{A})^T)^\dagger$, where the symbol “ \dagger ” denotes Moore–Penrose pseudoinverse of the matrix [51]. So, \mathbf{C} can be updated by adding \mathbf{C}_{new} which is represented by

$$\mathbf{C} = \begin{bmatrix} \mathbf{C}_{\text{ori}} \\ \mathbf{C}_{\text{new}} \end{bmatrix} = \begin{bmatrix} \mathbf{C}_{\text{ori}} \\ \mathbf{X}_{\text{new}(3)} ((\mathbf{B} \odot \mathbf{A})^T)^\dagger \end{bmatrix}. \quad (19)$$

Secondly, factor matrix \mathbf{A} is computed while factor matrices \mathbf{B} and \mathbf{C} are fixed. Similar to 16, the loss function of estimating \mathbf{A} is written as

$$\mathcal{L} = \frac{1}{2} \|\mathbf{X}_{(1)} - \mathbf{A}(\mathbf{C} \odot \mathbf{B})^T\|^2. \quad (20)$$

Derive \mathcal{L} with respect to \mathbf{A} ; then, we have

$$\frac{\partial \mathcal{L}}{\partial \mathbf{A}} = \mathbf{X}_{(1)} (\mathbf{C} \odot \mathbf{B}) - \mathbf{A} (\mathbf{C} \odot \mathbf{B})^T (\mathbf{C} \odot \mathbf{B}). \quad (21)$$

To simplify equation (21), denote $\mathbf{P} = \mathbf{X}_{(1)} (\mathbf{C} \odot \mathbf{B})$ and $\mathbf{Q} = (\mathbf{C} \odot \mathbf{B})^T (\mathbf{C} \odot \mathbf{B})$; thus, when $\partial \mathcal{L} / \partial \mathbf{A} = 0$, we have $\mathbf{A} = \mathbf{P} \mathbf{Q}^{-1}$. According to [47], \mathbf{Q} can be rewritten as

$$\mathbf{Q} = (\mathbf{C} \odot \mathbf{B})^T (\mathbf{C} \odot \mathbf{B}) = (\mathbf{C}^T \mathbf{C}) \otimes (\mathbf{B}^T \mathbf{B}). \quad (22)$$

For computing \mathbf{P} , we also divide $\mathbf{X}_{(1)}$ and \mathbf{C} into two terms; i.e.,

$$\begin{aligned} \mathbf{P} &= \mathbf{X}_{(1)} (\mathbf{C} \odot \mathbf{B}) = [\mathbf{X}_{\text{ori}(1)}, \mathbf{X}_{\text{new}(1)}] \left(\begin{bmatrix} \mathbf{C}_{\text{ori}} \\ \mathbf{C}_{\text{new}} \end{bmatrix} \odot \mathbf{B} \right) \\ &= [\mathbf{X}_{\text{ori}(1)}, \mathbf{X}_{\text{new}(1)}] \left(\begin{bmatrix} \mathbf{C}_{\text{ori}} \odot \mathbf{B} \\ \mathbf{C}_{\text{new}} \odot \mathbf{B} \end{bmatrix} \right) = \mathbf{X}_{\text{ori}(1)} (\mathbf{C}_{\text{ori}} \odot \mathbf{B}) + \mathbf{X}_{\text{new}(1)} (\mathbf{C}_{\text{new}} \odot \mathbf{B}). \end{aligned} \quad (23)$$

Since \mathbf{B} are fixed as \mathbf{B}_{ori} , the first term of equation (23) contains only the information of original tensor, which can be expressed by

$$\mathbf{P}_{\text{ori}} = \mathbf{X}_{\text{ori}(1)} (\mathbf{C}_{\text{ori}} \odot \mathbf{B}), \quad (24)$$

so, equation (23) is rewritten as

$$\mathbf{P} = \mathbf{P}_{\text{ori}} + \mathbf{X}_{\text{new}(1)} (\mathbf{C}_{\text{new}} \odot \mathbf{B}), \quad (25)$$

Hence, \mathbf{P} can be updated from \mathbf{P}_{ori} using mode-1 unfolding matrix of \mathbf{X}_{new} and factor matrix mentioned above \mathbf{C}_{new} . Generally, \mathbf{P} is initialized by $\mathbf{X}(\tau) \in \mathbb{R}^{I \times J \times \tau}$, which is a small front part of \mathbf{X}_{ori} , and updated iteratively by (25). Analogously, the update process of \mathbf{Q} can be represented by

$$\mathbf{Q} = \mathbf{Q}_{\text{ori}} + (\mathbf{C}_{\text{new}} \odot \mathbf{B})^T (\mathbf{C}_{\text{new}} \odot \mathbf{B}) = \mathbf{Q}_{\text{ori}} + (\mathbf{C}_{\text{new}}^T \mathbf{C}_{\text{new}}) \otimes (\mathbf{B}^T \mathbf{B}). \quad (26)$$

The update of \mathbf{A} may be summarized as

$$\begin{aligned} \mathbf{P} &\leftarrow \mathbf{P} + \mathbf{X}_{\text{new}(1)} (\mathbf{C}_{\text{new}} \odot \mathbf{B}), \\ \mathbf{Q} &\leftarrow \mathbf{Q} + (\mathbf{C}_{\text{new}}^T \mathbf{C}_{\text{new}}) \otimes (\mathbf{B}^T \mathbf{B}), \\ \mathbf{A} &\leftarrow \mathbf{P} \mathbf{Q}^{-1}. \end{aligned} \quad (27)$$

Finally, the update of factor matrix \mathbf{B} may likewise be expressed by

$$\begin{aligned} \mathbf{U} &\leftarrow \mathbf{U} + \mathbf{X}_{\text{new}(2)} (\mathbf{C}_{\text{new}} \odot \mathbf{A}), \\ \mathbf{V} &\leftarrow \mathbf{V} + (\mathbf{C}_{\text{new}}^T \mathbf{C}_{\text{new}}) \otimes (\mathbf{A}^T \mathbf{A}), \\ \mathbf{B} &\leftarrow \mathbf{U} \mathbf{V}^{-1}, \end{aligned} \quad (28)$$

where $\mathbf{U} = \mathbf{X}_{(2)} (\mathbf{C} \odot \mathbf{A})$ and $\mathbf{V} = (\mathbf{C}^T \mathbf{C}) \otimes (\mathbf{A}^T \mathbf{A})$.

To make the process clearer, the proposed CTCF of third-order tensor is summarized by Algorithm 1.

2.2.3. CTCF of Nth-Order Tensor. On the basis of Section 2.2.2, we try to extend CTCF to higher-order tensors. Suppose an N -dimensional cumulative tensor $\mathbf{X}_{\text{ori}} \in \mathbb{R}^{I_1 \times I_2 \times \dots \times I_{N-1} \times T_{\text{ori}}}$ where the last dimension is temporal dimension. The CP factorization of \mathbf{X}_{ori} is represented as $\mathbf{X}_{\text{ori}} \approx [\mathbf{A}_{\text{ori}}^{(1)}, \dots, \mathbf{A}_{\text{ori}}^{(N-1)}, \mathbf{A}_{\text{ori}}^{(N)}]$. When a new tensor $\mathbf{X}_{\text{ori}} \in \mathbb{R}^{I_1 \times I_2 \times \dots \times I_{N-1} \times T_{\text{new}}}$ is added in the time dimension, the updated cumulative tensor is $\mathbf{X} \in \mathbb{R}^{I_1 \times I_2 \times \dots \times I_{N-1} \times (T_{\text{ori}} + T_{\text{new}})}$, of which the CP factorization is denoted by $\mathbf{X} \approx [\mathbf{A}^{(1)}, \dots, \mathbf{A}^{(N-1)}, \mathbf{A}^{(N)}]$.

Similar to Section 2.2.2, temporal dimensional factor matrix $\mathbf{A}^{(N)}$ is firstly updated with other $N-1$ matrices fixed. Like 17, the optimization problem of estimating $\mathbf{A}^{(N)}$ is formulated by

$$\mathbf{A}^{(N)} = \arg \min_{\mathbf{A}^{(N)}} \frac{1}{2} \left\| \mathbf{X}_{(N)} - \mathbf{A}^{(N)} (\odot^{N-1} \mathbf{A}^{(i)})^T \right\|^2. \quad (29)$$

We also separate original part from new added part; i.e.,

$$\mathbf{A}^{(N)} = \begin{bmatrix} \mathbf{A}_{\text{ori}}^{(N)} \\ \mathbf{A}_{\text{new}}^{(N)} \end{bmatrix} = \begin{bmatrix} \mathbf{A}_{\text{ori}}^{(N)} \\ \mathbf{X}_{\text{new}} \left((\odot^{N-1} \mathbf{A}^{(i)})^T \right)^\dagger \end{bmatrix}, \quad i = 1, 2, \dots, N-1. \quad (30)$$

The original part is minimized by fixing the first $N-1$ factor matrix and the new part is updated by \mathbf{X}_{new} .

The updates of nontemporal dimensional factor matrices $\mathbf{A}^{(n)}$ ($n \in [1, N-1]$) may refer to the ones of factor matrices \mathbf{A} and \mathbf{B} in Section 2.2.2. The loss function $\mathcal{L}^{(n)}$ of estimating $\mathbf{A}^{(n)}$ is the same as 16. Let $\partial \mathcal{L}^{(n)} / \partial \mathbf{A}^{(n)} = 0$ and introduce matrices $\mathbf{P}^{(n)}$ and $\mathbf{Q}^{(n)}$; the update of $\mathbf{A}^{(n)}$ may be summarized as

$$\begin{aligned} \mathbf{P}^{(n)} &\leftarrow \mathbf{P}^{(n)} + \mathbf{X}_{\text{new}(n)} (\mathbf{A}_{\text{new}}^{(N)} \odot \mathbf{K}^{(n)}), \\ \mathbf{Q}^{(n)} &\leftarrow \mathbf{Q}^{(n)} + (\mathbf{A}_{\text{new}}^{(N)T} \mathbf{A}_{\text{new}}^{(N)}) \otimes \mathbf{R}^{(n)}, \\ \mathbf{A}^{(n)} &\leftarrow \mathbf{P}^{(n)} (\mathbf{Q}^{(n)})^{-1}, \end{aligned} \quad (31)$$

where $\mathbf{K}^{(n)} = \odot_{i \neq n}^{N-1} \mathbf{A}^{(i)}$ and $\mathbf{R}^{(n)} = \otimes_{i \neq n}^{N-1} \mathbf{A}^{(i)T} \mathbf{A}^{(i)}$.

2.2.4. CTCF-Based Detection Method. In HSV, the sequential data is expressed as a 4D cumulative tensor; the temporal dimension increases with new frames are added in. Whenever a new frame presents, the results of original cumulative tensor CP factorization are updated to obtain the factor matrices of the new cumulative tensor, and the CP tensor approximation of the newly added frame is obtained at the same time. If the target is absent, the CP tensor approximation will lead to a small error, since the background information is similar between adjacent frames. On the contrary, if the error is large, the target is likely to present. We define the fitness between the new frame and its approximation in 34. If the fitness is smaller than the threshold, the target is supposed to appear in the new frame. Otherwise, the new frame is added in the temporal dimension and used to update original cumulative tensor.

The original 4D cumulative tensor is denoted by $\mathbf{X}_{\text{ori}} \in \mathbb{R}^{I_1 \times I_2 \times I_3 \times n}$; n denotes the frame number of initial video. The factor matrices of four dimensions are represented as

$$\mathbf{X}_{\text{ori}} \approx [\mathbf{A}_{\text{ori}}^{(1)}, \mathbf{A}_{\text{ori}}^{(2)}, \mathbf{A}_{\text{ori}}^{(3)}, \mathbf{A}_{\text{ori}}^{(4)}], \quad (32)$$

where $\mathbf{A}_{\text{ori}}^{(1)} \in \mathbb{R}^{I_1 \times R}$, $\mathbf{A}_{\text{ori}}^{(2)} \in \mathbb{R}^{I_2 \times R}$, $\mathbf{A}_{\text{ori}}^{(3)} \in \mathbb{R}^{I_3 \times R}$, and $\mathbf{A}_{\text{ori}}^{(4)} \in \mathbb{R}^{n \times R}$ and R denotes the number of component rank-one tensors in CP factorization. When a new frame $\mathbf{X}_{\text{new}} \in \mathbb{R}^{I_1 \times I_2 \times I_3}$ is added in the temporal dimension of

Input: original 3D cumulative tensor $\mathbf{X}_{\text{ori}} \in \mathbb{R}^{I \times J \times T_{\text{ori}}} \approx [\mathbf{A}_{\text{ori}}, \mathbf{B}_{\text{ori}}, \mathbf{C}_{\text{ori}}]$ new tensor $\mathbf{X}_{\text{new}} \in \mathbb{R}^{I \times J \times T_{\text{new}}}$
 Step 1: new tensor is added in the time dimension and $\mathbf{X} \in \mathbb{R}^{I \times J \times (T_{\text{ori}} + T_{\text{new}})}$ is obtained
 Step 2: decompose \mathbf{X} by CP factorization $\mathbf{X} \approx [\mathbf{A}, \mathbf{B}, \mathbf{C}]$
 Step 3: update \mathbf{C} by (19), with \mathbf{A} and \mathbf{B} are fixed
 Step 4: update \mathbf{A} by (27), with \mathbf{B} and \mathbf{C} are fixed
 Step 5: update \mathbf{B} by (28), with \mathbf{A} and \mathbf{C} are fixed
 Step 6: estimate \mathbf{X} by updated \mathbf{A} , \mathbf{B} and \mathbf{C}
Output: approximation of updated cumulative tensor \mathbf{X}

ALGORITHM 1: CTCF of third-order tensor.

original 4D cumulative tensor, the 4D cumulative tensor is updated and denoted by $\mathbf{X} \in \mathbb{R}^{I_1 \times I_2 \times I_3 \times (n+1)}$. The factor matrices of \mathbf{X} are expressed by

$$\mathbf{X} \approx [\mathbf{A}^{(1)}, \mathbf{A}^{(2)}, \mathbf{A}^{(3)}, \mathbf{A}^{(4)}], \quad (33)$$

where $\mathbf{A}^{(1)} \in \mathbb{R}^{I_1 \times R}$, $\mathbf{A}^{(2)} \in \mathbb{R}^{I_2 \times R}$, $\mathbf{A}^{(3)} \in \mathbb{R}^{I_3 \times R}$, and $\mathbf{A}^{(4)} \in \mathbb{R}^{(n+1) \times R}$. Based on Section 2.2.3, we estimate $\mathbf{A}^{(1)} \sim \mathbf{A}^{(4)}$ and obtain the approximation of \mathbf{X} and $\tilde{\mathbf{X}}_{\text{new}}$, where $\tilde{\mathbf{X}}_{\text{new}} \approx [\mathbf{A}^{(1)}, \mathbf{A}^{(2)}, \mathbf{A}^{(3)}, \mathbf{A}^{(4)}(n+1, :)]$. Actually, it is the specific case when $N = 4$.

We define the *fitness* ($\mathbf{X}_{\text{new}}, \tilde{\mathbf{X}}_{\text{new}}$) as

$$\text{fitness}(\mathbf{X}_{\text{new}}, \tilde{\mathbf{X}}_{\text{new}}) = 1 - \frac{\|\mathbf{X}_{\text{new}} - \tilde{\mathbf{X}}_{\text{new}}\|_F}{\|\mathbf{X}_{\text{new}}\|_F}. \quad (34)$$

If the target does not appear, the approximation error is small and the result of fitness is large. Given a preset threshold η , when $\text{fitness}(\mathbf{X}_{\text{new}}, \tilde{\mathbf{X}}_{\text{new}}) > \eta$, i.e., the fitness is larger than η , we decide that the target is absent. Then, the nontarget frame is added in temporal dimension and the updated 4D cumulative tensor becomes the new original 4D cumulative tensor, which can be expressed as

$$\mathbf{X}_{\text{ori}} \leftarrow \mathbf{X}, \mathbf{A}_{\text{ori}}^{(n)} \leftarrow \mathbf{A}^{(n)}, \quad n \in [1, 4]. \quad (35)$$

If the target appears, the approximation error is large and the fitness is smaller than η . The residual of \mathbf{X}_{new} and $\tilde{\mathbf{X}}_{\text{new}}$ is the approximation of the target tensor; i.e.,

$$\mathbf{X}_{\text{tar}} \approx \mathbf{X}_{\text{new}} - \tilde{\mathbf{X}}_{\text{new}}. \quad (36)$$

The target of each frame will be shown in 2D form by taking the maximum value of every spectrum. In this way, the proposed CTCF-based detection method can extract not only the key-frames where the target presents, but also the approximate region of target in every key-frame. The flowchart of the proposed method is shown in Figure 3. In Section 3, experiments on real HSV data are conducted and the proposed method is compared with some representative techniques.

2.3. The Proposed STTF-Based Super-Resolution Method. In Section 2.2, we present an approach to detect the frames where the target appears in HSV and the approximate region of the target. However, as discussed in Section 1, there has to be a tradeoff between spectral resolution and the spatial resolution in HSI imaging systems [52]. The spatial resolution is always low since high spectral resolution is required

in HSIs and HSV. So, we are interested in improving the spatial resolution of targets after the detecting process. Instead of fusing HR-MSI and LR-HSI, we try to handle the target SR problem by what we have got, which is more practical in real cases.

2.3.1. Problem Formulation. In this subsection, HSIs are represented as 3D tensors with three indexes (H, W, S), which stand for the height, width, and spectral modes. $\mathbf{X} \in \mathbb{R}^{H \times W \times S}$ denotes the HR-HSI and the LR-HSI is denoted by $\mathbf{Y} \in \mathbb{R}^{h \times w \times S}$, where $W > w$ and $H > h$. The goal is to estimate \mathbf{X} from \mathbf{Y} .

There are two significant characteristics of HR-HSIs [53]: the first one is that spectral vectors can be well approximated in low dimensional subspaces, and the second one is that HSIs are spatially self-similar. This means that sparsity exists in both spectral and spatial dimensions. Inspired by sparse representation [54], the low dimensionality in spectral domain gives the possibility to form a spectral mode dictionary \mathbf{S} with few nonzero atoms; the self-similarities in spatial domain guarantee the sparse representations of the height and width modes with spatial dictionaries \mathbf{H} and \mathbf{W} . In this way, the conventional Tucker factorization is transformed into the multiplication of the core tensor and three modes dictionaries. The factorization is illustrated in Figure 4. The HR-HSI is represented as

$$\mathbf{X} = \mathbf{Z} \times_1 \mathbf{H} \times_2 \mathbf{W} \times_3 \mathbf{S}, \quad (37)$$

where $\mathbf{H} \in \mathbb{R}^{H \times z_h}$, $\mathbf{W} \in \mathbb{R}^{W \times z_w}$, and $\mathbf{S} \in \mathbb{R}^{S \times z_s}$. The variables z_h , z_w , and z_s denote the atoms (i.e., the number of columns) of \mathbf{H} , \mathbf{W} , and \mathbf{S} , respectively. The core tensor \mathbf{Z} contains the coefficients of \mathbf{X} over three modes dictionaries. We can see that 37 incorporates the information of separated modes into a unified framework.

The LR key-frame of HSV \mathbf{Y} can be seen as the spatially downsampled version of HR-HSI \mathbf{X} , which is written as

$$\mathbf{Y} = \mathbf{X} \times_1 \mathbf{D}_1 \times_2 \mathbf{D}_2, \quad (38)$$

where $\mathbf{D}_1 \in \mathbb{R}^{h \times H}$ and $\mathbf{D}_2 \in \mathbb{R}^{w \times W}$ are downsampling matrices of the height and width modes. Substituting 37 into (38), \mathbf{Y} is represented by

$$\mathbf{Y} = \mathbf{Z} \times_1 (\mathbf{D}_1 \mathbf{H}) \times_2 (\mathbf{D}_2 \mathbf{W}) \times_3 \mathbf{S} = \mathbf{Z} \times_1 \mathbf{H}^* \times_2 \mathbf{W}^* \times_3 \mathbf{S}, \quad (39)$$

where $\mathbf{H}^* = \mathbf{D}_1 \mathbf{H} \in \mathbb{R}^{h \times z_h}$ and $\mathbf{W}^* = \mathbf{D}_2 \mathbf{W} \in \mathbb{R}^{w \times z_w}$ denotes the downsampled dictionary of height and width modes. To

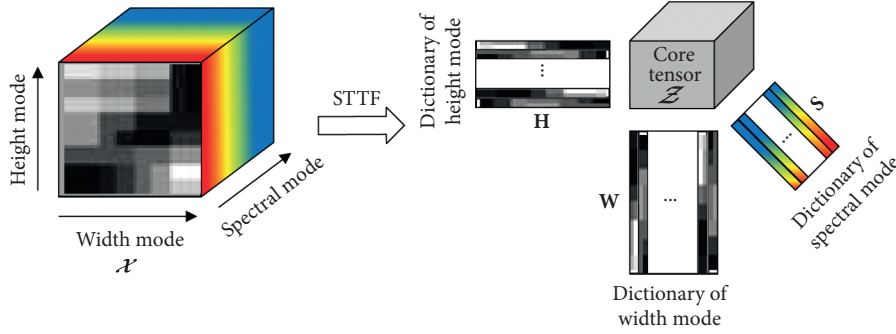


FIGURE 4: Sparse-based tensor Tucker factorization of an HSI.

recover \mathbf{X} , we focus on estimating the dictionaries \mathbf{H} , \mathbf{W} , and \mathbf{S} and the core tensor \mathbf{Z} .

2.3.2. The Proposed STTF-Based SR Algorithm. Since \mathbf{Y} is a downsampled version, recovering \mathbf{X} from \mathbf{Y} is a typical inverse problem, which is badly ill-posed. So, some prior knowledge of \mathbf{X} is needed to regularize the super-resolution problem. In HSI processing, the spectral sparsity is a widespread regularizer applied to solve varieties of ill-posed problems [55–58]. In such regularization, spectral vectors are linearly combined by a small quantity of different spectral signatures. However, these schemes only take advantage of the sparsity of the spectral domain. In the proposed algorithm, taking into account the HSI self-similarity, sparsity regularization is extended to the spatial domain by exploiting the sparse-based tensor Tucker factorization (STTF). In STTF, the HR-HSI performs a united sparse representation of the core tensor and three modes dictionaries.

On the basis of equation (39), the HSV frame super-resolution is formulated as a constrained least-squares optimization problem:

$$\begin{aligned} \min_{\mathbf{H}, \mathbf{W}, \mathbf{S}, \mathbf{Z}} \|\mathbf{Y} - \mathbf{Z} \times_1 \mathbf{H}^* \times_2 \mathbf{W}^* \times_3 \mathbf{S}\|_F^2, \\ \text{s.t. } \|\mathbf{Z}\|_0 \leq \theta, \end{aligned} \quad (40)$$

where $\|\cdot\|_F$ represents the Frobenius norm and θ denotes the number of maximum nonzero elements of \mathbf{Z} . Because of the ℓ_0 -norm constraint, equation (40) is nonconvex. To make the optimization processable, the ℓ_0 -norm is replaced by the ℓ_1 -norm and 40 is transformed into an unconstrained version:

$$\min_{\mathbf{H}, \mathbf{W}, \mathbf{S}, \mathbf{Z}} \|\mathbf{Y} - \mathbf{Z} \times_1 \mathbf{H}^* \times_2 \mathbf{W}^* \times_3 \mathbf{S}\|_F^2 + \lambda \|\mathbf{Z}\|_1, \quad (41)$$

where λ is the parameter of sparse regularizer. Equation (41) is also nonconvex, and the solutions of \mathbf{H} , \mathbf{W} , and \mathbf{S} and \mathbf{Z} are not unique. Nonetheless, if we focus on only one variable with other variables fixed, the objective function in equation (41) is convex. Inspired by [59, 60], equation (41) can be solved by proximal alternating optimization scheme, which is guaranteed to reach convergence in a particular situation. Concretely, \mathbf{H} , \mathbf{W} , \mathbf{S} , and \mathbf{Z} are updated iteratively by

$$\begin{aligned} \mathbf{H} &= \arg \min_{\mathbf{H}} f(\mathbf{H}, \mathbf{W}, \mathbf{S}, \mathbf{Z}) + \alpha \|\mathbf{H} - \mathbf{H}_{\text{pre}}\|_F^2, \\ \mathbf{W} &= \arg \min_{\mathbf{W}} f(\mathbf{H}, \mathbf{W}, \mathbf{S}, \mathbf{Z}) + \alpha \|\mathbf{W} - \mathbf{W}_{\text{pre}}\|_F^2, \\ \mathbf{S} &= \arg \min_{\mathbf{S}} f(\mathbf{H}, \mathbf{W}, \mathbf{S}, \mathbf{Z}) + \alpha \|\mathbf{S} - \mathbf{S}_{\text{pre}}\|_F^2, \\ \mathbf{Z} &= \arg \min_{\mathbf{Z}} f(\mathbf{H}, \mathbf{W}, \mathbf{S}, \mathbf{Z}) + \alpha \|\mathbf{Z} - \mathbf{Z}_{\text{pre}}\|_F^2, \end{aligned} \quad (42)$$

where $(\cdot)_{\text{pre}}$ denotes the previous estimation in the last iteration and α denotes a positive number. Equation (41) defines the object function $f(\mathbf{H}, \mathbf{W}, \mathbf{S}, \mathbf{Z})$. The optimizations of \mathbf{H} , \mathbf{W} , \mathbf{S} , and \mathbf{Z} will be presented detailedly in the appendix. The conjugate gradient (CG) method [61] and the alternating direction method of multipliers (ADMM) [62] will be used in the optimizations.

2.3.3. Initialization of the Proposed Method. Since the optimization problem in (41) is nonconvex, the solution would result in poor local minima if we set the initialization carelessly. In this paper, we initialize the spatial dictionaries \mathbf{H}^* and \mathbf{W}^* from $\mathbf{Y}_{(1)}$ and $\mathbf{Y}_{(2)}$ dictionary-updates-cycles KSVd (DUC-KSVd) [63]; this method can promote sparse representations. Then, initialization of spectral dictionary \mathbf{S} is accomplished by simplex identification split augmented Lagrangian (SISAL) algorithm [64]; this approach can efficiently identify a minimum unit that contains the spectral vectors.

The proposed STTF-based SR algorithm is summarized in Algorithm 2.

3. Results and Discussion

3.1. Experimental Data Set. To highlight the advantages of HSIs, we choose invisible gas plume to be the target. The proposed algorithms can be extended to other types of data reasonably. In this section, the HSV data set is acquired by the infrared imaging spectrometer “HyperCam-LW.” Sulfur hexafluoride (SF_6) is chosen to be the target, since it is a kind of odorless and colorless gas plume with a distinct absorption peak in LWIR range. The HSV data set consists of 60 infrared hyperspectral frames with the size of


```

Input: LR-HSI  $\mathbf{Y}$ 
Initialize  $\mathbf{S}$  with SISAL
Initialize  $\mathbf{H}^*$  and  $\mathbf{W}^*$  with DUC-KSVD
Initialize  $\mathbf{Z}$  with (39)
while no convergence do
  Step 1: update  $\mathbf{H}$  by solving (A.3) with CG
   $\mathbf{H}^* = \mathbf{D}_1 \mathbf{H}, \mathbf{H}_{\text{pre}} = \mathbf{H}$ 
  Step 2: update  $\mathbf{W}$  by solving (A.6) with CG
   $\mathbf{W}^* = \mathbf{D}_2 \mathbf{W}, \mathbf{W}_{\text{pre}} = \mathbf{W}$ 
  Step 3: update  $\mathbf{S}$  by solving (A.9) with CG
   $\mathbf{S}_{\text{pre}} = \mathbf{S}$ 
  Step 4: update  $\mathbf{Z}$  by solving (A.15) with CG
   $\mathbf{Z}_{\text{pre}} = \mathbf{Z}$ 
end while
Estimate  $\mathbf{X}$  by (37)
Output: HR-HSI  $\mathbf{X}$ 

```

ALGORITHM 2: STTF-based SR method.

$128 \times 320 \times 127$. The imaging interval is 4.8 s, and the wavelength of the data ranges from $7.8 \mu\text{m}$ to $11.8 \mu\text{m}$.

In SR method, only the middle 128×128 pixels are used in the experiment (specifically, column 71 to column 198) for reasons connected with the algorithm process. And we remove the spectral band 41–127 because of water vapor absorption and extremely low SNR. At last, the size of input LR-HSI is $128 \times 128 \times 40$.

3.2. Compared Methods. For CTCF-based detection method, we compare it with two representative methods: MSD (matched subspace detector) [25] and CMF (constrained matrix factorization) [29]. For STTF-based SR method, we compare it with three state-of-the-art algorithms: bicubic interpolation, sparse representation-based SR method [54], and sequence information-based SR method [65].

3.3. Qualitative and Quantitative Metrics. For detection methods, receiver operating characteristic (ROC) curves [66] are used to evaluate the performance. Generally, a detector outperforms another one if the area under its ROC curve is larger [67]. As suggested in [68], the area under the ROC curve (AUC) is also calculated as a measure of performance of these detection methods. Usually, a better detector gets a higher AUC value.

For SR algorithms, since we directly process the LR-HSI, there is no original HR-HSI (i.e., the ground truth) for reference. Thus, some popular quantitative metrics are not available, such as RMSE (root-mean-square error) [69], PSNR (peak signal to noise ratio), and SAM (spectral angle mapper). In this section, entropy and average gradient are introduced to evaluate the performance of SR methods.

3.3.1. Entropy. Super-resolution aims to introduce more useful information into images, so we may measure the performance of SR methods by calculating the contained information in the experimental results. The entropy is indicated as

$$E = - \sum_{i=1}^n P(i) \log_2 P(i). \quad (43)$$

The probability of a pixel i in the image is denoted by $P(i)$ and n denotes the grey value range ($0 \sim 255$). The larger the entropy value of the image, the richer the information contained in the image.

3.3.2. Average Gradient. Another assessment to measure the performance of super-resolution is the change of the amount of detailed information in the image. We may evaluate the experimental results by average gradient, since it can reflect the ability of expressing the details and measuring the clarity of the image. The gradient increases if the greyscale level rate in one direction of the image varies quickly. The average gradient is formulated as

$$\bar{G} = \frac{1}{m \times n} \sum_{i=1}^m \sum_{j=1}^n \sqrt{\left((\partial f_{i,j} / \partial x_i)^2 + (\partial f_{i,j} / \partial y_i)^2 \right) / 2}, \quad (44)$$

where m and n denote the height and width of the image, respectively; $f_{i,j}$ denotes the greyscale value of pixel (i, j) in the image. The larger the average gradient value of the image is, the clearer the image will be.

Besides, the visual quality of output images is an important qualitative metric.

3.4. Parameters Setting. In MSD, we pick 463 spectrums of gas target and 846 spectrums of background from the 12th frame of HSV to build up the training set. The size of the target subspace and background space is 127×112 and 127×115 , respectively. In CMF, the number of endmembers is 3, the sparsity of factor matrices is 2, and number of iteration is 3. In the proposed CTCF-based method, the original cumulative tensor is obtained by ALS, the tensor rank is 3, the maximum iteration number is 100, and the reconstruction error is 10^{-8} ; in update stage, the threshold of fitness is 0.9. In the proposed STTF-based SR method, the

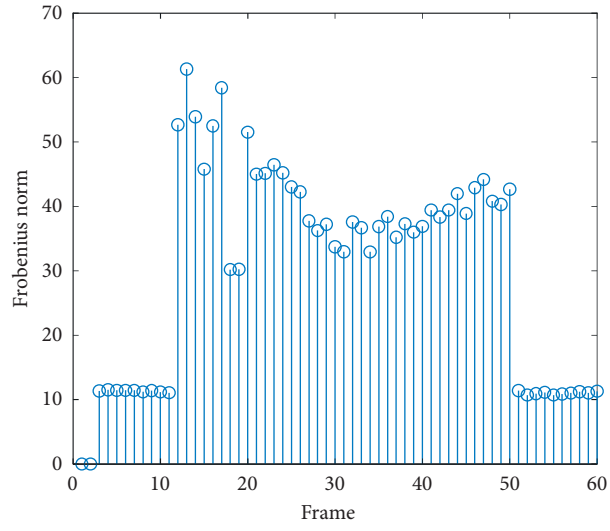


FIGURE 5: The value of Frobenius norm of each frame.

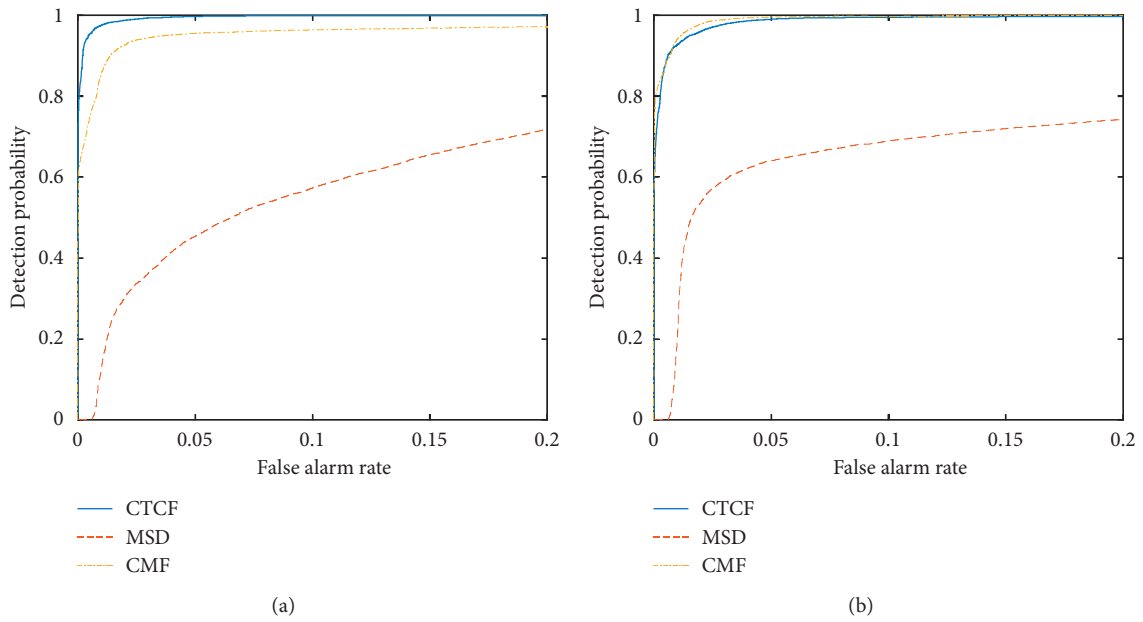


FIGURE 6: Continued.

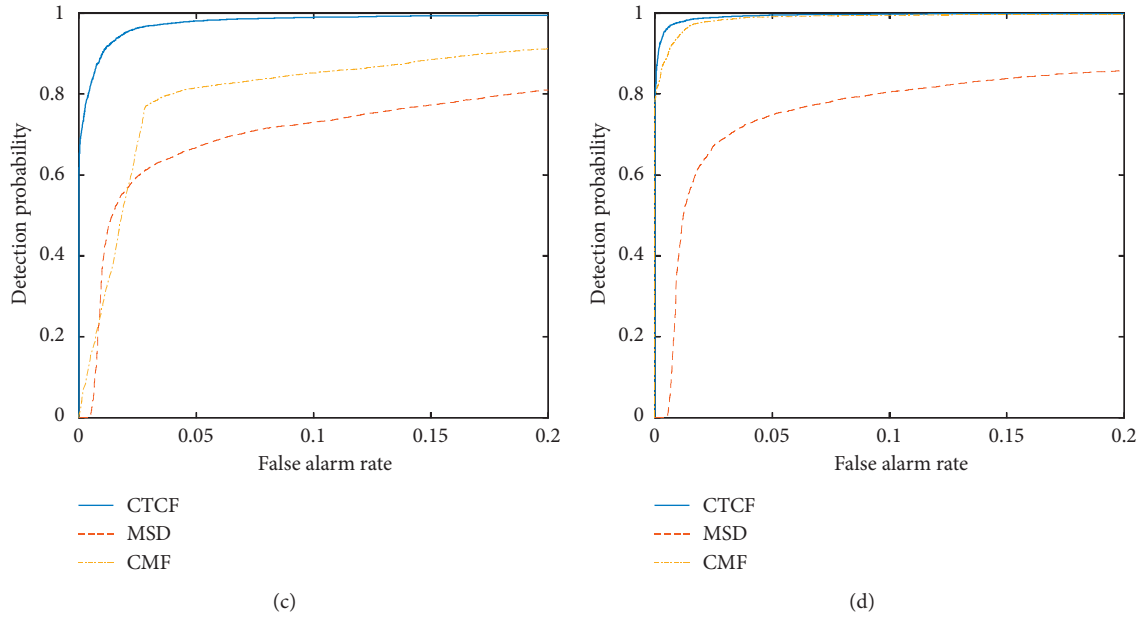


FIGURE 6: The comparison of ROC curves of three detection methods: (a) frame 13; (b) frame 23; (c) frame 34; (d) frame 44.

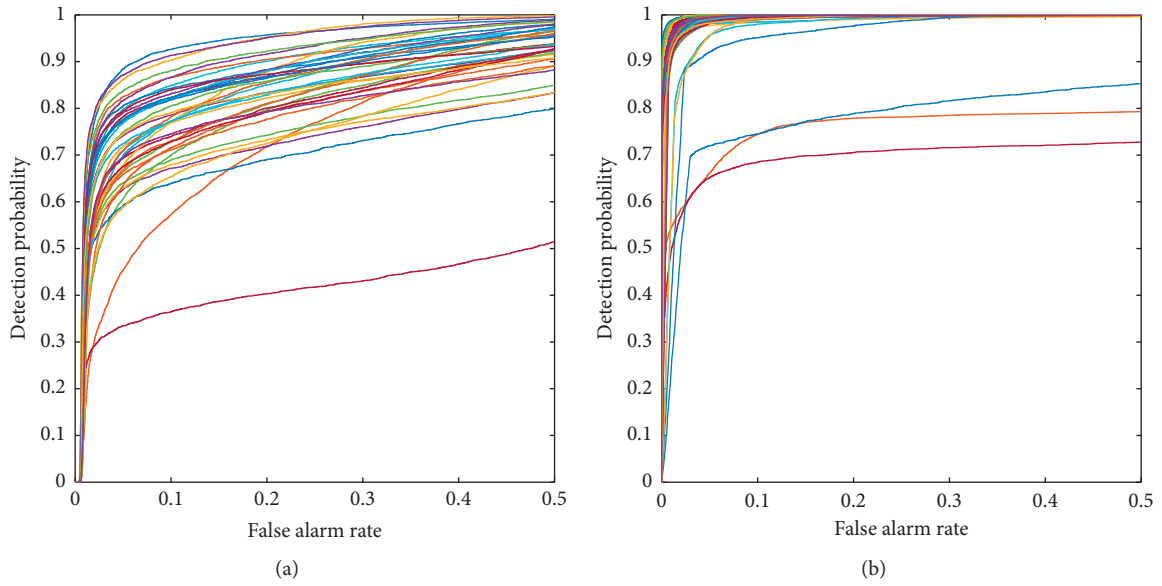


FIGURE 7: Continued.

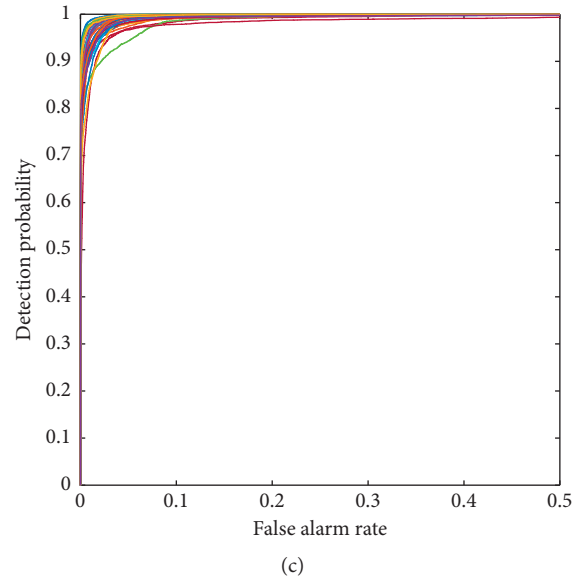


FIGURE 7: The ROC curves of 39 key-frames by three detection methods: (a) MSD; (b) CMF; (c) CTCF.

TABLE 1: Detection quantitative results (AUC value) of the test methods on key-frames.

Frame	MSD [25]	CMF [29]	CTCF
12	0.9655	0.9993	0.9980
13	0.8462	0.9995	0.9980
14	0.8878	0.9994	0.9981
15	0.8189	0.9965	0.9981
16	0.8734	0.9995	0.9977
17	0.9348	0.9987	0.9946
18	0.5792	0.7477	0.9915
19	0.7894	0.9988	0.9958
20	0.9336	0.8991	0.9934
21	0.8222	0.9980	0.9966
22	0.9001	0.9915	0.9969
23	0.8388	0.9986	0.9945
24	0.8914	0.9990	0.9983
25	0.9169	0.9989	0.9961
26	0.9254	0.9947	0.9989
27	0.8722	0.9974	0.9951
28	0.8503	0.9978	0.9930
29	0.9490	0.9892	0.9974
30	0.9011	0.9341	0.9885
31	0.9157	0.9867	0.9965
32	0.8881	0.8582	0.9811
33	0.9345	0.9771	0.9933
34	0.9007	0.9977	0.9922
35	0.9273	0.9952	0.9933
36	0.9349	0.9989	0.9950
37	0.9528	0.9986	0.9984
38	0.9299	0.9875	0.9981
39	0.8838	0.9979	0.9962
40	0.9295	0.9976	0.9966
41	0.9165	0.9939	0.9976
42	0.9665	0.9986	0.9988
43	0.9660	0.9763	0.9969
44	0.9083	0.9995	0.9979
45	0.9046	0.9977	0.9935
46	0.9156	0.9964	0.9918
47	0.9225	0.9979	0.9950

TABLE 1: Continued.

Frame	MSD [25]	CMF [29]	CTCF
48	0.8623	0.9980	0.9967
49	0.8894	0.9992	0.9980
50	0.8640	0.9969	0.9947
Average	0.8926	0.9817	0.9954
Variance	0.4407×10^{-2}	0.2290×10^{-2}	0.1134×10^{-6}

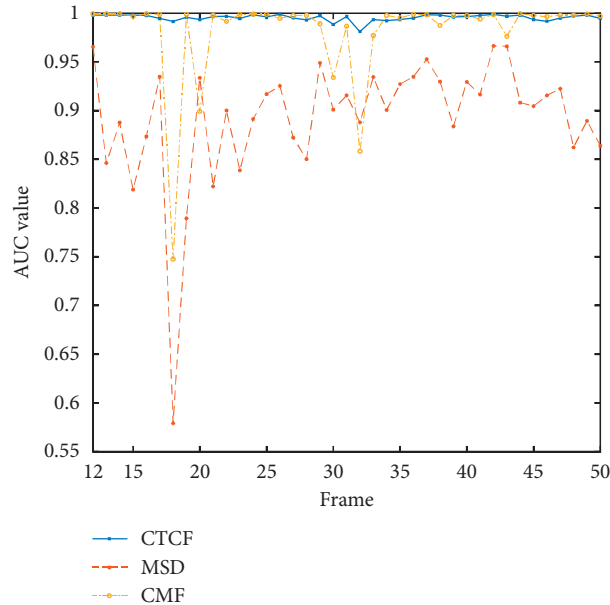


FIGURE 8: The AUC values 39 key-frames by three detection methods.

number of iterations is 5; the parameter α is the weight in (42) and we set $\alpha = 10^{-3}$; parameter λ controls the sparsity of \mathbf{Z} ; we set $\lambda = 10^{-5}$; parameter μ is set by $\mu = 10^{-2}$; the size of \mathbf{Z} is set by $z_h = 240$, $z_w = 240$, and $z_s = 12$. The parameters above are decided after sufficient number of experiments to make a balance between efficiency and stability.

3.5. Experimental Results and Discussion. In this subsection, we show the experimental results of the various methods for detection and super-resolution.

After processing the HSV by the proposed CTCF-based method, we compute the values of Frobenius norm of each frame, which are presented in Figure 5. It is obvious that target gas appears in the 12th frame and disappears in the 51st frame. Figure 6 compares the ROC curves of test methods on four frames in detail, and Figure 7 illustrates the general trends of ROC curves of MSD, CMF, and CTCF, respectively. As can be seen from Figures 6 and 7, the proposed CTCF-based detection algorithm outperforms the other two methods. The AUC values of three approaches are shown in Table 1. In each row, the bold value represents the highest AUC value. Although the AUC values of CMF in some frames are better, we can see that the AUC values of CMF in some other frames are very low (less than 0.98). On the contrast, all the results of CTCF lie in the range of 0.98 to 1. From the average value and the variance (the bold value

represents the highest value), we can conclude that the proposed method is superior and more stable. The graphical results are illustrated in Figure 8.

The target of each key-frame is shown in 2D form (grey image) by taking the maximum value of every spectrum. To save the length of the paper, we choose 8 frames to show the comparison of three detectors, which are shown in Figure 9. The first row to the eighth row present the detection result of the chosen frame, of which the frame number is 15, 18, 22, 28, 31, 39, 48, and 50. The higher the greyscale of the pixel in the image is, the closer it is to the target. It is apparent that our method extracts more accurate targets.

Table 2 shows the entropy and average gradient of the key-frames by four SR algorithms. Since sequence-based method needs 5 LR frames to form 1 HR frame, the compared frame number is changed from range 12~50 to range 14~48. In each row, the bold values represent the highest entropy value and the highest average gradient value. From Table 2, we can conclude that firstly, although interpolation can add more information in the frame, the details of the target are lost; secondly, sparse representation SR and sequence information SR have almost the same entropy, but the latter approach offers more details because in the method the HR dictionary is formed by several LR dictionaries; finally, the proposed STTF-based SR method outperforms the other three methods in both metrics.

Figure 10 presents the visual quality of the results obtained by four test methods. We choose the 16th, 21st, 34th,

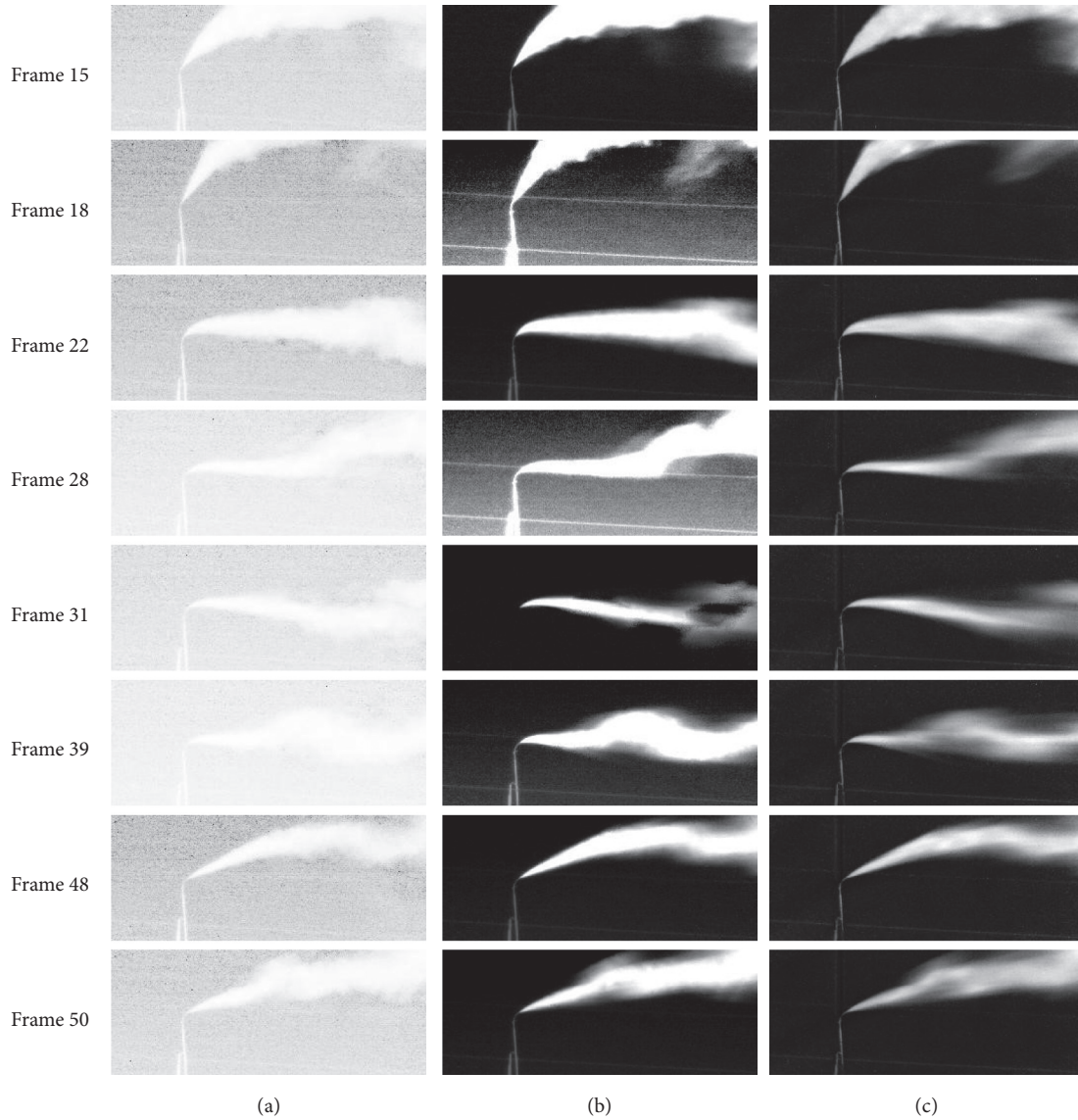


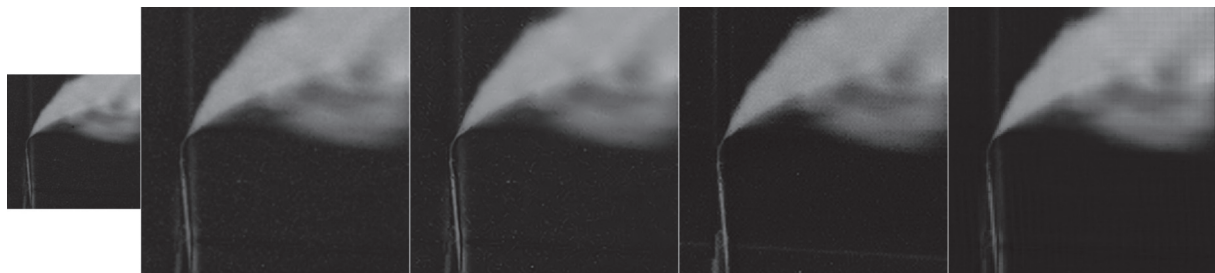
FIGURE 9: The 2D form of the detection results by three detection methods.

TABLE 2: SR quantitative results (entropy and average gradient) of the test methods on key-frames.

Methods	LR frame		Bicubic interpolation		Sparse representation-based SR [54]		Sequence information-based SR [65]		STTF-based SR	
	Entropy	Average gradient	Entropy	Average gradient	Entropy	Average gradient	Entropy	Average gradient	Entropy	Average gradient
14	5.1603	0.0076	5.3744	0.0052	5.4996	0.0078	5.4259	0.0090	5.6098	0.0121
15	4.7086	0.0077	5.1407	0.0063	5.2398	0.0089	5.2184	0.0103	5.3678	0.0139
16	5.5521	0.0084	5.8013	0.0060	5.8765	0.0085	5.8203	0.0103	5.9772	0.0135
17	5.5293	0.0086	5.7054	0.0056	5.7918	0.0081	5.6125	0.0094	5.8831	0.0129
18	4.2989	0.0072	4.8339	0.0062	4.9794	0.0088	5.0423	0.0106	5.1108	0.0138
19	4.4843	0.0073	5.0045	0.0063	5.1327	0.0089	5.1831	0.0106	5.2644	0.0140
20	5.1442	0.0075	5.4307	0.0060	5.5039	0.0086	5.3987	0.0099	5.6122	0.0137
21	4.8821	0.0071	5.2234	0.0060	5.3264	0.0086	5.2578	0.0100	5.4491	0.0137
22	4.3472	0.0067	4.8929	0.0065	4.9858	0.0090	4.9409	0.0102	5.1261	0.0141
23	4.6127	0.0067	5.0430	0.0061	5.1534	0.0086	5.0806	0.0098	5.2823	0.0135
24	4.4189	0.0064	4.8688	0.0060	4.9850	0.0085	4.8916	0.0096	5.1168	0.0133
25	4.3273	0.0066	4.9091	0.0066	5.0061	0.0091	4.9607	0.0103	5.1494	0.0143

TABLE 2: Continued.

Methods	LR frame		Bicubic interpolation		Sparse representation-based SR [54]		Sequence information-based SR [65]		STTF-based SR	
Frame	Entropy	Average gradient	Entropy	Average gradient	Entropy	Average gradient	Entropy	Average gradient	Entropy	Average gradient
26	4.1394	0.0064	4.7589	0.0066	4.8438	0.0090	4.8078	0.0103	4.9919	0.0141
27	4.1127	0.0065	4.6995	0.0066	4.7878	0.0091	4.7713	0.0104	4.9366	0.0142
28	3.9657	0.0061	4.6576	0.0066	4.7467	0.0091	4.7507	0.0107	4.8902	0.0142
29	4.1885	0.0063	4.7545	0.0064	4.8611	0.0088	4.8481	0.0101	5.0066	0.0137
30	3.9672	0.0063	4.6345	0.0067	4.7253	0.0092	4.7241	0.0106	4.8752	0.0144
31	3.9440	0.0061	4.6135	0.0065	4.7131	0.0090	4.7349	0.0104	4.8654	0.0141
32	3.8661	0.0060	4.5799	0.0064	4.6914	0.0088	4.6971	0.0101	4.8497	0.0138
33	4.0479	0.0060	4.7100	0.0064	4.8126	0.0088	4.8114	0.0100	4.9631	0.0137
34	4.1691	0.0060	4.7824	0.0066	4.8621	0.0088	4.8462	0.0102	5.0072	0.0136
35	4.0933	0.0062	4.7169	0.0067	4.8010	0.0091	4.8245	0.0108	4.9515	0.0143
36	3.9157	0.0063	4.5995	0.0067	4.6881	0.0092	4.6712	0.0103	4.8508	0.0142
37	3.7810	0.0059	4.5028	0.0064	4.6088	0.0089	4.5984	0.0100	4.7666	0.0138
38	3.8814	0.0061	4.5479	0.0065	4.6483	0.0090	4.6395	0.0101	4.8050	0.0140
39	4.3168	0.0060	4.8397	0.0061	4.9406	0.0084	4.9135	0.0099	5.0792	0.0130
40	3.9333	0.0061	4.6597	0.0067	4.7380	0.0091	4.7209	0.0104	4.8906	0.0142
41	4.2009	0.0063	4.7897	0.0066	4.8711	0.0089	4.8346	0.0102	5.0138	0.0138
42	4.1083	0.0063	4.7514	0.0067	4.8362	0.0091	4.8398	0.0103	4.9836	0.0142
43	4.0485	0.0063	4.6827	0.0067	4.7602	0.0091	4.7117	0.0101	4.9109	0.0142
44	4.0521	0.0062	4.6510	0.0063	4.7587	0.0087	4.7273	0.0097	4.9165	0.0136
45	4.3442	0.0060	4.9011	0.0061	5.0079	0.0085	4.9380	0.0097	5.1413	0.0134
46	4.0006	0.0061	4.5913	0.0062	4.7080	0.0087	4.6467	0.0097	4.8587	0.0136
47	4.4749	0.0062	5.0109	0.0060	5.1015	0.0084	5.0007	0.0095	5.2302	0.0131
48	4.0685	0.0065	4.6843	0.0065	4.7859	0.0090	4.7607	0.0101	4.9384	0.0141
Avg.	4.3167	0.0066	4.8671	0.0063	4.9651	0.0088	4.9329	0.0101	5.1049	0.0138



(a)



(b)

FIGURE 10: Continued.

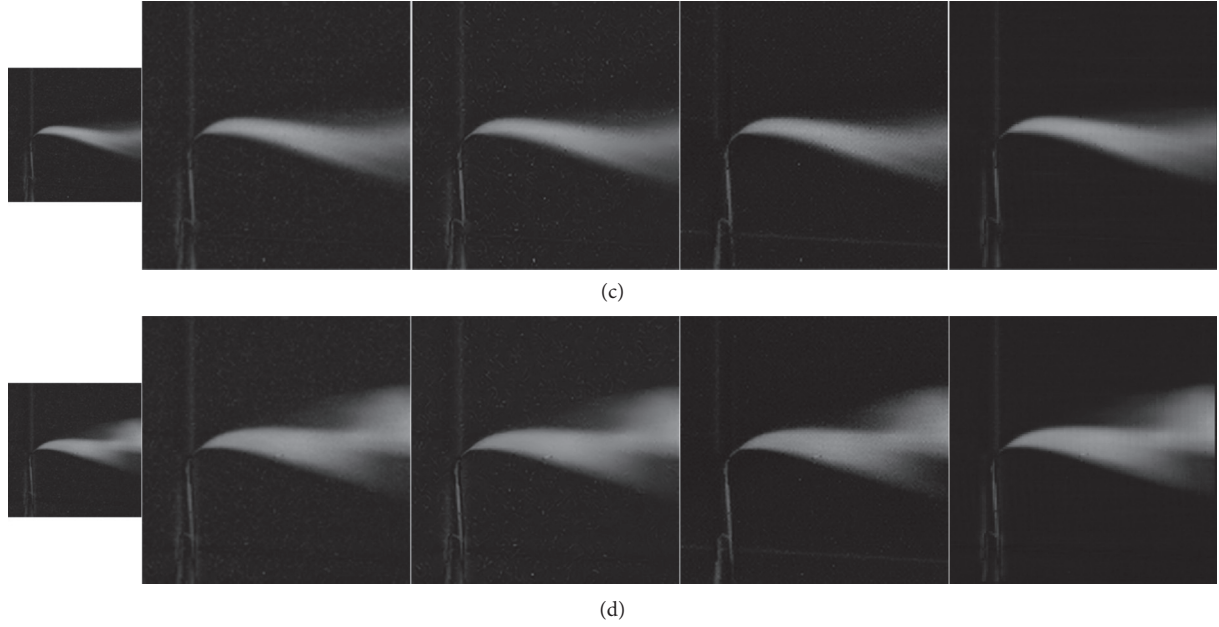


FIGURE 10: The SR results of four test methods, from left to right: original LR frame, bicubic interpolation, sparse representation-based SR method [54], sequence information-based SR method [65], the proposed STTF-based SR method: (a) frame 16; (b) frame 21; (c) frame 34; (d) frame 47.

and 47th frames as a representative. The smaller one with size of 128×128 is the LR 2D-form frame. The bigger ones with size of 256×256 are the SR results of different algorithms. As can be seen from Figure 10, the proposed approach yields clearer outputs with sharper edges and more textures. A drawback is the “checkerboard artifacts,” which may be caused by the deconvolution operations in the method. We desired to fix it in our future work.

4. Conclusions

In this paper, aiming at hyperspectral video, we propose a novel key-frame and target detection method based on cumulative tensor CP factorization, termed as CTCF, and a super-resolution algorithm based on sparse-based tensor Tucker factorization, called STTF. Unlike conventional matrix factorization based methods, CTCF considers hyperspectral video (HSV) as 4D cumulative tensor and approximates new added frames by updating factor matrices. To break the limit of conventional methods and make super-resolution (SR) more practical, STTF exploits the sparsity of HSV frames and factorizes them as a sparse core tensor multiplied by three modes dictionaries. In this way, spatial resolution of LR-HSI is enhanced directly without HR samples. The experimental results systematically prove that the proposed CTCF and STTF methods outperform other state-of-the-art algorithms.

In the future works, we focus on tensor factorization based target tracking methods which are able to extract target region more accurately and clearly. For super-resolution, we aim at exploiting nonlocal similarities in tensor factorization framework, which has been widely used in inverse problems. Besides target tracking and super-resolution, regions of interest (ROI) approaches will be investigated, in order to make

HSV target recognition more efficient and full featured. Inspired by [70] and other related works, we believe that the researches of chemical gas detecting methods will benefit the agricultural application of HSI/HSV. These studies will be of great significance in internet of things (IoT), smart agriculture, pollution monitoring, etc.

Appendix

The optimizations of \mathbf{H} , \mathbf{W} , \mathbf{S} , and \mathbf{Z} in Section 2.3.2 are presented as follows.

- (1) Optimization of \mathbf{H} : when \mathbf{W} , \mathbf{S} , and \mathbf{Z} are fixed, the optimization of \mathbf{H} in (42) is represented as

$$\min_{\mathbf{H}} \|\mathbf{Y} - \mathbf{Z} \times_1 \mathbf{H}^* \times_2 \mathbf{W}^* \times_3 \mathbf{S}\|_F^2 + \alpha \|\mathbf{H} - \mathbf{H}_{\text{pre}}\|_F^2, \quad (\text{A.1})$$

where \mathbf{H}_{pre} denotes the previous estimation of height mode dictionary in last iteration. Using characteristics of n -mode product (see (3)), (A.1) is represented as

$$\min_{\mathbf{H}} \|\mathbf{Y}_{(1)} - \mathbf{D}_1 \mathbf{H} \mathbf{M}_h\|_F^2 + \alpha \|\mathbf{H} - \mathbf{H}_{\text{pre}}\|_F^2, \quad (\text{A.2})$$

where $\mathbf{Y}_{(1)}$ denotes the mode-1 unfolding matrix of \mathbf{Y} and $\mathbf{M}_h = (\mathbf{Z} \times_2 \mathbf{W}^* \times_3 \mathbf{S})_{(1)}$. Equation (A.2) is quadratic and can be solved by computing general Sylvester matrix equation; i.e.,

$$\mathbf{D}_1^T \mathbf{D}_1 \mathbf{H} \mathbf{M}_h \mathbf{M}_h^T + \alpha \mathbf{H} = \mathbf{D}_1^T \mathbf{Y}_{(1)} \mathbf{M}_h^T + \alpha \mathbf{H}_{\text{pre}}. \quad (\text{A.3})$$

The conjugate gradient (CG) method is utilized to solve (A.3). After several iterations, CG will reach the convergence in certain conditions. In our experiments, it has been found that the solution of (A.3) is well approximated after 20 iterations.

(2) Optimization of \mathbf{W} : when \mathbf{H} , \mathbf{S} , and \mathbf{Z} are fixed, the optimization of \mathbf{W} in (42) is expressed by

$$\min_{\mathbf{W}} \|\mathbf{Y} - \mathbf{Z} \times_1 \mathbf{H}^* \times_2 \mathbf{W}^* \times_3 \mathbf{S}\|_F^2 + \alpha \|\mathbf{W} - \mathbf{W}_{\text{pre}}\|_F^2, \quad (\text{A.4})$$

where \mathbf{W}_{pre} denotes the previous estimation of width mode dictionary in last iteration. Similar to the optimization of \mathbf{H} , (A.4) can be transformed into

$$\min_{\mathbf{W}} \|\mathbf{Y}_{(2)} - \mathbf{D}_2 \mathbf{W} \mathbf{M}_w\|_F^2 + \alpha \|\mathbf{W} - \mathbf{W}_{\text{pre}}\|_F^2, \quad (\text{A.5})$$

where $\mathbf{Y}_{(2)}$ denotes the mode-2 unfolding matrix of \mathbf{Y} and $\mathbf{M}_w = (\mathbf{Z} \times_1 \mathbf{H}^* \times_3 \mathbf{S})_{(2)}$. Equation (A.5) is also quadratic and can be solved by computing general Sylvester matrix equation; i.e.,

$$\mathbf{D}_2^T \mathbf{D}_2 \mathbf{W} \mathbf{M}_w \mathbf{M}_w^T + \alpha \mathbf{W} = \mathbf{D}_2^T \mathbf{Y}_{(2)} \mathbf{M}_w^T + \alpha \mathbf{W}_{\text{pre}}. \quad (\text{A.6})$$

Likewise, CG is used to solve (A.6).

(3) Optimization of \mathbf{S} : when \mathbf{H} , \mathbf{W} , and \mathbf{Z} are fixed, the optimization with respect to \mathbf{S} in (42) can be formulated as

$$\min_{\mathbf{S}} \|\mathbf{Y} - \mathbf{Z} \times_1 \mathbf{H}^* \times_2 \mathbf{W}^* \times_3 \mathbf{S}\|_F^2 + \alpha \|\mathbf{S} - \mathbf{S}_{\text{pre}}\|_F^2, \quad (\text{A.7})$$

where \mathbf{S}_{pre} denotes the previous estimation of spectral mode dictionary in last iteration. Same as the processing in the two subsections above, we have

$$\min_{\mathbf{S}} \|\mathbf{Y}_{(3)} - \mathbf{S} \mathbf{M}_s\|_F^2 + \alpha \|\mathbf{S} - \mathbf{S}_{\text{pre}}\|_F^2, \quad (\text{A.8})$$

where $\mathbf{Y}_{(3)}$ denotes the mode-3 unfolding matrix of \mathbf{Y} and $\mathbf{M}_s = (\mathbf{Z} \times_1 \mathbf{H}^* \times_2 \mathbf{W}^*)_{(3)}$. Similarly, (A.8) can be solved by computing general Sylvester matrix equation; i.e.,

$$\mathbf{S} \mathbf{M}_s \mathbf{M}_s^T + \alpha \mathbf{S} = \mathbf{Y}_{(3)} \mathbf{M}_s^T + \alpha \mathbf{S}_{\text{pre}}. \quad (\text{A.9})$$

We apply CG to solve (A.9) and the convergence is achieved in a few iterations.

(4) Optimization of \mathbf{Z} : when \mathbf{H} , \mathbf{W} , and \mathbf{S} are fixed, the optimization of \mathbf{Z} in (42) can be written as

$$\min_{\mathbf{Z}} \|\mathbf{Y} - \mathbf{Z} \times_1 \mathbf{H}^* \times_2 \mathbf{W}^* \times_3 \mathbf{S}\|_F^2 + \lambda \|\mathbf{Z}\|_1 + \alpha \|\mathbf{Z} - \mathbf{Z}_{\text{pre}}\|_F^2, \quad (\text{A.10})$$

where \mathbf{Z}_{pre} denotes the previous estimation of core tensor in last iteration. Equation (A.10) is convex, so we can employ the ADMM to solve the optimization problem. Introducing splitting variables $\mathbf{Z}_1 = \mathbf{Z}$ and $\mathbf{Z}_2 = \mathbf{Z}$, (A.10) can be transformed into the equivalent constrained form:

$$\begin{aligned} & \min_{\mathbf{Z}_1, \mathbf{Z}_2} f_1(\mathbf{Z}_1) + f_2(\mathbf{Z}_2), \\ & \text{s.t. } \mathbf{Z}_1 = \mathbf{Z}, \\ & \quad \mathbf{Z}_2 = \mathbf{Z}, \end{aligned} \quad (\text{A.11})$$

where

$$f_1(\mathbf{Z}_1) = \lambda \|\mathbf{Z}_1\|_1 + \alpha \|\mathbf{Z}_1 - \mathbf{Z}_{1\text{pre}}\|_F^2, \quad (\text{A.12})$$

$$f_2(\mathbf{Z}_2) = \|\mathbf{Y} - \mathbf{Z}_2 \times_1 \mathbf{H}^* \times_2 \mathbf{W}^* \times_3 \mathbf{S}\|_F^2.$$

Equation (A.11) is a typical form of optimization problem that corresponds to the standard ADMM. The augmented Lagrangian function for (A.11) is represented as

$$\begin{aligned} g(\mathbf{Z}_1, \mathbf{Z}_2, \beta) = & \lambda \|\mathbf{Z}_1\|_1 + \alpha \|\mathbf{Z}_1 - \mathbf{Z}_{1\text{pre}}\|_F^2 \\ & + \|\mathbf{Y} - \mathbf{Z}_2 \times_1 \mathbf{H}^* \times_2 \mathbf{W}^* \times_3 \mathbf{S}\|_F^2 \\ & + \mu \|\mathbf{Z}_1 - \mathbf{Z}_2 - \beta\|_F^2, \end{aligned} \quad (\text{A.13})$$

where β denotes the Lagrangian multiplier and μ denotes the penalty parameter. The process of ADMM is formulated as

$$\begin{aligned} \mathbf{Z}_1 & \leftarrow \arg \min_{\mathbf{Z}_1} g(\mathbf{Z}_1, \mathbf{Z}_2, \beta); \\ \mathbf{Z}_2 & \leftarrow \arg \min_{\mathbf{Z}_2} g(\mathbf{Z}_1, \mathbf{Z}_2, \beta); \\ \beta & \leftarrow \beta - (\mathbf{Z}_1 - \mathbf{Z}_2), \end{aligned} \quad (\text{A.14})$$

Here, the optimizations of \mathbf{Z}_1 and \mathbf{Z}_2 are independent because function $g(\cdot)$ is decoupled with respect to these variables. Next, (A.14) will be discussed more detailedly.

(i) Update \mathbf{Z}_1 : based on (A.13), we have

$$\mathbf{Z}_1 \in \arg \min_{\mathbf{Z}_1} \lambda \|\mathbf{Z}_1\|_1 + \alpha \|\mathbf{Z}_1 - \mathbf{Z}_{1\text{pre}}\|_F^2 + \mu \|\mathbf{Z}_1 - \mathbf{Z}_2 - \beta\|_F^2, \quad (\text{A.15})$$

and the closed-form solution of (A.15) is

$$\mathbf{Z}_1 = \text{soft} \left[\frac{\mu(\mathbf{Z}_2 + \beta) + \alpha \mathbf{Z}_{1\text{pre}}}{\mu + \alpha}, \frac{\lambda}{2\mu + 2\alpha} \right], \quad (\text{A.16})$$

where $\text{soft}(m, n) = \text{sign}(m) * \max(|m| - n, 0)$.

(ii) Update \mathbf{Z}_2 : based on (A.13), we have

$$\mathbf{Z}_2 \in \arg \min_{\mathbf{Z}_2} \|\mathbf{Y} - \mathbf{Z}_2 \times_1 \mathbf{H}^* \times_2 \mathbf{W}^* \times_3 \mathbf{S}\|_F^2 + \mu \|\mathbf{Z}_2 - \mathbf{Z}_1 + \beta\|_F^2. \quad (\text{A.17})$$

Based on (6) and (7), (A.17) is equivalent to

$$\arg \min_{\mathbf{z}_2} \|\mathbf{y} - \mathbf{E} \mathbf{z}_2\|_F^2 + \mu \|\mathbf{z}_2 - \mathbf{z}_1 + \beta\|_F^2, \quad (\text{A.18})$$

where the vectors $\mathbf{y} = \text{vec}(\mathbf{Y})$, $\mathbf{z}_2 = \text{vec}(\mathbf{Z}_2)$, $\mathbf{z}_1 = \text{vec}(\mathbf{Z}_1)$, and $\beta = \text{vec}(\beta)$ are the vectorization form of tensors \mathbf{Y} , \mathbf{Z}_2 , \mathbf{Z}_1 , and β , respectively, and matrix $\mathbf{E} = \mathbf{S} \otimes \mathbf{W}^* \otimes \mathbf{H}^*$. Equation (A.18) has the closed-form solution which is denoted by

$$\mathbf{z}_2 = (\mathbf{E}^T \mathbf{E} + \mu \mathbf{I})^{-1} (\mathbf{E}^T \mathbf{y} + \mu \mathbf{z}_1 - \mu \beta). \quad (\text{A.19})$$

However, $\mathbf{E} \in \mathbb{R}^{hwS \times z_1 z_2 z_3}$ is so large that (A.19) is too heavy to be solved. We rewrite the first term of (A.19) as follows:

$$(\mathbf{E}^T \mathbf{E} + \mu \mathbf{I})^{-1} = (\mathbf{P}_3 \otimes \mathbf{P}_2 \otimes \mathbf{P}_1)(\mathbf{Q}_3 \otimes \mathbf{Q}_2 \otimes \mathbf{Q}_1 + \mu \mathbf{I})^{-1} \times (\mathbf{P}_3^T \otimes \mathbf{P}_2^T \otimes \mathbf{P}_1^T), \quad (\text{A.20})$$

where \mathbf{P}_i and \mathbf{Q}_i ($i = [1, 3]$) denote eigenvector matrices and eigenvalue matrices of $\mathbf{H}^{*T} \mathbf{H}^*$, $\mathbf{W}^{*T} \mathbf{W}^*$, and $\mathbf{S}^T \mathbf{S}$, respectively. So, $(\mathbf{Q}_3 \otimes \mathbf{Q}_2 \otimes \mathbf{Q}_1 + \mu \mathbf{I})^{-1}$ is diagonal and can be computed easily. Moreover, the operation of \mathbf{P}_i and of \mathbf{P}_i^T is i -mode products and the multiplication in (A.20) is elementwise. Finally, $\mathbf{E}^T \mathbf{y}$ in the second term of (A.19) can be computed by

$$\mathbf{E}^T \mathbf{y} = \text{vec}(\mathbf{Y} \times_1 \mathbf{H}^{*T} \times_2 \mathbf{W}^{*T} \times_3 \mathbf{S}^T). \quad (\text{A.21})$$

(iii) Update β : based on (A.14), β is updated by

$$\beta \leftarrow \beta - (\mathbf{Z}_1 - \mathbf{Z}_2). \quad (\text{A.22})$$

Data Availability

The data used to support the findings of this study are available from the corresponding author upon request.

Conflicts of Interest

The authors declare no conflicts of interest.

Acknowledgments

The authors would like to thank Professor Gu from Heilongjiang Province Key Laboratory of Space-Air-Ground Integrated Intelligent Remote Sensing for his selfless help. This work was supported by the National Natural Science Foundation of China (Grant no. 61671184) and the National Natural Science Foundation of Key International Cooperation of China (Grant no. 61720106002).

References

- [1] H. Fan, C. Li, Y. Guo, G. Kuang, and J. Ma, "Spatial-spectral total variation regularized low-rank tensor decomposition for hyperspectral image denoising," *IEEE Transactions on Geoscience and Remote Sensing*, vol. 56, no. 10, pp. 6196–6213, 2018.
- [2] X. Zheng, Y. Yuan, and X. Lu, "Hyperspectral image denoising by fusing the selected related bands," *IEEE Transactions on Geoscience and Remote Sensing*, vol. 57, no. 5, pp. 2596–2609, 2019.
- [3] D. Hong, N. Yokoya, J. Chanussot, and X. X. Zhu, "CoSpace: common subspace learning from hyperspectral-multispectral correspondences," *IEEE Transactions on Geoscience and Remote Sensing*, vol. 57, no. 7, pp. 4349–4359, 2019.
- [4] D. Hong, N. Yokoya, J. Chanussot, J. Xu, and X. X. Zhu, "Learning to propagate labels on graphs: an iterative multitask regression framework for semi-supervised hyperspectral dimensionality reduction," *ISPRS Journal of Photogrammetry and Remote Sensing*, vol. 158, pp. 35–49, 2019.
- [5] T. Liu, Y. Gu, X. Jia, J. A. Benediktsson, and J. Chanussot, "Class-specific sparse multiple kernel learning for spectral-spatial hyperspectral image classification," *IEEE Transactions on Geoscience and Remote Sensing*, vol. 54, no. 12, pp. 7351–7365, 2016.
- [6] Y. Gu, T. Liu, X. Jia, J. A. Benediktsson, and J. Chanussot, "Nonlinear multiple kernel learning with multiple-structure-element extended morphological profiles for hyperspectral image classification," *IEEE Transactions on Geoscience and Remote Sensing*, vol. 54, no. 6, pp. 3235–3247, 2016.
- [7] T. Liu, Y. Gu, J. Chanussot, and M. Dalla Mura, "Multimorphological superpixel model for hyperspectral image classification," *IEEE Transactions on Geoscience and Remote Sensing*, vol. 55, no. 12, pp. 6950–6963, 2017.
- [8] T. Liu, X. Zhang, and Y. Gu, "Unsupervised cross-temporal classification of hyperspectral images with multiple geodesic flow kernel learning," *IEEE Transactions on Geoscience and Remote Sensing*, vol. 57, no. 12, pp. 9688–9701, 2019.
- [9] Y. Gu, T. Liu, and J. Li, "Superpixel tensor model for spatial-spectral classification of remote sensing images," *IEEE Transactions on Geoscience and Remote Sensing*, vol. 57, no. 7, pp. 4705–4719, 2019.
- [10] D. Hong, N. Yokoya, N. Ge, J. Chanussot, and X. X. Zhu, "Learnable manifold alignment (LeMA): a semi-supervised cross-modality learning framework for land cover and land use classification," *ISPRS Journal of Photogrammetry and Remote Sensing*, vol. 147, pp. 193–205, 2019.
- [11] M. Song, X. Shang, Y. Wang, C. Yu, and C.-I. Chang, "Class information-based band selection for hyperspectral image classification," *IEEE Transactions on Geoscience and Remote Sensing*, vol. 57, no. 11, pp. 8394–8416, 2019.
- [12] Y. Zhang, W. Ke, B. Du, and X. Hu, "Independent encoding joint sparse representation and multitask learning for hyperspectral target detection," *IEEE Geoscience and Remote Sensing Letters*, vol. 14, no. 11, pp. 1933–1937, 2017.
- [13] N. M. Nasrabadi, "Hyperspectral target detection: an overview of current and future challenges," *IEEE Signal Processing Magazine*, vol. 31, no. 1, pp. 34–44, 2014.
- [14] Y. Wang, L. Wang, C. Yu et al., "Constrained-target band selection for multiple-target detection," *IEEE Transactions on Geoscience and Remote Sensing*, vol. 57, no. 8, pp. 6079–6103, 2019.
- [15] R. Dian, S. Li, and L. Fang, "Learning a low tensor-train rank representation for hyperspectral image super-resolution," *IEEE Transactions on Neural Networks and Learning Systems*, vol. 30, no. 9, pp. 2672–2683, 2019.
- [16] L. Fang, H. Zhuo, and S. Li, "Super-resolution of hyperspectral image via superpixel-based sparse representation," *Neurocomputing*, vol. 273, no. 17, pp. 171–177, 2018.
- [17] R. Dian, L. Fang, and S. Li, "Hyperspectral image super-resolution via non-local sparse tensor factorization," in *Proceedings of the 2017 IEEE Conference on Computer Vision and Pattern Recognition (CVPR)*, pp. 3862–3871, Honolulu, HI, USA, July 2017.
- [18] Y. Wang, L. Wang, H. Xie, and C.-I. Chang, "Fusion of various band selection methods for hyperspectral imagery," *Remote Sensing*, vol. 11, no. 18, p. 2125, 2019.
- [19] Z. Huang, L. Fang, and S. Li, "Subpixel-pixel-superpixel guided fusion for hyperspectral anomaly detection," *IEEE Transactions on Geoscience and Remote Sensing*, pp. 1–10, 2020.
- [20] X. Zhang, G. Wen, and W. Dai, "A tensor decomposition-based anomaly detection algorithm for hyperspectral image," *IEEE Transactions on Geoscience and Remote Sensing*, vol. 54, no. 10, pp. 5801–5820, 2016.
- [21] S. Li, K. Zhang, Q. Hao, P. Duan, and X. Kang, "Hyperspectral anomaly detection with multiscale attribute and edge-preserving filters," *IEEE Geoscience and Remote Sensing Letters*, vol. 15, no. 10, pp. 1605–1609, 2018.

- [22] Y. Wang, L.-C. Lee, B. Xue et al., "A posteriori hyperspectral anomaly detection for unlabeled classification," *IEEE Transactions on Geoscience and Remote Sensing*, vol. 56, no. 6, pp. 3091–3106, 2018.
- [23] I. S. Reed and X. Yu, "Adaptive multiple-band CFAR detection of an optical pattern with unknown spectral distribution," *IEEE Transactions on Acoustics, Speech, and Signal Processing*, vol. 38, no. 10, pp. 1760–1770, 1990.
- [24] D. Meng, X. Wang, M. Huang, L. Wan, and B. Zhang, "Robust weighted subspace fitting for DOA estimation via block sparse recovery," *IEEE Communications Letters*, vol. 24, no. 3, pp. 563–567, 2020.
- [25] L. L. Scharf and B. Friedlander, "Matched subspace detectors," *IEEE Transactions on Signal Processing*, vol. 42, no. 8, pp. 2146–2157, 1994.
- [26] D. Hong, N. Yokoya, J. Chanussot, and X. X. Zhu, "An augmented linear mixing model to address spectral variability for hyperspectral unmixing," *IEEE Transactions on Image Processing*, vol. 28, no. 4, pp. 1923–1938, 2019.
- [27] X. Li, X. Jia, L. Wang, and K. Zhao, "On spectral unmixing resolution using extended support vector machines," *IEEE Transactions on Geoscience and Remote Sensing*, vol. 53, no. 9, pp. 4985–4996, 2015.
- [28] M.-D. Iordache, J. M. Bioucas-Dias, and A. Plaza, "Sparse unmixing of hyperspectral data," *IEEE Transactions on Geoscience and Remote Sensing*, vol. 49, no. 6, pp. 2014–2039, 2011.
- [29] N. Akhtar and A. Mian, "RCMF: robust constrained matrix factorization for hyperspectral unmixing," *IEEE Transactions on Geoscience and Remote Sensing*, vol. 55, no. 6, pp. 3354–3366, 2017.
- [30] Q. Wei, N. Dobigeon, and J. Tourneret, "Bayesian fusion of hyperspectral and multispectral images," in *Proceedings of the 2014 IEEE International Conference on Acoustics, Speech and Signal Processing (ICASSP)*, pp. 3176–3180, Florence, Italy, May 2014.
- [31] V. P. Shah, N. H. Younan, and R. L. King, "An efficient pansharpening method via a combined adaptive PCA approach and contourlets," *IEEE Transactions on Geoscience and Remote Sensing*, vol. 46, no. 5, pp. 1323–1335, 2008.
- [32] R. Dian, S. Li, A. Guo, and L. Fang, "Deep hyperspectral image sharpening," *IEEE Transactions on Neural Networks and Learning Systems*, vol. 29, no. 11, pp. 5345–5355, 2018.
- [33] W. Dong, F. Fu, G. Shi et al., "Hyperspectral image super-resolution via non-negative structured sparse representation," *IEEE Transactions on Image Processing*, vol. 25, no. 5, pp. 2337–2352, 2016.
- [34] B. Huang, H. Song, H. Cui, J. Peng, and Z. Xu, "Spatial and spectral image fusion using sparse matrix factorization," *IEEE Transactions on Geoscience and Remote Sensing*, vol. 52, no. 3, pp. 1693–1704, 2014.
- [35] N. Akhtar, F. Shafait, and A. Mian, "Bayesian sparse representation for hyperspectral image super resolution," in *Proceedings of the 2015 IEEE Conference on Computer Vision and Pattern Recognition (CVPR)*, pp. 3631–3640, Boston, MA, USA, June 2015.
- [36] X. Fu, K. Huang, B. Yang, W.-K. Ma, and N. D. Sidiropoulos, "Robust volume minimization-based matrix factorization for remote sensing and document clustering," *IEEE Transactions on Signal Processing*, vol. 64, no. 23, pp. 6254–6268, 2016.
- [37] X. Fu, K. Huang, and N. D. Sidiropoulos, "On identifiability of nonnegative matrix factorization," *IEEE Signal Processing Letters*, vol. 25, no. 3, pp. 328–332, 2018.
- [38] K. Huang, N. D. Sidiropoulos, and A. Swami, "Non-negative matrix factorization revisited: uniqueness and algorithm for symmetric decomposition," *IEEE Transactions on Signal Processing*, vol. 62, no. 1, pp. 211–224, 2014.
- [39] W.-K. Ma, J. M. Bioucas-Dias, T.-H. Chan et al., "A signal processing perspective on hyperspectral unmixing: insights from remote sensing," *IEEE Signal Processing Magazine*, vol. 31, no. 1, pp. 67–81, 2014.
- [40] N. Yokoya, T. Yairi, and A. Iwasaki, "Coupled nonnegative matrix factorization unmixing for hyperspectral and multispectral data fusion," *IEEE Transactions on Geoscience and Remote Sensing*, vol. 50, no. 2, pp. 528–537, 2012.
- [41] C. Lanaras, E. Baltsavias, and K. Schindler, "Hyperspectral super-resolution by coupled spectral unmixing," in *Proceedings of the 2015 IEEE International Conference on Computer Vision (ICCV)*, pp. 3586–3594, Santiago, Chile, December 2015.
- [42] K. Zhang, M. Wang, and S. Yang, "Multispectral and hyperspectral image fusion based on group spectral embedding and low-rank factorization," *IEEE Transactions on Geoscience and Remote Sensing*, vol. 55, no. 3, pp. 1363–1371, 2017.
- [43] Y. Xu, Z. Wu, J. Chanussot, and Z. Wei, "Nonlocal patch tensor sparse representation for hyperspectral image super-resolution," *IEEE Transactions on Image Processing*, vol. 28, no. 6, pp. 3034–3047, 2019.
- [44] Y. Xu, Z. Wu, J. Chanussot, and Z. Wei, "Hyperspectral images super-resolution via learning high-order coupled tensor ring representation," *IEEE Transactions on Neural Networks and Learning Systems*, pp. 1–14, 2020.
- [45] R. Dian and S. Li, "Hyperspectral image super-resolution via subspace-based low tensor multi-rank regularization," *IEEE Transactions on Image Processing*, vol. 28, no. 10, pp. 5135–5146, 2019.
- [46] T. G. Kolda and B. W. Bader, "Tensor decompositions and applications," *Siam Review*, vol. 51, no. 3, pp. 455–500, 2009.
- [47] H. A. L. Kiers, "Towards a standardized notation and terminology in multiway analysis," *Journal of Chemometrics*, vol. 14, no. 3, pp. 105–122, 2000.
- [48] J. B. Kruskal, "Three-way arrays: rank and uniqueness of trilinear decompositions, with application to arithmetic complexity and statistics," *Linear Algebra and its Applications*, vol. 18, no. 2, pp. 95–138, 1977.
- [49] A. Smilde, R. Bro, and P. Geladi, *Multi-Way Analysis: Applications in the Chemical Sciences*, Wiley, West Sussex, England, UK, 2004.
- [50] L. R. Tucker, "Some mathematical notes on three-mode factor analysis," *Psychometrika*, vol. 31, no. 3, pp. 279–311, 1966.
- [51] G. H. Golub and C. F. Van Loan, *Matrix Computations*, Johns Hopkins University Press, Baltimore, MD, USA, 1996.
- [52] L. Loncan, L. B. de Almeida, J. M. Bioucas-Dias et al., "Hyperspectral pansharpening: a review," *IEEE Geoscience and Remote Sensing Magazine*, vol. 3, no. 3, pp. 27–46, 2015.
- [53] L. Zhuang and J. M. Bioucas-Dias, "Fast hyperspectral image denoising and inpainting based on low-rank and sparse representations," *IEEE Journal of Selected Topics in Applied Earth Observations and Remote Sensing*, vol. 11, no. 3, pp. 730–742, 2018.
- [54] J. Yang, J. Wright, T. S. Huang, and Y. Ma, "Image super-resolution via sparse representation," *IEEE Transactions on Image Processing*, vol. 19, no. 11, pp. 2861–2873, 2010.
- [55] T. Lu, S. Li, L. Fang, Y. Ma, and J. A. Benediktsson, "Spectral-spatial adaptive sparse representation for hyperspectral image

- denoising,” *IEEE Transactions on Geoscience and Remote Sensing*, vol. 54, no. 1, pp. 373–385, 2016.
- [56] R. Arablouei and F. de Hoog, “Hyperspectral image recovery via hybrid regularization,” *IEEE Transactions on Image Processing*, vol. 25, no. 12, pp. 5649–5663, 2016.
- [57] L. Zhang, W. Wei, C. Tian, F. Li, and Y. Zhang, “Exploring structured sparsity by a reweighted Laplace prior for hyperspectral compressive sensing,” *IEEE Transactions on Image Processing*, vol. 25, no. 10, pp. 4974–4988, 2016.
- [58] L. Fang, C. Wang, S. Li, and J. A. Benediktsson, “Hyperspectral image classification via multiple-feature-based adaptive sparse representation,” *IEEE Transactions on Instrumentation and Measurement*, vol. 66, no. 7, pp. 1646–1657, 2017.
- [59] H. Attouch, J. Bolte, and B. F. Svaiter, “Convergence of descent methods for semi-algebraic and tame problems: proximal algorithms, forward-backward splitting, and regularized gauss-seidel methods,” *Mathematical Programming*, vol. 137, no. 1-2, pp. 91–129, 2013.
- [60] H. Attouch, J. Bolte, P. Redont, and A. Soubeyran, “Proximal alternating minimization and projection methods for non-convex problems: an approach based on the Kurdyka-Łojasiewicz inequality,” *Mathematics of Operations Research*, vol. 35, no. 2, pp. 438–457, 2010.
- [61] O. Axelsson, *Iterative Solution Methods*, Cambridge Univ. Press, Cambridge, UK, 1996.
- [62] S. Boyd, N. Parikh, E. Chu, B. Peleato, and J. Eckstein, “Distributed optimization and statistical learning via the alternating direction method of multipliers,” *Foundations and Trends in Machine Learning*, vol. 3, no. 1, pp. 1–122, 2010.
- [63] L. N. Smith and M. Elad, “Improving dictionary learning: multiple dictionary updates and coefficient reuse,” *IEEE Signal Processing Letters*, vol. 20, no. 1, pp. 79–82, 2013.
- [64] J. M. Bioucas-Dias, “A variable splitting augmented Lagrangian approach to linear spectral unmixing,” in *Proceedings of the 2009 First Workshop on Hyperspectral Image and Signal Processing: Evolution in Remote Sensing*, pp. 1–4, Grenoble, France, August 2009.
- [65] R. Zhou, G. Wang, D. Zhao, Y. Zou, and T. Zhang, “Super-resolution of low-quality images based on compressed sensing and sequence information,” in *Proceedings of the 2019 IEEE 90th Vehicular Technology Conference (VTC2019-Fall)*, pp. 1–5, Honolulu, HI, USA, September 2019.
- [66] W. Li and Q. Du, “Collaborative representation for hyperspectral anomaly detection,” *IEEE Transactions on Geoscience and Remote Sensing*, vol. 53, no. 3, pp. 1463–1474, 2015.
- [67] Y. Zhang, B. Du, L. Zhang, and S. Wang, “A low-rank and sparse matrix decomposition-based Mahalanobis distance method for hyperspectral anomaly detection,” *IEEE Transactions on Geoscience and Remote Sensing*, vol. 54, no. 3, pp. 1376–1389, 2016.
- [68] L. Wang, C.-I. Chang, L.-C. Lee et al., “Band subset selection for anomaly detection in hyperspectral imagery,” *IEEE Transactions on Geoscience and Remote Sensing*, vol. 55, no. 9, pp. 4887–4898, 2017.
- [69] X. Wang, L. Wan, M. Huang, C. Shen, Z. Han, and T. Zhu, “Low-complexity channel estimation for circular and non-circular signals in virtual MIMO vehicle communication systems,” *IEEE Transactions on Vehicular Technology*, vol. 69, no. 4, pp. 3916–3928, 2020.
- [70] W. Lu, X. Xu, G. Huang et al., “Energy efficiency optimization in SWIPT enabled WSNs for smart agriculture,” *IEEE Transactions on Industrial Informatics*, p. 1, 2020.

Research Article

ISAR Imaging Based on Multiple Measurement Vector Model Sparse Signal Recovery Algorithm

Junjie Feng 

School of Physics and Electrical Engineering, Liupanshui Normal University, Liupanshui, Guizhou, China

Correspondence should be addressed to Junjie Feng; fzy028@163.com

Received 13 May 2020; Accepted 17 June 2020; Published 13 July 2020

Guest Editor: Liangtian Wan

Copyright © 2020 Junjie Feng. This is an open access article distributed under the Creative Commons Attribution License, which permits unrestricted use, distribution, and reproduction in any medium, provided the original work is properly cited.

A multiple measurement vector (MMV) model blocks sparse signal recovery. ISAR imaging algorithm is proposed to improve ISAR imaging quality. Firstly, the sparse imaging model is built, and block sparse signal recovery algorithm-based MMV model is applied to ISAR imaging. Then, a negative exponential function is proposed to approximately block L0 norm. The optimization solution of smoothed function is obtained by constructing a decreasing sequence. Finally, the correction steps are added to ensure the optimal solution of the block sparse signal along the fastest descent direction. Several simulations and real data simulation experiments verify the proposed algorithm has advantages in imaging time and quality.

1. Introduction

Due to the characteristics of long distance, all-weather and all-weather, the inverse synthetic aperture radar (ISAR) imaging technology has been widely used in military, civil, and other fields [1, 2]. Generally, the wide-band signal is used to improve range resolution in ISAR imaging. In order to obtain a high azimuth resolution, it is necessary to improve the target rotation accumulation angle or increase the time interval of coherent processing. For a long coherent processing interval (CPI), complex motion compensation is needed; however, it is difficult to achieve real-time imaging. When the number of echo pulses is limited or the echo pulse is interfered strongly, it is difficult to achieve the effect. Therefore, the imaging algorithm based on short CPI is necessary.

The theory of compressive sensing (CS) uses a small amount of measurement information to reconstruct the original signal with a large probability through optimization, which is the research hot spot in the field of signal processing [3–6]. It has been used in ISAR imaging [7, 8], MIMO radar signal processing [9, 10], and radar parameter estimation [11–14]. Because the actual contour of the target in sky imaging background is smaller than imaging area, the scatters of the target have sparse structure compared with

the imaging area. The traditional sparse ISAR imaging algorithm mainly considers the recovery of individual scatters. However, the scatters are not independent. Because the target is a whole, different parts of the target are connected together. The strong scatterers of ISAR target can occupy many resolution cells, which have usually clusters or blocks in the imaging region. In this case, the common sparse reconstruction algorithm cannot completely describe the characteristic of target.

The analysis shows that, by using the inherent structural characteristics of the signal, it can improve signal reconstruction performance greatly. If the block property structure of ISAR target is exploited, the better recovery performance can be obtained. Two-dimensional pattern-coupled sparse Bayesian learning (PC-SBL) algorithm is proposed in [15]. However, the algorithm is computational expensive. One block sparse reconstruction algorithm is proposed to reconstruct the scattering coefficient of the target in the paper.

At present, most of the applications of sparse signal recovery algorithm in ISAR imaging are based on the single measurement vector (SMV) model, in which the ISAR echo signals are divided according to the distance unit and then the image can be obtained by combining the reconstructed result of each distance unit. However, ISAR imaging

reconstruction algorithm based on the SMV model has low efficiency and poor real-time performance. The compressive sensing multiple measurement vector model can repeat observations of the information, and the MMV model can obtain better performance and improve the sparse signal reconstruction efficiency compared with that of the SMV model.

In order to improve ISAR imaging quality, a two-dimensional sparse signal reconstruction algorithm of ISAR imaging based on MMV model is proposed. All one-dimensional range images are written together as a whole to be recovered by utilizing the potential block characteristics of ISAR target. The algorithm can not only improve the efficiency of reconstruction but also improve the quality of ISAR imaging.

The structure of the article is as follows: Section 2 introduces necessary ISAR imaging model and sparse signal recovery ISAR imaging algorithm. In section 3, the block sparse recovery algorithm for ISAR imaging algorithm based on MMV model is introduced in detail. Simulation and real data imaging results of ISAR are presented in section 4. Finally, section 5 provides the conclusion.

2. ISAR Imaging Model

ISAR uses the relative motion of target and radar to obtain high resolution azimuth. Assuming the LFM signal transmitted by the radar is

$$y(t) = \text{rect}\left(\frac{t}{T_a}\right) \exp\left[j2\pi\left(f_c t + \frac{1}{2}\lambda t^2\right)\right], \quad (1)$$

where t is the fast time, f_c expresses the carrier frequency, γ is the chirp rate, and T_a indicates the pulse duration, the backscattered ISAR signal can be written as

$$s(t) = A \cdot \text{rect}\left(\frac{t}{T_a}\right) \cdot \text{rect}\left(\frac{t}{T}\right) \cdot \exp\left\{j2\pi\left(\left(t - \frac{2R(t)}{c}\right) + \frac{1}{2}\gamma\left(t - \frac{2R(t)}{c}\right)^2\right)\right\}, \quad (2)$$

where c is the speed of light, T is the CPI, and A is the signal amplitude. After the distance pulse is compressed, the received signal can be expressed as

$$s(t) = A \cdot \text{sin c}\left[T_a \gamma \left(t - \frac{2(R_0 + y)}{c}\right)\right] \cdot \exp\left[-j4\pi \frac{(R_0 + y)}{\lambda}\right] \cdot \text{rect}\left(\frac{t}{T}\right) \cdot \exp\left[-j2\pi\left(f \cdot t + \frac{1}{2}\beta \cdot t^2\right)\right], \quad (3)$$

where λ is the wavelength, f is the Doppler frequency, and β is change rate of Doppler frequency. It is assumed that there are K strong scattering centers in a certain distance unit and the time-varying scattering can be ignored in short coherence processing; it can be expressed as

$$y(t) = \sum_{k=1}^K x_k \cdot \text{rect}\left(\frac{t}{T}\right) \cdot \exp(-j2\pi f_k t) + n, \quad (4)$$

where x_k and f_k are the k^{th} scattering centers' complex coefficient and Doppler frequency, respectively, and n is the noise. The time sequence can be expressed as $t = [1: N]^T \cdot \Delta t$, where $\Delta t = (1/f_r)$ is the time interval and f_r is the pulse repetition frequency. $N = (T/\Delta t)$ is the number of pulses. Δf_d is the Doppler frequency resolution interval, and the sparse Doppler sequence is $f_d = [1: M] \cdot \Delta f_d$, where $M = (f_r/\Delta f_d)$ and M is the number of Doppler unit corresponding to Δf_d . So, construct the basis matrix as $\Psi = \{\phi_1, \phi_2, \dots, \phi_m, \dots, \phi_M\}$, $\phi_M(t) = \exp(-j2\pi f_d(m)t)$, $0 < m \leq M$. The discrete signal equation received by ISAR can be expressed as

$$y = \Phi w + n, \quad (5)$$

where w is the coefficient vector composed of the reflection coefficient and n is the noise vector.

Because w contains the information of the strong scattering point of the target, it is a sparse vector. The solution of w is equivalent to the following optimization problem:

$$\hat{w} = \arg \min \|w\|_p \quad \text{subject to } \|y - \Phi w\|_2 < \eta, \quad (6)$$

where η is a small constant, and the value is related to noise variance; P is the Lp norm.

According to the above optimization, the signal of each distance unit is recovered and then combined together to obtain the ISAR image. Because every distance element needs to be recovered, it will increase the computational burden and affect the imaging efficiency. Based on this, the paper studies the ISAR imaging model based on MMV. If all one-dimensional range profiles are written together as a whole, the total received signal can be expressed as

$$Y = \Phi W + N, \quad (7)$$

where W is the target scatter point coefficient matrix, which is the ISAR image.

In the traditional MMV model, the nonzero signals in each column of matrix W have the same supporting set. For the equation (7), the scatter points of distance unit have different supporting set. Because the scatter points of ISAR targets have the characteristics of cluster or block distribution, the imaging result can be obtained by the following block L0 sparse signal recovery algorithm:

$$\min_w \|W\|_0 \quad \text{s.t. } \|Y(:,n) - \Phi W(:,n)\| < \eta \quad n = 1, \dots, N, \quad (8)$$

where $\|W\|_0$ expresses a block sparse L0 norm of a matrix, η is a small positive number relating with noise, and N is the number of columns of W .

The smoothed function $G_\sigma(w) = N - \sum_i \exp(-w_i^2/\sigma)$ approaches the L0 norm when the parameter σ approaches zero [16]. When the parameter $\sigma \rightarrow \infty$, $G_\sigma(w)$ approximates the L2 norm. Therefore, the algorithm does not search for sparse solution because L2 norm cannot describe


```

(I) Initialization
(1)  $\widehat{W}_0$  is the minimum  $l_2$  norm solution of  $Y = \Phi W$ 
(2) One decreasing sequence  $\sigma: [\sigma_1, \dots, \sigma_J]$ 
(II) For  $j = 1, \dots, J$ :
(1) Let  $\sigma = \sigma_j, \beta = (J - (j/2) + 1/J)$ 
(2) Minimize the function  $F_\sigma(W)$  on the feasible set
(a) Initialization:  $W = \widehat{W}_{j-1}$ 
(b) Let  $\delta$  be gradient of  $F_\sigma(W)$ 
(c)  $W(:, n) \leftarrow W(:, n) - \mu\sigma\delta$  (where  $\mu$  is a small positive constant)
(d) If  $|AW(:, n) - Y(:, n)|_2 > \eta$ , project  $W$  back into the feasible set  $W$ :
 $G_\sigma(W_2) > G_\sigma(W)$ 
(e) Compare step
    If  $F_\sigma(X_2) > F_\sigma(X)$ 
 $\widehat{W}_j = W$ 
    If  $F_\sigma(X_2) < F_\sigma(X)$ 
 $W = \widehat{W}_j$ 
(3) Set  $\widehat{W}_j = W$ .
(III) Final solution is  $W = \widehat{W}_J$ 

```

ALGORITHM 1: The block SL0 sparse signal recovery algorithm based on MMV model.

sparsity. A negative exponential function $F_\sigma(w) = N - \sum_i \exp(-|w_i|/\sigma)$ as smoothed function is proposed to obtain an approximate L0 norm solution. When the parameter $\sigma \rightarrow \infty$, $F_\sigma(w)$ approaches L0 norm. Thus, the sparse solution can be obtained by using the new function at the very beginning of iteration.

For the one-dimensional block discrete signal w , the block structure is expressed as follows:

$$w = [w_1, \dots, w_d, \dots, w_{2d}, \dots, w_{Pd}], \quad (9)$$

where P is the size of the block and d is the number of blocks. The block smoothed L0 function can be expressed as

$$F_\sigma(w) = P - \sum_{P=1}^P g_\sigma \left(\sqrt{\sum_{i=1}^d |w((P-1)d + i)|^2} \right). \quad (10)$$

3. MMV Block Sparse Signal ISAR Imaging Algorithm

In the double-loop-layer SL0 algorithm [16], the solution of $\sigma = \sigma_j$ is only the initial value when $\sigma = \sigma_{j+1}$. So, it is not necessary to solve the precise solution of $\sigma = \sigma_j$. According to this observation, the inner loop layer is canceled, at the same time, the step size in the out layer is decreased. It means that the searching density of the variable parameter σ is increased. For every σ_j , only one fastest descent searching is used to solve the minimization solution of the function $F_{\sigma_j}(w)$. The proposed algorithm ensures the block reconstruction accuracy, and the computation amount does not increase. The steepest descent method should reduce the cost function in every step, but it is not necessarily the descent direction in the actual solution process. Therefore, for the above algorithm, the step of checking whether the solution is descending is added in each iteration. If it is not along descent direction, the midpoint of the previous point and the

current point is used to ensure that the search direction follows the fastest descent direction. The proposed algorithm is called improved MMB block sparse smoothed L0 algorithm (simplified as MBSSL0). The high ISAR imaging algorithm based on MMV mode is expressed as Algorithm 1.

If the selected step size is large, the algorithm will not converge. If the selected step size is too small, it will affect the convergence speed and reduce the calculation efficiency. Therefore, a larger step size is selected in the initial search because the search point is far from the minimum value point. When the search point is gradually close to the minimum value, the search step size should be gradually reduced. J is the iterative loop number, and σ_j should be chosen as less than the minimum value of the sparse solution. Letting $\mu = \beta \max|X|/L_0$ guarantees that it moves only a small part of the maximum value.

4. Simulation Results

4.1. One-Dimensional Block Spike Signal Recovery. The signal model is $y = Aw + n$, and the sparse matrix A is 80×160 . Each element of A is Gaussian distributed. w is a block sparse signal, whose nonzero block coefficients are uniform ± 1 . The block size is 8. n is the independent Gaussian random vector. The performance using BOMP [17], BCoSaMp [18], BSL0 [19], BSPG L1 [20], and MBSSL0 are compared. For BSL0 algorithm, the number of outer loops and inner loops is 20 and 10, respectively. For BSSL0 algorithm, the loop number is 200. Define minimum mean absolute value error $MAE = 10 \log_{10} (\|x - \hat{x}\|/N)$, where x is the true solution and \hat{x} is the estimation value. The experiment was repeated 500 times. The computational times, correct position reconstruction frequencies, and MAE are averaged.

Figure 1 shows the average computational times with different block sparsity by different algorithms. We can see that BOMP, BSL0, and MBSSL0 algorithms have less computation than the other algorithms. The correct position

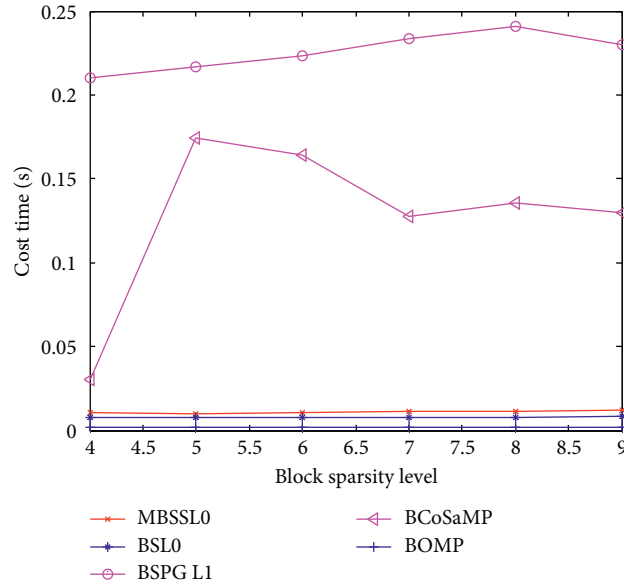


FIGURE 1: Computational costs for different algorithms with block sparsity.

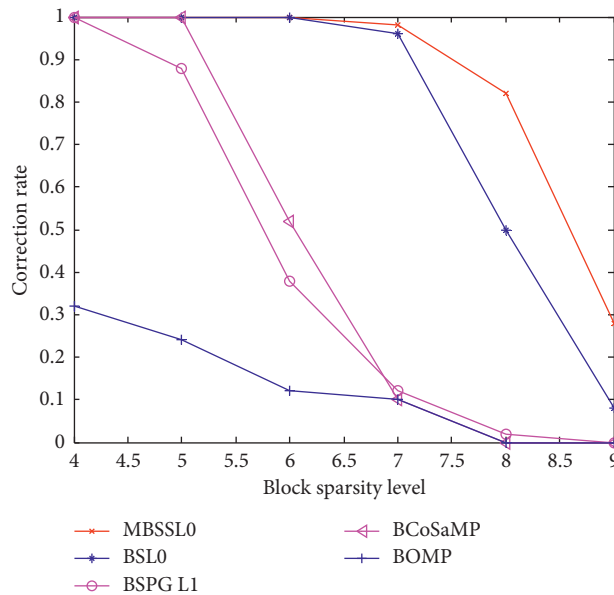


FIGURE 2: Correct estimation for different algorithms with block sparsity.

estimation and MAE with different block sparsities for different algorithms are shown in Figures 2 and 3. We can see that the performances of MBSSL0 algorithm are competitive with other algorithms.

4.2. ISAR Imaging Using Real Data. The real data are the measured echo data of yak-42 aircraft from the ISAR system. The radar parameters are as follows: the signal frequency band width 400 MHz, the center carrier frequency 10 GHz, and the data pulse repetition frequency 100 Hz. 256 echo pulses are selected in the simulation. Figures 4–6 show the imaging results obtained by these algorithms using 16, 32, and 64 pulses that are randomly chosen from 256 pulses. The

uniform block is used in the block sparse reconstruction. The ISAR image is divided as 4×2 small blocks, where 4 is 4 cross-range units. The loop number of algorithm is 200. The simulation results are compared visually and quantitatively with those images obtained by some sparse signal recovery methods including MOMP algorithm [21], SBL algorithm [22], PC-SBL algorithm, and MBSSL0 algorithm in this paper, respectively. The recovery images of MBSSL0 algorithm show more information in the neck of plane when pulse number is 16. The images obtained by MBSSL0 algorithm are similar to PC-SBL algorithm when the plus numbers are 32 and 64. The imaging results of MBSSL0 algorithm generate better visual quality, and the ISAR images are more intensive than MOMP algorithm and MSBL.

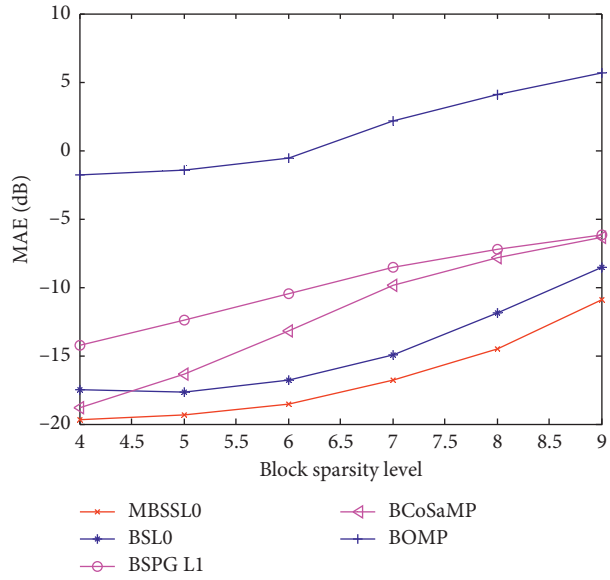


FIGURE 3: MAE for different algorithms with block sparsity.

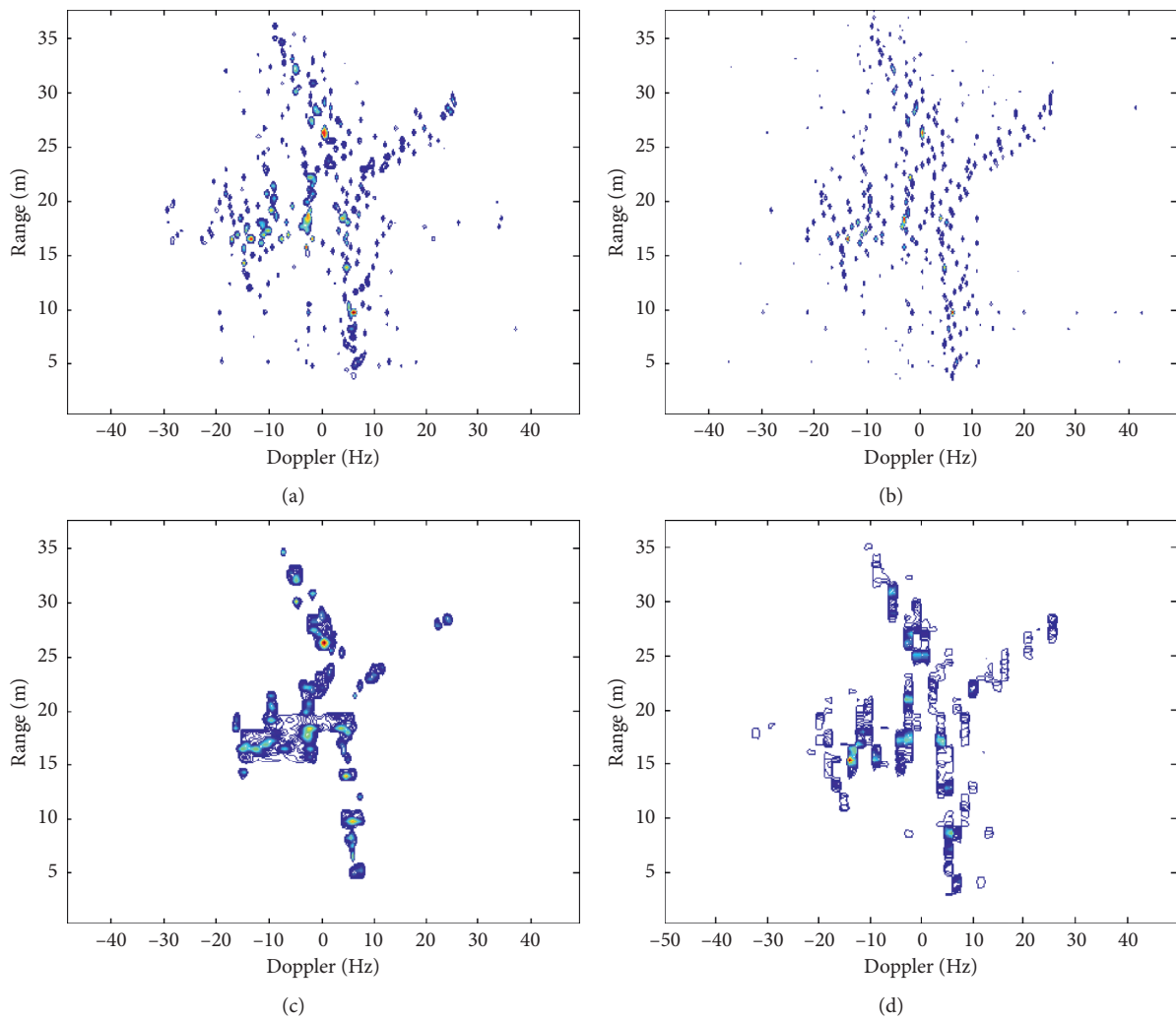


FIGURE 4: Reconstructed images using 16 pulse numbers: (a) MOMP, (b) MSBL, (c) PC-SBL, and (d) MBSSL0.

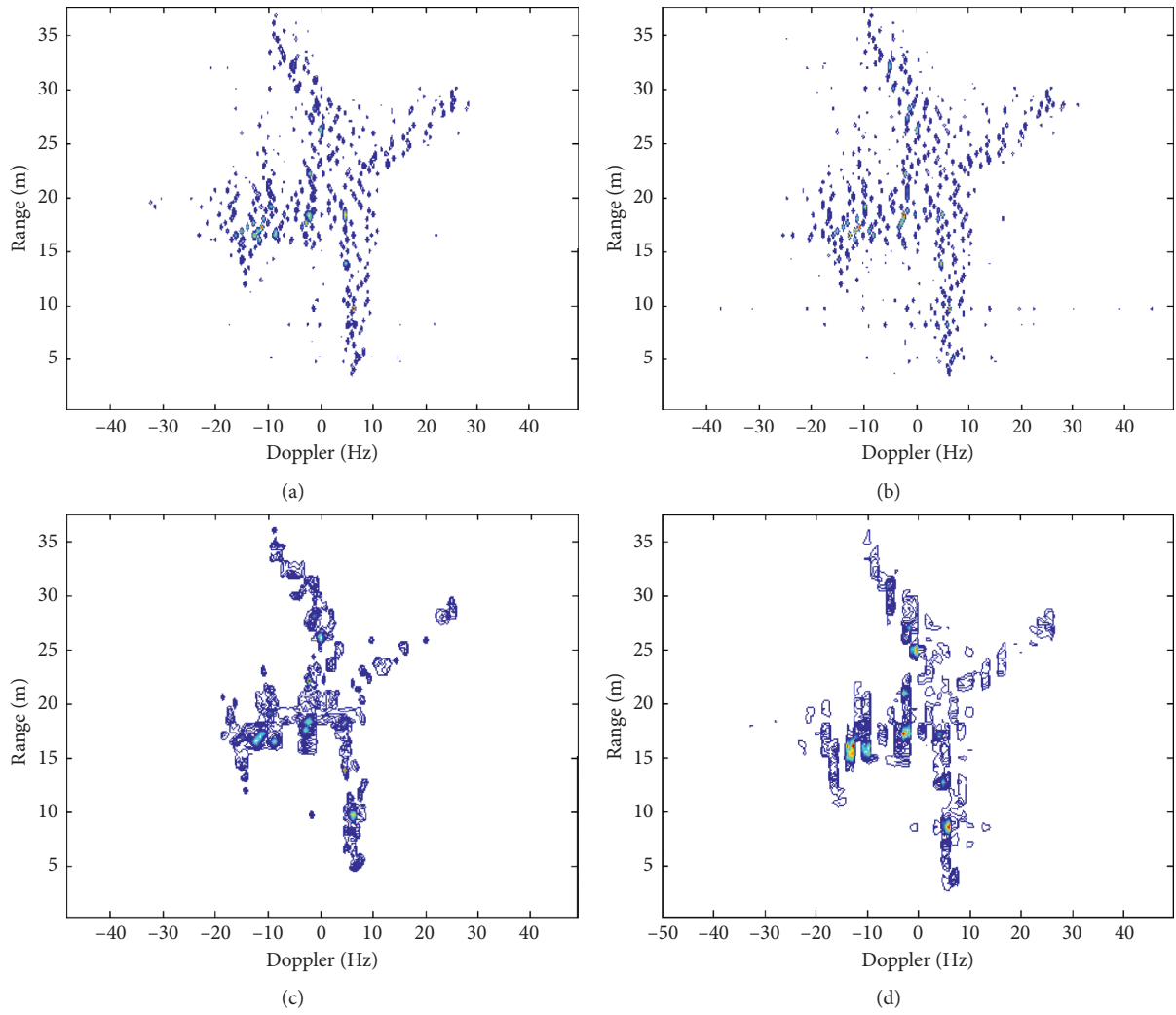


FIGURE 5: Reconstructed images using 32 pulse numbers: (a) MOMP, (b) MSBL, (c) PC-SBL, and (d) MBSSL0.

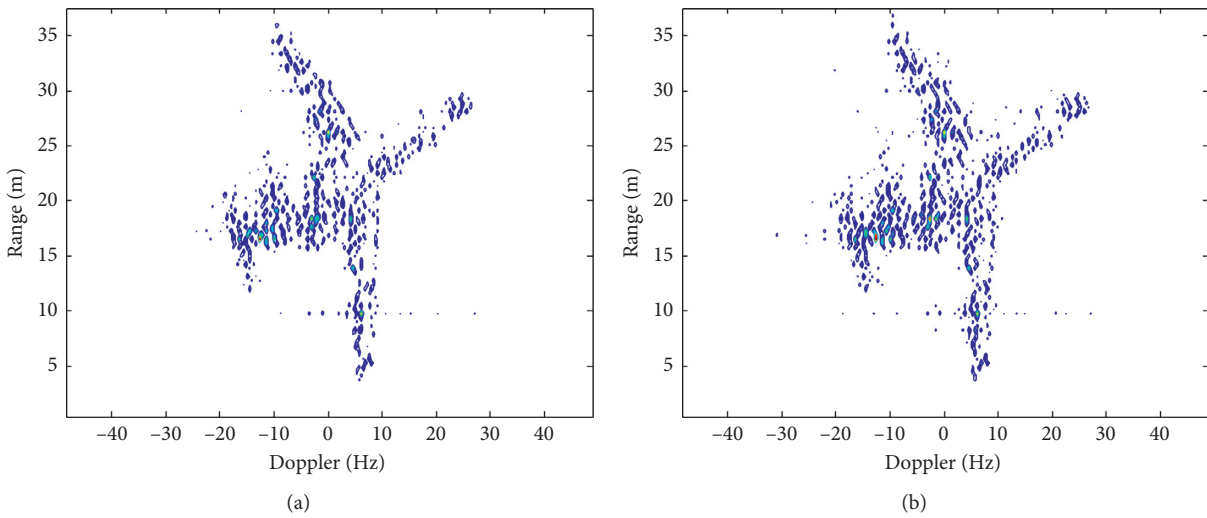


FIGURE 6: Continued.

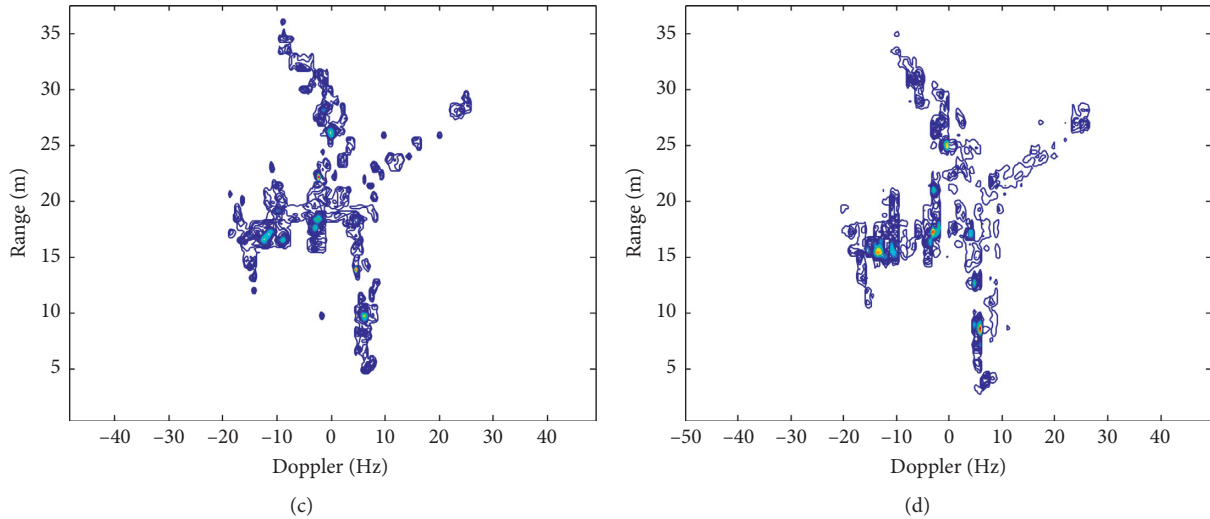


FIGURE 6: Reconstructed images using 64 pulse numbers: (a) MOMP, (b) MSBL, (c) PC-SBL, and (d) MBSSL0.

TABLE 1: Average running times of the algorithm.

Algorithm	MOMP	MSBL	PC-SBL	MBSSL0
Run time (sec)	97	172	228	102

Considering the block sparsity, MBSSL0 algorithm can describe the characteristics of the signal better and has better signal reconstruction performance. The computation time using different algorithms are provided when the pulse number is 32 in Table 1. It can be seen that the MBSSL0 algorithm saves computational time.

5. Conclusion

In this paper, one ISAR imaging algorithm of MMV block sparse reconstruction is proposed by considering the block structure of ISAR target in the imaging scene. Based on the recovery algorithm of smoothed block L0 norm, a revised step is added to ensure that the optimal solution is searched along the direction of the fastest descent. Experimental results show that the algorithm can save imaging time and improve ISAR imaging quality effectively with fewer pulses.

Data Availability

The data used to support the findings of this study are included within the article.

Conflicts of Interest

The author declares no conflicts of interest.

Acknowledgments

This work was partially supported by the National Science Foundation of China (no. 61471191).

References

- [1] Y. Chen, Q. Zhang, N. Yuan, Y. Luo, and H. Lou, "An adaptive ISAR-imaging-considered task scheduling algorithm for multi-function phased array radars," *IEEE Transactions on Signal Processing*, vol. 63, no. 19, pp. 5096–5110, 2015.
- [2] L. Zhao, L. Wang, G. Bi, and L. Yang, "An autofocus technique for high-resolution inverse synthetic aperture radar imagery," *IEEE Transactions on Geoscience and Remote Sensing*, vol. 52, no. 10, pp. 6392–6403, 2014.
- [3] F. Wen, Z. Zhang, K. Wang, G. Sheng, and G. Zhang, "Angle estimation and mutual coupling self-calibration for ULA-based bistatic MIMO radar," *Signal Processing*, vol. 144, pp. 61–67, 2018.
- [4] J. Li, X. Zhang, R. Cao, and M. Zhou, "Reduced-dimension MUSIC for angle and array gain-phase error estimation in bistatic MIMO radar," *IEEE Communications Letters*, vol. 17, no. 3, pp. 443–446, 2013.
- [5] F. Wen, Z. Zhang, and G. Zhang, "Joint DOD and DOA estimation for bistatic MIMO radar: a covariance trilinear decomposition perspective," *IEEE Access*, vol. 7, no. 1, pp. 53273–53283, 2019.
- [6] F. Wen, X. Xiong, and Z. Zhang, "Angle and mutual coupling estimation in bistatic MIMO radar based on PARAFAC decomposition," *Digital Signal Processing*, vol. 65, pp. 1–10, 2017.
- [7] X.-Y. Pan, W. Wang, and G.-Y. Wang, "Sub-nyquist sampling jamming against ISAR with CS-based HRRP reconstruction," *IEEE Sensors Journal*, vol. 16, no. 6, pp. 1597–1602, 2016.
- [8] X. Zhang, T. Bai, H. Meng, and J. Chen, "Compressive sensing-based ISAR imaging via the combination of the sparsity and nonlocal total variation," *IEEE Geoscience and Remote Sensing Letters*, vol. 11, no. 5, pp. 990–994, 2014.
- [9] L. Ding and W. Chen, "MIMO radar Sparse Imaging with phase mismatch," *IEEE Geoscience and Remote Sensing Letters*, vol. 12, no. 4, pp. 816–820, 2015.

- [10] F. Q. Wen and J. P. Shi, "Fast direction finding for bistatic EMVS-MIMO radar without pairing," *Signal Processing*, vol. 173, Article ID 107512, 2020.
- [11] L. Wan, G. Han, L. Shu, S. Chan, and T. Zhu, "The application of DOA estimation approach in patient tracking systems with high patient density," *IEEE Transactions on Industrial Informatics*, vol. 12, no. 6, pp. 2353–2364, 2016.
- [12] X. Wang, L. Wan, M. Huang, C. Shen, Z. Han, and T. Zhu, "Low-complexity channel estimation for circular and non-circular signals in virtual MIMO vehicle communication systems," *IEEE Transactions on Vehicular Technology*, vol. 69, no. 4, pp. 3916–3928, 2020.
- [13] L. Wan, G. Han, J. Jiang, J. J. P. C. Rodrigues, N. Feng, and T. Zhu, "DOA estimation for coherently distributed sources considering circular and noncircular signals in massive MIMO systems," *IEEE Systems Journal*, vol. 11, no. 1, pp. 41–49, 2017.
- [14] H. Wang, L. Wan, M. Dong, K. Ota, and X. Wang, "Assistant vehicle localization based on three collaborative base stations via SBL-based robust DOA estimation," *IEEE Internet of Things Journal*, vol. 6, no. 3, pp. 5766–5777, 2019.
- [15] H. Duan, L. Zhang, J. Fang, L. Huang, and H. Li, "Pattern-coupled sparse Bayesian learning for inverse synthetic aperture radar imaging," *IEEE Signal Processing Letters*, vol. 22, no. 11, pp. 1995–1999, 2015.
- [16] H. Mohimani, M. Babaie-Zadeh, and C. Jutten, "A fast approach for overcomplete sparse decomposition based on smoothed ℓ_0 norm," *IEEE Transactions on Signal Processing*, vol. 57, no. 1, pp. 289–301, 2009.
- [17] Y. C. Eldar, P. Kuppinger, and H. Bolcskei, "Block-sparse signals: uncertainty relations and efficient recovery," *IEEE Transactions on Signal Processing*, vol. 58, no. 6, pp. 3042–3054, 2010.
- [18] R. G. Baraniuk, V. Cevher, M. F. Duarte, and C. Hegde, "Model-based compressive sensing," *IEEE Transactions on Information Theory*, vol. 56, no. 4, pp. 1982–2001, 2010.
- [19] H. S. Chalehjegh, M. Babaie-Zadeh, and C. Jutten, "Fast block-sparse decomposition based on SL0," in *Proceedings of the 9th International Conference on Latent Variable Analysis and Signal Separation*, Springer, Berlin, Germany, pp. 426–433, September 2010.
- [20] E. Van Den Berg and M. P. Friedlander, "Sparse optimization with least-squares constraints," *SIAM Journal on Optimization*, vol. 21, no. 4, pp. 1201–1229, 2011.
- [21] S. S. Chen, D. L. Donoho, and M. A. Saunders, "Atomic decomposition by basis pursuit," *SIAM Review*, vol. 43, no. 1, pp. 129–159, 2001.
- [22] D. P. Wipf and B. D. Rao, "An empirical Bayesian strategy for solving the simultaneous sparse approximation problem," *IEEE Transactions on Signal Processing*, vol. 55, no. 7, pp. 3704–3716, 2007.

Research Article

JPEG Lifting Algorithm Based on Adaptive Block Compressed Sensing

Yongjun Zhu ^{1,2} Wenbo Liu ¹ Qian Shen ¹ Yin Wu ³ and Han Bao ¹

¹College of Automation Engineering, Nanjing University of Aeronautics and Astronautics, Nanjing 211106, China

²School of Electronic and Information Engineering, Suzhou University of Science and Technology, Suzhou 215009, China

³College of Information Science and Technology, Nanjing Forestry University, Nanjing 210037, China

Correspondence should be addressed to Yongjun Zhu; zyj@mail.usts.edu.cn

Received 25 May 2020; Accepted 12 June 2020; Published 11 July 2020

Guest Editor: Liangtian Wan

Copyright © 2020 Yongjun Zhu et al. This is an open access article distributed under the Creative Commons Attribution License, which permits unrestricted use, distribution, and reproduction in any medium, provided the original work is properly cited.

This paper proposes a JPEG lifting algorithm based on adaptive block compressed sensing (ABCS), which solves the fusion between the ABCS algorithm for 1-dimension vector data processing and the JPEG compression algorithm for 2-dimension image data processing and improves the compression rate of the same quality image in comparison with the existing JPEG-like image compression algorithms. Specifically, mean information entropy and multifeature saliency indexes are used to provide a basis for adaptive blocking and observing, respectively, joint model and curve fitting are adopted for bit rate control, and a noise analysis model is introduced to improve the antinoise capability of the current JPEG decoding algorithm. Experimental results show that the proposed method has good performance of fidelity and antinoise, especially at a medium compression ratio.

1. Introduction

Image processing technology has always been a research hotspot in the field of computer science. Especially, in the recent years, under the emergence of high-definition and large-scale images and the impact of massive video information, image compression processing technology has become particularly noticeable. Image compression technology can use limited storage space to save a larger proportion of image data; at the same time, it can also reduce the data size of images of the same quality, which can effectively improve the efficiency of network data transmission. The traditional image compression technology includes two independent parts, image acquisition and image compression, which limit the fusion improvement method of the two correlated compression technology parts. The emergence of compressed sensing (CS) theory breaks the above frame of image compression, and it completes the image acquisition and compression in the step of sparse observation synchronously; on the one hand, it simplifies the image processing process, and on the other hand, it also provides new research areas for image fusion compression.

There are many types of images processed in image compression technology, and this article selects a still image as the research object. The common still image compression formats include JPEG, JPEG2000, JPEG-XR, TIFF, GIF, and PCX. This paper focuses on the research of image compression algorithms with a JPEG similar structure and improves them with the combination of CS technology. In addition, the algorithms with a similar principle architecture to JPEG are collectively referred to as JPEG-like algorithms, including traditional JPEG, JPEG-LS, JPEG2000, and JPEG-XR. Data redundancy is essential to the compression of a still image. JPEG-like algorithms use time-frequency transform algorithms and entropy coding as main methods to eliminate data redundancy [1–3]. Although having achieved certain effects of still image compression, these algorithms have insufficient considerations on three types of data redundancy (coding redundancy, interpixel redundancy, and psychological visual redundancy) [4]. Firstly, the simple image blocking without guidance could not support the effective coding efficiency to eliminate redundancy in the existing JPEG-like algorithms. Secondly, the uniform time-frequency transform of the same dimension cannot

reasonably use the a priori information between pixels of different subimage blocks to reduce interpixel redundancy. In the end, the former JPEG-like algorithms fail to eliminate psychological visual redundancy by considering overall and local saliency. CS technology breaks through the limitations of the Nyquist sampling theorem to provide innovative ideas for sparse reconstruction of signals [5]. In particular, the adaptive block compressed sensing (ABCS) combined with adaptive partitioning and sampling provides a feasible solution for the optimization of JPEG-like algorithms [6, 7]. That is, the block compression measurement matrix could be used as the forward discrete cosine transform (FDCT) matrix in the JPEG coding, and the inverse discrete cosine transform (IDCT) process is replaced by sparse reconstruction. In addition, multiple feature saliency and noise analysis are introduced to implement adaptive control of the observation matrix and minimal error iterative reconstruction [8, 9].

In this article, we proposed a JPEG lifting algorithm based on the ABCS, and named it as JPEG-ABCS. This proposed algorithm focuses on the following aspects: (1) guiding best morphological blocking by minimizing mean information entropy (MIE); (2) generating an element vector of subimage pixels using the texture feature and 2-dimensional direction DCT; (3) selecting the dimension of the measurement matrix by variance and local significance factors; (4) rate control by matching the overall sampling rate and the quantization matrix; (5) realizing iterative reconstruction of a minimum error under noise condition by using noise influence model analysis.

The remainder of this paper is organized as follows. In Section 2, the basic theories of JPEG-like algorithms and the ABCS algorithm are illustrated. In Section 3, we focus on the introduction of the JPEG-ABCS algorithm. Then, the implementation of the proposed JPEG-ABCS algorithm is analyzed in Section 4. In Section 5, the experiment and result analysis shows the benefit of the JPEG-ABCS. The paper concludes in Section 6.

2. Preliminary Knowledge

2.1. Background of the Existing JPEG-Like Algorithms. The existing JPEG-like algorithms are similar in structure, mainly including blocking, forward time-frequency transform, quantization, entropy coding, and the inverse operation of the above four processes. As the basic one of JPEG-like algorithms, the structure of the JPEG model is shown in Figure 1.

It can be seen from Figure 1 that in the entire JPEG model, the original image I is treated as two-dimensional data, and its key link is adopting the 2-dimensional DCT. Generally, the block size is square, such as 8×8 , and the recommended quantization matrix (light-table) is given in equation (1) [10]. Based on the Hoffman coding, the encoding part adopts differential pulse code modulation (DPCM) for DC coefficients and run length coding (RLC) for AC coefficients:

$$\text{light-table} = \mathbf{Q}_0 = \begin{bmatrix} 16 & 11 & 10 & 16 & 24 & 40 & 51 & 61 \\ 12 & 12 & 14 & 19 & 26 & 58 & 60 & 55 \\ 14 & 13 & 16 & 24 & 40 & 57 & 69 & 56 \\ 14 & 17 & 22 & 29 & 51 & 84 & 80 & 62 \\ 18 & 22 & 37 & 56 & 68 & 109 & 103 & 77 \\ 24 & 35 & 55 & 64 & 81 & 104 & 113 & 92 \\ 49 & 64 & 78 & 87 & 103 & 121 & 120 & 101 \\ 72 & 92 & 95 & 98 & 112 & 100 & 103 & 99 \end{bmatrix}. \quad (1)$$

Compared with the fixed bit rate of the JPEG algorithm, the JPEG-LS algorithm adds the function of rate control by using a quality factor. JPEG2000 adopts nonfixed square blocking (tile) and discrete wavelet transform (DWT) to improve the quality of the restored image. JPEG-XR introduces the lapped orthogonal transform (LOT) to reduce the blocking artifact at low bit rates.

2.2. Basic Theory of CS Algorithm. CS theory was originally proposed by Candès et al. in 2006, which proved that the original signal can be accurately reconstructed by partial Fourier transform coefficients. The advent of CS technology solves the problem that image sampling and compression cannot be performed simultaneously. In general, the main contents of the research on CS theory include sparse representation, compression observation, and optimization reconstruction [11]. Firstly, the main task of sparse representation is to find a set of bases that can make the signal sparse representation, which is the premise and foundation of the entire CS theory. Secondly, the primary task of compression observation is to design a linear measurement matrix uncorrelated with the basis vector to obtain dimensionality reduction observation data, which is the key content of CS theory. Lastly, optimization reconstruction is a difficult problem in CS theory, and its main goal is to solve the original signal through the reverse optimization problem of the sparse vector. The specific solution method of this process is the constrained optimization method.

CS mathematical model is based on the assumption of signal sparsity. Let $\mathbf{x} \in R^N$ be the original signal with n dimension. Suppose that the sparse matrix $\Psi \in R^{N \times N}$ makes the sparse representation coefficient of x as $\mathbf{s} = \Psi^{-1}\mathbf{x}$, where $\mathbf{s} \in R^N$ contains only K ($K \ll N$) nonzero elements. The original signal x is called the K sparse signal under sparse basis Ψ . The number of nonzero elements in the coefficient vector \mathbf{s} can be calculated by $K = \|\mathbf{s}\|_0$, where $\|\cdot\|_0$ denotes l_0 norm.

CS theory states that the information content in sparse signals can be effectively captured by a smaller number of observations. Let $\Phi \in R^{M \times N}$ be the measurement matrix, where $M < N$. The linear dimension-reduction acquisition vector of the original signal \mathbf{x} is given as $\mathbf{y} = \Phi\mathbf{x}$, where $\mathbf{y} \in R^M$ represents the CS observation signal. In addition, the CS theory points out that to accurately recover the original

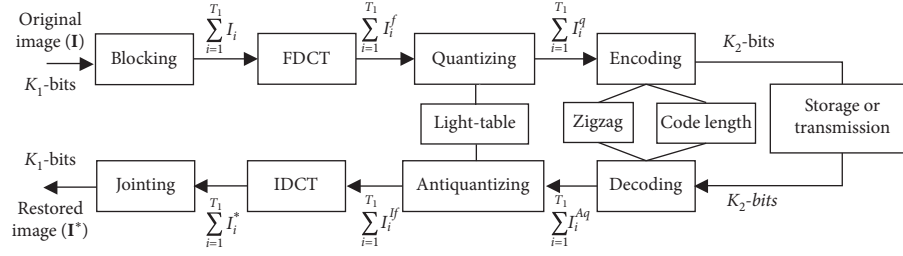


FIGURE 1: Structure of the JPEG model.

signal by the observation signal, its dimensions must obey the following condition: $M \geq cK \log(N)$, where c is an adjustment constant.

Since $M < N$, the reconstruction of the sparse signal \mathbf{x} from the measurement vector \mathbf{y} is ill-posed which requires us to solve the underdetermined system of equations. There are many solutions for such a system. It is common practice to achieve effective signal reconstruction by using signal sparsity as an additional constraint. The accurate signal reconstruction is accomplished through solving the following optimization problem:

$$\min_{\mathbf{s}} \|\mathbf{s}\|_p \quad \text{s.t. } \mathbf{y} = \Phi \mathbf{x} = \Phi \Psi \mathbf{s} = \Omega \mathbf{s}, \quad (2)$$

where Ω is the sensing matrix, $\|\cdot\|_p$ denotes the L_p norm, and the value of p is usually 0, 1, and 2 according to different optimization goals. This is a NP-hard problem, and in order to ensure the stability and robustness of the reconstruction process, the measurement matrix Φ must satisfy the restricted isometric property (RIP).

The above is the description of the three important problems of the CS algorithm, which solves the separation problem of traditional image acquisition and compression. However, when CS is applied to large-scale high-definition images and video processing, because the 2-dimensional image contains a lot of information, the overall projection requires a large-scale measurement matrix, which will inevitably lead to two major problems: excessive storage and reconstruction algorithm complexity. The above problems limit the application of CS in image processing. The emergence of block compressed sensing (BCS) theory solves this problem well. The solution is to cut the whole image into several small unit blocks, reconstruct after independent observation, and then perform stitching to restore and reconstruct the original image.

Traditional block compressed sensing (BCS) technology introduces the idea of blocks in CS theory to solve the dimensional disaster of data processing, and then improves the processing speed of the algorithm [12]. Its basic model is shown in the following equation:

$$\mathbf{y} = \begin{bmatrix} \mathbf{y}_1 \\ \mathbf{y}_2 \\ \vdots \\ \mathbf{y}_{T_1} \end{bmatrix} = \Phi \mathbf{x} = \begin{bmatrix} \Phi_B & \cdots & 0 \\ \vdots & \ddots & \vdots \\ 0 & \cdots & \Phi_B \end{bmatrix} \begin{bmatrix} \mathbf{x}_1 \\ \mathbf{x}_2 \\ \vdots \\ \mathbf{x}_{T_1} \end{bmatrix}, \quad (3)$$

where $\mathbf{x}_i \in R^n$, $\mathbf{y}_i \in R^m$, and $\Phi_B \in R^{m \times n}$ are the i -th subblocks of the original signal, observation signal, and block measurement matrix and $T_1 = (N/n) = (M/m)$ is the number of blocks. In addition, a coefficient $\eta = (M/N)$ is often defined in the BCS, which is called the mean sampling rate. In the analysis of the above BCS algorithm model, although the blocking strategy solves the problems of dimensional disaster and computational complexity, the model uses a unified measurement matrix which can neither reflect the inherent differences between each subimage, nor can it achieve differentiated blocking.

In order to overcome the above shortcomings, the nonuniform blocking and observing are introduced into BCS, and combined with the idea of the adaptive algorithm, the ABCS algorithm is generated. The ABCS algorithm mentioned in this article is the introduction of the adaptive strategy into BCS, which is mainly reflected in adaptive blocking and observation [13, 14]. The ABCS algorithm model is as follows:

$$\mathbf{y} = \begin{bmatrix} \mathbf{y}_1 \\ \mathbf{y}_2 \\ \vdots \\ \mathbf{y}_{T_1} \end{bmatrix} = \Phi \mathbf{x} = \begin{bmatrix} \Phi_1 & \cdots & 0 \\ \vdots & \Phi_i & \vdots \\ 0 & \cdots & \Phi_{T_1} \end{bmatrix} \begin{bmatrix} \mathbf{x}_1 \\ \mathbf{x}_2 \\ \vdots \\ \mathbf{x}_{T_1} \end{bmatrix}, \quad (4)$$

where $\mathbf{x}_i \in R^{n_i}$, $\mathbf{y}_i \in R^{m_i}$, and $\Phi_i \in R^{m_i \times n_i}$ are the i -th subblocks of the original signal, observation signal, and measurement matrix. The difference between the ABCS algorithm and the BCS algorithm is that it gives the dimensional freedom of subblock and measurement matrix, which provides conditions for the reasonable use of the correlation of the internal elements of the original signal.

3. Fusion of JPEG Model and ABCS Algorithm

3.1. Workflow of JPEG Lifting Algorithm. According to the above section, the JPEG image compression model mainly includes blocking, FDCT, quantization, coding, and the inverse process of the above four parts. The focus of this section is to do the research about the method on how to embed the advantages of the ABCS algorithm into the JPEG model. The basis for the fusion of the JPEG model and the ABCS algorithm is that the consistent purpose is for image compression. The former mainly compresses the image by reducing the number of bits occupied by each pixel, and the

latter mainly compresses the data by reducing the amount of sampled data, so the ABCS algorithm is suitable to be embedded to the data acquisition stage of the JPEG model; that is, the ABCS algorithm is fused in the blocking and FDCT processes to reduce the amount of input data in the quantization process. In addition, the distinction of the data processing method in JPEG and ABCS is noticed. The image data in the JPEG algorithm are processed in the form of two-dimensional data, which is conducive to saving the two-dimensional structural characteristics of the image, while the input signal in the ABCS algorithm is a simple one-dimensional vector form and does not have two-dimensional characteristics. The proposed algorithm JPEG-ABCS mainly includes the solution of two main problems: (a) the conversion problem between two-dimensional time-frequency transformation of JPEG and one-dimensional measurement model of ABCS; (b) the specific method of applying ABCS to the JPEG compression algorithm.

In typical JPEG image compression, after the pre-processing stage, an $R \times C$ input image \mathbf{I} is divided into 8×8 size subimages \mathbf{I}_i , $i = 1, 2, \dots, T_1$, $T_1 = ((R \times C)/(8 \times 8))$. Each subimage is transmitted to a 2D DCT transform, and the 2D DCT can be completed using two one-dimensional DCTs according to the separability of the DCT. In addition, the blocking method designed in this paper adopts the variable shape blocking method under a unified dimension ($n = r \times c$), so the FDCT process can be described as follows:

$$\mathbf{I}_i^f = \text{dct2}(\mathbf{I}_i) = \mathbf{D}_r \mathbf{I}_i \mathbf{D}_c^T, \quad (5)$$

where \mathbf{I}_i^f is the subimage in the DCT domain, $\mathbf{D}_r \in R^{r \times r}$ and $\mathbf{D}_c \in R^{c \times c}$ are the 1D vertical and horizontal DCT orthogonal matrices, respectively, and r and c are the number of rows and columns of each subimage [15].

The block sparse representation and the flexible uniform-dimension blocking are introduced into the ABCS algorithm. Equation (4) can be rewritten as follows:

$$\{\mathbf{y}_i\}_{i=1}^{T_1} = \{\Phi_i \mathbf{x}_i\}_{i=1}^{T_1} = \{\Phi_i \Psi_i \mathbf{s}_i\}_{i=1}^{T_1} = \{\Omega_i \mathbf{s}_i\}_{i=1}^{T_1}, \quad (6)$$

where $\mathbf{x}_i \in R^n$, $\mathbf{y}_i \in R^{m_i}$, and $\mathbf{s}_i \in R^n$ are the i -th subblocks of the original signal, observation signal, and sparse signal; $\Phi_i \in R^{m_i \times n}$, $\Psi_i \in R^{n \times n}$, and $\Omega_i \in R^{m_i \times n}$ are the i -th subblocks of the measurement matrix, sparse matrix, and sensing matrix; $\eta_i = (m_i/n)$ is the subsampling rate of the i -th subblock.

For retaining the two-dimensional characteristics of the image signal in the application of JPEG-ABCS, it is necessary to analyze the two-dimensional DCT transform in JPEG and the compression observation in ABCS. It is impossible that the 1-dimension vector \mathbf{x}_i generated directly from the subimage \mathbf{I}_i through column/row scanning has two-dimensional structural characteristics. The inverse solution of the reconstructed signal $\hat{\mathbf{x}}_i$ in the ABCS algorithm is generally denoted as $\hat{\mathbf{x}}_i = \Psi_i \hat{\mathbf{s}}_i = \Psi_i \Omega_i^+ \mathbf{y}_i = \Psi_i \Omega_i^+ \Phi_i \mathbf{x}_i = \Psi_i \Omega_i^+ \Omega_i \mathbf{s}_i$; that is, the reconstruction of the original signal is only related to the sparse representation coefficient \mathbf{s}_i . If the sparse representation coefficient \mathbf{s}_i has two-dimensional structure information, it is equivalent to the original signal \mathbf{x}_i

with two-dimensional structure information. Therefore, the equivalent two-dimensional block vector generation can be achieved by taking the sparse matrix of ABCS as the corresponding matrix under the two-dimensional DCT transform:

$$\mathbf{D}_r \mathbf{I}_i \mathbf{D}_c^T = \mathbf{I}_i^f \Leftrightarrow \Psi_i^+ \mathbf{x}_i = \mathbf{s}_i. \quad (7)$$

Analyzing equation (7), the function between the sparse matrix and the DCT orthogonal matrices is established as follows:

$$\Psi_i = \text{kron}(\mathbf{D}_c^T, \mathbf{D}_r^T), \quad (8)$$

where $\text{kron}(\ast)$ represents the Kronecker product function. Original signal vector \mathbf{x}_i is obtained by scanning the pixel value of the subimage \mathbf{I}_i vertically. In addition, if the texture of the image is not in the vertical and horizontal directions, the directional DCT is used instead of the horizontal and vertical DCT orthogonal matrix.

Replacing FDCT and IDCT in the JPEG with adaptive sparse observing and sparse restoring, respectively, replacing blocking in the JPEG with adaptive blocking and vectorization, adding noise to the data storage or data transmission are done, and then the workflow of the proposed JPEG-ABCS algorithm is shown in Figure 2. Comparing the two image compression models shown in Figures 1 and 2, the key points of the JPEG-ABCS model are (1) adaptive blocking, that is, replacing a fixed block with a variable block; (2) adaptive vectorization, that is, providing a matching vector generation method based on image orientation characteristics; (3) adaptive observing, that is, replacing uniform observing with nonuniform observing; (4) adding a controllable variable in the rate control process to improve the JPEG algorithm; (5) designing a denoising method in adaptive restoring to reduce the noise impact on restored data.

3.2. Innovation of JPEG Lifting Algorithm. The innovations of the above JPEG lifting algorithm are as follows:

- (1) Adding the mean sampling rate to overcome the deficiency of the traditional JPEG-like algorithm that can only use the time-frequency transform and the quantization matrix to eliminate redundant information in image compression.
- (2) By analyzing the correlation between sparseness and error, the optimal OMP iterative algorithm is established to enhance the JPEG-like algorithm's noise immunity performance.
- (3) In the adaptive block observation, the MIE-based adaptive block reduces the information entropy of the subimage set to lower the bpp, the ASM-based adaptive vectorization can ensure the maximum avoidance of image information loss, and the adaptive observation based on multifeature saliency ensures a reasonable distribution of the total measurement number.

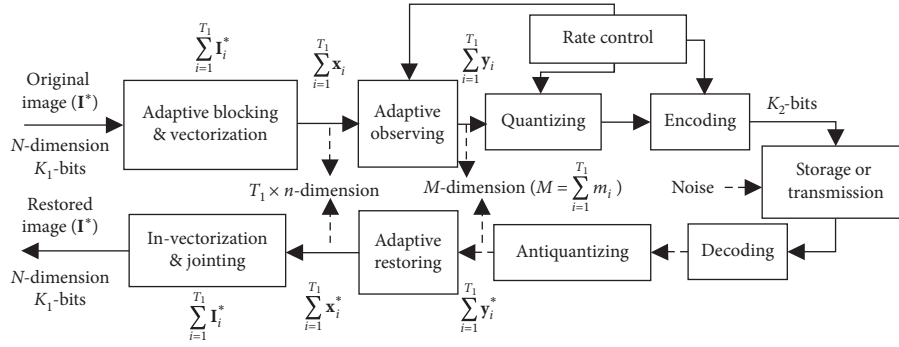


FIGURE 2: Workflow of JPEG-ABCS.

4. Implementation of JPEG-ABCS

This section mainly describes the implementation of the JPEG-ABCS algorithm mentioned in the previous section. The specific implementation is discussed from four aspects: adaptive blocking, adaptive vectorization, adaptive observing, and denoising by optimizing the number of iterations.

4.1. Adaptive Blocking Method Based on MIE. The adaptive blocking method proposed in this paper is a variable partitioning in the same dimension, that is, $n = r \times c$, where n is a fixed value, typical value is 64, and r and c are the number of rows and columns of the variable block, typical value $\{r \times c\}_j = 2^j \times 2^{6-j}$, $j = 0, 1, 2, \dots, 6$. Specifically, the optimized block $n_{\text{opt}} = r_{\text{opt}} \times c_{\text{opt}}$ is based on minimizing the mean information entropy (MIE) of the block observation signal set. Since blocking process needs to be completed before observation, it is impossible to use an ungenerated observation set $\{\mathbf{y}_i\}_{i=1}^{T_1}$ for guiding the blocking optimization. Therefore, an alternative method is introduced to guide the reasonable blocking by minimizing the MIE of the original signal's block set:

$$\begin{cases} r_{\text{opt}} \times c_{\text{opt}} = \arg \min_{\{r \times c\}_j} \left\{ \text{MIE}(\{\mathbf{x}_i\}_{i=1}^{T_1}) \right\}_{j=0}^{T_2-1} \\ \text{MIE}(\{\mathbf{x}_i\}_{i=1}^{T_1}) = \frac{1}{T_1} \sum_{i=1}^{T_1} \text{IE}(\mathbf{x}_i) = \frac{1}{T_1} \sum_{i=1}^{T_1} \left(- \sum_{j=h_{\min}}^{h_{\max}} p_{i,j} \log_2 p_{i,j} \right), \end{cases} \quad (9)$$

where $\text{MIE}(\ast)$ represents the MIE function of the pixel set, $\text{IE}(\mathbf{x}_i)$ represents the information entropy of the i -th sub-image in the pixel domain, $p_{i,j}$ represents the proportion of elements with the pixel gray value j in the i -th subimage, T_2 is the number of blocking ways, and h_{\min} and h_{\max} are the minimum and maximum values of the pixel gray in the original signal, respectively. However, the effectiveness of the above method lies on consistency between the observation signal's MIE and the original signal's MIE at the same partitioning. In order to verify the above consistency problem, this paper conducted a test experiment using multiple standard images, and its experimental results are shown in Figure 3. The experimental data show that, under the constraint of minimizing MIE, the optimal block of the

original signal and the observed signal is consistent, which verifies the feasibility and rationality of the proposed block optimization method. Specifically, it can be seen from Figure 3 that under the constraint of minimum MIE, the optimal block shape is only related to the test image itself, not to the sampling rate. In addition, it has been verified by a large number of other standard test images that the method of finding the best block has the same trend whenever applied to the observation signal and the original signal, and there must be an extreme point.

4.2. Adaptive Vectorization Based on ASM. The basis of adaptive vectorization is how to identify the directional characteristics of the image. There are many methods for identifying direction features in the field of array signal processing, especially in DOA estimation research, such as the Capon algorithm, MUSIC algorithm, maximum likelihood algorithm, subspace fitting algorithm, and ESPRIT algorithm [16, 17]. In this article, the angular second-order moment (ASM) value under the gray-level cooccurrence matrix (GLCM) is used to characterize the saliency of the direction [18]:

$$\begin{cases} g_{\text{ASM}}(i, j | d, \theta) = \sum_{i=0}^{N_h-1} \sum_{j=0}^{N_h-1} \{p(i, j | d, \theta)\}^2 = \sum_{i=0}^{N_h-1} \sum_{j=0}^{N_h-1} \left\{ \frac{\mathbf{P}(i, j | d, \theta)}{R} \right\}^2, \\ \mathbf{P} = \text{gray comatrix}(\mathbf{I} | d, \theta), \end{cases} \quad (10)$$

where gray comatrix(\ast) is the GLCM function, $\mathbf{P}(i, j | d, \theta)$ is the (i, j) term of \mathbf{P} , $p(i, j | d, \theta)$ is the normalized form of $\mathbf{P}(i, j | d, \theta)$, $\mathbf{I}(i, j | d, \theta)$ is the adjacent pixel pairs in the image with distance d , direction θ , and gray values (i, j) , and R is the ideal maximum number of pixel pairs under the selected conditions.

Combined with the rectangular shape of adaptive blocking, the ASM values in four directions are defined for adaptive vectorization, namely, g_{ASM}^0 , g_{ASM}^{90} , g_{ASM}^{45} , and g_{ASM}^{135} [19]. In addition, the maximum value of these four values is defined as $g_{\text{MAX}} = \max\{g_{\text{ASM}}^0, g_{\text{ASM}}^{90}, g_{\text{ASM}}^{45}, g_{\text{ASM}}^{135}\}$.

$$\begin{cases} g_{\text{ASM}}^0 = g_{\text{ASM}}(i = j | 1, 0^\circ), & g_{\text{ASM}}^{90} = g_{\text{ASM}}(i = j | 1, 90^\circ), \\ g_{\text{ASM}}^{45} = g_{\text{ASM}}(i = j | 1, 45^\circ), & g_{\text{ASM}}^{135} = g_{\text{ASM}}(i = j | 1, 135^\circ). \end{cases} \quad (11)$$

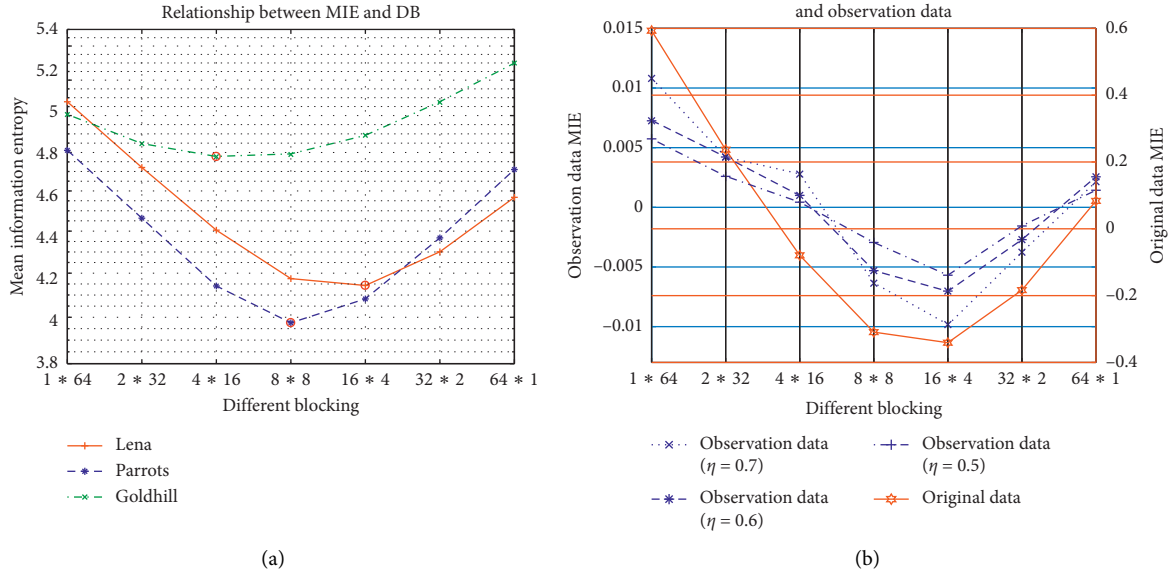


FIGURE 3: MIE changes in terms of different blocking. (a) MIE comparison of different images; (b) MIE consistency between original and observation data.

The specific method of adaptive vectorization is based on the relationship between the four ASM values. If $g_{ASM}^0 \times g_{ASM}^{90} \geq g_{ASM}^{45} \times g_{ASM}^{135}$ and $g_{MAX} = g_{ASM}^0$, then the vectorization set $\sum_{i=1}^{T_1} \mathbf{x}_i$ of the original subimage set $\sum_{i=1}^{T_1} \mathbf{I}_i$ is generated using horizontal scanning and vertical linking; if $g_{ASM}^0 \times g_{ASM}^{90} \geq g_{ASM}^{45} \times g_{ASM}^{135}$ and $g_{MAX} = g_{ASM}^{90}$, then the vectorization set $\sum_{i=1}^{T_1} \mathbf{x}_i$ of the original subimage set $\sum_{i=1}^{T_1} \mathbf{I}_i$ is generated using vertical scanning and horizontal linking; if $g_{ASM}^0 \times g_{ASM}^{90} < g_{ASM}^{45} \times g_{ASM}^{135}$ and $g_{MAX} = g_{ASM}^{45}$, then the vectorization set $\sum_{i=1}^{T_1} \mathbf{x}_i$ of the original subimage set $\sum_{i=1}^{T_1} \mathbf{I}_i$ uses zigzag generation along the main diagonal direction; if $g_{ASM}^0 \times g_{ASM}^{90} < g_{ASM}^{45} \times g_{ASM}^{135}$ and $g_{MAX} = g_{ASM}^{135}$, then the vectorization set $\sum_{i=1}^{T_1} \mathbf{x}_i$ of the original subimage set $\sum_{i=1}^{T_1} \mathbf{I}_i$ uses zigzag generation along the counter-diagonal direction. It should be noted that the adaptive vectorization of each subimage must be related to the design of the sparse matrix to jointly realize the one-dimensional vectorization that preserves the two-dimensional structural characteristics of the subimage data.

4.3. Adaptive Observing Based on Multifeature Saliency and Bit Rate Control. The key point of the nonuniform measurement matrix $\Phi_i \in R^{m_i \times n}$ is the determination of m_i . Considering that different subimages contain different amounts of information and the sensitivity of the human eye's attention mechanism to different images is different, this paper proposes an adaptive measurement matrix $\Phi_i = \sqrt{n/m_i} \Gamma_{m_i}$ based on multifeature saliency $J(\mathbf{x}_i)$ and the orthogonal symmetric Toeplitz matrix (OSTM):

$$\left\{ \begin{array}{l} \Gamma_{m_i} = \text{OSTM}(m_i, n), \\ m_i = \eta_i \times n = \frac{J(\mathbf{x}_i)}{\left(\sum_{i=1}^{T_1} J(\mathbf{x}_i)/T_1\right)} \times \eta \times n, \\ J(\mathbf{x}_i) = \gamma \log_2(J_1(\mathbf{x}_i)^\alpha \times J_2(\mathbf{x}_i)^\beta), \\ J_1(\mathbf{x}_i) = \frac{1}{n} \sum_{j=1}^n (\mathbf{x}_{ij} - \mu_i)^2, J_2(\mathbf{x}_i) = \frac{1}{n} \sum_{j=1}^n \frac{\sum_{k=1}^q |\mathbf{x}_{ij}^k - \mathbf{x}_{ij}|}{\mathbf{x}_{ij}}, \end{array} \right. \quad (12)$$

where γ is the adjustment factor, $J_1(*)$ stands for the overall variance function, $J_2(*)$ is the local saliency function according to Weber's theorem [20], q is the number of elements in the salient domain determined by the optimal bounding box, OSTM(m_i, n) is formed by randomly taking m_i rows of $n \times n$ -dimensional OSTM [21], and $\alpha = 2$ and $\beta = 1$ are the recommended values. The purpose of designing the adaptive measurement matrix in this way is to rationalize the sampling process and to achieve more sampling of detail blocks and less sampling of smooth blocks.

The traditional JPEG-like algorithms control the bit rate (bits per pixel, bpp) through the quantization matrix, encoding, and bit-stream organization [22]. In this paper, the mean sampling rate η has been used to improve the compression performance of the JPEG-ABCS algorithm. The bit rate control for an 8-bit 256-level grayscale image is as follows:

$$\text{bpp} = 8 \times \frac{\eta}{\mu \times \varepsilon}, \quad (13)$$

where η is the mean sampling rate and also corresponds to information decay ratio caused by sparse measurement, μ ($\mu \geq 1$) represents information decay ratio caused by the quantization, and ε ($\varepsilon \geq 1$) is the bit compression ratio of the entropy encoding and bit-stream organization.

Analysis of the above three factors that affect the rate control in the JPEG-ABCS model shows that once the encoding method is determined, the only factors that can be optimized are η and μ , while ε is a fixed number. In order to reduce the bit rate of restored images at the same quality, the value of these two factors must be set reasonably. This article focuses on the analysis of image performance impact in terms of different η under the same bpp and matching design of the quantization matrix that can determine the value of μ . In the process of analyzing the impact of η on the performance of compressed images, the synthetic indicator composed of the peak signal-to-noise rate (PSNR) and structural similarity (SSIM) is used as evaluation criteria to find the best η under different bpp. At the same time, in order to complete the comparison experiment of different η under the same bpp, it is necessary to set different quantization matrices. This article uses the quality factor (QF) to design different quantization matrices [23]. Because the data ($\sum_{i=1}^{T_1} \mathbf{y}_i$) quantized in the JPEG-ABCS algorithm are a one-dimensional vector and are also a normalized measurement of the frequency domain sparse coefficients of the original signal ($\sum_{i=1}^{T_1} \mathbf{x}_i$), the quantization matrix is weakened into a quantization vector whose elements no longer characterize frequency domain property and have the same importance. Therefore, the elements of the quantization matrix for the subimage designed in this paper have the same value ($\mathbf{Q}_0^* = \text{ones}(m_i)$). The goal of the quantization matrix matching design is only to find a fitting function to approximate the relationship between bpp and QF. Figure 4 shows the experimental data of the above test process using Lena. According to Figure 4(a), it can be seen that under the constraint of maximizing synthetic features, the optimal mean sampling rate (η) increases with the increase in bpp. Meanwhile, an η obtaining function can be summarized, as shown in equation (14), and the typical values of B_{th}^1 and B_{th}^2 in the equation are 0.15 and 0.3. In addition, it should be noted that equation (14) can only be directly applied to images with a similar MIE of Lena. For other images, the threshold determination condition in the equation should be corrected according to the MIE of the image block set. Specifically, the coefficient ξ is introduced for the correction of the above two threshold conditions (that is, $B_{\text{th}}^1 = 0.15\xi$ and $B_{\text{th}}^2 = 0.3\xi$). The coefficient ξ can be defined as the MIE ratio of other images to the Lena image. The design of the fitting function ($\text{QF} = f(\text{bpp})$) adopts the cubic curve fitting method whose data are derived from the actual measurement value of QF and bpp. Figure 4(b) shows the comparison of consistency between the actual light-table's QF and the design value obtained from equation (15). From the results, the QF obtained by equation (15) satisfies the actual requirements well:

$$\eta = \begin{cases} 0.3, & \text{bpp} < B_{\text{th}}^1, \\ 0.4 + \left[\frac{\text{bpp} - 0.15}{0.05} \right] \times 0.1, & B_{\text{th}}^1 \leq \text{bpp} \leq B_{\text{th}}^2, \\ 0.7, & \text{bpp} > B_{\text{th}}^2, \end{cases} \quad (14)$$

$$\begin{cases} \text{light-table} = \left\lfloor \frac{\text{QFS} \times \mathbf{Q}_0^* + 50}{100} \right\rfloor, \\ \mathbf{Q}_0^* = \text{ones}(m_i), \\ \text{QFS} = \begin{cases} \frac{5000}{\text{QF}}, & 0 < \text{QF} \leq 50, \\ 200 - 2\text{QF}, & 100 \geq \text{QF} > 50, \end{cases} \\ \text{QF} = f(\text{bpp}) = \lambda_2 \times \text{bpp}^2 + \lambda_1 \times \text{bpp} + \lambda_0, \end{cases} \quad (15)$$

where $\lfloor \cdot \rfloor$ is the floor function and $\lambda_2 = 38.5972$, $\lambda_1 = 6.1241$, and $\lambda_0 = -0.0938$ are obtained by quadratic curve fitting.

4.4. Denoising by Optimizing the Number of Iterations. Consider the noise observation model as follows:

$$\tilde{\mathbf{y}}_i = \Phi_i \mathbf{x}_i + \mathbf{w}_i = \Phi_i (\mathbf{x}_i + \Phi_i^+ \mathbf{w}_i) = \Phi_i \tilde{\mathbf{x}}_i, \quad (16)$$

where \mathbf{w}_i is the additive white Gaussian noise with zero-mean and standard deviation σ_w and $\tilde{\mathbf{x}}_i$ is the equivalent noisy original signal.

Since the reconstructed original signal (\mathbf{x}_i^*) is recovered from the noisy observation signal ($\tilde{\mathbf{y}}_i$), the reconstruction error ($e_{\mathbf{x}_i}$) is mainly caused by the noise and reconstruction algorithm, and its mathematical expression can be defined as the following equation using the l_2 norm:

$$e_{\mathbf{x}_i} = \frac{1}{n} \|\mathbf{x}_i - \mathbf{x}_i^*\|_2^2, \quad (17)$$

where \mathbf{x}_i^* is restored by the pseudoinverse operation, that is, $\mathbf{x}_i^* = \Psi_i \mathbf{s}_i^* = \Psi_i \Omega_i^+ \tilde{\mathbf{y}}_i$, and \mathbf{s}_i^* is the reconstructed sparse signal. The abovementioned Ω_i^+ is the pseudoinverse of Ω_i , usually $\Omega_i^+ = \Omega_i^T (\Omega_i \Omega_i^T)^{-1}$, and also represents the reconstruction algorithm in CS. The reconstruction algorithm of CS is based on the sparse representation of the signal [24], that is, the reconstruction sparsity (v_i) of \mathbf{s}_i^* satisfies the inequality ($v_i \ll m < n$), so the pseudoinverse operation to get \mathbf{x}_i^* can be rewritten as follows:

$$\begin{aligned} \mathbf{x}_i^* &= \Psi_{i,v} \Omega_{i,v}^+ \tilde{\mathbf{y}}_i = \Psi_{i,v} (\Omega_{i,v}^T \Omega_{i,v})^{-1} \Omega_{i,v}^T \tilde{\mathbf{y}}_i \\ &= \Psi_{i,v} (\Omega_{i,v}^T \Omega_{i,v})^{-1} \Omega_{i,v}^T \Phi_i \tilde{\mathbf{x}}_i, \end{aligned} \quad (18)$$

where $\Psi_{i,v}$ is the $n \times v_i$ matrix generated of v_i column vectors in $\Psi_i = [\psi_{i,1} \ \psi_{i,2} \ \dots \ \psi_{i,m}]$ and $\Omega_{i,v}$ is the $m \times v_i$ matrix generated of v_i column vectors in $\Omega_i = [\omega_{i,1} \ \omega_{i,2} \ \dots \ \omega_{i,m}]$ that has the greatest correlation with $\tilde{\mathbf{y}}_i$.

Because equation (17) cannot be calculated directly, we add $\tilde{\mathbf{x}}_i$ to help in analysis and calculation:

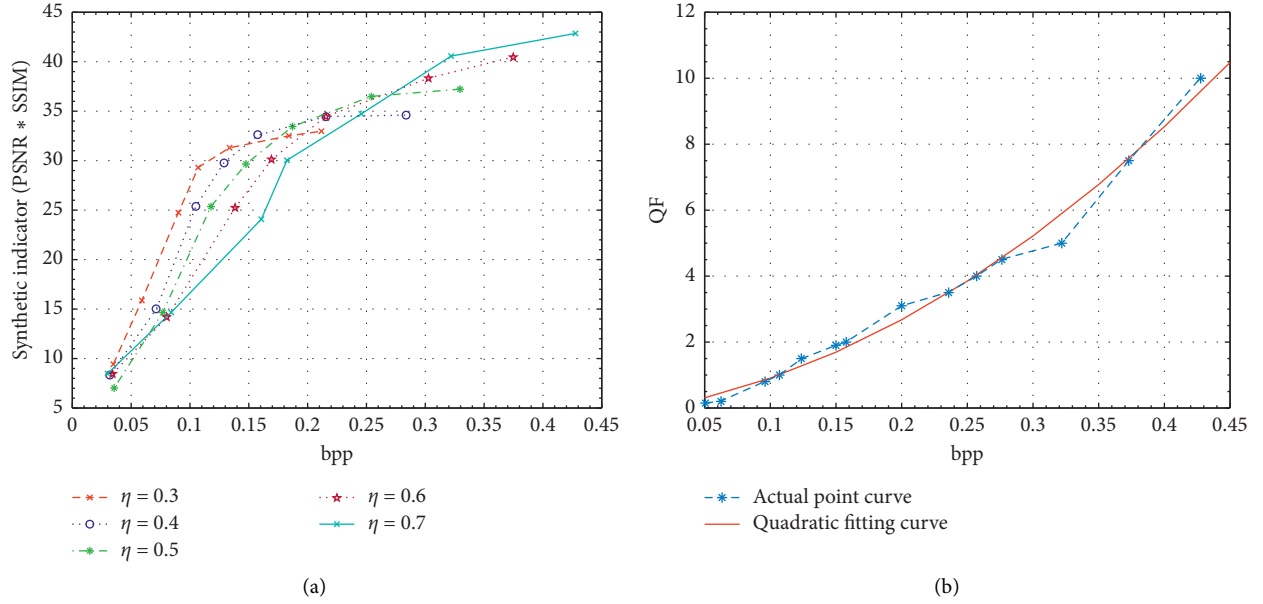


FIGURE 4: Optimization of mean sampling rate (η) and quality factor (QF) in terms of bpp. (a) Impact of mean sampling rate (η) on image quality. (b) Comparison of the actual optimal value of QF with the value calculated by equation (15).

$$\begin{aligned}
 e_{\mathbf{x}_i} &= \frac{1}{n} \left\| (\mathbf{x}_i - \tilde{\mathbf{x}}_i) + (\tilde{\mathbf{x}}_i - \mathbf{x}_i^*) \right\|_2^2 \\
 &= \frac{1}{n} \left\| -\Phi_i^+ \mathbf{w}_i + (\mathbf{I} - \Psi_{i,v} \Omega_{i,v}^+ \Phi_i) \tilde{\mathbf{x}}_i \right\|_2^2 \\
 &= \frac{1}{n} \left\| -\Psi_{i,v} \Omega_{i,v}^+ \mathbf{w}_i + (\mathbf{I} - \Psi_{i,v} \Omega_{i,v}^+ \Phi_i) \mathbf{x}_i \right\|_2^2 \\
 &= \frac{1}{n} \left\| \mathbf{G}_{\mathbf{x}_i} \mathbf{x}_i - \mathbf{G}_{\mathbf{w}_i} \mathbf{w}_i \right\|_2^2,
 \end{aligned} \tag{19}$$

$$\begin{cases} \mathbf{G}_{\mathbf{x}_i} = \mathbf{I} - \Psi_{i,v} \Omega_{i,v}^+ \Phi_i, \\ \mathbf{G}_{\mathbf{w}_i} = \Psi_{i,v} \Omega_{i,v}^+, \end{cases} \tag{20}$$

where $\mathbf{G}_{\mathbf{x}_i}$ is a projection matrix of rank $n - v_i$ and $\mathbf{G}_{\mathbf{w}_i}$ is a projection matrix of rank v_i . Since $\mathbf{G}_{\mathbf{x}_i}$ and $\mathbf{G}_{\mathbf{w}_i}$ satisfy orthogonality, the inner product of $\mathbf{G}_{\mathbf{x}_i} \mathbf{x}_i$ and $\mathbf{G}_{\mathbf{w}_i} \mathbf{w}_i$ is equal to zero. Therefore, equation (19) can be transformed into the following form:

$$e_{\mathbf{x}_i} = \frac{1}{n} \left\| \mathbf{G}_{\mathbf{x}_i} \mathbf{x}_i - \mathbf{G}_{\mathbf{w}_i} \mathbf{w}_i \right\|_2^2 = \frac{1}{n} \left\| \mathbf{G}_{\mathbf{x}_i} \mathbf{x}_i \right\|_2^2 + \frac{1}{n} \left\| \mathbf{G}_{\mathbf{w}_i} \mathbf{w}_i \right\|_2^2 = e_{\mathbf{x}_i}^a + e_{\mathbf{x}_i}^b. \tag{21}$$

Equation (21) reveals that the reconstruction error ($e_{\mathbf{x}_i}$) is composed of the algorithm error ($e_{\mathbf{x}_i}^a$) and the noise error ($e_{\mathbf{x}_i}^b$). $e_{\mathbf{x}_i}^a$ decreases as the reconstruction sparsity (v_i) increases, and $e_{\mathbf{x}_i}^b$ increases with the reconstruction sparsity (v_i) [25, 26]. Therefore, reconstruction error and reconstruction sparsity are a bias-variance trade-off, and there must be an optimal reconstruction sparsity (v_i^{opt}) that minimizes the reconstruction error ($e_{\mathbf{x}_i}$):

$$v_i^{\text{opt}} = \arg \min_{v_i} \{e_{\mathbf{x}_i}\} = \arg \min_{v_i} \left\{ \frac{1}{n} \left\| \mathbf{G}_{\mathbf{x}_i} \mathbf{x}_i \right\|_2^2 + \frac{1}{n} \left\| \mathbf{G}_{\mathbf{w}_i} \mathbf{w}_i \right\|_2^2 \right\}. \tag{22}$$

Figure 5 shows the relationship between reconstruction sparsity and reconstruction error under different noise conditions by using a modified Lena test image. The modified Lena image is generated by intercepting 60 sparse coefficients under a discrete cosine basis; that is, its original sparsity (K) is 60. The noise added in the test is zero-mean Gaussian white noise, and its standard deviation ($\sigma_w = \text{noise} - \text{std}$) also represents the intensity of the noise. The indicator PSNR is used to characterize the size of the reconstruction error. It can be seen from Figure 5 that the optimal reconstruction sparsity decreases as the noise intensity increases and is less than the original sparsity ($v_i^{\text{opt}} \leq K$).

From the verification experiment shown in Figure 5, we can see that there is indeed an optimal reconstruction sparsity in the reconstruction process under the noise background. However, equation (22) is not a feasible solution that can be directly used to optimize the reconstruction process. In the actual reconstruction process, only the observation data at the receiving end can be used for the optimization algorithm. Therefore, this paper designs a solution that uses observation data to optimize the reconstruction sparsity.

According to the definition of CS, the measurement matrix (Φ_i) obeys the RIP criteria, and therefore

$$\begin{cases} (1 - \delta_K) e_{\mathbf{x}_i} \leq e_{\mathbf{y}_i} \leq (1 + \delta_K) e_{\mathbf{x}_i}, \\ e_{\mathbf{y}_i} = \frac{1}{m_i} \left\| \mathbf{y}_i - \mathbf{y}_i^* \right\|_2^2 = \frac{1}{m_i} \left\| \Phi_i (\mathbf{x}_i - \mathbf{x}_i^*) \right\|_2^2, \end{cases} \tag{23}$$

where δ_K is a coefficient related to Φ_i and K , and $e_{\mathbf{y}_i}$ is the reconstruction error of observation data. The transformation of formula (23) can get the boundaries of the original data reconstruction error as follows:

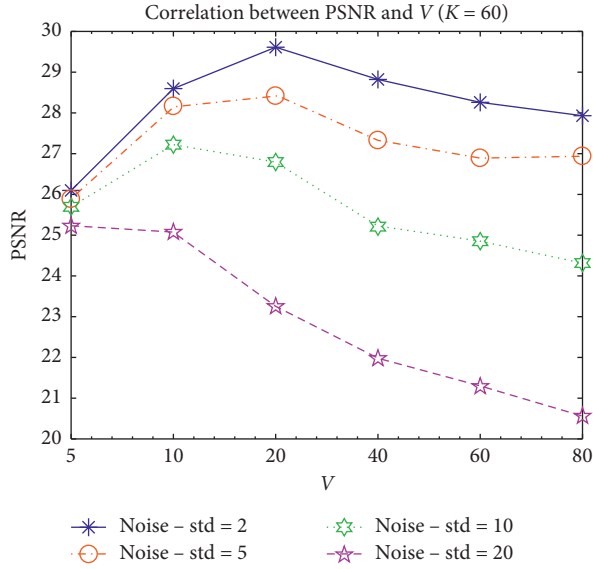


FIGURE 5: Testing the correlation between PSNR and v_i using modified Lena as a test image.

$$\frac{e_{y_i}}{(1 + \delta_K)} \leq e_{x_i} \leq \frac{e_{y_i}}{(1 - \delta_K)}. \quad (24)$$

It can be seen from the above two equations that the reconstruction errors of the original data and the observation data are consistent, so the reconstruction sparsity can be optimized by minimizing the errors of the observation data:

$$\begin{aligned} v_i^{\text{opt}} &= \arg \min_{v_i} \{e_{y_i}\} = \arg \min_{v_i} \left\{ \frac{1}{m_i} \|\mathbf{y}_i - \mathbf{y}_i^*\|_2^2 \right\} \\ &= \arg \min_{v_i} \left\{ \frac{1}{m_i} \|C_{y_i} \mathbf{y}_i\|_2^2 + \frac{1}{m_i} \|C_{w_i} \mathbf{w}_i\|_2^2 \right\}, \\ &\begin{cases} C_{y_i} = \mathbf{I} - \mathbf{\Omega}_{i,v} \mathbf{\Omega}_{i,v}^+, \\ C_{w_i} = \mathbf{\Omega}_{i,v} \mathbf{\Omega}_{i,v}^+, \end{cases} \end{aligned} \quad (25)$$

$$\frac{m_i}{\sigma_w^2} e_{y_i} \sim \chi_{v_i}^2.$$

It is known from the above equation that the reconstruction errors of the observation signal satisfies the chi-square distribution, so the upper and lower boundary of e_{y_i} can be derived from the chi-square distribution probability. In addition, when calculating the minimum value of e_{y_i} , the worst condition is considered, that is, by calculating the minimum value of the upper bound of e_{y_i} .

In the l_0 norm reconstruction algorithm of CS, the reconstruction sparsity is equal to the number of iterations. Therefore, optimizing the number of iterations can reduce the noise impact on image quality in using orthogonal matching pursuit (OMP) as the signal recovery algorithm [27, 28]. According to the Bayesian information criterion (the tuning parameters of confidence probability and effective probability are taken as $\sqrt{v_i} \log m$ and 0, respectively)

[29], the optimal value of iteration number v_i^{opt} can be achieved by minimizing the noise influence:

$$v_i^{\text{opt}} = \arg \min_{v_i} \left\{ \left(\frac{(2 + \sqrt{2} \log_2 m_i) \times v_i}{m_i} - 1 \right) \sigma_w^2 + e_{y_i} \right\}, \quad (26)$$

where $e_{y_i} = (1/m_i) \|\tilde{\mathbf{y}}_i - \mathbf{y}_i^*\|_2^2 = (1/m_i) \|\tilde{\mathbf{y}}_i - \Phi_i \mathbf{x}_i^*\|_2^2$ is the noise error of observation data.

4.5. Pseudocode of JPEG-ABCS. The JPEG lifting algorithm (JPEG-ABCS) described in this article mainly consists of the above four sections, except for the entropy codec, and its full pseudocode is shown in Algorithm 1.

5. Experiment and Result Analysis

In order to verify the superiority of the JPEG-ABCS algorithm, experiments were conducted in two cases: noiseless and noisy. Standard JPEG and JPEG2000 algorithms were used as comparison algorithms, and multiple grayscale standard images with 256×256 resolution were used in the following experiments which were conducted in the simulation software environment of Matlab2016b. In order to objectively evaluate the performance of the algorithm, peak signal-to-noise ratio (PSNR) and structural similarity (SSIM) were introduced as image reconstruction evaluation indexes.

The PSNR index is the most widely used objective standard for characterizing the quality of reconstructed images:

$$\text{PSNR} = 20 \times \log_{10} \left(\frac{255}{\sqrt{(1/N) \sum_{i=1}^N [\mathbf{x}(i) - \mathbf{x}^*(i)]^2}} \right), \quad (27)$$

where $\mathbf{x}(i)$ and $\mathbf{x}^*(i)$ are the i -th element of the original image signal and the reconstructed original image signal, respectively.

The SSIM is another common signal reconstruction quality evaluation index used to describe the similarity between the original image signal and the reconstructed image signal:

$$\text{SSIM} = \frac{(2\mu_{\mathbf{x}}\mu_{\mathbf{x}^*} + c_1)(2\sigma_{\mathbf{x}\mathbf{x}^*} + c_2)}{(\mu_{\mathbf{x}}^2 + \mu_{\mathbf{x}^*}^2 + c_1)(\sigma_{\mathbf{x}}^2 + \sigma_{\mathbf{x}^*}^2 + c_2)}, \quad (28)$$

where $\mu_{\mathbf{x}}$ and $\mu_{\mathbf{x}^*}$ are the average gray value of all elements in \mathbf{x} and \mathbf{x}^* , $\sigma_{\mathbf{x}}$ and $\sigma_{\mathbf{x}^*}$ are the standard deviation of all elements in \mathbf{x} and \mathbf{x}^* , $\sigma_{\mathbf{x}\mathbf{x}^*}$ is the covariance of \mathbf{x} and \mathbf{x}^* , $c_1 = 0.01 \times H^2$ and $c_2 = 0.03 \times H^2$ are the constants, and $H = h_{\text{max}} - h_{\text{min}}$ is the range of pixel gray values.

5.1. Experiments and Analysis without Noise. The experiments under noiseless condition is mainly divided into three parts.

5.1.1. Effectiveness Experiment about Reducing bpp of JPEG Image by MIE Minimization Adaptive Blocking. In order to verify the effectiveness of the proposed MIE

minimization adaptive blocking method, this paper has conducted experiments on two standard images (Lena and Parrots), whose MIE under different blocks is known in the above section, and the experimental data are recorded in Table 1. The basic JPEG algorithm is used in the experiment, and the quantization matrix (light-table) is generated using formula (15), where QF is 50 and 25, respectively.

From the data in Table 1, it can be seen that the Lena and Parrots recovery images have the minimum bpp in the block shape of 16×4 and 8×8 , which just coincides with the minimum MIE block in the above section.

5.1.2. Verification Experiment of ASM-Based Adaptive Vectorization to Improve the 2D Image Reconstruction Performance in BCS Algorithm. The application of CS to image signal processing requires vectorization of two-dimensional images. Therefore, the proposed JPEG-ABCS algorithm also needs to vectorize the subimages. Different vectorization methods directly affect the reconstruction quality of the image.

In this article, three common vectorization methods (vertical scanning, 2D scanning, and zigzag scanning) are compared and analyzed. The verification experiment is carried out in the CS algorithm, using two kinds of images (standard test image and texture test image) to test under different blocking and sampling rates. The experimental data are recorded in Tables 2 and 3, respectively.

It can be seen from Table 2 that for standard test images that meet ASM conditions 1 or 2, vectorization using 2D scanning is optimal, and its PSNR and SSIM of the reconstructed image have a relative advantage than the other two methods.

Table 3 shows the results of texture test image reconstruction using three vectorization methods. Obviously, the vector generation using zigzag scanning has better performance at this case.

It can be seen from the above tables that for different types of test images, the use of a single mode of the vector generation method cannot always effectively improve the quality of image reconstruction, and the multimode method combined with image texture direction feature detection is recommended. Therefore, this paper proposes an adaptive vectorization method based on ASM to maximize the performance of 2D image reconstruction in the BCS algorithm.

5.1.3. Performance Comparison of Various JPEG-Like Algorithms. The image reconstruction quality of the three algorithms was compared with each other under noiseless condition to verify the benefit and universality of the proposed JPEG-ABCS. The experiment includes two parts: verification under different bpp and different test images. Figure 6 shows the experimental results of the Lena test image under three JPEG-like algorithms. Figures 6(a) and 6(b) show that compared with the JPEG and JPEG2000 algorithms, the proposed algorithm has advantages in PSNR and SSIM indicators under different

bpp conditions. Furthermore, from the transformation trend of the curve, it can be seen that the JPEG-ABCS algorithm has good performance at medium and high bit rates, but as the bit rate decreases, the performance of the algorithm proposed in this article has declined, the main reason is that as the dimension of the measurement matrix decreases with bpp, the observation process cannot cover all the information of the image. Figure 6(c) is the restored grayscale images of Lena using the three algorithms under 0.25 bpp condition. It can be seen from a subjective vision that JPEG-ABCS's performance is better than the other two algorithms.

In addition, Table 4 records the experimental results of the three algorithms for different images under the condition of $\text{bpp} = 0.25, 0.3, \text{ and } 0.4$. The data in the table show that the improvement effect of the proposed algorithm is universal for different images. For instance, at the condition of $\text{bpp} = 0.3$, the PSNR index of the four standard test images under the JPEG-ABCS algorithm is improved by 8.34%, 15.09%, 4.46%, and 8.13% compared to the JPEG algorithm and 6.19%, 12.98%, 3.39%, and 6.39% compared to the JPEG2000 algorithm, respectively; the SSIM index has also been improved, compared to JPEG it increased by 0.96%, 0.88%, 1.22%, and 0.59% and compared to JPEG2000 it increased by 0.62%, 0.64%, 0.84%, and 0.30%.

As can be seen from Figure 6 and Table 4, compared to the JPEG and JPEG2000 algorithms, the proposed JPEG-ABCS algorithm has a large improvement on PSNR and SSIM, mainly due to the adaptive blocking and adaptive sampling reducing MIE of image blocks under the same conditions, while sparse restoration guarantees image restoration quality.

5.2. Experiments and Analysis under Gaussian Noisy Conditions. In the Gaussian noise condition, it is verified that the JPEG-ABCS algorithm has improved antinoise performance compared to the standard JPEG algorithm. Figure 7 shows the experimental results which are obtained by using the monarch, peppers, and cameraman as test images. It can be clearly seen from Figure 7 that the test images reconstructed using JPEG-ABCS are superior to the test images reconstructed by JPEG in different noise intensities (here, the noise standard deviation is used as the noise intensity), especially the more noise intensity, the more obvious the superiority.

Table 5 shows the PSNR and SSIM comparison records of the noisy monarch test image under two different algorithms. As can be seen from the data in Table 5, the noisy image reconstruction performance of the JPEG-ABCS algorithm under different bpp conditions is better than that of the JPEG algorithm. For example, at the condition of $\text{bpp} = 0.25$, the PSNR index of the JPEG-ABCS algorithm under the four noise intensities is improved by 9.68%, 4.25%, 0.74%, and 3.06% compared to the JPEG algorithm; the SSIM index has also been improved, compared to JPEG by 4.54%, 3.69%, 1.53%, and 7.71%. In other words, JPEG-ABCS adds antinoise capability that the JPEG algorithm does not have.


```

(1) Input:
    Original image  $\mathbf{I}$ ; rate control bpp;
    Subimage dimension  $n = 64$ ;
(2) Initialization:
     $(R, C) = \text{size of } (\mathbf{I}); N = R \times C$ ;
     $T_1 = (N/n)$ ; //quantity of subimages
     $T_2 = 1 + \log_2 n$ ; //type number of adaptive blocking
    //step1: adaptive blocking and vectorization
(3) for  $j = 1, \dots, T_2$  do
(4)    $r_j \times c_j = 2^{j-1} \times 2^{T_2-j}$ ;
(5)    $\{\mathbf{I}_i \mid \text{size of } (\mathbf{I}_i) = r_j \times c_j, i = 1, \dots, T_1\} \leftarrow \mathbf{I}$ 
(6)    $\{\mathbf{x}_i, i = 1, \dots, T_1\}_j \leftarrow \{\mathbf{I}_i, i = 1, \dots, T_1\}_j$ ;
(7)    $\mathcal{G}_{\text{MIE}}^j = \text{MIE}(\{\mathbf{x}_i, i = 1, \dots, T_1\}_j)$ ;
(8) end for
(9)  $j_{\text{opt}} = \arg \min_j (\{\mathcal{G}_{\text{MIE}}^j, j = 1, \dots, T_2\})$ ;
(10)  $r \times c = 2^{j_{\text{opt}}-1} \times 2^{T_2-j_{\text{opt}}}$ ;
(11)  $\{\mathbf{I}_i \mid \text{size of } (\mathbf{I}_i) = r \times c, i = 1, \dots, T_1\} \leftarrow \mathbf{I}$ ;
(12)  $\{\mathcal{G}_{\text{ASM}}^0, \mathcal{G}_{\text{ASM}}^{45}, \mathcal{G}_{\text{ASM}}^{90}, \mathcal{G}_{\text{ASM}}^{135}\} \leftarrow \mathbf{I}$ 
(13) if  $(\mathcal{G}_{\text{ASM}}^0 \times \mathcal{G}_{\text{ASM}}^{90} \geq \mathcal{G}_{\text{ASM}}^{45} \times \mathcal{G}_{\text{ASM}}^{135})$ ;
(14)   if  $(\mathcal{G}_{\text{MAX}} = \mathcal{G}_{\text{ASM}}^0)$  //Condition = 1
(15)      $\{\mathbf{x}_i, i = 1, \dots, T_1\}^1 \leftarrow \{\mathbf{I}_i, i = 1, \dots, T_1\}$ ;
     //1  $\leftarrow$  : horizontal scanning and vertical linking
(16)   else if  $(\mathcal{G}_{\text{MAX}} = \mathcal{G}_{\text{ASM}}^{90})$  //Condition = 2
(17)      $\{\mathbf{x}_i, i = 1, \dots, T_1\}^2 \leftarrow \{\mathbf{I}_i, i = 1, \dots, T_1\}$ ;
     //2  $\leftarrow$  : vertical scanning and horizontal linking
(18)   end if
(19)   else if  $(\mathcal{G}_{\text{ASM}}^0 \times \mathcal{G}_{\text{ASM}}^{90} < \mathcal{G}_{\text{ASM}}^{45} \times \mathcal{G}_{\text{ASM}}^{135})$ 
(20)     if  $(\mathcal{G}_{\text{MAX}} = \mathcal{G}_{\text{ASM}}^{45})$  //Condition = 3
(21)        $\{\mathbf{x}_i, i = 1, \dots, T_1\}^3 \leftarrow \{\mathbf{I}_i, i = 1, \dots, T_1\}$ ;
       //3  $\leftarrow$  : zigzag along the main diagonal direction
(22)     else if  $(\mathcal{G}_{\text{MAX}} = \mathcal{G}_{\text{ASM}}^{135})$  //Condition = 4
(23)        $\{\mathbf{x}_i, i = 1, \dots, T_1\}^4 \leftarrow \{\mathbf{I}_i, i = 1, \dots, T_1\}$ ;
       //4  $\leftarrow$  : zigzag along the counter-diagonal direction
(24)     end if
(25)   end if
    //step2: adaptive observing and bit rate control
(26) for  $i = 1, \dots, T_1$  do
(27)    $J_1(\mathbf{x}_i) \leftarrow \mathbf{x}_i$ ;  $J_2(\mathbf{x}_i) \leftarrow \mathbf{I}_i$ ;
(28)    $J(\mathbf{x}_i) = \gamma \log_2 (J_1(\mathbf{x}_i)^\alpha \cdot J_2(\mathbf{x}_i)^\beta)$ ;
     //synthetic feature ( $J$ )
(29) end for
(30)  $\{\lambda_i, i = 1, \dots, T_1\} = (\log_2 J(\{\mathbf{x}_i, i = 1, \dots, T_1\}) / (1/T_1) \sum_{i=1}^{T_1} \log_2 J(\mathbf{x}_i))$ ;
(31)  $\eta \leftarrow$  equation (14) bpp;
(32)  $\{\eta_i, i = 1, \dots, T_1\} = \{\lambda_i, i = 1, \dots, T_1\} \times \eta$ ;
     // $\eta_i$  -- sampling ratio of subimages
(33)  $\{m_i, i = 1, \dots, T_1\} = \{\eta_i, i = 1, \dots, T_1\} \times n$ ;
(34)  $\{\widehat{m}_i, i = 1, \dots, T_1\} \leftarrow \{m_i, i = 1, \dots, T_1\} \& m_{\min} \& m_{\max}$ 
     //prevent undersampling and oversampling
(35)  $\Gamma = \text{OSTM}(n), \chi_i = \text{randperm}(n), \Gamma_{\chi_i} = \Gamma(\chi_i, :)$ ;
(36)  $\{\Phi_i, i = 1, \dots, T_1\} = \left\{ \sqrt{n/\widehat{m}_i} \Phi_{\chi_i}([1, \dots, \widehat{m}_i], :), i = 1, \dots, T_1 \right\}$ ;
(37)  $\{\mathbf{y}_i, i = 1, \dots, T_1\} \leftarrow$  equation (16)  $\{\Phi_i \mathbf{x}_i, i = 1, \dots, T_1\} \& \sigma_w$ ;
     // $\sigma_w = 0$ : noiseless;  $\sigma_w \neq 0$ : noise
(38) light - table  $\leftarrow$  equation (15) QF  $\leftarrow$  equation (15) bpp;
(39)  $\{\mathbf{y}_i^q, i = 1, \dots, T_1\} \leftarrow$  light - table  $\& \{\mathbf{y}_i, i = 1, \dots, T_1\}$ 
    //step3: codec and anti-quantization
(40) Bit Stream  $\leftarrow \{\mathbf{y}_i^q, i = 1, \dots, T_1\} \& \text{RLC encoding}$ 
(41)  $\{\widehat{\mathbf{y}}_i^q, i = 1, \dots, T_1\} \leftarrow$  Bit Stream  $\& \text{RLC decoding}$ 
(42)  $\{\widehat{\mathbf{y}}_i, i = 1, \dots, T_1\} \leftarrow$  light - table  $\& \{\widehat{\mathbf{y}}_i^q, i = 1, \dots, T_1\}$ 

```

```

//step4: reconstruction and denoising
(43) if Condition == 1
(44)    $\Psi = \text{kron}(\mathbf{D}_c^T, \mathbf{D}_r^T)$ 
(45) else if Condition == 2
(46)    $\Psi = \text{kron}(\mathbf{D}_r^T, \mathbf{D}_c^T)$ 
(47) else  $\Psi = \mathbf{D}_n^T$ 
(48) end if
(49)  $\{\Omega_i, i = 1, \dots, T_1\} = \{\Phi_i \Psi, i = 1, \dots, T_1\}$ 
(50) for  $i = 1, \dots, T_1$  do
(51)    $\Omega_i = \{\omega_{i1}, \dots, \omega_{in}\}, r = \hat{y}_i, A = \emptyset, \mathbf{s}^* = \mathbf{0}^n;$ 
// $\{\omega_{ij}, j = 1, \dots, n\}$ -- column vector of  $\Omega_i$ 
(52)    $v_i^{\text{opt}} \leftarrow \text{equation(28)}\{v_i | \text{argmin}_{v_i} \overline{e_{y_i}}\};$ 
//calculate optimal iterative of subimages
(53)   for  $j = 1, \dots, v_i^{\text{opt}}$  do
(54)      $\wedge = \text{argmin}_j |\langle r, \omega_{ij} \rangle|;$ 
(55)      $A = AU\{\wedge\};$ 
(56)      $r = \hat{y}_i - \Omega_i(:, A)[\Omega_i(:, A)]^+ \hat{y}_i;$ 
(57)   end for
(58)    $\mathbf{s}_i^* = [\Omega_i(:, A)]^+ \hat{y}_i;$ 
// $\mathbf{s}_i^*$ : reconstruction sparse representation
(59)    $\mathbf{x}_i^* = \Psi \mathbf{s}_i^*;$ 
// $\mathbf{x}_i^*$ : reconstruction original signal of subimages
(60) end for
(61)  $\mathbf{x}^* = \{\mathbf{x}_i^*, i = 1, \dots, T_1\};$ 
//step5: antivectorization and jointing
(62)  $\mathbf{I}_i^* = \{\mathbf{x}_i^*, r, c\}; \mathbf{I}^* = \{\mathbf{I}_i^* | i = 1, \dots, T_1, \text{size of } (\mathbf{I}^*) = R \times C\}$ 
// $\mathbf{I}^*$ : recovered image with JPEG-ABCS

```

ALGORITHM 1: JPEG-ABCS algorithm based on OMP (orthogonal matching pursuit).

TABLE 1: Effecton of different block shapes on bpp of the JPEG image.

Test image	QF	Correlation between bpp and block shape ($r \times c$)						
		1×64	2×32	4×16	8×8	16×4	32×2	64×1
Lena	50	1.3235	1.2179	0.9351	0.7430	0.7290	0.8324	0.9068
	25	0.8776	0.8304	0.6227	0.4838	0.4733	0.5462	0.5892
Parrots	50	1.1168	0.9629	0.7463	0.6161	0.6498	0.7674	0.8308
	25	0.7104	0.6353	0.4824	0.3988	0.4246	0.4972	0.5403

TABLE 2: Comparison experiments of different vectorization methods on image reconstruction performance using standard test images.

Test image	Verification method		Vertical scanning	2D scanning PSNR/SSIM	Zigzag scanning
	ASM condition	$r \times c$			
Lena	Condition = 2	64×4	30.69/0.8907	32.11/0.9402	30.86/0.8984
		32×8	31.39/0.9150	32.74/0.9477	31.31/0.9138
		16×16	31.72/0.9227	32.87/0.9470	31.73/0.9261
		8×32	31.68/0.9248	32.02/0.9325	31.72/0.9257
		4×64	31.07/0.9221	31.64/0.9321	30.78/0.9175
		64×4	29.12/0.8783	29.71/0.9211	29.14/0.8787
Goldhill	Condition = 1	32×8	29.45/0.8977	30.21/0.9251	29.38/0.8923
		16×16	29.83/0.9134	30.35/0.9335	29.95/0.9146
		8×32	30.02/0.9113	30.28/0.9288	30.13/0.9192
		4×64	29.98/0.9102	30.17/0.9191	29.87/0.9112
		64×4	29.73/0.9031	30.90/0.9547	29.70/0.9034
		32×8	30.09/0.9068	31.67/0.9585	30.20/0.9158
Peppers	Condition = 2	16×16	30.77/0.9309	32.02/0.9638	30.76/0.9293
		8×32	30.91/0.9413	31.36/0.9565	30.60/0.9325
		4×64	30.38/0.9421	30.63/0.9506	30.38/0.9418

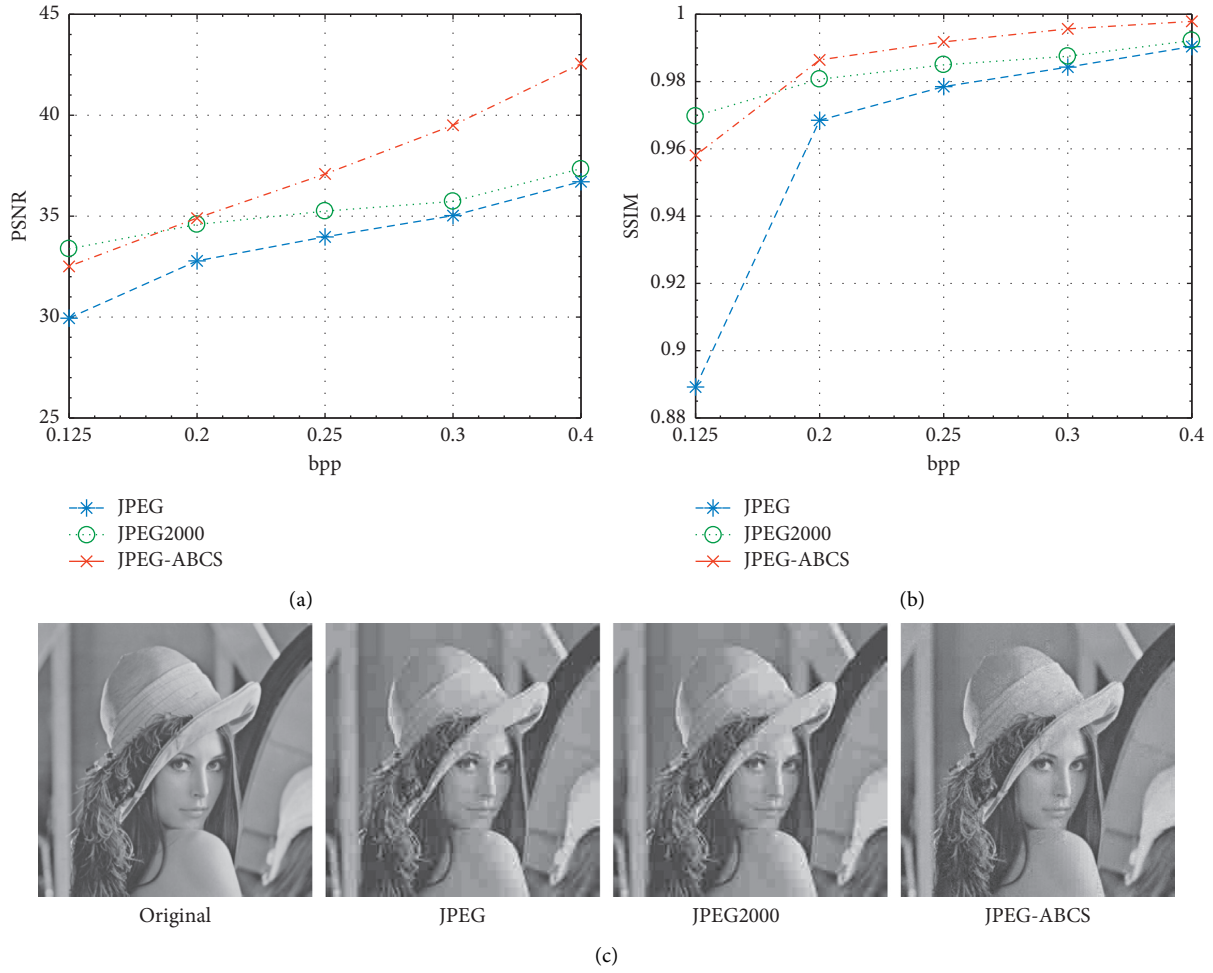
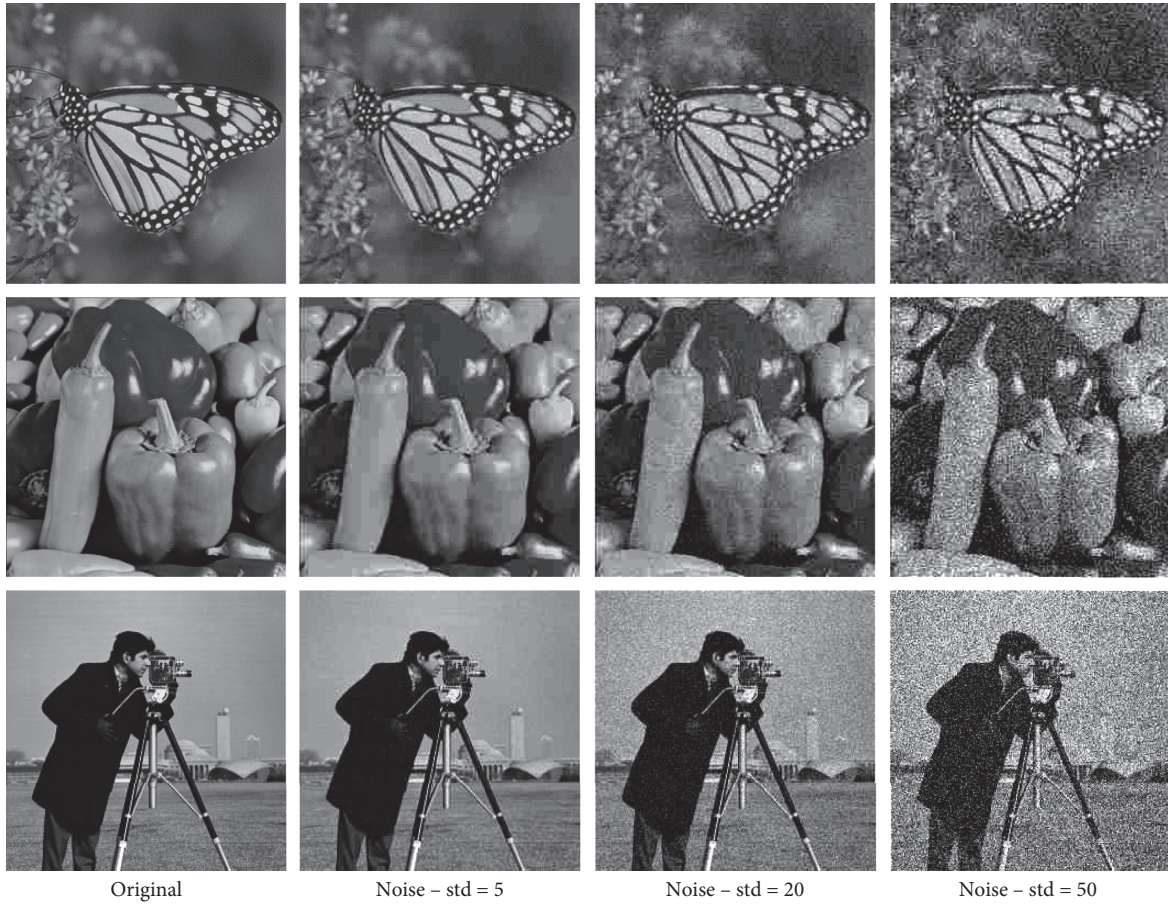


FIGURE 6: Comparative experiment of the three JPEG-like algorithms using Lena as a test image. (a) PSNR of the three algorithms in terms of different bpp. (b) SSIM of the three algorithms in terms of different bpp. (c) Restored images generated by three JPEG-like algorithms (bpp = 0.25).

TABLE 3: Comparison experiments of different vectorization methods on image reconstruction performance using texture test images.

Verification method			Vertical scanning	2D scanning	Zigzag scanning
Test image	η	$r \times c$		PSNR/SSIM	
	0.3	32 × 8	30.92/0.7101	31.52/0.7461	32.43/0.8244
		16 × 16	31.50/0.7620	32.04/0.7878	33.06/0.8407
		8 × 32	31.39/0.7433	31.54/0.7439	32.55/0.8291
	0.4	32 × 8	32.05/0.8195	32.51/0.8276	33.97/0.8846
		16 × 16	32.53/0.8430	32.91/0.8497	34.01/0.8823
		8 × 32	32.39/0.8377	32.27/0.8256	33.87/0.8851
ASM condition = 4					
	0.3	32 × 8	28.47/0.8046	28.84/0.8715	29.14/0.9033
		16 × 16	28.62/0.8179	29.01/0.8834	29.17/0.8967
		8 × 32	28.53/0.8113	28.90/0.8740	29.25/0.9119
ASM Condition = 3	0.4	32 × 8	28.84/0.8659	29.44/0.9261	29.69/0.9365
		16 × 16	29.04/0.8817	29.65/0.9329	29.74/0.9353
		8 × 32	29.08/0.8941	29.34/0.9220	29.67/0.9354



(a)

FIGURE 7: Continued.

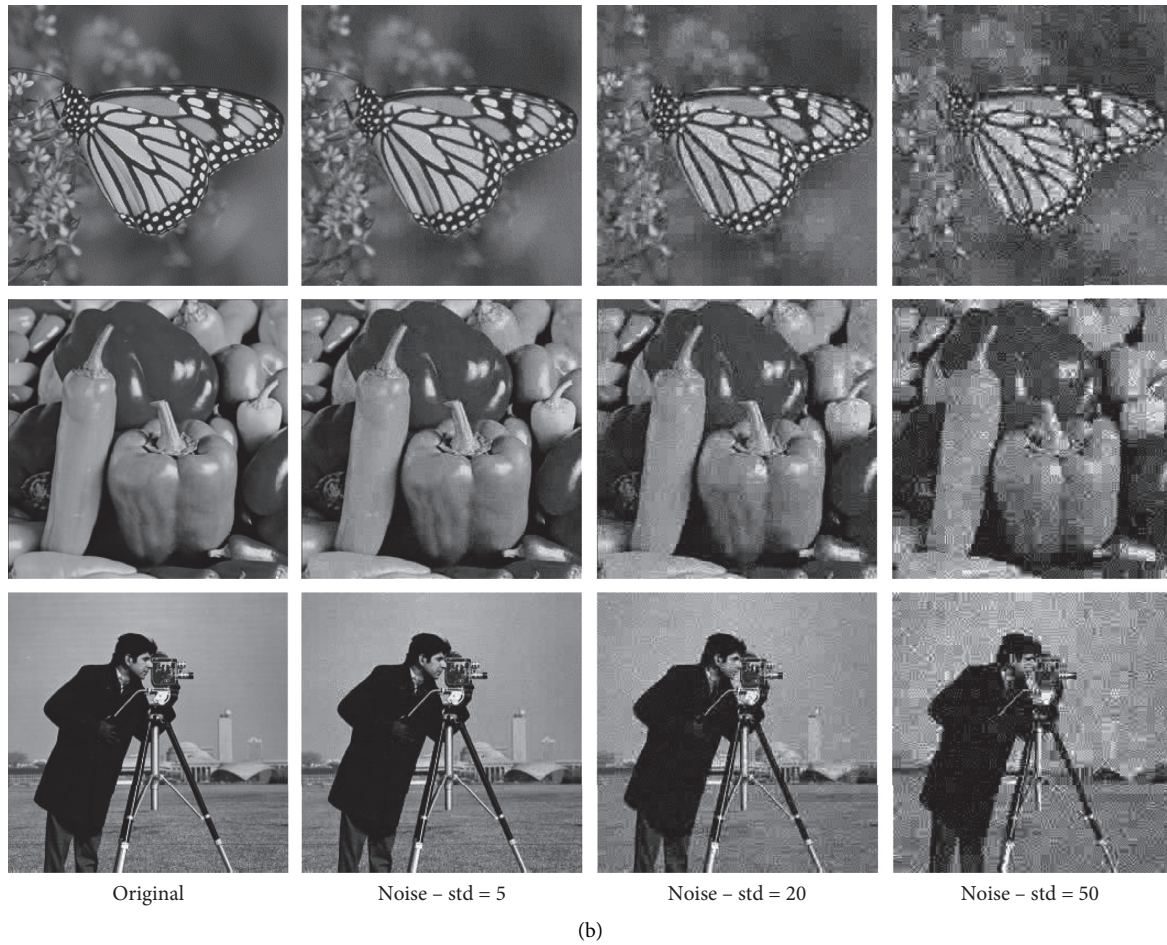


FIGURE 7: Monarch, peppers, and cameraman restored images under different noise intensities (bpp = 0.4). (a) Using the JPEG algorithm. (b) Using the JPEG-ABCS algorithm.

TABLE 4: Performance comparison of the three algorithms in terms of different test images.

Test image		Lena	Peppers	PSNR/SSIM		Parrots
				Goldhill	Parrots	
bpp = 0.25	JPEG	33.97/0.9785	33.17/0.9845	31.62/0.9685	35.80/0.9882	
	JPEG2000	35.25/0.9850	34.32/0.9887	32.05/0.9718	36.52/0.9923	
	JPEG-ABCS	37.09/0.9918	37.42/0.9962	32.29/0.9767	39.38/0.9966	
bpp = 0.3	JPEG	35.02/0.9842	34.25/0.9890	32.09/0.9729	36.79/0.9912	
	JPEG2000	35.73/0.9875	34.89/0.9914	32.42/0.9766	37.39/0.9940	
	JPEG-ABCS	37.94/0.9936	39.42/0.9977	33.52/0.9848	39.78/0.9970	
bpp = 0.4	JPEG	36.63/0.9902	35.76/0.9934	32.72/0.9789	38.27/0.9944	
	JPEG2000	37.33/0.9922	36.33/0.9945	32.84/0.9814	39.11/0.9963	
	JPEG-ABCS	42.01/0.9976	41.36/0.9985	33.84/0.9868	42.78/0.9985	

TABLE 5: PSNR and SSIM of the monarch restored image using JPEG and JPEG-ABCS under different noise intensities.

Method	Condition	Noise – std = 5	Noise – std = 10	Noise – std = 20	Noise – std = 50
JPEG	bpp = 0.25	32.14/0.9452	32.03/0.9432	31.05/0.9309	28.39/0.7677
	bpp = 0.3	32.73/0.9601	32.45/0.9576	30.85/0.9387	28.27/0.7459
	bpp = 0.4	33.69/0.9726	32.94/0.9671	30.84/0.9373	28.44/0.7820
JPEG-ABCS	bpp = 0.25	35.25/0.9881	33.39/0.9780	31.28/0.9451	29.26/0.8269
	bpp = 0.3	36.48/0.9921	33.68/0.9803	31.46/0.9488	29.27/0.8245
	bpp = 0.4	36.74/0.9925	33.82/0.9809	31.43/0.9488	29.31/0.8290

The main reason for the above improvement is that the algorithm itself considers the noise model in the reconstruction algorithm and adds the idea of iterative optimization.

6. Conclusions

In this paper, a JPEG lifting algorithm based on ABCS was proposed, and its structure and implementation method were specifically introduced. At the same time, the improvements of the algorithm were described, and the feasibility and rationality of the above improvements were demonstrated by experiments. Finally, through comparison experiments with similar algorithms, the contribution of this lifting algorithm to JPEG-like algorithms, that is, to improve the quality of image reconstruction, reduce bit rate (bpp), and add the antinoise function has been evaluated

Data Availability

The simulation results used to support the findings of this study are included within the article.

Conflicts of Interest

The authors declare that there are no conflicts of interest regarding the publication of this paper.

Acknowledgments

This research was supported by the National Key Research and Development Program of the Ministry of Science and Technology of China (2018YFB2003304), the National Natural Science Foundation of China under Grant (61471191), and the Youth Program of the National Natural Science Foundation of China (31700478).

References

- [1] K. W. Gregory, "The JPEG still picture compression standard," *Communications of the ACM*, vol. 38, no. 1, pp. 18–34, 1992.
- [2] C. Christopoulos, A. Skodras, and T. Ebrahimi, "The JPEG2000 still image coding system: an overview," *IEEE Transactions on Consumer Electronics*, vol. 46, no. 4, pp. 1103–1127, 2000.
- [3] F. Dufaux, G. J. Sullivan, and T. Ebrahimi, "The JPEG XR image coding standard [standards in a nutshell]," *IEEE Signal Processing Magazine*, vol. 26, no. 6, pp. 195–204, 2009.
- [4] S. Yuan and J. Hu, "Research on image compression technology based on Huffman coding," *Journal of Visual Communication and Image Representation*, vol. 59, pp. 33–38, 2019.
- [5] D. L. Donoho, "Compressed sensing," *IEEE Transactions on Information Theory*, vol. 52, no. 4, pp. 1289–1306, 2006.
- [6] Y. Zhou and H. Guo, "Collaborative block compressed sensing reconstruction with dual-domain sparse representation," *Information Sciences*, vol. 472, pp. 77–93, 2019.
- [7] S. H. Liu, J. B. Jia, and Y. J. Yang, "Image reconstruction algorithm for electrical impedance tomography based on block sparse Bayesian learning," in *Proceedings of the 2017 IEEE International Conference on Imaging Systems and Techniques*, IEEE, Beijing, China, pp. 267–271, October 2017.
- [8] P. Mazumdar, K. Lamichhane, M. Carli, and F. Battisti, "A feature integrated saliency estimation model for omnidirectional immersive images," *Electronics*, vol. 8, no. 12, p. 1538, 2019.
- [9] S. Mahdi, Y. R. Tohid, A. T. Mohammad et al., "Block sparse signal recovery in compressed sensing: optimum active block selection and within-block sparsity order estimation," *Theory Circuits System Signal Process*, vol. 37, no. 4, pp. 1649–1668, 2018.
- [10] Y. Niu, B. Tondi, Y. Zhao, and M. Barni, "Primary quantization matrix estimation of double compressed JPEG images via CNN," *IEEE Signal Processing Letters*, vol. 27, pp. 191–195, 2020.
- [11] I. Orovic, V. Papic, C. Ioana et al., "Compressive sensing in signal processing: algorithms and transform domain formulations," *Mathematical Problems in Engineering*, vol. 2016, Article ID 7616393, 16 pages, 2016.
- [12] L. Gan, "Block compressed sensing of natural images," in *Proceedings of the 15th Proceedings of the International Conference on Digital Signal Processing*, pp. 403–406, IEEE, Cardiff, UK, July 2007.
- [13] S. Zhou, Z. Chen, Q. Zhong, and H. Li, "Block compressed sampling of image signals by saliency based adaptive partitioning," *Multimedia Tools and Applications*, vol. 78, no. 1, pp. 537–553, 2019.
- [14] W. Rui, Z. X. Yu, L. F. Du et al., "Saliency-based adaptive block compressive sampling for image signals," *Journal of Image and Graphics*, vol. 18, no. 10, pp. 1255–1260, 2013.
- [15] Z. Zhang, Y. Shi, D. Kong, W. Ding, and B. Yin, "Image decoding optimization based on compressive sensing," *Journal of Computational and Applied Mathematics*, vol. 236, no. 5, pp. 812–818, 2011.
- [16] F. Wen, J. Shi, and Z. Zhang, "Joint 2D-DOD, 2D-DOA, and polarization angles estimation for bistatic EMVS-MIMO radar via PARAFAC analysis," *IEEE Transactions on Vehicular Technology*, vol. 69, no. 2, pp. 1626–1638, 2020.
- [17] F. Q. Wen and J. P. Shi, "Fast direction finding for bistatic EMVS-MIMO radar without pairing," *Signal Processing*, vol. 173, pp. 34–36, 2020.
- [18] R. M. Haralick, K. Shanmugam, and I. H. Dinstein, "Textural features for image classification," *IEEE Transactions on Systems, Man, and Cybernetics*, vol. SMC-3, no. 6, pp. 610–621, 1973.
- [19] H. Xu, J. Z. Xu, and F. Wu, "Lifting-based directional DCT-Like transform for image coding," *IEEE Transactions on Circuits and Systems for Video Technology*, vol. 17, no. 10, pp. 1325–1335, 2007.
- [20] J. Shen, "Weber's law and weberized TV restoration," *Physica D: Nonlinear Phenomena*, vol. 175, no. 3–4, pp. 241–251, 2003.
- [21] A. Böttcher, "Orthogonal symmetric Toeplitz matrices," *Complex Analysis and Operator Theory*, vol. 2, no. 2, pp. 285–298, 2008.
- [22] Y. Z. Li, S. J. Yao, K. Yang et al., "A high-imperceptibility and histogram-shifting data hiding scheme for JPEG images," *IEEE Access*, vol. 7, pp. 73573–73582, 2003.
- [23] P. A. M. Oliveira, R. S. Oliveira, R. J. Cintra, F. M. Bayer, and A. Madanayake, "JPEG quantisation requires bit-shifts only," *Electronics Letters*, vol. 53, no. 9, pp. 588–590, 2017.
- [24] D. Meng, X. Wang, M. Huang, L. Wan, and B. Zhang, "Robust weighted subspace fitting for DOA estimation via block sparse recovery," *IEEE Communications Letters*, vol. 24, no. 3, pp. 563–567, 2020.

- [25] S. Beheshti and M. A. Dahleh, "Noisy data and impulse response estimation," *IEEE Transactions on Signal Processing*, vol. 58, no. 2, pp. 510–521, 2010.
- [26] M. Brajovic, I. Stankovic, M. Dakovic et al., "Error in the reconstruction of nonsparse images," *Mathematical Problems in Engineering*, vol. 2018, Article ID 4314527, 10 pages, 2018.
- [27] Y. Zhu, W. Liu, and Q. Shen, "Adaptive algorithm on block-compressive sensing and noisy data estimation," *Electronics*, vol. 8, no. 7, p. 753, 2019.
- [28] R. Qi, D. Yang, Y. Zhang, and H. Li, "On recovery of block sparse signals via block generalized orthogonal matching pursuit," *Signal Processing*, vol. 153, pp. 34–46, 2018.
- [29] T. Liu, F. Wen, L. Zhang, and K. Wang, "Off-grid DOA estimation for colocated MIMO radar via reduced-complexity sparse Bayesian learning," *IEEE Access*, vol. 7, pp. 99907–99916, 2019.

Research Article

Improved Shrinkage Estimator of Large-Dimensional Covariance Matrix under the Complex Gaussian Distribution

Bin Zhang ^{1,2}

¹College of Education, Hubei Minzu University, Enshi, Hubei 445000, China

²College of Mathematics, Sichuan University, Chengdu, Sichuan 610064, China

Correspondence should be addressed to Bin Zhang; 2009021@hbmy.edu.cn

Received 29 March 2020; Revised 5 May 2020; Accepted 28 May 2020; Published 7 July 2020

Guest Editor: Jianfeng Li

Copyright © 2020 Bin Zhang. This is an open access article distributed under the Creative Commons Attribution License, which permits unrestricted use, distribution, and reproduction in any medium, provided the original work is properly cited.

Estimating the covariance matrix of a random vector is essential and challenging in large dimension and small sample size scenarios. The purpose of this paper is to produce an outperformed large-dimensional covariance matrix estimator in the complex domain via the linear shrinkage regularization. Firstly, we develop a necessary moment property of the complex Wishart distribution. Secondly, by minimizing the mean squared error between the real covariance matrix and its shrinkage estimator, we obtain the optimal shrinkage intensity in a closed form for the spherical target matrix under the complex Gaussian distribution. Thirdly, we propose a newly available shrinkage estimator by unbiasedly estimating the unknown scalars involved in the optimal shrinkage intensity. Both the numerical simulations and an example application to array signal processing reveal that the proposed covariance matrix estimator performs well in large dimension and small sample size scenarios.

1. Introduction

The problem of estimating the covariance matrix of a random vector arises in both multivariate statistical theory and various applications [1, 2]. In large sample setting, where the dimension of a random vector is small and the sample size is large enough, the sample covariance matrix (SCM) is a reliable estimator of the real covariance matrix and is widely employed in many scenarios. However, suffering from the curse of dimensionality, the SCM becomes ill-conditioned or even singular in large dimension scenarios [3]. Then, severe consequences may appear if the SCM remained as the covariance matrix estimator [4, 5].

During the last two decades, scientists have proposed many regularization strategies to generate outperformed covariance matrix estimators in large dimension scenarios [6–10]. Among these, the linear shrinkage estimation is an effective strategy to inspire a well-conditioned covariance matrix estimator when the dimension is large compared to the sample size [11, 12]. When the prior information of the covariance structure is available, the linear shrinkage

estimator is modeled as a linear combination between the SCM and a proper target matrix. In the existing literature, the target matrices, which are usually formed through structuring the SCM in line with the prior information, include the spherical target and others, such as the diagonal target, the Toeplitz rectified target, and the tapered SCM [13].

With the aid of prior information, the linear shrinkage estimator can always outperform the SCM when the involved tuning parameter is carefully selected [14]. Therefore, one of the crucial difficulties in linear shrinkage estimation is to determine the optimal tuning parameter which is also called as the shrinkage intensity. By minimizing the mean squared error (MSE) between the shrinkage estimator and the real covariance matrix, the optimal tuning parameter can be expressed in a closed form for an arbitrary target. However, it is comprised of unknown scalars which involve the expectation operator and the real covariance matrix, leading to a chief difficulty in generating an available shrinkage estimator. In particular, when the data follow a specific distribution such as Gaussian distribution or

elliptical distribution, the expectation can be further calculated [11]. What is noteworthy is that the optimal tuning parameter owns different expressions under different distributions, even for the same target [15]. Therefore, it is necessary to discover the specific properties of shrinkage intensity under some typical distributions. In many applications, such as array signal processing, the data come from the complex domain. There have been some related research studies on it. In [16], a linear shrinkage estimator for Toeplitz rectified target is developed under the complex Gaussian distribution, whereas the involved unknown scalars in the optimal tuning parameter are not unbiasedly estimated, resulting in a suboptimal covariance matrix estimator [17]. In [18], a linear shrinkage estimator is proposed via low-complexity crossvalidation under an arbitrary complex distribution. Therefore, when the data follow a specific distribution, the linear shrinkage estimator could be further improved by making full use of the distribution information.

In this paper, we further research the linear shrinkage estimator under the complex Gaussian distribution. The target matrix is chosen as the spherical target which has been widely studied under the real number field [6, 11, 14]. The optimal tuning parameter is obtained by minimizing the MSE. We remind that the above optimal tuning parameter involves both the expectation operator and the real covariance matrix. By developing a novel moment property of the complex Wishart distribution, we can calculate the expectation operator. Then, the optimal tuning parameter turns to be only related to some unknown scalars concerning the real covariance matrix. A popular approach is adopted by replacing these unknown scalars with their estimates to obtain an available tuning parameter. Furthermore, good estimates of unknown scalars can benefit the corresponding available tuning parameter and the corresponding shrinkage estimator [11, 19].

The main contributions of this paper are summarized as three-fold:

- (1) A necessary moment property of the complex Wishart distribution is developed. On this basis, the optimal tuning parameter for the spherical target is analytically expressed under the complex Gaussian distribution.
- (2) All the unknown scalars involved in the optimal tuning parameter are unbiasedly estimated. Then, the corresponding available linear shrinkage estimator under the complex Gaussian distribution is proposed.
- (3) The performance of the proposed covariance matrix estimator is verified with comparison to the existing estimators in numerical simulations and an example application to adaptive beamforming.

The rest of this paper is organized as follows: Section 2 formulates the linear shrinkage estimation under the complex Gaussian distribution as a quadratic programming problem. The optimal solution is analytically obtained. Section 3 unbiasedly estimates the relative unknown scalars and subsequently proposes a new shrinkage estimator for the

spherical target. Section 4 provides some numerical simulations and an example application for verifying the performance of the proposed covariance matrix estimator. Section 5 concludes.

1.1. Notations. The notation \mathbb{C}^m is the set of all m -dimensional complex column vectors, and \mathbb{H}^n is the set of all $n \times n$ Hermitian matrices. The symbol \mathbb{E} denotes the mathematical expectation. The bold symbols $\mathbf{0}$ and $\mathbf{1}$ respectively denote the column vectors having all entries 0 and 1 with an appropriate dimension. The symbol \mathbf{I}_n denotes the $n \times n$ identity matrix. For a matrix \mathbf{A} , \mathbf{A}^H and $\|\mathbf{A}\|$ respectively denote its conjugate transpose and Frobenius matrix norm. For a squared matrix \mathbf{A} , \mathbf{A}^{-1} and $\text{tr}(\mathbf{A})$ respectively denote its inverse and trace. For two real numbers a and b , $a \wedge b$ and $a \vee b$ respectively mean the maximum and minimum of a and b .

2. Formulation and the Optimal Solution

Assume a p -dimensional random vector $\mathbf{x} \in \mathbb{C}^p$ follows the complex Gaussian distribution $\mathcal{CN}(\mathbf{0}, \Sigma)$, where Σ is the unknown covariance matrix. Let $\mathbf{x}_1, \mathbf{x}_2, \dots, \mathbf{x}_n \in \mathbb{C}^p$ be an independent and identically distributed (i.i.d.) sample, then the sample covariance matrix \mathbf{S} is defined by

$$\mathbf{S} = \frac{1}{n} \sum_{i=1}^n \mathbf{x}_i \mathbf{x}_i^H. \quad (1)$$

For an arbitrary prespecified target matrix $\mathbf{T} \in \mathbb{H}^p$ which represents an aspect prior information of the real covariance matrix structure [20], the linear shrinkage estimator of covariance matrix Σ is modeled as

$$\hat{\Sigma} = (1 - w)\mathbf{S} + w\mathbf{T}, \quad (2)$$

where $w \in [0, 1]$ is the tuning parameter which is also called shrinkage intensity [21]. Because \mathbf{S} and \mathbf{T} are Hermitian, we have $\hat{\Sigma} \in \mathbb{H}^p$ for an arbitrary $w \in [0, 1]$.

To find the optimal shrinkage intensity, we employ the MSE criterion:

$$\mathcal{M}_{\mathbf{T}}(w) = \mathbb{E}[\|\hat{\Sigma} - \Sigma\|^2] = \mathbb{E}[\|(1 - w)\mathbf{S} + w\mathbf{T} - \Sigma\|^2]. \quad (3)$$

Furthermore, we have

$$\mathcal{M}_{\mathbf{T}}(w) = w^2 \mathbb{E}[\text{tr}(\mathbf{T} - \mathbf{S})^2] - 2w \mathbb{E}[\text{tr}(\mathbf{T} - \mathbf{S})(\Sigma - \mathbf{S})] + c, \quad (4)$$

where $c = \mathbb{E}[\text{tr}(\Sigma - \mathbf{S})(\Sigma - \mathbf{S})^2]$ is a constant. Therefore, the optimal shrinkage intensity can be obtained through solving the following optimization problem:

$$\begin{aligned} \min \quad & w^2 \mathbb{E}[\text{tr}(\mathbf{T} - \mathbf{S})^2] - 2 \mathbb{E}[\text{tr}(\mathbf{T} - \mathbf{S})(\Sigma - \mathbf{S})]w, \\ \text{s.t.} \quad & 0 \leq w \leq 1. \end{aligned} \quad (5)$$

It is worth noticing that the objective function in optimization problem (5) is a convex quadratic function of w , and the optimal shrinkage intensity can be expressed in a closed form as follows:

$$w_0^* = 0 \wedge \frac{\mathbb{E}[\text{tr}(\mathbf{T} - \mathbf{S})(\boldsymbol{\Sigma} - \mathbf{S})]}{\mathbb{E}[\text{tr}(\mathbf{T} - \mathbf{S})^2]} \sqrt{1}. \quad (6)$$

Furthermore, for the spherical target $\mathbf{T} = (\text{tr}(\mathbf{S})/p)\mathbf{I}_p$, the optimal shrinkage intensity w_0^* given by (6) becomes

$$w_1^* = 0 \wedge \frac{(1/p)\text{tr}^2(\boldsymbol{\Sigma}) - \text{tr}(\boldsymbol{\Sigma}^2) + \mathbb{E}[\text{tr}(\mathbf{S}^2)] - (1/p)\mathbb{E}[\text{tr}^2(\mathbf{S})]}{\mathbb{E}[\text{tr}(\mathbf{S}^2)] - (1/p)\mathbb{E}[\text{tr}^2(\mathbf{S})]} \sqrt{1}. \quad (7)$$

Denote the matrix

$$\mathbf{E}_n = \begin{pmatrix} 1 & \frac{1}{n} \\ \frac{1}{n} & 1 \end{pmatrix}. \quad (8)$$

We can obtain the following moment property of the complex Gaussian distribution.

Proposition 1. Assume an i.i.d. sample $\mathbf{x}_1, \mathbf{x}_2, \dots, \mathbf{x}_n \in \mathbb{C}^p$ follows the complex Gaussian distribution $\mathcal{CN}(\mathbf{0}, \boldsymbol{\Sigma})$ and \mathbf{S} is the sample covariance matrix; we have

$$\mathbb{E}[\text{tr}^2(\mathbf{W})] = \sum_{i=1}^p \sum_{j=1}^p \sum_{k=1}^p \sum_{l=1}^p \mathbb{E}[w_{ij}w_{kl}] = \sum_{i=1}^p \sum_{j=1}^p \sum_{k=1}^p \sum_{l=1}^p (b_1 \delta_{ij} \delta_{kl} + b_2 \delta_{il} \delta_{jk}) = b_1 \text{tr}^2(\mathbf{I}_p) + b_2 \text{tr}(\mathbf{I}_p), \quad (13)$$

where $b_1 = n^2$ and $b_2 = n$. For a random matrix \mathbf{W} which follows complex Wishart distribution $\mathcal{CW}(\boldsymbol{\Sigma}, n)$ with degree of freedom n , let $\boldsymbol{\Sigma} = \mathbf{G}\mathbf{G}^H$; then, we have $\mathbf{G}^{-1}\mathbf{W}\mathbf{G}^{-H} \sim \mathcal{CW}(\mathbf{I}_p, n)$. In the same manner, we can obtain

$$\mathbb{E}[\text{tr}^2(\mathbf{W})] = n^2 \text{tr}^2(\boldsymbol{\Sigma}) + n \text{tr}(\boldsymbol{\Sigma}^2). \quad (14)$$

Noticing that $n\mathbf{S} \sim \mathcal{CW}(\boldsymbol{\Sigma}, n)$, we can obtain

$$\mathbb{E}[\text{tr}^2(n\mathbf{S})] = n^2 \text{tr}^2(\boldsymbol{\Sigma}) + n \text{tr}(\boldsymbol{\Sigma}^2). \quad (15)$$

Therefore, we have

$$\mathbb{E}[\text{tr}^2(\mathbf{S})] = \text{tr}^2(\boldsymbol{\Sigma}) + \frac{1}{n} \text{tr}(\boldsymbol{\Sigma}^2). \quad (16)$$

By (10) and (16), equality (9) holds. \square

Theorem 1. When the target matrix is $\mathbf{T} = (\text{tr}(\mathbf{S})/p)\mathbf{I}_p$, the optimal shrinkage intensity under the complex Gaussian distribution is

$$w^* = \frac{p \text{tr}^2(\boldsymbol{\Sigma}) - \text{tr}(\boldsymbol{\Sigma}^2)}{(p-n)\text{tr}^2(\boldsymbol{\Sigma}) + (np-1)\text{tr}(\boldsymbol{\Sigma}^2)} \in [0, 1]. \quad (17)$$

Proof. By plugging equalities (10) and (16) into (7), we have

$$\mathbb{E} \begin{pmatrix} \text{tr}(\mathbf{S}^2) \\ \text{tr}^2(\mathbf{S}) \end{pmatrix} = \mathbf{E}_n \begin{pmatrix} \text{tr}(\boldsymbol{\Sigma}^2) \\ \text{tr}^2(\boldsymbol{\Sigma}) \end{pmatrix}. \quad (9)$$

Proof. Because the sample $\mathbf{x}_1, \mathbf{x}_2, \dots, \mathbf{x}_n \in \mathbb{C}^p$ follows a complex Gaussian distribution with mean $\mathbf{0}$, we have $n\mathbf{S} \sim \mathcal{CW}(\boldsymbol{\Sigma}, n)$. By the moment properties of complex Wishart distribution [22], we can obtain

$$\mathbb{E}[\text{tr}(\mathbf{S}^2)] = \text{tr}(\boldsymbol{\Sigma}^2) + (1/n)\text{tr}^2(\boldsymbol{\Sigma}). \quad (10)$$

Furthermore, when a random matrix $\mathbf{W} = (w_{ij})_{p \times p}$ follows complex Wishart distribution $\mathcal{CW}(\mathbf{I}_p, n)$ with degree of freedom n , we have

$$\text{tr}(\mathbf{W}) = \sum_{i=1}^p \sum_{j=1}^p w_{ij}, \quad (11)$$

$$\text{tr}^2(\mathbf{W}) = \sum_{i=1}^p \sum_{j=1}^p \sum_{k=1}^p \sum_{l=1}^p w_{ij}w_{kl}. \quad (12)$$

By taking expectation on both sides, we have

$$\mathbb{E}[\text{tr}(\mathbf{S}^2)] - \frac{1}{p} \mathbb{E}[\text{tr}^2(\mathbf{S})] = \frac{np-1}{np} \text{tr}(\boldsymbol{\Sigma}^2) + \frac{p-n}{np} \text{tr}^2(\boldsymbol{\Sigma}). \quad (18)$$

Therefore, we can obtain

$$w^* = 0 \wedge \frac{p \text{tr}^2(\boldsymbol{\Sigma}) - \text{tr}(\boldsymbol{\Sigma}^2)}{(p-n)\text{tr}^2(\boldsymbol{\Sigma}) + (np-1)\text{tr}(\boldsymbol{\Sigma}^2)} \sqrt{1}. \quad (19)$$

By Cauchy-Schwarz inequality, we have $w^* \in [0, 1]$. Hence, we have

$$w^* = \frac{p \text{tr}^2(\boldsymbol{\Sigma}) - \text{tr}(\boldsymbol{\Sigma}^2)}{(p-n)\text{tr}^2(\boldsymbol{\Sigma}) + (np-1)\text{tr}(\boldsymbol{\Sigma}^2)} \in [0, 1]. \quad (20)$$

By Theorem 1, the corresponding optimal linear shrinkage estimator is

$$\hat{\boldsymbol{\Sigma}} = (1 - w^*)\mathbf{S} + w^* \frac{\text{tr}(\mathbf{S})}{p} \mathbf{I}_p. \quad (21)$$

We remind that the optimal shrinkage estimator concerns with the real covariance matrix. Thus, it is unavailable in practical applications. Despite this, it provides a theoretical optimal value for evaluating the available ones. \square

3. Available Linear Shrinkage Estimator

Theorem 2. Under the complex Gaussian distribution, the unbiased estimates of $\text{tr}(\Sigma^2)$ and $\text{tr}^2(\Sigma)$ are, respectively, given by

$$\begin{aligned}\alpha &= \frac{1}{n^2 - 1} (n^2 \text{tr}(\mathbf{S}^2) - n \text{tr}^2(\mathbf{S})), \\ \beta &= \frac{1}{n^2 - 1} (n^2 \text{tr}^2(\mathbf{S}) - n \text{tr}(\mathbf{S}^2)).\end{aligned}\quad (22)$$

Proof. Because the inverse matrix of \mathbf{E}_n is

$$\mathbf{E}_n^{-1} = \frac{n^2}{n^2 - 1} \begin{pmatrix} 1 & \frac{1}{n} \\ -\frac{1}{n} & 1 \end{pmatrix}, \quad (23)$$

we have

$$\mathbb{E} \left(\mathbf{E}_n^{-1} \begin{pmatrix} \text{tr}(\mathbf{S}^2) \\ \text{tr}^2(\mathbf{S}) \end{pmatrix} \right) = \begin{pmatrix} \text{tr}(\Sigma^2) \\ \text{tr}^2(\Sigma) \end{pmatrix}. \quad (24)$$

Therefore, we can obtain

$$\begin{aligned}\mathbb{E}[\alpha] &= \text{tr}(\Sigma^2), \\ \mathbb{E}[\beta] &= \text{tr}^2(\Sigma),\end{aligned}\quad (25)$$

revealing that α and β are unbiased estimates of $\text{tr}(\Sigma^2)$ and $\text{tr}^2(\Sigma)$, respectively.

Through plugging the unbiased estimates given by (22) into the optimal shrinkage intensity w^* , we can obtain the available shrinkage intensity:

$$\hat{w} = 0 \wedge \frac{p\beta - \alpha}{(p-n)\beta + (np-1)\alpha} \vee 1. \quad (26)$$

Therefore, the available linear shrinkage estimator is

$$\hat{\Sigma} = (1 - \hat{w})\mathbf{S} + \hat{w} \frac{\text{tr}(\mathbf{S})}{p} \mathbf{I}_p. \quad (27)$$

The linear shrinkage estimator given by (27) is positive definite even when the dimension exceeds the sample size, except that $\hat{\Sigma}$ degenerates into the SCM. \square

4. Numerical Simulations and Adaptive Beamforming

In this section, we provide some numerical simulations and an example application to adaptive beamforming for verifying the performance of the proposed covariance matrix estimator. The proposed linear shrinkage estimator is denoted as T1cg. The linear shrinkage estimator corresponding to the spherical target matrix in [18] is denoted as T1cv.

4.1. Numerical Simulations. As mentioned before, an accurate shrinkage intensity estimate can benefit the linear shrinkage estimator. In this section, we compare the

proposed available shrinkage intensity and the existing one based on crossvalidation in [18] to reveal the advantage of the proposed shrinkage estimator. In our simulations, the real covariance matrix is $\Sigma = (\sigma_{ij})_{p \times p}$ with

$$\sigma_{ij} = t^{|i-j|}. \quad (28)$$

The model parameter t is set to be 0.5, resulting in the real covariance matrix being close to a spherical structured matrix. The data come from the complex Gaussian distribution $\mathcal{CN}(\mathbf{0}, \Sigma)$. The MSE of each available shrinkage intensity relative to the optimal intensity given by (17) is computed by averaging 5×10^4 Marlo runs.

Figure 1 reports the MSEs of available shrinkage intensities versus the sample size and the dimension. We can see that the MSEs of available shrinkage intensities in T1cv and T1cg decrease as the sample size or the dimension gets larger. Because the proposed T1cg by plugging in the unbiased estimates of unknown scalars employs the complex Gaussian distribution information, it outperforms the T1cv based on the nonparameter approach.

4.2. Adaptive Beamforming. In this section, we apply the proposed covariance estimators to array signal processing. Specifically, we consider a uniform linear array (ULA) which consists of p sensors with half-wavelength spacing. At time $t = 1, \dots, n$, the received signal can be modeled as

$$\mathbf{x}(t) = \mathbf{a}(\theta_0)s_0(t) + \sum_{k=1}^K \mathbf{a}(\theta_k)s_k(t) + \mathbf{n}(t) \in \mathbb{C}^p, \quad (29)$$

where θ_0 and θ_k are the directions of desired signal $s_0(t)$ and interference signals $s_k(t)$, respectively, $\mathbf{a}(\theta_0)$ and $\mathbf{a}(\theta_k)$ are the corresponding array responses, and $\mathbf{n}(t)$ is the noise [23]. Then, the minimum variance distortionless response (MVDR) beamformer is expressed as

$$\mathbf{w} = \frac{\Sigma^{-1} \mathbf{a}(\theta_0)}{\mathbf{a}(\theta_0)^H \Sigma^{-1} \mathbf{a}(\theta_0)}. \quad (30)$$

The covariance matrix Σ in (30) is unknown and suggested to be replaced with its estimate $\hat{\Sigma}$ [24]. Then, the corresponding output signal-to-interference-plus-noise ratio (SINR) is

$$\text{SINR} = \frac{\sigma_0^2 |\hat{\mathbf{w}}^H \mathbf{a}(\theta_0)|^2}{\hat{\mathbf{w}}^H (\hat{\Sigma} - \mathbf{a}(\theta_0)\mathbf{a}(\theta_0)^H) \hat{\mathbf{w}}}, \quad (31)$$

where $\hat{\mathbf{w}}$ is the estimated beamformer corresponding to $\hat{\Sigma}$. The covariance matrix estimator with larger output SINR is preferred in array signal processing.

In our simulations, we assume the desired signal has an angle of arrival of $\theta_0 = 5^\circ$ with power $\sigma_0^2 = 10$ dB, and the interference signals come from the directions $\{-10^\circ, 0^\circ, 10^\circ\}$ with power 8 dB. For each covariance estimator, the corresponding output SINR is approximated by averaging 5×10^6 repetitions.

Figures 2 and 3 report the SINR and corresponding elapsed time of the adaptive beamformers based on different

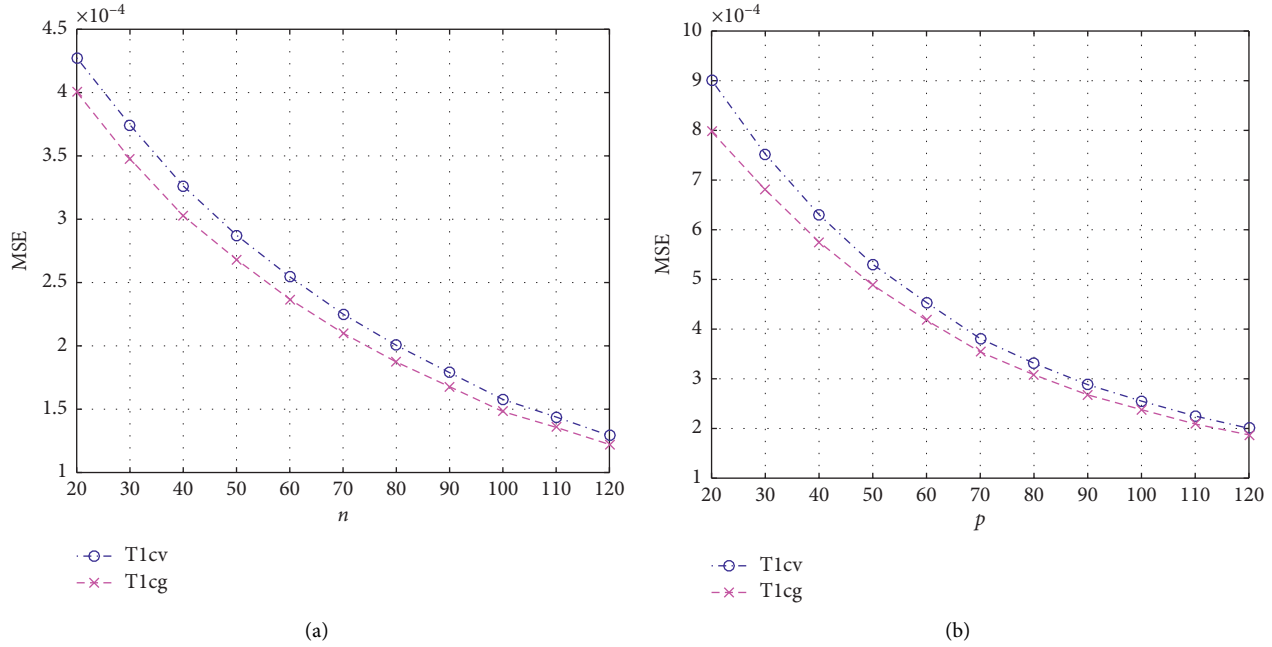


FIGURE 1: The MSEs of available shrinkage intensities when $p = 60$ (a) and $n = 60$ (b).

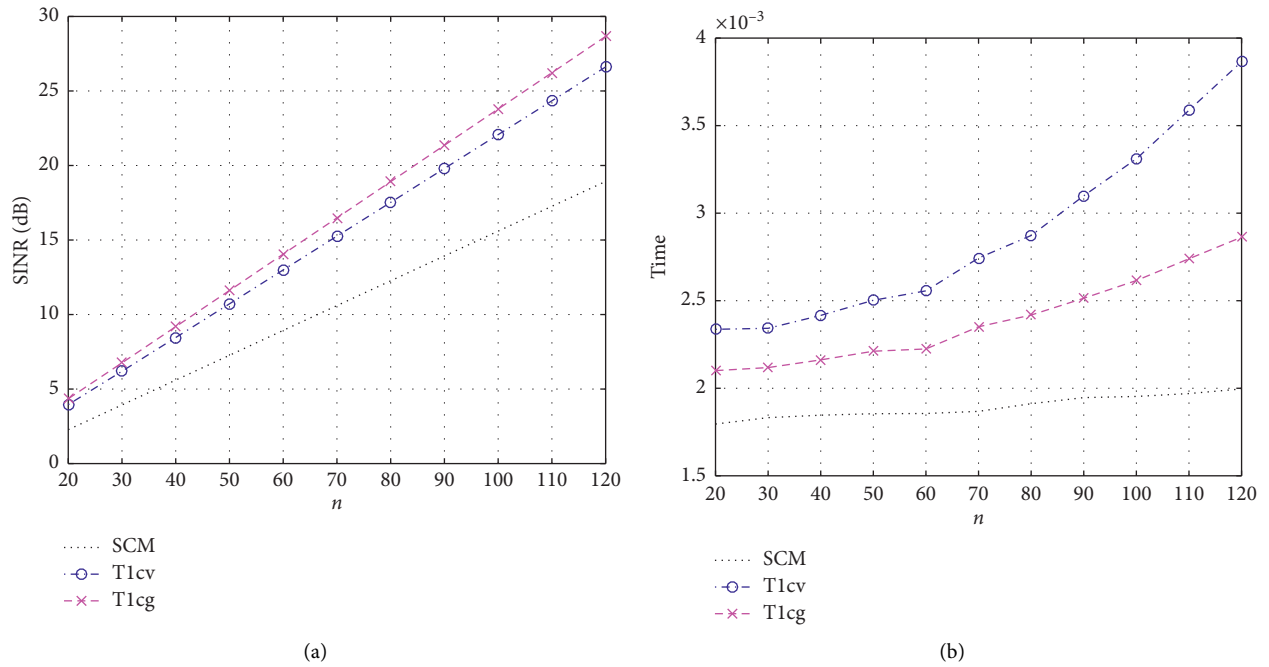


FIGURE 2: The SINR (a) and corresponding elapsed time (b) of adaptive beamformer based on each covariance matrix estimator versus the sample size under the complex Gaussian distribution.

covariance matrix estimators under the complex Gaussian scenario, where the noise $\mathbf{n}(t)$ follows the complex Gaussian distribution with power 0 dB. In Figure 2, the dimension is $p = 60$ and the sample size ranges from 20 to 120. In Figure 3, the sample size is $n = 60$ and the dimension ranges from 20 to 120. Our observations and analyses are summarized as follows:

- (1) Even though enjoying the lowest computation cost, the classic covariance estimator SCM has an unsatisfactory performance in small sample size scenarios. Therefore, it is not an ideal covariance matrix estimator any more in these scenarios.
- (2) The SINR based on each covariance matrix estimator increases when the sample size gets larger but

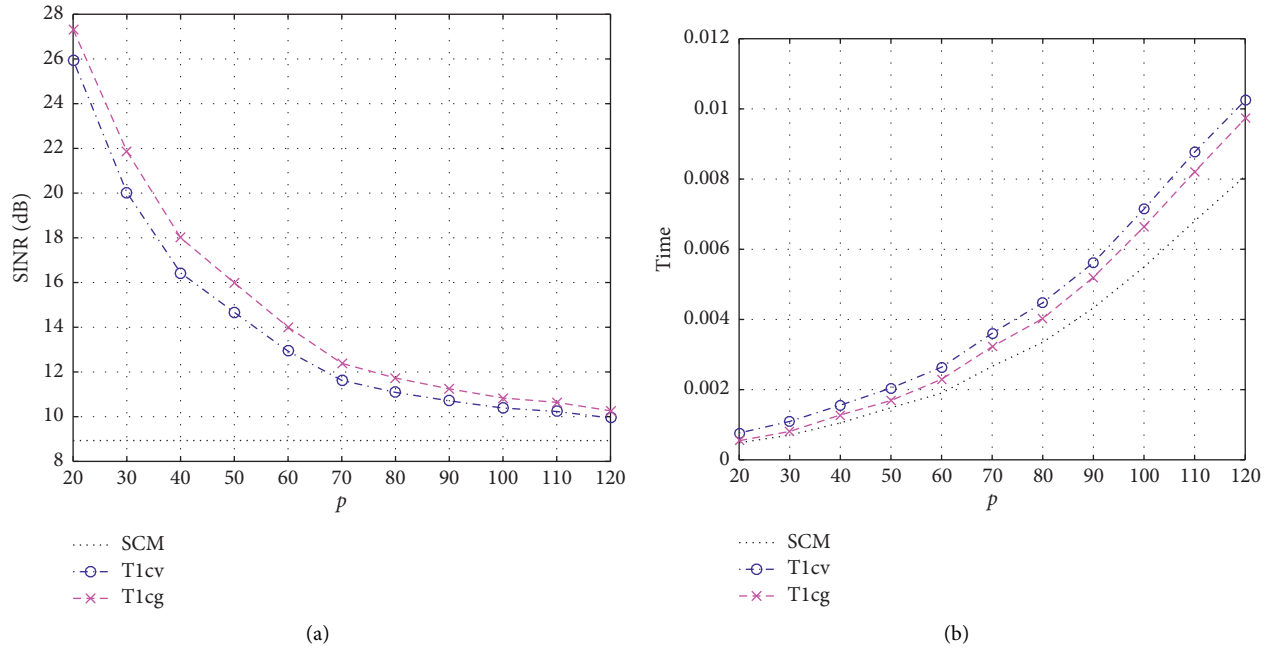


FIGURE 3: The SINR (a) and corresponding elapsed time (b) of adaptive beamformer based on each covariance matrix estimator versus the dimension under the complex Gaussian distribution.

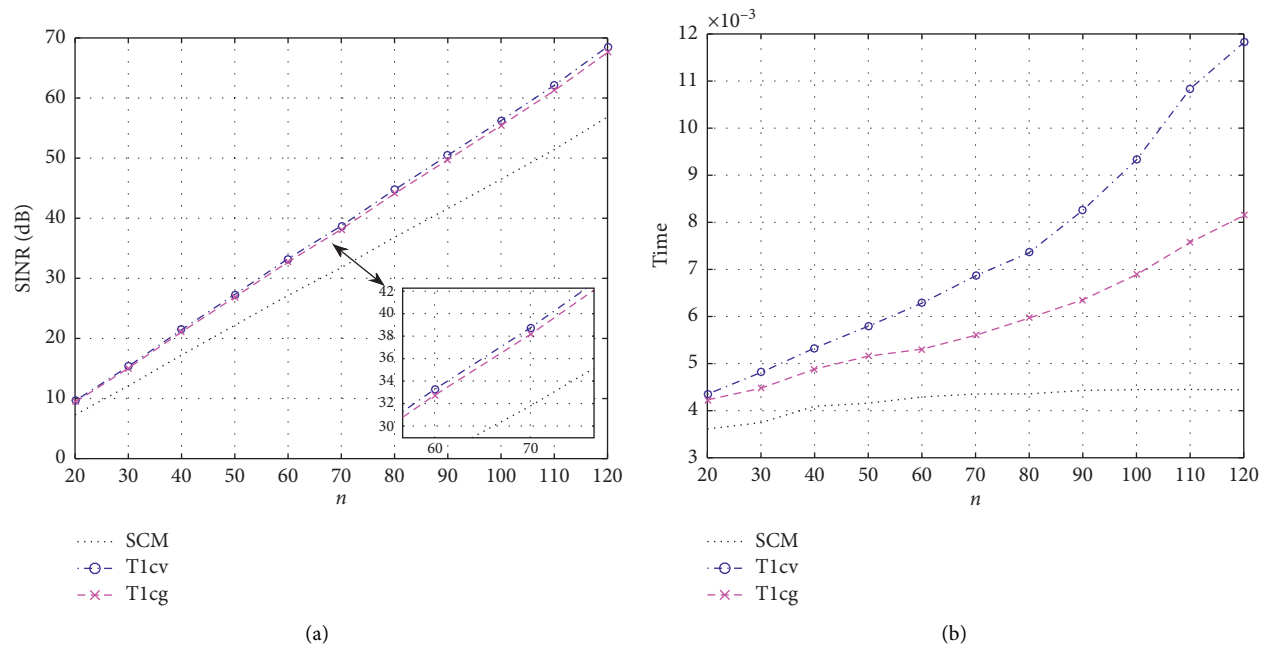


FIGURE 4: The SINR (a) and corresponding elapsed time (b) of adaptive beamformer based on each covariance matrix estimator versus the sample size under the complex non-Gaussian distribution.

decreases when the dimension gets larger. It reveals that the covariance matrix estimators play an important role in adaptive beamforming in large dimension and small sample size scenarios.

- (3) Both the proposed shrinkage estimator T1cg and the existing shrinkage estimator T1cv outperform the SCM with an additional but reasonable

computation cost. Furthermore, the proposed T1cg dominates the T1cv on both SINR and computation cost because the signal comes from the complex Gaussian distribution in the simulation setting, and the proposed covariance matrix estimator has considered the specific distribution information.

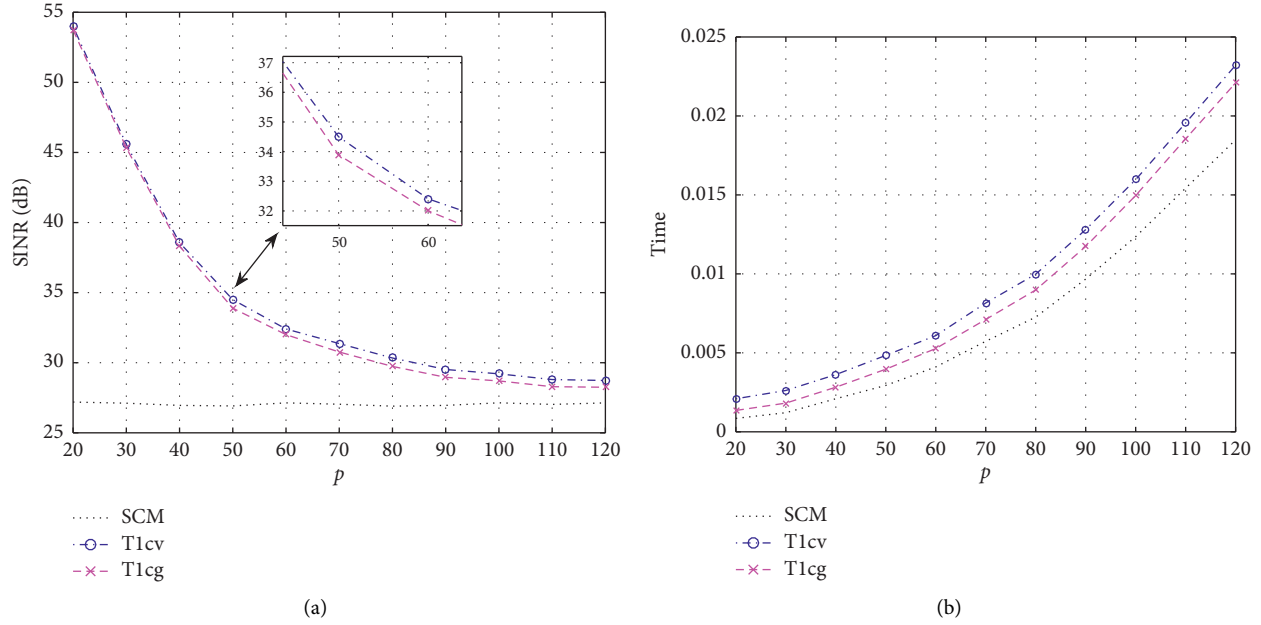


FIGURE 5: The SINR (a) and corresponding elapsed time (b) of adaptive beamformer based on each covariance matrix estimator versus the dimension under the complex non-Gaussian distribution.

Figures 4 and 5 report the SINR and corresponding elapsed time of the adaptive beamformers when each variate in the noise follows the complex Gaussian mixture distribution $0.3\mathcal{CN}(-20, 1) + 0.4\mathcal{CN}(0, 1) + 0.3\mathcal{CN}(20, 1)$ with power 6 dB. We can see that the SINR and elapsed time show the same varying tendencies, as in Figures 2 and 3. When the received signal comes from the complex non-Gaussian distribution, the proposed estimator T1cg performs inferior to the existing T1cv in adaptive beamforming. It is worthy noticing that both T1cg and T1cv have analytical expressions, and there are $(np^2 + np + 3p^2)$ multiplication in the proposed estimators T1cg and $(np^2 + 3np + 5p^2)$ multiplication in T1cv. Therefore, the proposed T1cg can always enjoy a lower computation complexity than T1cv.

On the whole, by employing additional distribution information, the proposed estimator T1cg outperforms T1cv in the complex Gaussian scenario and enjoys a comparable performance with T1cv in the complex non-Gaussian scenario. Moreover, the proposed estimator T1cg always enjoys an advantage over T1cv in computation cost.

5. Conclusion

In this paper, we have proposed a new covariance matrix estimator via linear shrinkage procedure under the complex Gaussian distribution. Through calculating the moment of Wishart distribution, we obtain the optimal shrinkage intensity for the spherical target. Furthermore, the involved unknown scalars are unbiasedly estimated. Subsequently, we propose the corresponding available linear shrinkage estimator. Numerical simulations and application to adaptive beamforming show that the proposed covariance matrix estimator is outperformed compared with the existing estimators. In future work, we will investigate the Cramér–Rao

bound for the linear shrinkage estimation and develop nonlinear shrinkage estimation of the large-dimensional covariance matrix.

Data Availability

All data included in this study are available from the corresponding author upon request.

Conflicts of Interest

The authors declare that there are no conflicts of interests regarding the publication of this paper.

Acknowledgments

This work was supported in part by the Youth Research Foundation of Hubei Minzu University under Grant MY2017Q021.

References

- [1] J. Bai and S. Shi, “Estimating high dimensional covariance matrices and its applications,” *Annals of Economics and Finance*, vol. 12, no. 2, pp. 199–215, 2011.
- [2] B. D. Van Veen, “Adaptive convergence of linearly constrained beamformers based on the sample covariance matrix,” *IEEE Transactions on Signal Processing*, vol. 39, no. 6, pp. 1470–1473, 1991.
- [3] Z. Bai and J. W. Silverstein, *Spectral Analysis of Large Dimensional Random Matrices*, Springer, New York, NY, USA, 2010.
- [4] F. Gini and M. Greco, “Covariance matrix estimation for CFAR detection in correlated heavy tailed clutter,” *Signal Processing*, vol. 82, no. 12, pp. 1847–1859, 2002.

- [5] D. M. Witten and R. Tibshirani, "Covariance-regularized regression and classification for high dimensional problems," *Journal of the Royal Statistical Society: Series B (Statistical Methodology)*, vol. 71, no. 3, pp. 615–636, 2009.
- [6] O. Ledoit and M. Wolf, "Improved estimation of the covariance matrix of stock returns with an application to portfolio selection," *Journal of Empirical Finance*, vol. 10, no. 5, pp. 603–621, 2003.
- [7] T. T. Cai and M. Yuan, "Adaptive covariance matrix estimation through block thresholding," *The Annals of Statistics*, vol. 40, no. 4, pp. 2014–2042, 2012.
- [8] A. J. Rothman, "Positive definite estimators of large covariance matrices," *Biometrika*, vol. 99, no. 3, pp. 733–740, 2012.
- [9] O. Besson and Y. I. Abramovich, "Regularized covariance matrix estimation in complex elliptically symmetric distributions using the expected likelihood approach-Part 2: the under-sampled case," *IEEE Transactions on Signal Processing*, vol. 61, no. 23, pp. 5819–5829, 2013.
- [10] J. Bien, F. Bunea, and L. Xiao, "Convex banding of the covariance matrix," *Journal of the American Statistical Association*, vol. 111, no. 514, pp. 834–845, 2016.
- [11] T. J. Fisher and X. Sun, "Improved Stein-type shrinkage estimators for the high-dimensional multivariate normal covariance matrix," *Computational Statistics & Data Analysis*, vol. 55, no. 5, pp. 1909–1918, 2011.
- [12] X. Chen, Z. J. Wang, and M. J. McKeown, "Shrinkage-to-tapering estimation of large covariance matrices," *IEEE Transactions on Signal Processing*, vol. 60, no. 11, pp. 5640–5656, 2012.
- [13] J. Schäfer and K. Strimmer, "A shrinkage approach to large-scale covariance matrix estimation and implications for functional genomics," *Statistical Applications in Genetics and Molecular Biology*, vol. 4, no. 1, pp. 1–32, 2009.
- [14] Y. Ikeda, T. Kubokawa, and M. S. Srivastava, "Comparison of linear shrinkage estimators of a large covariance matrix in normal and non-normal distributions," *Computational Statistics & Data Analysis*, vol. 95, pp. 95–108, 2016.
- [15] Y. Konno, "Shrinkage estimators for large covariance matrices in multivariate real and complex normal distributions under an invariant quadratic loss," *Journal of Multivariate Analysis*, vol. 100, no. 10, pp. 2237–2253, 2009.
- [16] Y. Liu, X. Sun, and S. Zhao, "A covariance matrix shrinkage method with Toeplitz rectified target for DOA estimation under the uniform linear array," *AEÜ-International Journal of Electronics and Communications*, vol. 81, pp. 50–55, 2017.
- [17] B. Zhang, J. Zhou, and J. Li, "Improved shrinkage estimators of covariance matrices with Toeplitz-structured targets in small sample scenarios," *IEEE Access*, vol. 7, pp. 116 785–116 798, 2019.
- [18] J. Tong, R. Hu, J. Xi, Z. Xiao, Q. Guo, and Y. Yu, "Linear shrinkage estimation of covariance matrices using low-complexity cross-validation," *Signal Processing*, vol. 148, pp. 223–233, 2018.
- [19] Y. Chen, A. Wiesel, Y. C. Eldar, and A. O. Hero, "Shrinkage algorithms for MMSE covariance estimation," *IEEE Transactions on Signal Processing*, vol. 58, no. 10, pp. 5016–5029, 2010.
- [20] A. Hannart and P. Naveau, "Estimating high dimensional covariance matrices: a new look at the Gaussian conjugate framework," *Journal of Multivariate Analysis*, vol. 131, no. 131, pp. 149–162, 2014.
- [21] O. Ledoit and M. Wolf, "A well-conditioned estimator for large-dimensional covariance matrices," *Journal of Multivariate Analysis*, vol. 88, no. 2, pp. 365–411, 2004.
- [22] J. A. Tague and C. I. Caldwell, "Expectations of useful complex Wishart forms," *Multidimensional Systems and Signal Processing*, vol. 5, no. 3, pp. 263–279, 1994.
- [23] X. Mestre and M. A. Lagunas, "Finite sample size effect on minimum variance beamformers: optimum diagonal loading factor for large arrays," *IEEE Transactions on Signal Processing*, vol. 54, no. 1, pp. 69–82, 2006.
- [24] J. Serra and M. Nájar, "Asymptotically optimal linear shrinkage of sample LMMSE and MVDR filters," *IEEE Transactions on Signal Processing*, vol. 62, no. 14, pp. 3552–3564, 2014.